# Methods of Evaluation of the Positioning Capability of Cartesian and Non-Cartesian Machines

Andrew Peter Longstaff

A thesis submitted to the University of Huddersfield
in partial fulfilment of the requirements for
the degree of Doctor of Philosophy

The University of Huddersfield

April 2002

# Abstract

Manufacture and assembly of ever more precise components has been the driving force for many research projects. Error avoidance and error correction are used to improve the accuracy of the final output, but it is only by error evaluation that a manufacturer can quantify his production capability.

The ability of a machine to perform the task designated to it is of critical importance. In particular it is essential to be able to determine the capability of a production machine to produce a part accurately, a measuring machine to dimension a part reliably or a handling machine to place a part in the appropriate position. In order to achieve this it is necessary to establish the positioning accuracy of the device throughout its working volume.

In addition to the need for the assessment of machining performance, there is a strong desire within the machine-building community to allow for the post-assembly correction of errors inherent in the manufacture of machines. Such techniques are often a cost-effective complement to error avoidance.

During this project, a new geometric model and supporting measurement methods are produced for the evaluation of errors in Cartesian-based machines. This work is an extension of that performed by Ford, *et. al.* [1] as discussed in chapter 3. The new work addresses the previously unresolved problem of determining the errors throughout the working volume of a machine with volumetric compensation and a tool or probe offset. This simulation method is in contrast to other techniques that quantify machine performance based upon a small subset of the machine volume.

It is proposed that a figure for volumetric accuracy derived from these methods cannot stand on its own as a description of the manufacturing capability of a machine. The effects of measurement uncertainty on the synthesis technique have been examined and modelled. This has produced a method of quantifying machining capability based upon machine configuration, tool or head configuration, and supported by uncertainty based upon the test data input to the model.

An alternative method of evaluating errors through the working volume is to measure directly using, for example, a tracking laser. One such system (LaserTrace) is based upon absolute position being resolved by trilateration from two tracking lasers. This system has been investigated for its applicability to the measurement process. Two methods have been produced to improve the accuracy of the system and reduce the time required for its calibration. One is based upon photogrammetry techniques, the other on a novel use of a

machine checking gauge (MCG). The artefact is used for acquisition of data to perform parameter identification on a model of the system that has been found from first principles.

This MCG-based calibration technique was successful, within the constraints of the resolution and repeatability of the control loop. Attempts were then made to apply this methodology to a second machine of the non-Cartesian type and configuration (UMD). Simulation shows this technique to be applicable, but the instability of the prototype precluded comprehensive on-machine testing.

In the course of this research a thermal model of the UMD has also been produced to overcome the sensitivity of the prototype device to temperature changes. Such a model could be used to provide software correction of UMD position values.

## Acknowledgements

The author would like to thank Professor Derek Ford and Dr Mike Freeman for their immense patience in supervising the project and providing support and guidance throughout the duration of the work.

The author would also like to thank Dr Scott Postlethwaite for both his technical expertise and encouragement whenever it was needed. His constant reminder of the reality of how small a micron really is should not be ignored.

The author would also like to thank Steve Millwood for his technical and software support. His supporting contribution has been invaluable for the majority of research work within the team.

Thanks also to Mike Mavromihales for his input in an advisory capacity.

Thanks also to the establishments who have provided both impetus and feedback for many aspects of the work. In particular UK Robotics, Renishaw Plc, ITP, DS Technologie, Rolls Royce and the various companies who allowed testing time on their production machines.

Thanks also to the members of the two EC projects [2, 3] who supported the work on Cartesian machine evaluation discussed in chapter 3 and chapter 4.

Finally, the author extends extreme gratitude to the members of his family, friends and colleagues who have helped in many ways, both professionally and personally. Their contribution is immeasurable.

# Table of contents

# Table of figures

# Equations

# Tables

# Glossary of terms

General

| | |
|---|---|
| BS | British Standard |
| CMM | Coordinate Measuring Machine |
| CNC | Computer Numerically Controlled |
| ESP | Error Simulation Program |
| ISO | International Standards Organisation |
| IPP | In-process probing |
| MCG | Machine Checking Gauge |
| MCP | Measurement Centre Point – the point for which volumetric errors are conventionally calculated |
| NC | Numerical Control |
| TCP | Tool Centre Point – the actual point of machining or probing. |
| UMD | Universal Measuring Device – a prototype non-Cartesian device |
| UoH | University of Huddersfield |
| VCS | Volumetric compensation system – a software-based compensation solution for geometric errors in machine tools |
| VMC | Vertical Machining Centre |

LaserTrace

| | |
|---|---|
| BEP | Beam Emergent Point |
| BRP | Beam Reference Point |
| Cat's eye | An optic made of two hemispherical lenses (see section 5.03.2) |

UMD

| | |
|---|---|
| 3bcup | Three ball cup used in place of touch trigger probe for efficient probing of the rubies on the ballplate calibration artefact |

Uncertainty of measurement

| | |
|---|---|
| Type A | method of evaluation of uncertainty by the statistical analysis of series of observations |
| Type B | method of evaluation of uncertainty by means other than the statistical analysis of series of observations |

# Nomenclature

Cartesian machine error calculation

| | |
|---|---|
| B | 'Bottom' axis – carries either the middle axis or the workpiece |
| M | 'Middle' axis – carries either the top axis or the workpiece |
| T | 'Top' axis – carries the tool |
| wBMTt | 'All axes carry the tool' configuration of three-axis Cartesian machine |
| BwMTt | 'One axis carries the workpiece' configuration of three-axis Cartesian machine |
| BMwTt | 'two axes carry the workpiece' configuration of three-axis Cartesian machine |
| $B_{error}$ | Error in B-axis |
| $M_{error}$ | Error in M-axis |
| $T_{error}$ | Error in T-axis |
| $B_{lin}$ | Linear positioning error in B-axis direction |
| $M_{lin}$ | Linear positioning error in M-axis direction |
| $T_{lin}$ | Linear positioning error in T-axis direction |
| $M_{str(B)}$ | Middle axis straightness in the B axis direction |
| $T_{str(B)}$ | Top axis straightness in the B axis direction |
| $B_{str(M)}$ | Bottom axis straightness in the M axis direction |
| $T_{str(M)}$ | Top axis straightness in the M axis direction |
| $B_{str(T)}$ | Bottom axis straightness in the T axis direction |
| $M_{str(T)}$ | Middle axis straightness in the T axis direction |
| $\varphi_{M(B)}$ | Bottom axis rotation about the middle axis |
| $\varphi_{T(B)}$ | Bottom axis rotation about the top axis |
| $\varphi_{B(B)}$ | Bottom axis rotation about the bottom axis |
| $\varphi_{M(T)}$ | Top axis rotation about the middle axis |
| $\varphi_{T(T)}$ | Top axis rotation about the top axis |
| $\varphi_{B(T)}$ | Top axis rotation about the bottom axis |
| $\varphi_{M(M)}$ | Middle axis rotation about the middle axis |
| $\varphi_{T(M)}$ | Middle axis rotation about the top axis |
| $\varphi_{B(M)}$ | Middle axis rotation about the bottom axis |
| $BM_{sqr}$ | Squareness between the bottom and middle axes |
| $BT_{sqr}$ | Squareness between the bottom and top axes |
| $MT_{sqr}$ | Squareness between the middle and Top axes |
| $\gamma_{K(L)}$ | Is the general description of the mechanical L-axis rotation about the K-axis. |

Uncertainty of Measurement

| | |
|---|---|
| u(y) | The standard uncertainty in y |
| s | The standard deviation |
| a | Half the range of uncertainty for a rectangular distribution |
| $u_c$ | Combined uncertainty |
| k | Coverage factor |
| U | Expanded uncertainty |

LaserTrace

| | |
|---|---|
| $X_{BEP}$ | X-coordinate of the beam emergent point |
| $X_{BRP}$ | X-coordinate of the beam reference point |
| $Y_{BEP}$ | Y-coordinate of the beam emergent point |
| $Y_{BRP}$ | Y-coordinate of the beam reference point |
| $Z_{BEP}$ | Z-coordinate of the beam emergent point |
| $Z_{BRP}$ | Z-coordinate of the beam reference point |
| M | Normal separation of LaserTrace mirrors |
| $\varphi$, $\theta$ | Angles of steering mirrors |
| d | Magnitude of vector between LaserTrace and optic |
| l, m, n | Direction cosines for emergent beam |

MCG calibration of LaserTrace

| | |
|---|---|
| $(a_{pivot}, b_{pivot}, c_{pivot})$ | Cartesian coordinate of centre of MCG pivot |
| $(a_{optic}, b_{optic}, c_{optic})$ | Cartesian coordinate of centre of MCG optic |
| $R_{MCG}$ | Radius of MCG sphere |

UMD

| | |
|---|---|
| p, q | Angle of horizontal barn door |
| r | Angle of vertical barn door |

# Chapter 1 Introduction

## 1.01 Machine utilisation

As manufacturing industry strives for higher productivity, there is a drive towards the manufacture of more precise components in terms of dimension, form and geometry [4]. The ability to produce accurate components has many advantages. For example, the resultant reduction in tolerances can allow the production of more accurate assemblies, thus widening the possible production range of a machine shop. Additionally, if components can be manufactured to a high precision and part-handling robots can operate with good accuracy a reduction in hand fitting can also be achieved.

Using a machine capable of producing accurate components results in a reduction in both reworking of components and scrapped parts. This has obvious economic and throughput advantages, as does the potential for more efficient use of resources by roughing and finishing on the same machine. Indeed, if a machine can be proven to perform with sufficient accuracy and repeatability, some dimensional checking of components by probing could also be performed on the manufacturing machine. Such component checking is termed "in-process probing" (IPP) or "on-machine inspection" and is becoming more widely used. [5-7]

## 1.02 Component accuracy

Component accuracy is affected by three main sources: environmental effects, user effects and machine accuracy. [8]

Environmental effects derive from changes in temperature, humidity, pressure and from external vibrations. Of these, thermal changes can have the most significant effect, with the magnitude and frequency of the change and temperature gradients being important influencing factors.

User effects are those resulting from the work-piece, tooling and machining process. The work-piece considerations include weight, stiffness, stress levels and distortion, datum surface quality, temperature coefficient and method of clamping. Tool geometry, stiffness and wear can all have an impact on component accuracy, as can swarf build-up on the tool cutting edge. The machining process can affect component accuracy by incorrect use of feeds and speeds, chatter and coolant usage.

The third source of inaccuracy in a manufactured component results from the accuracy of the machine on which the component was produced. Influencing parameters include stiffness, vibration damping, thermal stability, encoder specification and alignment, controller update time, and susceptibility to wear. A major consideration is the geometry of the machine – the quality of the various structural elements and the exactness with which they can be incorporated on the machine.

## 1.03 Geometric error of Cartesian machines

Perhaps the best understood of the errors in a Cartesian machine tool are the geometric errors in the machine axes. For each axis, these errors comprise three translation errors (linear positioning and two straightness errors) and three rotation errors (roll, pitch and yaw). These errors are summarised in figure 1.1 with their conventional names.

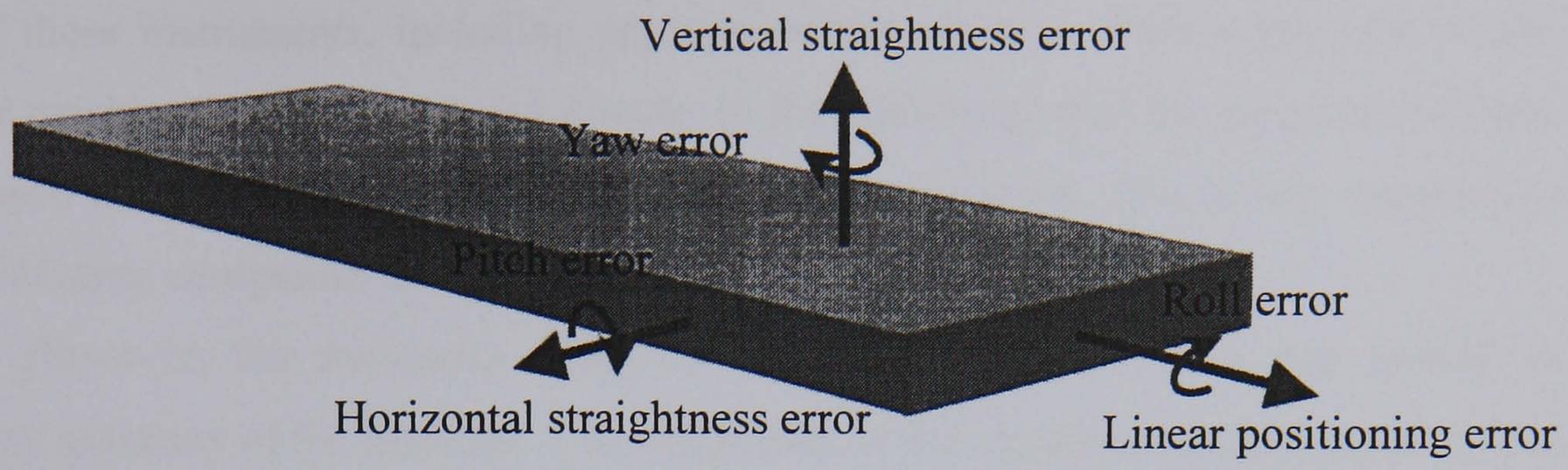


**Figure 1.1: Geometric errors in a Cartesian machine tool axis**

In addition to the six errors in each axis, the squareness between it and the other machine axes also has an effect on component accuracy. For a three-axis Cartesian machine there are, therefore, twenty-one sources of geometric error (table 1.1).

**Table 1.1: Number of geometric errors in a three-axis Cartesian machine**

| Error | Number per axis | Total |
|---|---|---|
| **Linear position** | 1 | 3 |
| **Straightness** | 2 | 6 |
| **Rotation about perpendicular axis** | 3 | 9 |
| **Squareness between axes** | - | 3 |
| **Total** | 6 | **21** |

Linear position, straightness, pitch and yaw errors in a Cartesian axis are commonly measured using a laser interferometer. World-wide, the main suppliers of such measurement equipment are the US-based manufacturers Hewlett-Packard [9] and the UK-based Renishaw Plc [10], although other manufacturers such as API [11] are attempting to break into the market.

Another commonly employed measurement system is the Talyvel electronic dual-level. Each Talyvel unit consists of a pendulum capable of angular measurement to a resolution of one tenth of an arc-second. Angular effects, such as the roll of a horizontal axis, are measured by mounting one Talyvel near the tool and another where a workpiece would be held. The errors in squareness between each pair of axes can be measured using either the laser, or more commonly by probing a precision granite block using a dial test indicator. The results of a ballbar measurement can also be used to measure squareness. [12]

ISO 230 parts 1 and 2 [13,14] provide an international standard governing the correct use of these instruments, including appropriate test regimes. Such a standard means that similar machines can be compared directly in the knowledge that the measurement data will have been taken in a similar manner, using similar equipment. This is very important when the calibrating companies are different for each machine.

However, the measured errors do not necessarily provide a true picture of the effective accuracy of the machine. The magnitude of the angular errors can certainly be used as comparative indices, but do not reveal the error that would be induced in a manufactured component. Section 2.03.1 and chapter 3 discuss methods of estimating the effect of geometric inaccuracies on manufactured components by synthesis.

## 1.04 Verification of component accuracy

Since components often require post-manufacture dimensional verification, it is important that reliable measurement techniques can be used to prove the quality of the measurement machine used for this purpose. The main tool is the coordinate measuring machine (CMM), which is normally a Cartesian device used to measure single components or batches of parts by manual or CNC methods.

Such dimensional checking of components can also be performed on the machine used for manufacturing. Quinlan [6] lists some advantages of in-process probing (IPP). These include lower scrap and rework rates, rapid detection of manufacturing errors and a reduction in the amount of required post-process gauging. The greatest benefit derives from the fact that the part is already fixtured on the machine and probing can be referenced to component features, rather than a datum on a stationary fixture. Quinlan claims that a manual set-up taking between fifteen and forty-five minutes can be reduced to a one minute cycle on a machine.

Such component verification relies on the accuracy of the machine tool used for the purpose. Pettigrew [15] notes that IPP should not be thought of as a replacement for the use of a CMM. Geometric errors affecting the manufactured component will be manifest in the IPP and so will go undetected.

The ISO standard for performance of coordinate measuring machines (CMMs) [16] does not permit the use of lasers for calibration, but relies on length bars and step gauge technology to provide measurement data. Although this can be useful in measuring the probing capability of a machine in a single line, it does not give an accurate picture of the

measuring capability of the machine over the whole working volume. A method of quantifying the performance using standard, traceable metrological techniques would be of great benefit.

## 1.05 Machine design

While the end-user can minimise the environmental and user effects on a component by good manufacturing practices, the inherent accuracy of the machine is the responsibility of the machine tool builder. This must be achieved by good design and application of error avoidance techniques [8, 17, 18] and by stringent quality control at the build stage.

The majority of machine tools are based upon a Cartesian configuration. In general, such a machine has three perpendicular axes built up from standard components. In order to achieve better manufacturing capability each component and its interaction with other parts is analysed and design changes made. However, some manufacturers are embracing radical design concepts such as non-Cartesian machines to avoid some of the problems of standard machines [19].

NEOS [20] have developed a system called "TRICEPT" which is designed to exploit the greater rigidity that is achievable using a tripod configuration. The TRICEPT 600 series has a repeatability of twenty microns and positioning accuracy of two hundred microns. The TRICEPT 800 has ten-micron repeatability and fifty-micron accuracy, and achieves rate of motion of sixty metres per minute. Although such designs are intended to provide a greater rigidity than conventional Cartesian machines they still require error avoidance analysis and introduce further problems in the form of a more complex control problem.

Error avoidance by either the machine tool manufacturer or by the user can prove expensive to implement, making the final product more costly. By modelling the effects of the error sources residual after economic avoidance has been practised, it is possible to estimate the capability of a machine. Furthermore, if the effects of a measurable error are repeatable it may be possible to compensate for these effects.

## 1.06 Part assembly

Economic realities require that the components should not only be accurately manufactured but also rapidly assembled in order to maximise rates of output. In an automated workshop such assembly should be performed by robots. However, this only becomes effective if the robot can operate with a sufficient degree of accuracy to perform the assembly.

Additionally, robot programming must be sufficiently flexible to allow rapid adaptation for the range of products for which it is required.

The number of robots being used world-wide is a small fraction of that predicted a generation ago [21]. Although robots are now more powerful, faster and more accurate, the technology differs little from that employed in the early nineteen eighties. Technologies such as adaptive control and off-line programming have yet to be extensively adopted in the industrial workplace, despite their potential benefits.

Because of the slow migration to more adaptable methods of control, industrial robot installations tend to remain restricted to a few specific applications. In the UK 53 percent of all robot installations are in the automotive industry [22]. The processing of rubber and plastics is the only other major robot user at 23 percent of installations. Spot welding is the single largest application of robots (reflecting the large proportion of usage in the car industry.)

To increase the number of robot installations a greater user base of small to medium companies must be established. This can be best achieved by making robot control more flexible by the implementation of off-line programming control. This can only be achieved by the availability of a geometrically accurate robot model to the control software. To provide such a model the relevant characteristics must be calibrated.

## 1.07 Robot control – on-line programming

Early industrial robots were designed to perform specific, repetitive jobs. Computer programming was still a highly labour intensive, time consuming task with few available experts. It was therefore deemed most cost-effective to use an on-line method of robot programming called a 'teaching pendant.'

The teaching pendant requires an operator to move the robot head to the positions and orientations required to perform each operation for a particular job. At each position the encoder values for each joint are recorded, thus specifying the pose. The robot can then perform the desired task by recreating the necessary sequence of encoder values. Any intermediate moves required for collision avoidance must be programmed in the same way.

The teaching pendant strategy was initially simple to implement, but the time required to programme the robot is obviously related to the complexity of the task. This method is more prohibitive for continuous-motion tasks, such as welding, than for discrete positioning tasks such as assembly. Additionally, this method of programming requires

direct human-machine interaction which is potentially dangerous. The discussed disadvantages are magnified since reprogramming is necessary after any robot maintenance during which robot parameters are likely to change.

Robot performance, like that of all machines used in manufacture, can be assessed by several different criteria. Repeatability is the critical factor for robots that are taught using the pendant method. It is sufficient that the robot reliably finds the same position for each point of its program since the human operator defines where these points are in the working volume. Because of this, absolute positional accuracy has not been a dominant factor in robot design. The consistency of robots in attaining position has been the underlying reason for their success in the car production industry.

## 1.08 Robot control – off-line programming

Clearly there are many disadvantages to on-line programming, in particular the loss of production time while the robot is being programmed. Improvements in computer power and the increase in expertise has considerably reduced the time required to generate robot control software from the mathematical model of the configuration of the robot. This allows simulation and programming to be undertaken off-line on a computer.

Not only can simulation lead to savings in programming time, but it can also avoid costly errors at the planning stage without unnecessary wastage of robot and production downtime. Wittenberg [23] quantifies the operational advantage of off-line programming by stating that, for small batch jobs, downtime can be reduced as much as 85 per cent. He also notes that Chrysler showed that programming time was reduced from between 12 and 18 hours to 6.5 hours per robot.

The time-savings from off-line programming do not solely derive from the ability to change applications rapidly. Benefits also arise since several robots performing the same task can be given the same program, suitably adjusted to account for variations in their signatures. Similarly, calibration can be used to adjust or compensate the model if a robot has to be repaired or replaced, reducing downtime required for re-programming.

Off-line programming is also much safer since potential collisions can be detected at the simulation stage. In an on-line programming strategy an operator in the robot cell during programming is susceptible to unpredicted collisions between robots.

As stated in section 1.07, it is acceptable for robots taught on-line to have large positional errors, as long as the error is repeatable. However, for robots to be programmed

off-line positional accuracy becomes just as important as repeatability. Trevelyan [21] attempted to apply off-line programming techniques to a robot designed for teaching by the pendant method. He states that 'the position to which a robot returns to within a fraction of a millimetre can be 10-20mm from the position calculated from the robot model.'

## 1.09 Robot error sources

To realise the benefits of off-line programming it is essential that the model describing the robot and its work cell represent the actual machine as closely as possible. The model should not contain redundant parameters, but must be complete enough to include all parameters significant to the robot system. The effectiveness of the model is determined by the choice of parameters used to describe the robot, and the accuracy to which they are known. However, small errors in the manufacture and construction of the robot can contribute to a large overall pose error.

The potential error sources for robot positioning are similar to those discussed in section 1.02 on machine tool error sources. It is generally accepted that thermal errors are not as significant on robots because they do not generate as much heat as a machine tool. Nevertheless, such phenomena cannot be ignored, since the heat produced by a motor on a robot can be sufficient to influence the overall positioning accuracy. Bearing this in mind, the most significant errors in robots can be classified into two categories:

**Geometric errors** - errors in links to inaccuracies in length, twist in the link mounting, offsets in the robot and tool mounting, etc. Also included are the errors in conversion from transducer reading to joint position.

**Non-geometric errors** - derived from deflections under load, servo-errors, gear meshing and tooth errors, thermal errors, etc.

Some of the most significant parameters are link lengths, joint-axis orientation, gear runout, actuator elasticity, coupling factors, gear backlash, etc. Trevelyan [21] states that non-geometric errors have been shown, by experience, to be small enough to be ignored in most industrial manipulators. It is not surprising therefore, that most robot calibration methods concentrate on measuring the geometric errors only.

The calibration of the individual errors is not always physically possible once the robot has been manufactured and assembled. Attempts can be made to provide implicit measurement of these errors from calibration data by the use of parameter identification.

This identification must be sufficiently reliable to reach a single solution that is within tolerance, with a reasonable level of confidence in the results. However, the parameter identification process is useless without a correspondingly reliable measurement procedure. Accurate robot calibration could offer a number of significant advantages:

1. A potentially profitable method of implementing calibration data is to operate a closed-loop CAD/CAM system. Passing calibration data back to the computer design model would facilitate re-design, enabling robot tasks to be optimised.
2. A further advantage of post-production robot calibration is that it may allow each component of the robot to be manufactured with wider tolerance, potentially lowering the cost of robot production.
3. Despite the fact that robots are fast, effective and can be more accurate and reliable than humans in very repetitive jobs, they can suffer from rapid loss of performance. Regular re-calibration is essential to maintain the accuracy of its computer-based model. Such calibration data can be used as a diagnostic tool to monitor component trends and so predict component failure. A predictive maintenance strategy can also help to reduce robot downtime.

A more widespread demand for robot calibration is hindered by the high costs of equipment and expertise. The high outlay required in converting to off-line programming, and a poor understanding of the value of calibration data precludes its more widespread adoption in industry.

One method of measuring errors in such systems is by directly mapping the errors using systems such as tracking lasers (sections 2.02.8 and 2.02.9). Such equipment has the potential advantage of being both accurate and efficient in performing a measurement of the errors of a machine moving in three-dimensional space. Part of this research (chapter 5 - chapter 9) investigates the suitability of tracking lasers for calibrating robots or machines and explores methods by which the performance of such systems can be improved.

## 1.10 Error compensation

Although the objective of this project was not to produce a compensation system, it is clear that the error modelling required to evaluate errors could be applied to compensation systems. If errors were found repeatable, the model could be used as part of an electronic compensation system. Some such compensation techniques for machine tools are discussed in section 2.05. The case of compensated machines extends to coordinate measuring

machines (CMMs), whose position feedback to the machine display is adjusted to compensate for errors using a mapping technique.

On robots, the collected calibration data for the model can be applied in one of two ways. Either the model can be adjusted to correspond to the actual robot, or compensation can be applied to the controller to correct for errors. A desirable method of implementing off-line programming is to change the model that is used by the controller of the robot. Controllers with the ability to utilise calibration data directly are not common, but it would be a major step forward if they become more freely available in the manufacturing workplace.

A compensated machine presents its own problem in terms of error evaluation since it is the effect of the error, not the error source, that is reduced. The machine can no longer be evaluated by synthesising the effects of the directly measured error sources [97]. This problem is further discussed in section 3.08 and chapter 4.

## 1.11 Uncertainty of measurement

Doiron, *et. al.*[24] state that "every measurement produces only an estimate of the answer." It is important that any accuracy figure be qualified by the certainty of the measurer that this be a true representation. Taylor, *et. al.* [25] summarise this concept by stating, "In general, the result of a measurement is only an approximation or estimate of the value of the specific quantity subject to measurement, that is the measurand, and thus the result is complete only when accompanied by a quantitative statement of its uncertainty."

Doiron, *et. al.*[24] quote Dr. Meyer's early attempts at quantifying the uncertainty of measurement of the heat capacity of ammonia:

"We think our reported value is good to 1 part in 10,000: we are willing to bet our own money at even odds that it is correct to 2 parts in 10,000. Furthermore, if by any chance our value is shown to be in error by more than 1 part in 1,000, we are prepared to eat the apparatus and drink the ammonia."

This anecdotal example clearly illustrates the basic concept of a measurement being supported by a confidence in the result. The approach to calculating uncertainty of measurement has now been formalised into one of a number of statistical methods (discussed in sections 2.04 and 3.13).

## 1.12 Summary

The ability of a machine to perform its role in a working environment is of critical importance. The many measures that quantify the ability of a machine to fulfil its function include speed, power, repeatability and cost. However, the performance measure that is often of greatest importance is the positioning accuracy of the machine in question, whether it be a machine tool, measuring machine or pick-and-place robot. In order to assess this important indicator an appropriate measurement technique and related interpretation is required. This method depends upon the machine under investigation and may lead to a method for compensating the errors. However, this can produce a further problem in quantifying the residual error.

This research will investigate methods of quantifying the positioning capability of Cartesian and non-Cartesian machines. Within this framework is the production of a system for estimating the performance of a machine tool based upon Cartesian axes, but incorporating an indexable probe head, thus providing a non-Cartesian element. The final accuracy figure predicted by this method must be supported by a value for the uncertainty due to the measurement process.

The research will then concentrate upon a laser tracking system, which can be used for direct measurement of errors throughout the working envelope of either Cartesian or non-Cartesian machines.

Finally, a novel method of calibrating non-Cartesian systems is devised and applied to two such problems – a dual laser tracking application and a prototype machine.

## 1.13 Aim

The aim of this project is to investigate and produce high performance calibration methods for the positioning capability of Cartesian and non-Cartesian machines.

## 1.14 Objectives

a) Produce a test regime and design analysis software capable of evaluating the positioning capability of Cartesian-based machines operating with either tool offsets or non-Cartesian elements such as an indexable probe.
b) Model the effects of measurement uncertainty and machine repeatability on the synthesis technique, thus producing a method of quantifying machining capability based upon machine configuration, measurement tools and repeated geometric measurements.

c) Investigate the calibration of static and dynamic behaviour of non-Cartesian systems within their working envelope.

d) Devise a calibration scheme and prototype software for a measurement system based on two tracking lasers.

e) Design a control algorithm to compensate for errors found in robots and other non-Cartesian structures. Produce and assess a novel method of calibrating a non-Cartesian robot.

# Chapter 2 Review Of Previous Research

## 2.01 Calibration philosophies

The philosophy of measurement for machine tools, CMMs and robots differ greatly. In general, machine tools and CMMs require a greatly superior level of spatial positioning accuracy than robots. Accuracy requirements for these machine types vary upon application, but typically, the linear accuracy of a Cartesian CMM is five microns, a machine tool twenty five microns*, and the positioning accuracy of a robot more than one millimetre. British Standards [27] state that the "total uncertainty of measurement shall not exceed 25 per cent of the magnitude of the repeatability of the characteristic under test." It can be seen that this influences the possible choices of calibration system for the various machine types.

The calibration philosophy for a system is also influenced by the typical duty of the machine. Because a machine tool cuts, the errors influencing the position and orientation of the tool at the cutting point are of critical importance. Because CMMs are used to probe, it is often thought sensible to calibrate the machine by techniques such as artefact probing which directly utilise this functionality.

---

* BSI [26] specifies a permissible position deviation of 25μm for an axis under 1m in length. cf. D1a, pp100.

The configuration of the machine will also affect the choice of calibration device and methodology since it will determine the nature of the geometric error source. A Cartesian machine will have an infinite number of errors since angular and straightness errors vary continuously over each axis length. For a non-Cartesian machine, the error sources can be limited to the number of links and joints in the system, although the error in each joint should be considered as a continuous function.

Because of the differences in philosophies, the review of calibration methods is broadly split into methods for non-Cartesian and Cartesian machines. Nevertheless, some latitude for overlapping techniques is evident.

## 2.02 Non-Cartesian machine calibration techniques

Ideally, the accuracy of a calibrated and corrected robot should approach the repeatability of the robot. To achieve this a suitable measurement device must be selected for the calibration. Assuming a typical repeatability for an industrial robot of ±1.0mm suggests a measuring system capable of measurement accuracy of ±0.1mm.

Robot calibration techniques currently employed in the manufacturing workplace are usually confined to rather basic static tests. Often these measurements are constrained to those poses and orientations to which a measurement transducer can be applied. The results of these tests are restricted to the measurement of repeatability, drift and hysteresis. It is not possible to determine absolute position accuracy using these tests.

The measurement of dynamic errors is more problematic, but is essential for accurate determination of position overshoot and tracking errors since the dynamic characteristics of a robot will change, depending upon the position and the load.

### 2.02.1 Choosing a calibration system

Calibration techniques vary according to the needs of the robot user. Roth [28] defines three different levels of calibration:

Level 1: Joint level calibration requiring calibration of drive and joint sensor mechanisms. This determines the correct relationship between the measured joint displacement and the actual joint displacement.

Level 2: The entire robot kinematic calibration. This is used to determine the basic kinematic geometry of the system as well as to correct the joint angle relationships.

Level 3: Non-geometric calibration, which calibrates for non-kinematic errors, such as thermal effects, contributing to errors in the tool centre point (TCP).

A level 1 calibration does not provide sufficient data for off-line programming. Attempting level 3 calibration requires specialist equipment and time-consuming procedures. In some cases, a full calibration is impossible, due to the random nature of the errors. It is therefore appropriate to calibrate to level 2 for off-line programming purposes.

Important factors in comparing calibration systems are cost, accuracy, repeatability, resolution, maximum speed of sampling, time required for set-up of equipment, type of measurement possible (static and /or dynamic), contact/non-contact, analysis software and 3D measuring capability.

A survey of 15 system manufacturers [29] indicated that, once accuracy and resolution considerations have been satisfied, the most important factors in the choice of measurement system are cost, set-up time and the ability to interface with the robot controller. To reduce costs it is desirable that the calibration method does not require extensive re-design of the robot.

It is also extremely desirable to have a measurement system which is non-contact and non-invasive. This is especially important when considering the elastic characteristics of the robot. Any constraints that the measurement system places on the robot can give a false impression of the robot performance. Ideally, the calibration should be performed with the robot undertaking its usual mode of operation.

Level 1 calibration only requires the robot-determined value of the joint angle to be compared with the actual value. This involves posing the robot in a 'known' joint configuration which can enable easy verification. To achieve this, the joint can be set to a known angle by including alignment holes in the joint into which a close-tolerance peg can be inserted. Actual and measured angles can therefore be compared. Another method is to drive the tool centre point (TCP) to a specific position where the required joint angles are known. However, determining this position is a problem in itself.

These methods are very simple, but cannot be used to calibrate for off-line programming because of the limited data provided. The remainder of this section will concentrate on techniques that can conform to a level 2 calibration.

### 2.02.2 Probing and pose-based tests

The high repeatability of robots can be used to calibrate them without the need for an external sensor. [21] One method of applying this is to orientate the robot to several known

positions using the teaching pendant system. The pose of the robot at each position is recorded so a local co-ordinate frame can be calculated. Although this method can help to reduce pose errors, it does not account for several significant sources of geometrical error. A further drawback of this system is the requirement of an accurate knowledge of the calibration target position.

Pathre [35] took a very practical approach to his robot control problems. A painting workcell, containing four 6-axis robots, was found to have errors of up to 30 cm when attempts were made to use off-line programming techniques. It was determined that the errors were due to inadequacies in matching the robot simulation model to the actual robot.

The first test requires that a reference be positioned near the centre of the working volume. The robot is programmed off-line, to move in such a way as to keep the tip stationary - in contact with the temporary reference. Any drift is due to the inaccuracies between the kinematic model and the actual robot. By specially designing the test program, the source of the errors can be identified to a greater or lesser degree. However, it seems that the actual error attributable to each joint cannot be determined by this method.

The method Pathre uses to calibrate for mechanical and modelled backlash errors is to command each joint to move to a zero near the centre of the working volume. Each joint is then used in turn to move the tip away from and then back to the reference in two directions.

These methods calibrate for specific errors, but do not give overall error measurements throughout the working volume.

### 2.02.3 Calibration without external instrument

A method of calibration that requires neither external sensing nor probing is potentially of greater benefit than one requiring expensive sensing equipment. The principle behind any calibration system is to derive a measurement residual, which is normally the discrepancy between the measured and computed manipulator pose or position. In self-calibration, the specification of a residual is much harder since there is no measurement of an actual feature with which to compare. Therefore, it is often necessary to introduce redundant sensing to the robot. This allows two robot position measurements to be computed, with the discrepancies between the solutions forming the measurement residual.

Self-calibration has several potential benefits [36]. It removes the dependence on external pose sensing information, produces measurement data over the entire working volume automatically and non-invasively, can attain a high measurement rate, facilitates on-

line accuracy compensation and can be cost effective. One possible drawback of this system is the need for retrofitting of transducers to robots that require conversion. Another possible problem is in determining optimised transducer placement and identifying errors from the calculated discrepancy. This is only possible if the robot modelling equations are robust to parameter identification.

In attempting the self-calibration of a robot with the configuration of a Stewart platform, Li [37] compares the measured and calculated strut lengths rather than taking pose measurements. Zhuang [36] also considers the self-calibration of a Stewart platform. He simulates the necessary method for deriving a measurement residual and analyses the results. These indicate that although only six measurement configurations are required for the estimation of the 36 parameters in the machine, several more are needed for the estimation to be robust. This is true for most calibration techniques, where several different poses are required to obtain a reasonable calibration. Studies [38] show that a minimum of two redundant sensors are required, and are sufficient, for the self-calibration.

Zhuang also simulates the effect of sensors with differing accuracy on the calibration strategy. He concluded that these must be at least five times that of the required accuracy of the platform to be measured. It is also stated that the accuracy of the redundant transducers must be comparable to that of the active joint sensors.

The above research seems very promising, but seems to concentrate too much on the simulation of results and sensitivity analysis, rather than on practical applications. The author does indicate that real-world testing is planned.

### 2.02.4 Theodolites

NIST (National Institute of Standards and Technology) in America have investigated various measurement systems for robot calibration. [35] They concluded that theodolites are the most accurate of the tested systems, are very reliable, but can be very costly and can be time-consuming to apply (automated versions of the Theodolite are even more expensive.)

Each theodolite is pointed at a target at some nominal position. Any error in the aim of the theodolite is corrected by image processing techniques. The 3D position of the intersecting lines of sight can then be calculated.

The high accuracy of the theodolite system is its major advantage. The system requires only unobstructed line of sight to each calibration point - not for tracking between points. The slow calibration has been partially addressed by the provision of motorised

theodolites. However, this calibration technique cannot be applied for dynamic testing due to the high processing time and the physical construction.

### 2.02.5 Low-cost methods – optical, spirit level and tape measure

Trevelyan [21] describes a method of optical alignment using a laser and relatively inexpensive optics to detect position and orientation errors in two planes. The system cannot measure displacement along, or rotation about the incident laser beam. Trevelyan asserts that sufficient data is available to provide 'accurate' calibration measurements. However, the exact cost of the system, its accuracy and resolution are not stated.

Trevelyan also notes the need for a simpler robot model, ideally able to be adapted for a variety of robots.

Nearly every calibration technique relies on iterative least-squares solution of the calibration equation. It is usually found that the equations are very poorly conditioned, requiring several unknown parameters to be removed after singular value decomposition to improve the conditioning of the remaining equations.

Trevelyan reports a combination of methods which uses a recursive extended Kalman filter in combination with a simpler modelling technique to produce simple equations which can be applied to any serial manipulator. He also states that simple measuring tools can be applied; measuring tapes and spirit levels are sufficient if only moderate accuracy is required. The above optical method will give even greater accuracy.

This calibration methodology is still being developed by Trevelyan to make it more flexible and functional.

### 2.02.6 RoboTrak

Robot Simulations [39] have one of the leading robot simulation and off-line programming packages; Workspace. In conjunction with this system they recommend and supply the RoboTrak calibration device, which consists of three non-stretch cords attached to the tool tip and to one of three barrels (figure 2.1). Rotary encoders determine the length of the three wires, which can then be resolved into a position measurement by trilateration.

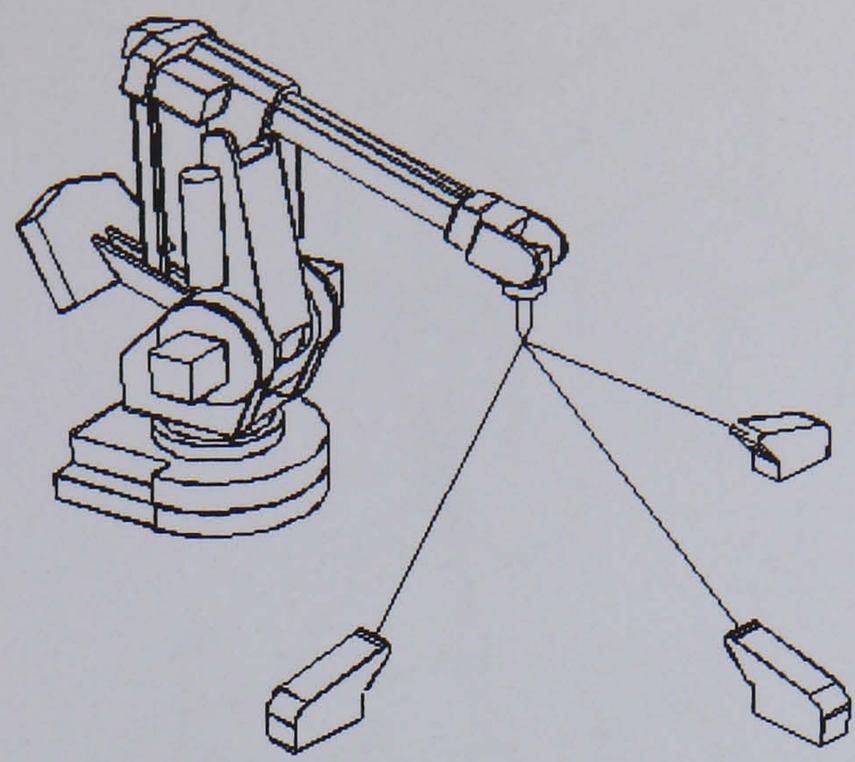

**Figure 2.1: Typical configuration for calibration using RoboTrak**

This system is relatively inexpensive and simple to operate. However, this is a contact device, which can affect robot performance during calibration. It seems obvious that the wires must remain in tension while measurements are being taken in order to obtain reasonable accuracy. This tension may encroach upon the performance of the system. It is also apparent that the robot movements and configurations must be such that the wires do not become entangled with the structure. The range of the system is also constrained by the length of the wires, so these should be long enough for most industrial robots to be accommodated.

Despite these drawbacks, the RoboTrak method is a good calibration system in robots where the required accuracy is greater than one millimetre.

### 2.02.7 Omnigage

A system similar in principle to the RoboTrack is the Omnigage [40] (figure 2.2). This is based upon ballbar technology, but utilises a laser interferometer rather than a LVDT as the length measurement device. It has a range of 330mm to 711mm and can provide polar coordinates from a set position. The device is then moved to two other locations and the measurement repeated. Trilateration is then used to establish the spatial position.

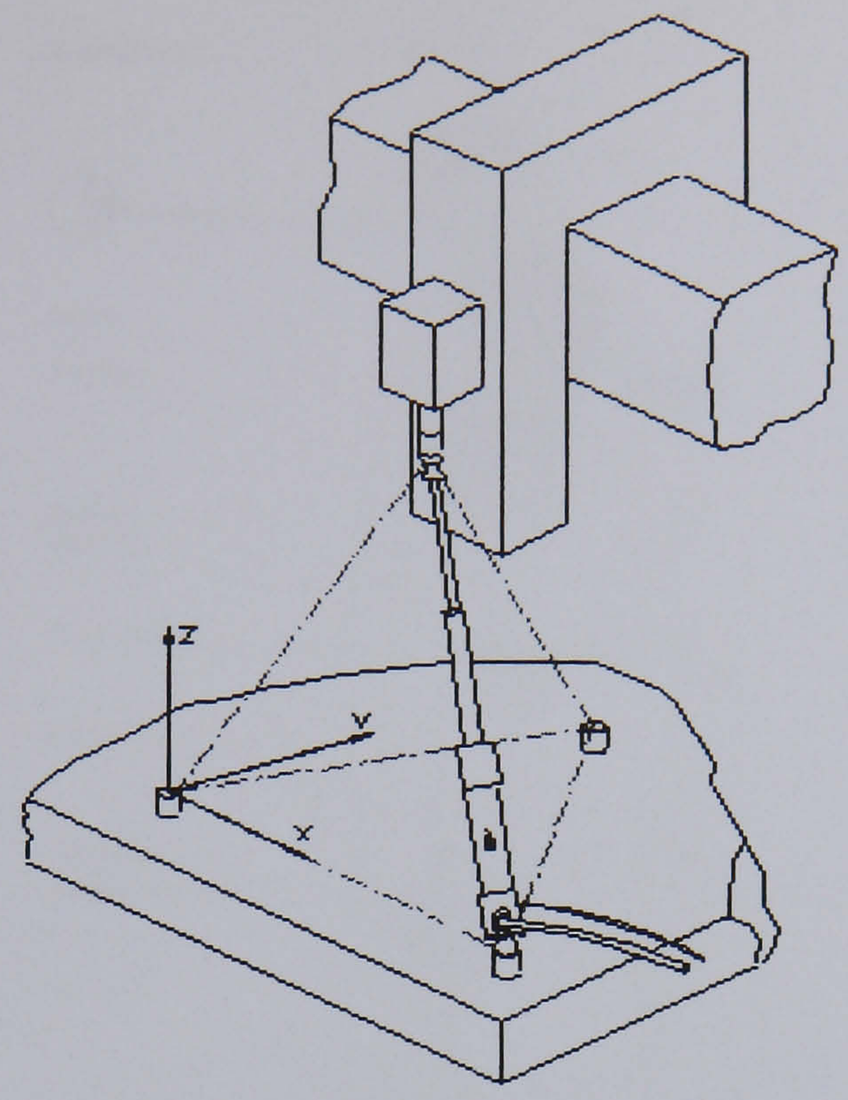


**Figure 2.2: Omnigage**

This system is relatively inexpensive and simple to operate, but has a limited range and displays poor performance when measuring near the horizontal. It also operates on a measurement volume based in a conical shape, rather than the usual machining volume of a cuboid. This limitation may leave areas of the working envelope unmeasured.

### 2.02.8 Leica laser tracker

Another method of calibration that Robot Simulations [39] advise for robot calibration is the Leica Laser Tracker (formerly known as SMART) system (figure 2.3), manufactured by LEICA [41,42]. The system is based upon a laser interferometer that can track a moving optical reflector. A co-ordinate system is determined using a calibration frame. An optic is then placed on the head of the robot to be calibrated. The angular encoder reading, combined with the interferometer measurement resolves to give the position in Cartesian space.

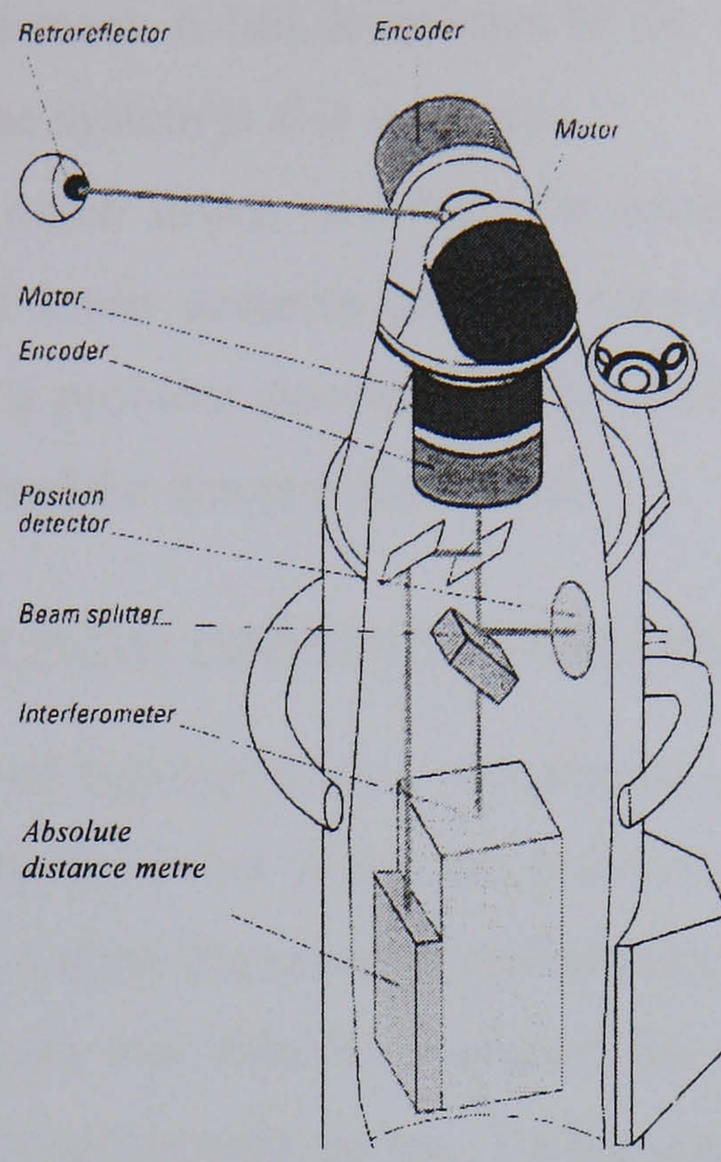


**Figure 2.3: Schematic of Leica laser tracker system**

The Leica system gives very good accuracy and is able to perform most of the calibration tasks suited to theodolites. In addition, the calibration procedure can be automated if its controlling software can detect loss of beam track. The system is also capable of dynamic measurements, which are extremely desirable in robot calibration.

The Leica system is unlikely to become widely adopted due to its very high cost, which is about £120 000. The system is also inapplicable for certain robots since it requires a line of sight from laser to tool head throughout the working volume. For some robot configurations it will not be possible to maintain a direct line of sight due to supporting struts, head twist, etc.

Similar laser trackers are also produced by API [11] and SMX [30], the three of whom have recently settled a patent infringement lawsuit out of court – indicating the similarity of their systems.

### 2.02.9 LaserTrace

LaserTrace is a system based around a tracking laser, comparable with the Leica [41] system as described in section 2.02.8. However this laser does not have an interferometer, and so does not produce any direct distance measurement. It is therefore necessary to use multiple lasers to obtain displacement values using triangulation techniques. The angular data from the two pods in both the horizontal and vertical directions can be used to calculate the

position at which the beams meet. A full description of the system is included in chapter 5, where the performance of the system is also evaluated.

This system has a much lower cost than the tracking interferometer system, but suffers the disadvantage of lower accuracy and the need for multiple lines of sight to a single target. There is also a problem associated with synchronisation of the timing of the multiple pods when being used for dynamic calibration.

## 2.03 Cartesian machine calibration techniques

In addition to the methods of measuring error components given in section 1.03 there is a drive towards understanding the errors within the entire working volume. One method of achieving this is to measure a three dimensional grid of points in the working volume and so generate an error map. Errors can then be predicted for the whole working volume by interpolating between the measurement points. Technologies such as those described in sections 2.02.4, 2.02.8 and 2.02.9 can be used to perform this measurement. However, the measurement grid must be of sufficiently fine resolution of stepsize to allow a good representation of any rapidly changing errors. It can also be noted that this method would not provide information on the source of the errors, simply the effect in positional accuracy. While the evaluation of performance is the ultimate goal, it does not provide information for error avoidance strategies.

For this reason, other strategies are used for calculating the errors throughout the volume for Cartesian machines. This is possible because restricting motion to simple features such as straight lines can be used to isolate individual error components.

### 2.03.1 Error synthesis

Previous research [31-34] has found the volumetric accuracy of a Cartesian machine by combining the errors in each of the axes. This accuracy analysis is used to determine the effect of the errors at the end of the ram, which is nominally the cutting point of the machine. If the measurements are taken in accordance with certain basic rules, the individual error components can be combined using a geometric model [32-34, 43-45] to determine the positioning errors throughout the working volume.

Postlethwaite [34] has produced a method by which this error data can be combined for any standard three-axis Cartesian machine tool, to evaluate the errors through the working volume. However, this technique predicts the errors at the position on the machine

where the measurement optics were mounted. It does not indicate the effect of offsets due to an indexable probe or an extended tool.

This model [1], as with others of its type, assumes that the machine is rigid body, which is a reasonable approximation for most machine tools. As such, the angular errors in an axis will produce a linear offset in the axis perpendicular to that axis, and that about which the rotation occurs. The magnitude of this linear offset depends upon the displacement from the axis. The model calculates the sum of all the linear effects in the direction of the three Cartesian axes. A vector sum of these three axis errors quantifies the volumetric accuracy of the machine.

### 2.03.2 New calibration tools for synthesis method

A number of institutions have sought to produce measurement equipment capable of reducing the amount of time required to perform a machine calibration. This is generally achieved by characterising a number of geometric error features with a single optical set-up, or by simplifying the set-up process.

API [11] have produced a laser capable of measuring six geometric errors in a single set-up. [47] Lau, *et. al.*, recognise the time-consuming nature of measuring all geometric sources of error on a machine tool (two to three days) and report a 75% saving in time when measuring a 'typical' machine. However, the system does not use the principle of interferometry for the measurement of straightness error in an axis. Instead a signal-strength transducer is used to measure the deviation from a straight line. This method is inherently less accurate than standard interferometry techniques. Nevertheless, the savings in time that can be achieved may outweigh the reduced accuracy for many measurement applications.

Chen, *et. al.* [46] have produced an auto-alignment laser which measures five of the error components of an axis (see 1.03). This is similar technology to other tracking lasers (sections 2.02.8 and 2.02.9) for maintaining the laser beam on the target. The acquired data is similar to that obtained by the API laser in that it obtains axis information in terms of standard geometric error data. As with the API system, this laser uses photodetectors rather than interferometry for measurement of perpendicular deviations – a less accurate technique.

The Optodyne [48] system uses a Doppler laser, rather than the conventional Michaelson interferometer for its calibration source. A single aperture is used for both the output and return beams and only two elements need to be aligned, rather than a laser head, interferometer and retroreflector as with most laser interferometer calibration systems.

Additionally, the laser source can be mounted on the machine using magnetic bases, rather than being mounted on a separate tripod.

The Optodyne system does not require a retroreflector, but can use a mirror, or polished surface as the reflector. This allows monitoring of, say, a rotating pin-gauge in a spindle. It also permits measurement along nominal machine diagonals while moving each axis in isolation, so performing a step-wise motion. This is not possible when using a retroreflector since the beam would soon lose the target. With this system the stepsize of motion on each axis is restricted by the size of the reflecting mirror. The values suggested by Optodyne are that a corner-cube retroreflector has a 5mm tolerance on set-up, while the mirror which is standard with their equipment allows steps of 50mm increments on each axis during a sequential step test.

Optodyne claim that this allows a measurement across the body diagonals to provide sufficient information for volumetric compensation by utilising a 'sequential diagonal movement.' It is claimed that the system can measure all these errors using four set-ups within a few hours, using a vector method. This represents a significant reduction on the time required for setting up a standard laser interferometer for all the necessary error sources.

The laser is compact relative to standard systems since it does not require as large a variety of optics as standard interferometer systems. The typical cost of the system is ten to twenty thousand US dollars for a single head laser. This rises to thirty thousand US dollars for a dual head laser, which would then be capable of measuring down two sides of an axis at once.

For each of these systems it is claimed that they are capable of measuring some or all of the calibration data necessary for the synthesis model as discussed in section 2.03.1. However, none of the systems claims to produce a single direct value for machining capability through their software.

### 2.03.3 Evaluation tools

Measurement tools that are not usually used to calibrate machines, but to check performance include the ballbar [10,11] and the Heidenhain gridplate. [49] Both systems are similar in that they are used to measure a prescribed circle in a plane. From the captured data it is possible to determine a number of errors based upon the deviation from the nominal circle path.

Although these devices are not used to obtain calibration data, they are often used to verify performance. They have the advantage over standard laser methods in that more than

one axis is in motion during the test. ASME B5.54 [50], the American standard for CNC performance evaluation, uses a diagonal test to assess volumetric performance. Although this can allow the rapid evaluation of a machine over the diagonals of the machine, like the ballbar and gridplate it does not provide information over the entire volume. Blackshaw *et. al.* [51] also advocate the use of body diagonals, although mention some problems setting up the test. The localised information produced is also only partially useful in discerning the source of the errors.

Morris [52] has performed further investigation into the use of diagonal testing. He suggests that body diagonal tests provide a "quick substitute" for full volumetric tests because maximum errors tend to occur at the extremities of axes. Although this is true, it will only provide an overall worst-case error. The available data cannot easily be manipulated to provide information on the unmeasured region of the machine.

Morris also proposes that the face diagonals provide a measure of the planar accuracy of the machine. From his experience at Cincinnati Machine tools [53] he notes that many customers are looking for two-dimensional accuracy. This conclusion is drawn from the fact that the most popular specification for a vertical machining centre (VMC) is for scale feedback on the X- and Y- axes, but a less-accurate rotary encoder on the Z-axis. However, this assertion cannot be guaranteed for all machine tools. In particular the aerospace industry demands volumetric accuracy figures [54] and specify linear scales on all axes of many of their machines.

The main advantage of the face-diagonal is the ability to calculate squareness based upon measurements over a significant portion of the machine axes. The ballbar describes a circle of fixed radius, while measurement of a granite square is obviously limited by the physical size of the artefact. Although measurements can be repeated with these devices located in different positions, the face diagonal method can obtain data for the entire plane in a single test. In addition, the size of the machine and its aspect ratio do not affect the set-up of the test.

### 2.03.4 Assessing errors in CMM probes

When considering the effect of the geometric errors during in-process probing some consideration should be given to the errors inherent in the probe unit. Analysis of these errors is found by performing 25 probing measurements on a calibration sphere and comparing the calculated and known radius [55]. The errors are found to be relatively low, when compared with those resulting from the overall machine structure. In particular the

repeatability of the indexable probe head is excellent, the specification for a typical unit being a repeatability better than 0.5μm [56].

An interesting study into the use of probing machines is a survey conducted by NIST into the use of measuring machines [57]. A calibrated ball plate was sent to a number of CMM users who were requested to measure the position of each ball and estimate the uncertainty of their measurement. This round robin was designed to assess the state of practice in the use of coordinate measuring machines in American industry. The typical result for the deviation was within ±5μm for the X and Y coordinates - the ballplate is only a two-dimensional artefact. However, the report notes that some measurements were in excess of 20μm in error. Of particular interest is that during the survey, which was conducted over a two year period, the artefact became damaged. This fact was not realised until the ballplate was returned to NIST at the end of the survey. The worst case was a three-micron movement of one of the balls, but this only serves to highlight the potential for damage to an artefact, and the possible repercussions if this is not detected.

### 2.03.5 Machine checking gauge

The Renishaw [10] machine checking gauge (MCG) is a device designed to be used as a health-checking tool. The system is used to measure deviations from a probed hemisphere to quantify the accuracy of CMMs and is not intended to acquire calibration data. A fuller description of the MCG is given in section 8.02.

## 2.04 Uncertainty of measurement

With all measurement techniques there is an uncertainty that the measured value is a true representation of the true value. The synthesis techniques discussed in section 2.03.1 combine the results of a number of measurements to generate an overall value for the accuracy of the machine. The uncertainty of this all-encompassing value is, therefore, a function of the individual uncertainties. Combining this with the repeatability of the machine itself is a non-trivial task.

The formal definition of the term "uncertainty of measurement" that is provided by the current VIM [58] is a "parameter, associated with the result of a measurement, that characterises the dispersion of the values that could reasonably be attributed to the measurand." Bell [59] gives a more colloquial definition stating that it is "the doubt which exists about the result of any measurement."

Measurement uncertainty is quantified by two numbers. The width of the margin of doubt is called the '**interval**', which must be qualified by the '**confidence level**'. This indicates how sure the measurer is that the 'true value' falls within the interval.

The problem of uncertainty of measurement has been analysed in various ways [58-63]. Abernathy, *et. al.* [60] draw direct parallels between uncertainty and machine errors in terms of bias and random sources (figure 2.4). These concepts can be related to systematic and random source of uncertainty.

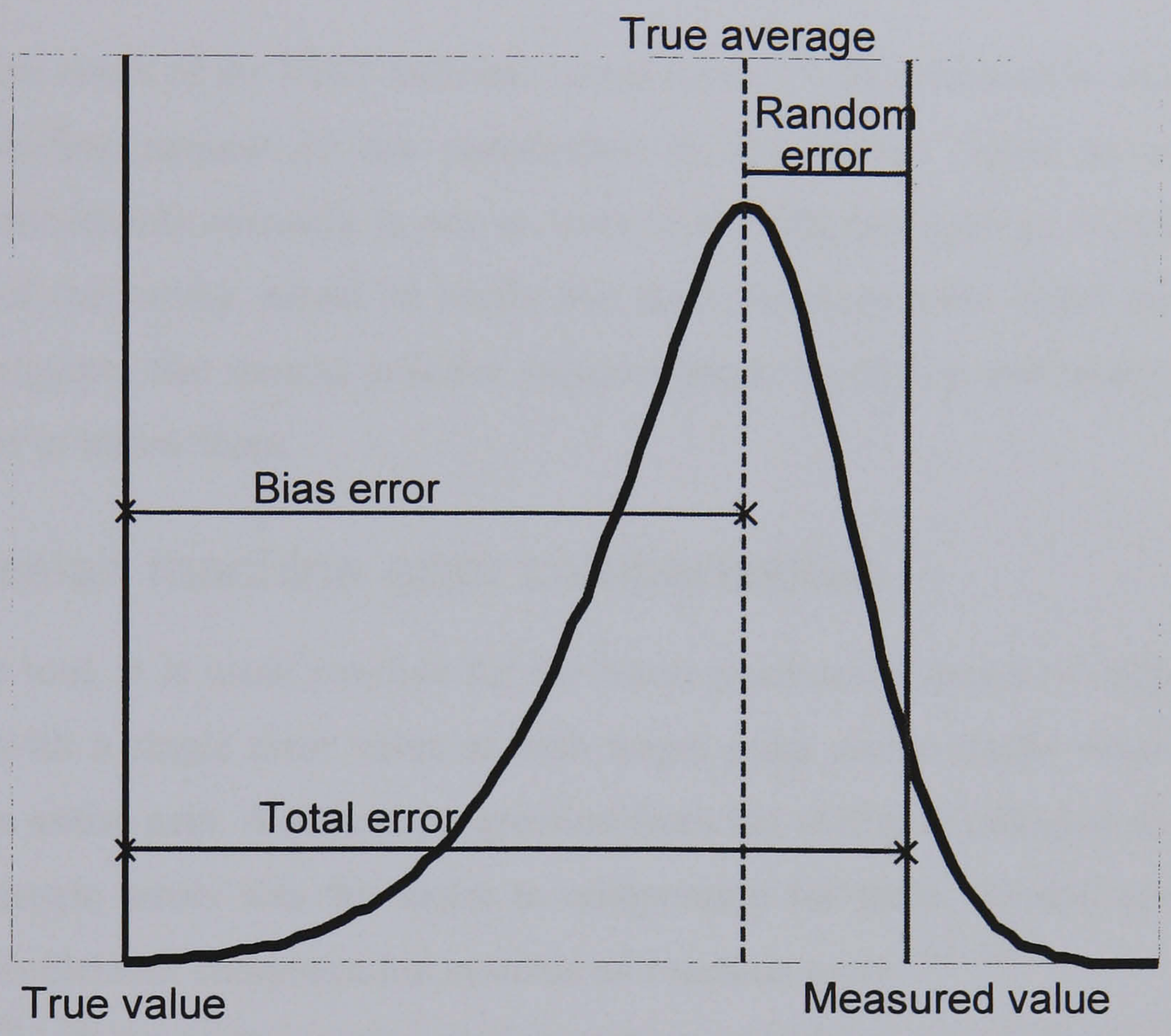


**Figure 2.4: Measurement error**

"In most cases a measurand is not measured directly, but is determined from N other quantities" [61]. This is certainly true of the use of laser interferometers, where the measurand (distance) is found by counting the number of elapsed wavelengths of light. Since the magnitude of a single wavelength of light can be calculated for a given air temperature, pressure and humidity, the overall distance can then be ascertained. However, this relies on accurate measurement of the specified environmental parameters, and a true knowledge of the conversion function. Furthermore, uncertainty in the measurement can arise from external influences such as draughts distorting the laser beam.

There are two main approaches to evaluating uncertainties. [61] The first is to take sample data and analyse this to provide an uncertainty figure. This is only appropriate where typical data covering the whole spectrum of measurement conditions is available. The second approach is to consider each factor which contributes to an uncertainty in the measurement and combine the uncertainties. The method by which these individual uncertainties are combined is usually a statistical approach, varying from simple summation, through weighted summation to more sophisticated techniques such as Monte Carlo simulation [62].

A further result of the NIST ballplate round robin [57], as discussed in section 2.03.4, is that seventy-five percent of the participants in the survey failed to estimate the measurement uncertainty correctly in one or more of the ballplate spheres. Considering that the members of the survey would be aware that their practices were under scrutiny from experts, this suggests that normal practice requires better regulation and understanding by those who need to utilise them.

## 2.05 Cartesian machine error compensation

For a machine tool, it is usual practice for the linear positioning errors of each axis to be compensated with a single error value at each target point and a single value describing reversal for the entire axis. A natural progression from the ability to calculate the effects of the other geometric errors was the desire to compensate for them. Several attempts have been made to implement compensation systems on machine tools. [64 - 74]

Mou [70 - 72] presents a compensation system combining pre-calibrated and active compensation. The adaptive element of the compensation is designed to correct for machine life-errors such as wear. The techniques used for data collection require specialist equipment. For example, Chen *et. al.* [75] developed a complex system involving a laser and special reflectors to measure five error components of a moving slide. Although such pieces of hardware can provide good results, they are not readily available to most machine users and often tend to be machine-specific.

Ford, *et. al.* [76] and Postlethwaite, *et. al.* [44, 54, 77] have produced and enhanced a compensation system for application to a machine tool either through a PC [44] or open architecture CNC controller [78]. The volumetric compensation system (VCS) can be applied to any three-axis machine to compensate for errors at the measurement centre point (MCP), which is normally the end of the ram of the machine. It achieves this by applying a linear

offset to the axis feedback that is equal and opposite to the effect of the geometric errors at that point.

CMM compensation is achieved differently since it is not necessary to move the axes for compensation, but simply to correct the readout from the measurement device. When a probe is triggered, correction for the errors for the current axis position are calculated and applied before the position readout is updated.

## 2.06 Summary

It is evident from the variety of the discussed calibration technologies that no single answer has been found to the calibration question. Because of the diversity of machine configurations and applications, the need for short downtime or low cost can outweigh the drive for high accuracy. A simple, cheap, automatic, yet accurate calibration system is the unattained ideal. It is unlikely that a single solution will ever be appropriate for all tasks due to the diversity of the calibration requirements.

The techniques for measuring the twenty-one geometric error sources in a Cartesian machine are well known. A method of predicting the errors in a three-axis machine tool by processing this error data has been described. While this is extremely useful for comparing machines, or for a machine builder and customer to draw up a specification, further analysis is required when tooling is to be considered. In particular, the use of rotating heads or indexable CMM probes requires an extension of the model for the true machine capability to be realised. Since CMM verification standards do not allow the use of lasers it is desirable that an acceptable, traceable standard for volumetric performance be provided. A technique for achieving these aims is described in chapter 3. Such quantification requires qualification in the form of an uncertainty figure.

In the following chapters, an extension of the Cartesian model sufficient to include tool offsets and indexable heads is presented. A strategy for calculating the volumetric uncertainty is also devised from the basic principles of uncertainty estimation. The method by which these analyses can be incorporated in a piece of the analysis software is also described. Furthermore, the more complex issue of applying this method to a machine with compensation of the type described by Postlethwaite, *et. al.* [44] or Fletcher, *et. al.* [78] is addressed. This results in a new measurement strategy, machine model and analysis software package. These techniques are directly applicable to CMMs, providing a neat overall solution to the volumetric evaluation problem of Cartesian machines.

For a non-Cartesian machine the error evaluation problem is different. Trevelyan's methods [21] (section 2.02.5) are an attempt to achieve the above aims for robots. Using the technique with a spirit level and measuring tape is obviously very inexpensive, but compromises on accuracy. Applying the method using a laser and optics will result in a higher system cost, but improved accuracy.

The work on redundant sensing (section 2.02.3) is very promising since it has the potential to be highly cost-effective, the drawback being the need to retrofit additional encoders on robots already in use.

The above systems have yet to become commercially available. Of those presently available the Leica tracking laser system (section 2.02.8) is highly accurate, but must be pre-calibrated using a large frame. The high cost is also difficult to justify for robot applications. The RoboTrak system is much less expensive, but operates over a limited range. Additionally, the tensioned cables could affect machine performance and may be impractical in some machines where they can become entangled on the robot frame.

A system which is much cheaper than the Leica tracking interferometer, though less accurate, is a system combining two tracking lasers which is discussed in chapter 5. This dual tracking system provides no direct positional measurement, since interferometry is not applied. This combined with the differing internal construction, results in a system with reduced cost, but with lower accuracy and resolution. The dual trace has the advantage over RoboTrak that, other than the small mass of the target optic, it does not impinge on machine performance. Indeed the optic should be mounted in place of the tool end-effector rendering its effect negligible.

Chapter 6 to chapter 9 discuss the methods used in attempting to improve the performance of the dual trace system without increasing the associated costs. Two methods are attempted, one using a novel application of the principle of photogrammetry, the other employing the MCG as a novel answer to the data collection problem for parameter identification. Attempts are then made to transfer the MCG principle to the calibration of other non-Cartesian machines.

It is no longer sufficient to consider only the effect of the errors at this single point on the machine structure. In-process probing, the use of long tools at an angle to the axis carrying it and the increased use of five-axis machining have all increased the need for more comprehensive analysis of the effects of geometric errors in the working volume. This

model does not consider the effect of the geometric errors when they are amplified by a tool extended from the measurement point.

# Chapter 3 Volumetric Assessment of a Cartesian Machine By Error Synthesis

## 3.01 Indirect measurement

As discussed in chapter 1, there is a requirement within the machine tool industry to be able to rely on the ability of machines to manufacture accurate components. Furthermore, compensation systems (section 2.05) have been devised to enhance the accuracy to which a given machine can cut parts. A repeatable and traceable method of quantifying performance of a machine with or without such compensation is required.

Literature has revealed (section 2.03.1) several methods of applying well established measurement technology in order to obtain an overall indication of machining performance. In particular the work by Postlethwaite [44] and Ford, *et. al.* [1] has resulted in a method of assessing the rigid-body volumetric performance of any three-axis machine tool by measuring the geometric error components contributing to an overall positioning error at the end of the ram. This position is chosen because it is close to where most machining with short tools is performed, for example face-milling operations. It has also been selected since it is the point at which the machine tool builder would choose to specify accuracy, leaving responsibility for the effect of tooling to the end-user. When calibrating the machine, all

measurements are made with respect to this part of the structure so we denote it the measurement centre point (MCP).

The errors at the MCP are not of paramount concern on machines with long tools or CMMs, where the error at the end of the probe is of greatest interest. For such machines, the error should be calculated at the tool centre point (TCP), which is where actual cutting or probing takes place. In this research, the approach to evaluating the errors in Cartesian machines will be generalised to encompass the effect of offsets from the MCP. The remainder of this chapter discusses the principles behind this theory and how they have been extended to the more general situation of a Cartesian machine with a polar head. Research has also been undertaken to allow calculation of the certainty with which the resultant geometric error value truly represents the performance of the machine.

The work performed within this chapter was supported by two EC grants [2, 3] who provided information on measurement uncertainty and feedback on the use of the resultant prototype software.

Unless otherwise specified, the derivation of the evaluation system provided in this chapter is directed at machines where compensation has been applied at the MCP and reference to volumetric compensation refers to such systems. A few machines will have volumetric correction for errors calculated at the TCP, however these are relatively rare since they require knowledge of tool length and orientation and must adapt correction based upon these values. Evaluation of such machines proves to be a simplified case of the general solution and is dealt with as part of the stated solution.

For the remainder of this chapter the term 'tool' can be replaced with 'probe' when considering machines with in-process measurement or dedicated coordinate measuring machines (CMMs). Similarly, the expression 'machine tool' can, in general, be taken to include CMMs.

## 3.02 Volumetric accuracy

The parameter of interest that results from this synthesis method of error evaluation is that of 'volumetric accuracy.' This function of the geometric errors in a machine is a measure of the positioning capability of the machine tool throughout the working volume. This is significantly different from the 'linear positioning' accuracy often quoted by manufacturers, since they only refer to a single geometric error component of an axis (see section 1.03).

The way in which the geometric errors manifest themselves throughout the working volume is inherent in the interdependence of the axes.

The following notation describes the machine configuration for a three-axis machine tool. The axes are **B**ottom (B), **M**iddle (M) and **T**op (T). The description of how the axes are linked is expressed in the notation by right-to-left precedence. The way in which the **w**orkpiece (w) and **t**ool (t) are carried is also denoted. So a wBMTt has no axis carrying the workpiece, the bottom axis carrying the middle axis, which carries the top axis, which in turn carries the tool. This configuration can also be described as 'all axes carry the tool.' Use of this notation allows a generic approach for applying the model to any three-axis Cartesian machine.

## 3.03 Effect of angular errors

Angular errors vary with the position of the axis as it translates along its length. However, the effect of these errors on position is only experienced when a second, amplifier axis moves. The resultant positional error is proportional to the amount of movement in this amplifier axis. A small angular error will produce a large positional error when amplified by a large axis movement, while a relatively large angular error may result in a small positioning error if the amplifier axis has only a short stroke.

The effect of the error is also dependent upon the machine configuration. Because the errors are calculated at the MCP, for a given machine configuration the full geometric model [1] can be simplified by eliminating those terms which have no effect at that point. This provides three models for three-axis machines, described in the notation of section 3.02 as wBMTt, BwMTt and BMwTt. A fourth case (BMTwt), where all axes carry the workpiece, is extremely rare but can be modelled in the same way as the other configurations.

## 3.04 Models for three-axis machine tools

For notation please see nomenclature on page xviii.

For **t**ool **B**ottom **M**iddle **T**op Machine Configurations (**tBMT**)

$$\left.\begin{aligned} B_{error} &= B_{lin} + M_{strt(B)} + T_{strt(B)} + \left(\Phi_{M(B)} \cdot T\right) + \left(\Phi_{M(M)} \cdot T\right) \\ &\quad + \left(\Phi_{T(B)} \cdot M\right) + \left(BT_{sqr.} \cdot T\right) + \left(BM_{sqr.} \cdot M\right) \\ M_{error} &= M_{lin} + B_{strt(M)} + T_{strt(M)} \\ &\quad + \left(\Phi_{B(B)} \cdot T\right) + \left(\Phi_{B(M)} \cdot T\right) + \left(MT_{sqr.} \cdot T\right) \\ T_{error} &= T_{lin} + B_{strt(T)} + M_{strt(T)} - \left(\Phi_{B(B)} \cdot M\right) \end{aligned}\right\} \quad \text{Equation 3.1}$$

For **B**ottom **t**ool **M**iddle **T**op Machine Configurations (**BtMT)**

$$\left.\begin{aligned} B_{error} &= B_{lin} + M_{strt(B)} + T_{strt(B)} + \left(\Phi_{M(B)} \cdot T\right) + \left(\Phi_{M(M)} \cdot T\right) \\ &\quad + \left(\Phi_{T(B)} \cdot M\right) + \left(BT_{sqr.} \cdot T\right) + \left(BM_{sqr.} \cdot M\right) \\ M_{error} &= M_{lin} + B_{strt(M)} + T_{strt(M)} \\ &\quad + \left(\Phi_{B(B)} \cdot T\right) + \left(\Phi_{B(M)} \cdot T\right) + \left(MT_{sqr.} \cdot T\right) \\ T_{error} &= T_{lin} + B_{strt(T)} + M_{strt(T)} - \left(\Phi_{B(B)} \cdot M\right) \end{aligned}\right\} \quad \text{Equation 3.2}$$

For **B**ottom **M**iddle **t**ool **T**op Machine Configurations (**BMtT**)

$$\left.\begin{aligned} B_{error} &= B_{lin} + M_{strt(B)} + T_{strt(B)} + \left(\Phi_{M(B)} \cdot T\right) \\ &\quad + \left(\Phi_{M(M)} \cdot T\right) + \left(BT_{sqr.} \cdot T\right) + \left(BM_{sqr.} \cdot M\right) \\ M_{error} &= M_{lin} + B_{strt(M)} + T_{strt(M)} + \left(\Phi_{B(B)} \cdot T\right) \\ &\quad + \left(\Phi_{B(M)} \cdot T\right) + \left(\Phi_{T(M)} \cdot B\right) + \left(MT_{sqr.} \cdot T\right) \\ T_{error} &= T_{lin} + B_{strt(T)} + M_{strt(T)} - \left(\Phi_{M(M)} \cdot B\right) \end{aligned}\right\} \quad \text{Equation 3.3}$$

A particular benefit of this system is that the error data used in the models is acquired using standard equipment and techniques, as described in section 1.03. This means that the

analysis is derived from practices that are already accepted within the machine tool industry using traceable equipment. Furthermore, for those who would perform a full calibration there is no additional data required so no increased machine downtime.

The Error Simulation Program (ESP) [34] was compiled at the University of Huddersfield (UoH) for the analysis of three-axis machine tools. The software has been successfully used to quantify the performance of many machines. However, the model requires modification to be applicable to either CMMs or other machines where the MCP and TCP are significantly displaced from each other. Additional data inputs and model terms are required to be able to estimate the effect at the TCP, and to include the residual error after three-axis compensation has been applied to such a machine. These issues are addressed in the remainder of this chapter.

## 3.05 Definitions

As part of this project it has been necessary to produce definitions of volumetric and planar accuracy for multi-axis machines. These are given in the remainder of section 3.05. The definitions are for an n-axis machine with defined Cartesian coordinate reference system and assume the rigid body model. In all cases, the final figures for each value are with reference to a specified datum position, which may conventionally be chosen to be the negative extremities of all axes, or a central position in the working volume.

### 3.05.1 Total geometric displacement error

At any point, the **total geometric displacement error** for each of the reference axes can be defined as the sum of the linear effects, in that direction, resulting from all the geometric errors of all n axes.

### 3.05.2 Volumetric error

The **volumetric error** at any point in the working volume is defined as the vector sum of the total geometric displacement error of the three reference axes at that point.

Figure 3.1 gives a pictorial representation of the volumetric error at a given point.

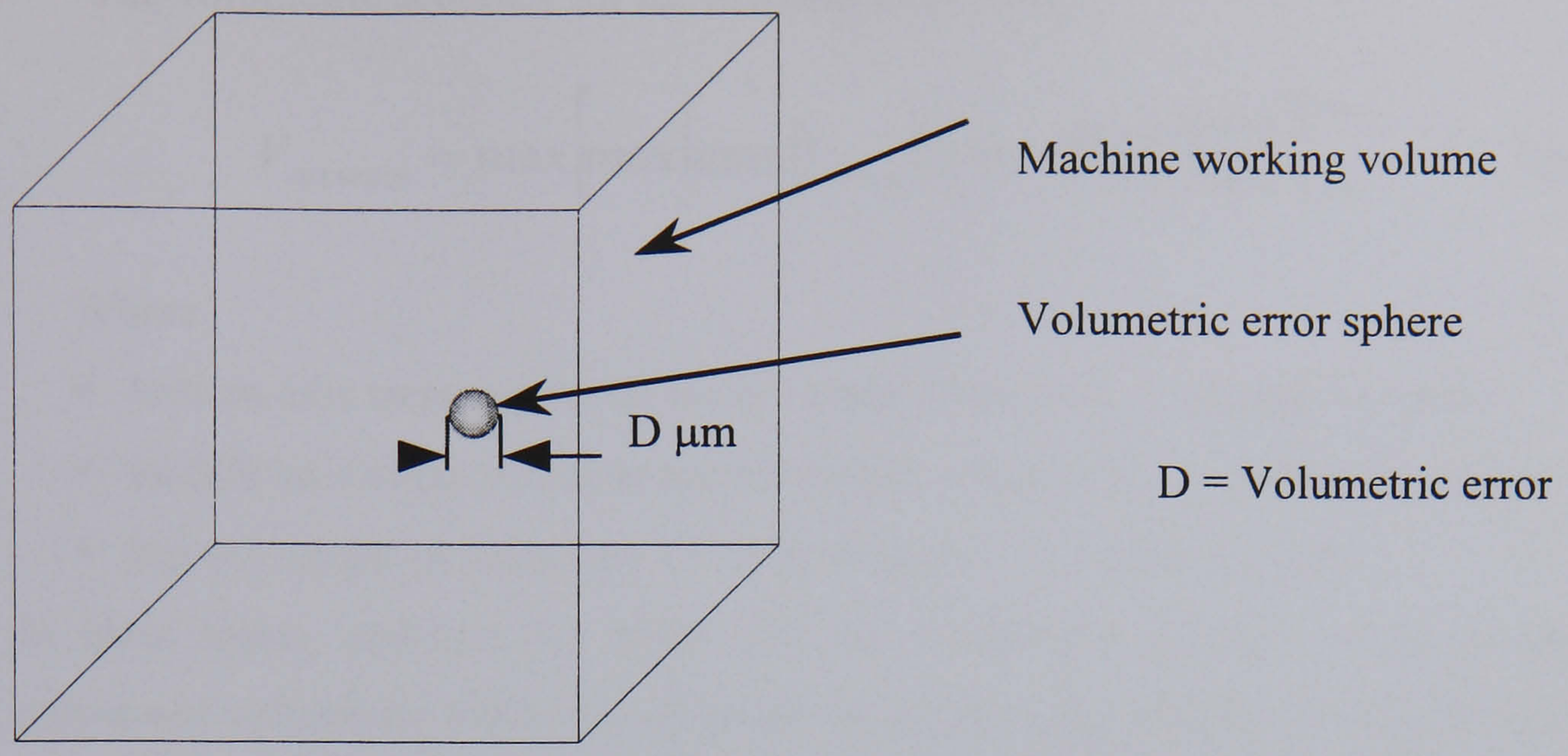


**Figure 3.1: Pictorial representation of volumetric error**

### 3.05.3 Volumetric accuracy

The **volumetric accuracy** of the machine is defined as the maximum of the volumetric errors in the working volume of the machine.

Pictorially this equates to the largest of the volumetric error spheres of figure 3.1.

### 3.05.4 Planar error

The **planar error** at any point in the working volume is defined as the vector sum of the total geometric displacement error of the two reference axes in the plane at that point.

### 3.05.5 Planar accuracy

The **planar accuracy** of the machine is defined as the maximum of the planar errors in the defined working plane of the machine.

### 3.05.6 Interpretation for three-axis machine tool

For a three-axis machine tool:

- The total geometric displacement error at point (b,m,t) is given as $B_{error}(b,m,t)$, $M_{error}(b,m,t)$ and $T_{error}(b,m,t)$ from the relevant set of equations in section 3.04.
- The volumetric error at point (b,m,t) is given by

$$V_{error}(b,m,t) = \sqrt{B_{error}^2 + M_{error}^2 + T_{error}^2} \qquad \text{Equation 3.4}$$

- The volumetric accuracy for the machine is given by

$$V_{accuracy} = \max\left[\max\left[\max\left[V_{error}(b,m,t)\right]_{b\,\min}^{b\,\max}\right]_{m\,\min}^{m\,\max}\right]_{t\,\min}^{t\,\max} \qquad \text{Equation 3.5}$$

Where

- bottom axis target positions are b = bmin, (bmin+1), …, (bmax-1), bmax
- middle axis target positions are m = mmin, (mmin+1), …, (mmax-1), mmax
- top axis target positions are t = tmin, (tmin+1), …, (tmax-1), tmax.

In plain terms, equation 3.5 states that the volumetric accuracy is the greatest of the calculated volumetric errors for all points in the working volume. With reference to figure 3.1, we may think of this pictorially as the largest of the spheres of volumetric error in the working volume.

Planar accuracy is calculated in a similar manner to volumetric accuracy, but with one of the axes fixed.

## 3.06 Tool offset

Using the original three-axis model, all errors are calculated at the measurement centre point (MCP). This is nominally the end of the ram and the point where the laser optics are mounted during measurement. This point also corresponds to the 'pivot point' on a CMM when considering where the probe is mounted. As previously noted, certain geometric effects will not influence the volumetric accuracy of a tool fitted to this part of the machine. However, this is not the case for a machine with a tool offset. For such a machine the errors should be assessed at the tool centre point (TCP). When one considers that the Renishaw PH10T [56] indexable probe head is capable of carrying a 300mm extension, it can be seen that the offset can become significant.

### 3.06.1 Tool in-line with tool-carrying axis

Since the positional error resulting from angular error is a function of the displacement from the datum position of the amplifier axis, any increase in this distance due to tool length will also result in an increase in the magnitude of the error. From figure 3.2 it can be seen that extending the length of the tool will result in an increase in horizontal error.

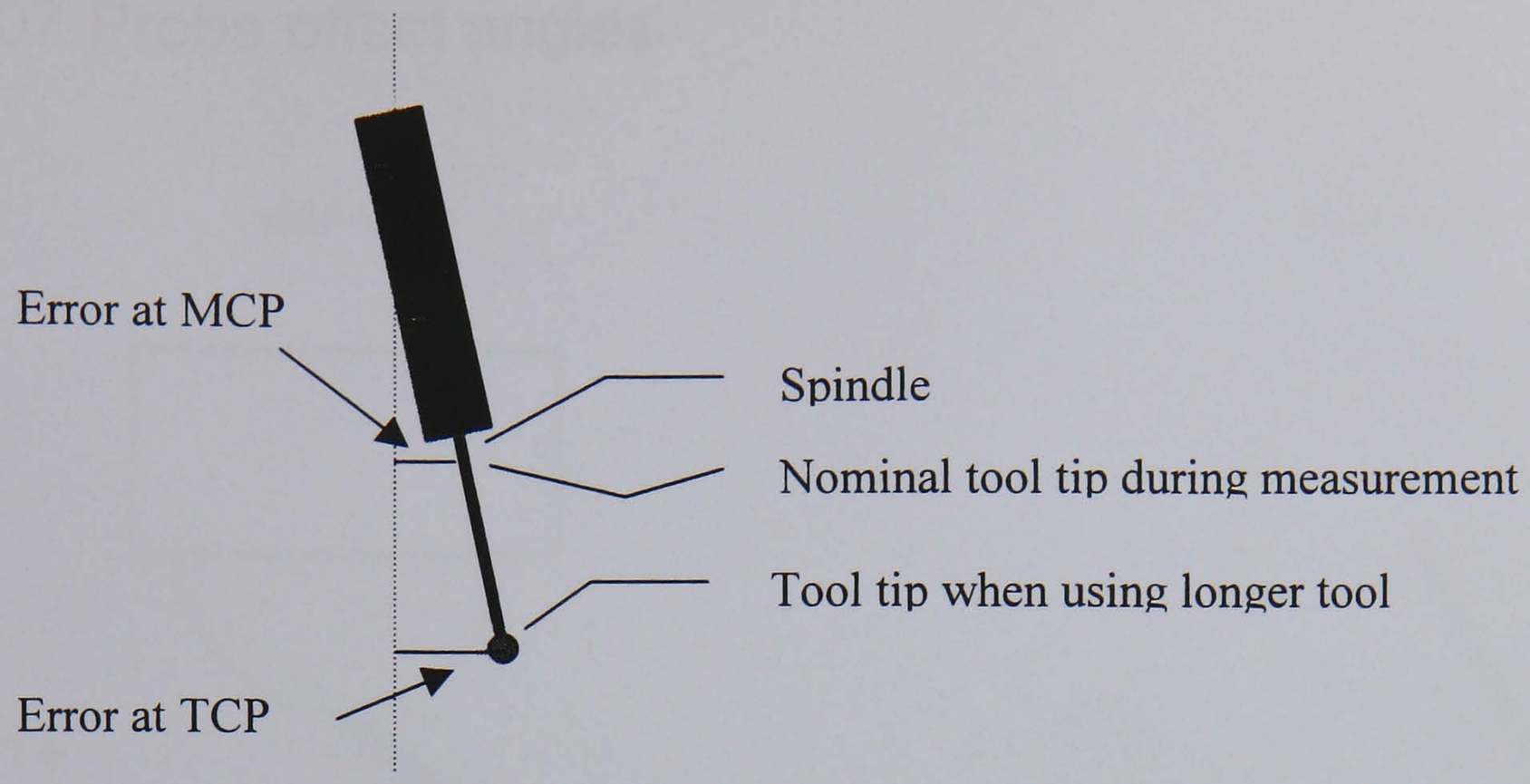


**Figure 3.2: Tool extension in line with ram**

Although not specifically incorporated in the model, this type of offset can be included as a single value addition to the length of the tool-carrying axis for all points in the working volume.

### 3.06.2 Tool offset at an angle to the tool-carrying axis

A more complex problem arises when the tool is no longer in line with the axis carrying the tool (figure 3.3). In this case, it is essential to have knowledge of additional error components and use a full model of the geometric errors.


**Figure 3.3: Tool extension at an angle to ram**

Consider a machine with a probe attached to the T-axis that is used to measure in the T-axis direction. Any pitch or yaw of the T-axis will not produce a measurement error at the MCP since there is no amplifier axis for the error. However, the inclusion of a tool perpendicular to the spindle axis (e.g. nominally in the B-axis) will amplify the angular error by the length of the tool in question, producing an error in the T-axis.

To be able to evaluate errors at the TCP for this configuration of machine it is essential to include all error sources in the machine model, derived in the following sections.

## 3.07 Probe offset angles

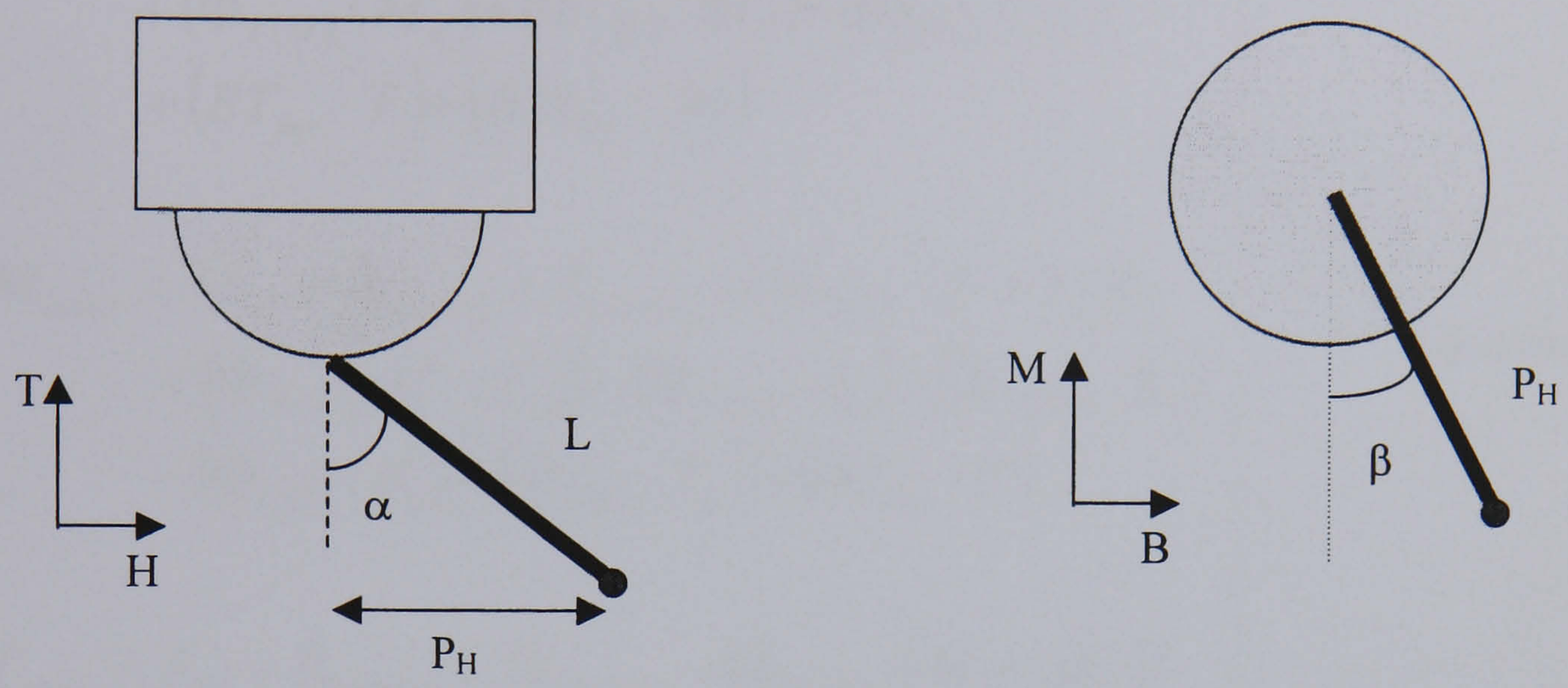


**Figure 3.4: Offset of tool tip from MCP**

The tool offset can be broken down into the constituent parts in the Cartesian frame of the machine.

$$P_T = L\cos\alpha \qquad \text{Equation 3.6}$$

$$\therefore P_H = L\sin\alpha \qquad \text{Equation 3.7}$$

$$P_B = P_H \sin\beta = L\sin\alpha\sin\beta \qquad \text{Equation 3.8}$$

Equation 3.9

### 3.07.1 Models for three-axis machine tools with rotating head

In the following equations $P_B$ is denoted $B_0$, $P_M$ is denoted $M_0$ and $P_T$ is denoted $T_0$ for clarity.

For **t**ool **B**ottom **M**iddle **T**op Machine Configurations (**tBMT**)

$$\left.\begin{aligned}
B_{error} &= B_{lin} + M_{strt(B)} + T_{strt(B)} + \left(\Phi_{M(B)} \cdot \left(T + T_o\right)\right) \\
&\quad + \left(\Phi_{M(M)} \cdot \left(T + T_o\right)\right) + \left(\Phi_{T(B)} \cdot \left(M + M_o\right)\right) \\
&\quad + \left(\Phi_{T(M)} \cdot M_o\right) + \left(\Phi_{T(T)} \cdot M_o\right) - \left(\Phi_{M(T)} \cdot T_o\right) \\
&\quad + \left(BT_{sqr.} \cdot T\right) + \left(BM_{sqr.} \cdot M\right) \\
\\
M_{error} &= M_{lin} + B_{strt(M)} + T_{strt(M)} + \left(\Phi_{B(B)} \cdot \left(T + T_o\right)\right) \\
&\quad + \left(\Phi_{B(M)} \cdot \left(T + T_o\right)\right) - \left(\Phi_{T(B)} \cdot B_o\right) - \left(\Phi_{T(M)} \cdot B_o\right) \\
&\quad - \left(\Phi_{T(T)} \cdot B_o\right) - \left(\Phi_{B(T)} \cdot T_o\right) + \left(MT_{sqr.} \cdot T\right) \\
\\
T_{error} &= T_{lin} + B_{strt(T)} + M_{strt(T)} - \left(\Phi_{B(B)} \cdot \left(M + M_o\right)\right) \\
&\quad - \left(\Phi_{M(B)} \cdot B_o\right) - \left(\Phi_{M(M)} \cdot B_o\right) + \left(\Phi_{M(T)} \cdot B_o\right) \\
&\quad - \left(\Phi_{B(M)} \cdot M_o\right) + \left(\Phi_{B(T)} \cdot M_o\right)
\end{aligned}\right\}$$

Equation 3.10

For **B**ottom **t**ool **M**iddle **T**op Machine Configurations (**BtMT**)

$$
\begin{aligned}
B_{error} &= B_{lin} + M_{strt(B)} + T_{strt(B)} + \left(\Phi_{M(B)} \cdot \left(T + T_o\right)\right) \\
&+ \left(\Phi_{M(M)} \cdot \left(T + T_o\right)\right) + \left(\Phi_{T(B)} \cdot \left(M + M_o\right)\right) \\
&+ \left(\Phi_{T(M)} \cdot M_o\right) + \left(\Phi_{T(T)} \cdot M_o\right) + \left(\Phi_{M(T)} \cdot T_o\right) \\
&+ \left(BT_{sqr.} \cdot T\right) + \left(BM_{sqr.} \cdot M\right)
\end{aligned}
$$

$$
\begin{aligned}
M_{error} &= M_{lin} + B_{strt(M)} + T_{strt(M)} + \left(\Phi_{B(B)} \cdot \left(T + T_o\right)\right) \\
&+ \left(\Phi_{B(M)} \cdot \left(T + T_o\right)\right) + \left(\Phi_{B(T)} \cdot T_o\right) - \left(\Phi_{T(M)} \cdot B_o\right) \\
&- \left(\Phi_{T(T)} \cdot B_o\right) + \left(MT_{sqr.} \cdot T\right)
\end{aligned}
$$

$$
\begin{aligned}
T_{error} &= T_{lin} + B_{strt(T)} + M_{strt(T)} - \left(\Phi_{B(B)} \cdot \left(M + M_o\right)\right) \\
&- \left(\Phi_{B(T)} \cdot M_o\right) - \left(\Phi_{B(M)} \cdot M_o\right) - \left(\Phi_{M(M)} \cdot B_o\right) \\
&- \left(\Phi_{M(T)} \cdot B_o\right)
\end{aligned}
$$

Equation 3.11

For **B**ottom **M**iddle **t**ool **T**op Machine Configurations (**BMtT**)

$$
\begin{aligned}
B_{error} &= B_{lin} + M_{strt(B)} + T_{strt(B)} + \left(\Phi_{M(B)} \cdot \left(T + T_o\right)\right) \\
&+ \left(\Phi_{M(M)} \cdot \left(T + T_o\right)\right) + \left(\Phi_{T(M)} \cdot M_o\right) \\
&+ \left(\Phi_{T(B)} \cdot M_o\right) + \left(\Phi_{T(T)} \cdot M_o\right) - \left(\Phi_{M(T)} \cdot T_o\right) \\
&+ \left(BT_{sqr.} \cdot T\right) + \left(BM_{sqr.} \cdot M\right)
\end{aligned}
$$

$$
\begin{aligned}
M_{error} &= M_{lin} + B_{strt(M)} + T_{strt(M)} + \left(\Phi_{B(B)} \cdot \left(T + T_o\right)\right) \\
&+ \left(\Phi_{B(M)} \cdot \left(T + T_o\right)\right) + \left(\Phi_{T(M)} \cdot \left(B - B_o\right)\right) \\
&- \left(\Phi_{B(T)} \cdot T_o\right) - \left(\Phi_{T(B)} \cdot B_o\right) - \left(\Phi_{T(T)} \cdot B_o\right) \\
&+ \left(MT_{sqr.} \cdot T\right)
\end{aligned}
$$

$$
\begin{aligned}
T_{error} &= T_{lin} + B_{strt(T)} + M_{strt(T)} - \left(\Phi_{M(M)} \cdot \left(B - B_o\right)\right) \\
&+ \left(\Phi_{B(M)} \cdot M_o\right) + \left(\Phi_{B(B)} \cdot M_o\right) - \left(\Phi_{B(T)} \cdot M_o\right) \\
&+ \left(\Phi_{M(B)} \cdot B_o\right) - \left(\Phi_{M(T)} \cdot B_o\right)
\end{aligned}
$$

Equation 3.12

## 3.08 Measurement of a compensated machine

Electronic compensation applies a linear compensation offset for the *effect* of an angular error (figure 3.5). In the case of some machine tools, this electronic compensation is applied by movement of the machine axis by the correction value. In the case of a CMM, it is usually simply a correction displayed on the screen. Since the effect of the angular error has been reduced, it is no longer correct to use the measured angle for the calculation of volumetric error.

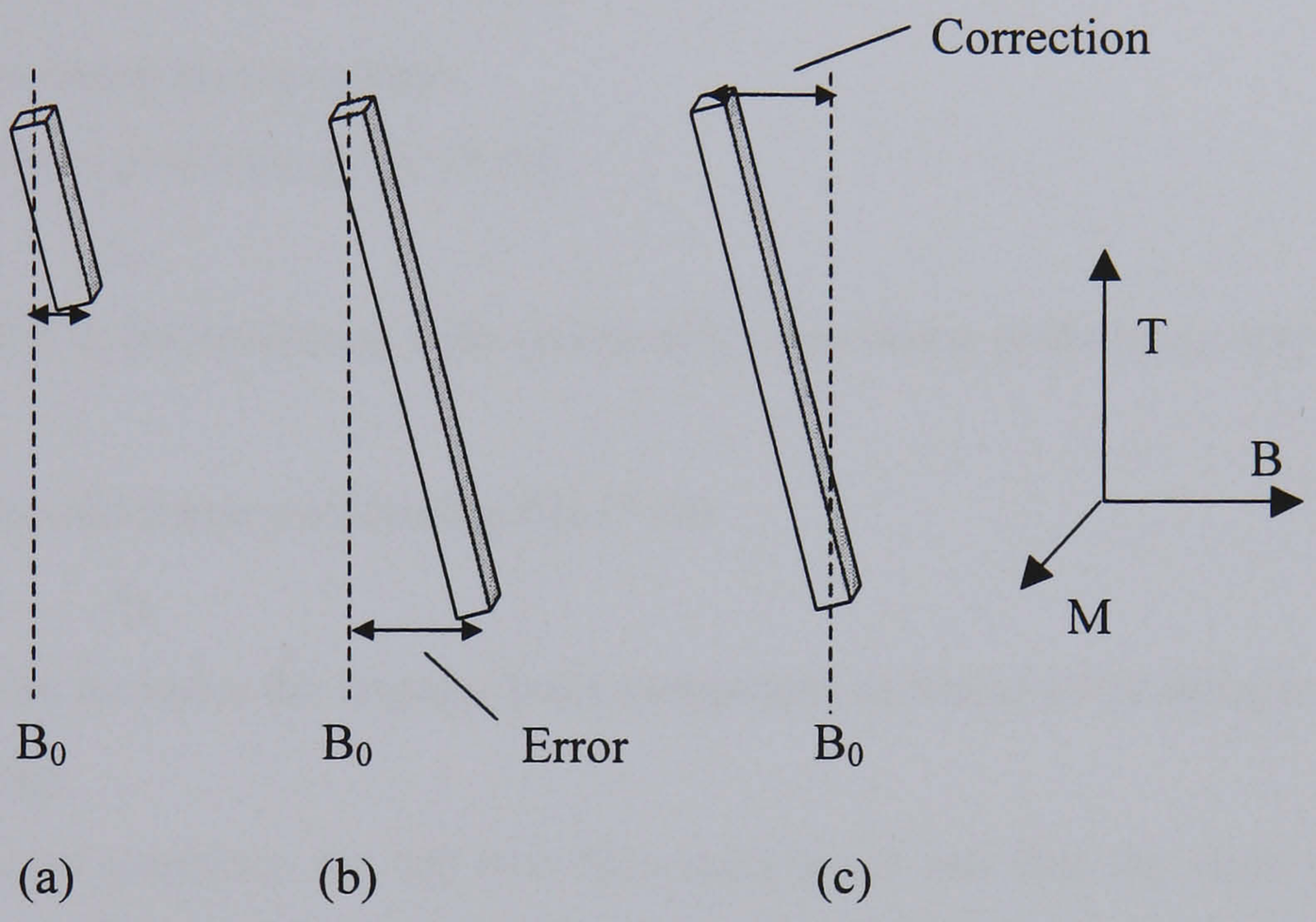


**Figure 3.5: Linear correction for effect of angular error**

Consider a wBMTt three-axis machine for which errors are calculated at the MCP. Figure 3.5 (a) and (b) show that, because of the rotation of the B-axis about the M-axis, for different positions of the T-axis the end of the ram is offset from the nominal position in the B-axis. This is the linear effect of the geometric error and is calculated by equation 3.13.

$$e\left(T, \phi_{M(B)}\right) = T.\phi_{M(B)} \qquad \text{Equation 3.13}$$

Figure 3.5 (c) then shows how this error can be reduced by moving the B-axis by an amount equal and opposite to this error either by actuation or by offsetting the display value in the case of a CMM. If the effect of the error is reduced by compensation a residual slope, $\delta\phi_{M(B)}$, remains. However, $T.\delta\phi_{M(B)} \neq T.\phi_{M(B)}$.

It is not correct to use directly-measured geometric angular error data in the models for a machine that has volumetric geometric error compensation. In order to assess volumetric performance on such a machine it is necessary to take two linear position measurements, with known displacement between the runs, to calculate the linear effect of the angular error.

DOS based software, which has been written in Borland C, is then applied in order to calculate the angular error. The software uses the following algorithm (section 3.08.1) in order to calculate the angular error.

### 3.08.1 Angular error calculation pseudo-code

**1. Load files using menu system**

- Load in linear positioning file (*.rtl)

  $a_1, a_2, \ldots, a_n$

  This file is the reference with (nominally) zero linear positioning error.

- Load in second linear positioning file (*.rtl)

  $b_1, b_2, \ldots, b_n$

  This file includes the angular error component as linear positioning error.

**2. Error Trap**

- Ensure target positions for the two files correspond and that the same number of runs have been made in each. This ensures that the following calculations are using corresponding data.

**3. User input**

- Ask user for displacement between two files, d (user input (mm)) This is a signed value describing either a positive or negative displacement. Sign convention issues will be resolved within the procedure by specifying files in the correct order and specifying the sign of the displacement.
- Ask user for the datum position in millimetres

**4. Error Check**

- If the datum position is not a valid target, an error is returned

**5. Calculation**

- Determine the error at the datum position, datumerror

  Determine point at which datum occurs and calculate

  $$\text{datumerror} = (b_{datum} - a_{datum})/d$$

- For each data point in turn calculate the angular error by the following loop:

  for i = 1 to n

  angerr $_i$ = ($b_i$- $a_i$)/d - datumerror

  end

**6. Output**

- The results are then saved as an angular file (*.rta)

In a machine that does not have volumetric compensation, the values obtained by using this technique should correspond to those obtained by directly measuring the angular error using angular optics, electronic level or other metrological instrument.

## 3.09 Tool offset on compensated machine

Electronic compensation does not remove the angular misalignment itself. On a CMM, for example, the effect of the angular error may have been corrected using an error map technique. This means that the effect of angular errors on the position of the MCP may have been reduced, but that the mechanical angle remains. As such the effect of the physical angle must be considered when a probe is offset from the MCP.

From figure 3.6 (a), it can be seen that applying an extension in the form of a probe or tool will result in an increase in horizontal error. The desired position is $B_0$ but, as a result of angular error, the end of the ram is at $B_1$. A long probe or tool would further amplify the error to $B_2$.

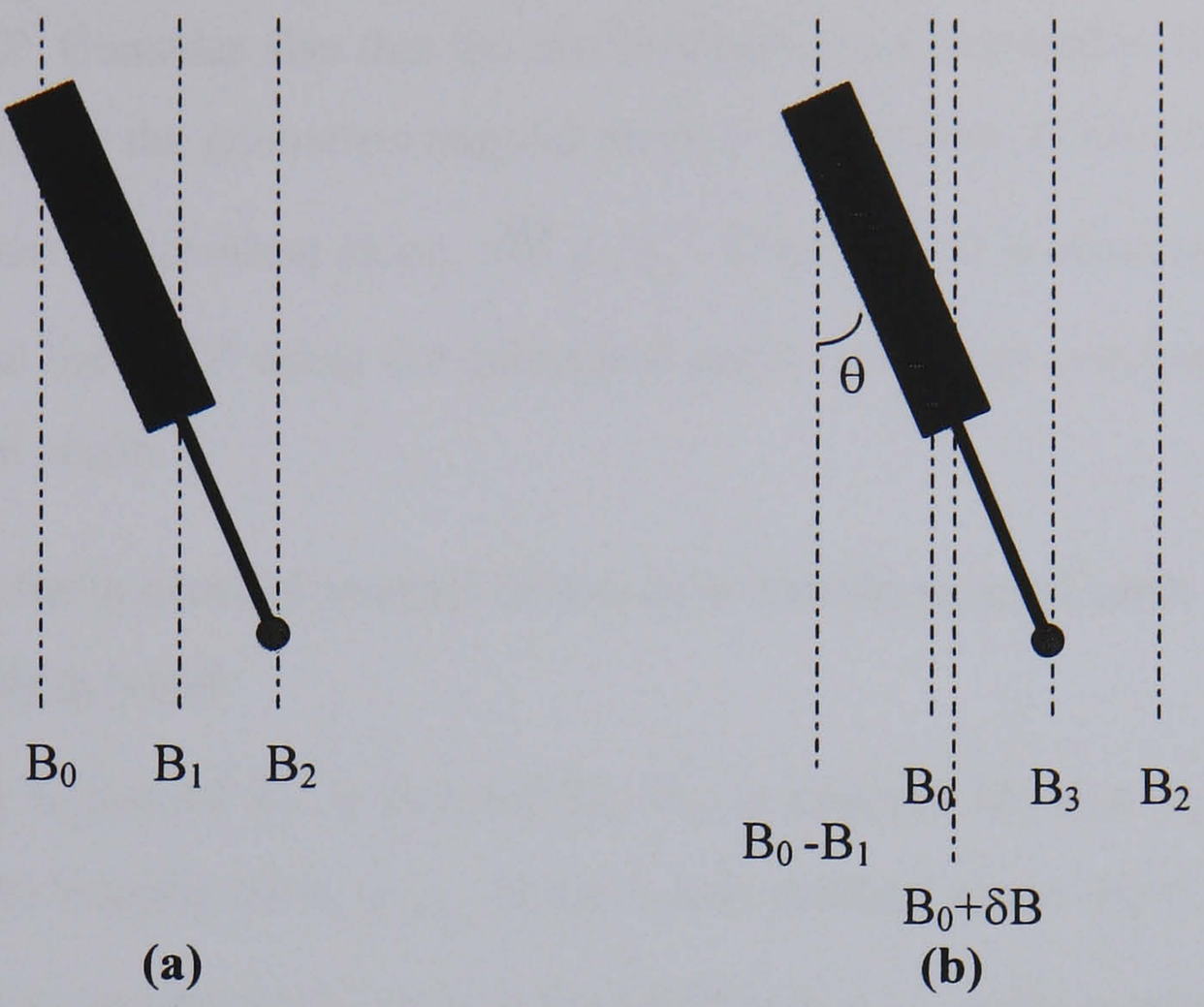


**Figure 3.6: Tool extension in line with ram**

Figure 3.6 (b) shows the case of a compensated machine. The axis has been linearly adjusted by an amount ($B_0 - B_1$) to compensate for the angular error, θ. However, a residual error δB exists, due to δθ, the difference between the angular value used by the compensation system and the true angle. This difference could result from uncertainties during measurement of the error, or mechanical changes over time.

δB is a function of ram extension and the residual angular error, which must be calculated from two linear positioning runs, as described above. However, the length of the tool amplifies the mechanical angular error, θ resulting in the end of the tool being at a point $B_3$. The distance $B_3$ from $B_0+\delta B$ is calculated from the angle taken using angular optics, or using the linear measurement method with no angular compensation applied.

Consider again a wBMTt three-axis machine with volumetric compensation for errors at the MCP. Consider also that the machine has a tool oriented in the B-axis direction. The tool will amplify the geometric angular error, it is therefore a function of the geometric angle, $\phi_{M(B)}$, not the residual slope, $\delta\phi_{M(B)}$. Therefore, it is necessary to calculate the effect of errors at the MCP using the calculated angle, and those resulting from tool length from the physical angle.

### 3.09.1 Models for a compensated three-axis machine tool with rotating head

In the following equations $P_B$ is denoted $B_0$, $P_M$ is denoted $M_0$ and $P_T$ is denoted $T_0$ for clarity. Where the angular error, $\phi_{K(L)}$ is the L-axis rotation about the K axis residual from compensation and contributing to error at the MCP and $\gamma_{K(L)}$ is the mechanical angle.

For **t**ool **B**ottom **M**iddle **T**op machine configurations (**tBMT**)

$$
\begin{aligned}
B_{error} &= B_{lin} + M_{strt(B)} + T_{strt(B)} + \left(\Phi_{M(B)} \cdot T + \gamma_{M(B)} \cdot T_0\right) \\
&+ \left(\Phi_{M(M)} \cdot T + \gamma_{M(M)} \cdot T_0\right) + \left(\Phi_{T(B)} \cdot M + \gamma_{T(B)} \cdot M_0\right) \\
&+ \left(\gamma_{T(M)} \cdot M_o\right) + \left(\gamma_{T(T)} \cdot M_o\right) - \left(\gamma_{M(T)} \cdot T_o\right) \\
&+ \left(BT_{sqr.} \cdot T\right) + \left(BM_{sqr.} \cdot M\right)
\end{aligned}
$$

$$
\begin{aligned}
M_{error} &= M_{lin} + B_{strt(M)} + T_{strt(M)} + \left(\Phi_{B(B)} \cdot T + \gamma_{B(B)} \cdot T_0\right) \\
&+ \left(\Phi_{B(M)} \cdot T + \gamma_{B(M)} \cdot T_0\right) - \left(\gamma_{T(B)} \cdot B_o\right) - \left(\gamma_{T(M)} \cdot B_o\right) \\
&- \left(\gamma_{T(T)} \cdot B_o\right) - \left(\gamma_{B(T)} \cdot T_o\right) + \left(MT_{sqr.} \cdot T\right)
\end{aligned}
$$

$$
\begin{aligned}
T_{error} &= T_{lin} + B_{strt(T)} + M_{strt(T)} - \left(\Phi_{B(B)} \cdot M + \gamma_{B(B)} \cdot M_0\right) \\
&- \left(\gamma_{M(B)} \cdot B_o\right) - \left(\gamma_{M(M)} \cdot B_o\right) + \left(\gamma_{M(T)} \cdot B_o\right) \\
&- \left(\gamma_{B(M)} \cdot M_o\right) + \left(\gamma_{B(T)} \cdot M_o\right)
\end{aligned}
$$

Equation 3.14

For **B**ottom **t**ool **M**iddle **T**op Machine Configurations (**BtMT)**

$$
\left.
\begin{aligned}
B_{error} &= B_{lin} + M_{strt(B)} + T_{strt(B)} + \left(\Phi_{M(B)} \cdot T + \gamma_{M(B)} \cdot T_0\right) \\
&\quad + \left(\Phi_{M(M)} \cdot T + \gamma_{M(M)} \cdot T_0\right) + \left(\Phi_{T(B)} \cdot M + \gamma_{T(B)} \cdot M_0\right) \\
&\quad + \left(\gamma_{T(M)} \cdot M_o\right) + \left(\gamma_{T(T)} \cdot M_o\right) + \left(\gamma_{M(T)} \cdot T_o\right) \\
&\quad + \left(BT_{sqr.} \cdot T\right) + \left(BM_{sqr.} \cdot M\right)
\end{aligned}
\right\}
$$

$$
\left.
\begin{aligned}
M_{error} &= M_{lin} + B_{strt(M)} + T_{strt(M)} + \left(\Phi_{B(B)} \cdot T + \gamma_{B(B)} \cdot T_0\right) \\
&\quad + \left(\Phi_{B(M)} \cdot T + \gamma_{B(M)} \cdot T_0\right) + \left(\gamma_{B(T)} \cdot T_o\right) - \left(\gamma_{T(M)} \cdot B_o\right) \\
&\quad - \left(\gamma_{T(T)} \cdot B_o\right) + \left(MT_{sqr.} \cdot T\right)
\end{aligned}
\right\}
$$

$$
\left.
\begin{aligned}
T_{error} &= T_{lin} + B_{strt(T)} + M_{strt(T)} - \left(\Phi_{B(B)} \cdot M + \gamma_{B(B)} \cdot M_0\right) \\
&\quad - \left(\gamma_{B(T)} \cdot M_o\right) - \left(\gamma_{B(M)} \cdot M_o\right) - \left(\gamma_{M(M)} \cdot B_o\right) \\
&\quad - \left(\gamma_{M(T)} \cdot B_o\right)
\end{aligned}
\right\}
$$

Equation 3.15

For **B**ottom **M**iddle **t**ool **T**op Machine Configurations (**BMtT**)

$$
\begin{aligned}
B_{error} &= B_{lin} + M_{strt(B)} + T_{strt(B)} + \left(\Phi_{M(B)} \cdot T + \gamma_{M(B)} \cdot T_0\right) \\
&+ \left(\Phi_{M(M)} \cdot T + \gamma_{M(M)} \cdot T_0\right) + \left(\gamma_{T(M)} \cdot M_o\right) \\
&+ \left(\gamma_{T(B)} \cdot M_o\right) + \left(\gamma_{T(T)} \cdot M_o\right) - \left(\gamma_{M(T)} \cdot T_o\right) \\
&+ \left(BT_{sqr.} \cdot T\right) + \left(BM_{sqr.} \cdot M\right)
\end{aligned}
$$

$$
\begin{aligned}
M_{error} &= M_{lin} + B_{strt(M)} + T_{strt(M)} + \left(\Phi_{B(B)} \cdot T + \gamma_{B(B)} \cdot T_0\right) \\
&+ \left(\Phi_{B(M)} \cdot T + \gamma_{B(M)} \cdot T_0\right) \\
&+ \left(\Phi_{T(M)} \cdot B - \gamma_{T(M)} \cdot B_0\right) - \left(\gamma_{B(T)} \cdot T_o\right) \\
&- \left(\gamma_{T(B)} \cdot B_o\right) - \left(\gamma_{T(T)} \cdot B_o\right) + \left(MT_{sqr.} \cdot T\right)
\end{aligned}
$$

$$
\begin{aligned}
T_{error} &= T_{lin} + B_{strt(T)} + M_{strt(T)} \\
&- \left(\Phi_{M(M)} \cdot B - \gamma_{M(M)} \cdot B_0\right) \\
&+ \left(\gamma_{B(M)} \cdot M_o\right) + \left(\gamma_{B(B)} \cdot M_o\right) - \left(\gamma_{B(T)} \cdot M_o\right) \\
&+ \left(\gamma_{M(B)} \cdot B_o\right) - \left(\gamma_{M(T)} \cdot B_o\right)
\end{aligned}
$$

Equation 3.16

## 3.10 Generic approach to volumetric evaluation

It is important that the approach to evaluation of volumetric error remains general so that a single piece of software can be use to evaluate all Cartesian systems. Measurement of angular errors and the measurement inputs to the model depend upon whether volumetric evaluation is calculated for the MCP or TCP and whether volumetric compensation is active. For this discussion of the general case, it is important that machines with compensation for the errors at the TCP be considered in addition to one where compensation is only for errors at the MCP. The evaluation strategy can be split into the following five cases:

### 3.10.1 Evaluation at MCP of machine without compensation

The case of a standard three-axis machine tool without compensation corresponds to the system described by Postlethwaite [34]. One of the configuration-specific models described in section 3.04 is used for calculating the errors. The angular errors used for the model

inputs can be measured either directly or by the indirect measurement technique discussed in section 3.01.

### 3.10.2 Evaluation at MCP of machine with compensation

The case of a standard three-axis machine tool with compensation utilises the same model as for the case without compensation. The angular errors used for the geometric inputs must be measured by the indirect measurement technique discussed in section 3.01.

### 3.10.3 Evaluation at TCP of machine without compensation

The case of a machine with a tool offset requires the use of one of the extended configuration-specific models described in section 3.07.1 for a nominal tool length. The angular errors used for the model inputs can be measured either directly or by the indirect measurement technique discussed in section 3.01.

### 3.10.4 Evaluation at TCP of machine compensated at the TCP

Some machines have compensation for the errors calculated at the TCP. Such systems involve a more sophisticated solution than for compensation at the MCP, since additional information regarding tool length and orientation needs to be transmitted to the compensation system.

One of the extended configuration-specific models described in section 3.07.1 is used for the evaluation of the errors at a nominal tool length. The angular errors used for the model inputs must be measured by the indirect measurement technique discussed in section 3.01. This should be performed with a tool of zero nominal length active in the compensation system.

### 3.10.5 Evaluation at TCP of machine compensated at the MCP

Machines with compensation for errors at the MCP are evaluated using the configuration-specific models given in section 3.09.1. As described in that section, the residual angle after compensation, $\phi_{K(L)}$, is measured using the indirect measurement technique discussed in section 3.01. The mechanical angle, $\gamma_{K(L)}$, is the measured directly using angular optics, or by using the indirect technique when compensation is inactive.

## 3.11 ESP volumetric error analysis software

The Error Simulation Program (ESP) was devised at the University of Huddersfield to aid the understanding of the way in which geometric errors in a three-axis Cartesian machine tool manifest themselves, and so affect machining accuracy.

Figure 3.7 is the first screen entered when using ESP to analyse a machine, and is used to choose which of the three models describes the machine. For the first configuration all three axes move the tool (wBMTt), in the second two axes move the tool (BwMTt) and in the third configuration only one axis moves the tool (BMwTt). The fourth possibility, where all three axes move the workpiece while the tool remains stationary is not considered in the software because such machines are extremely rare.

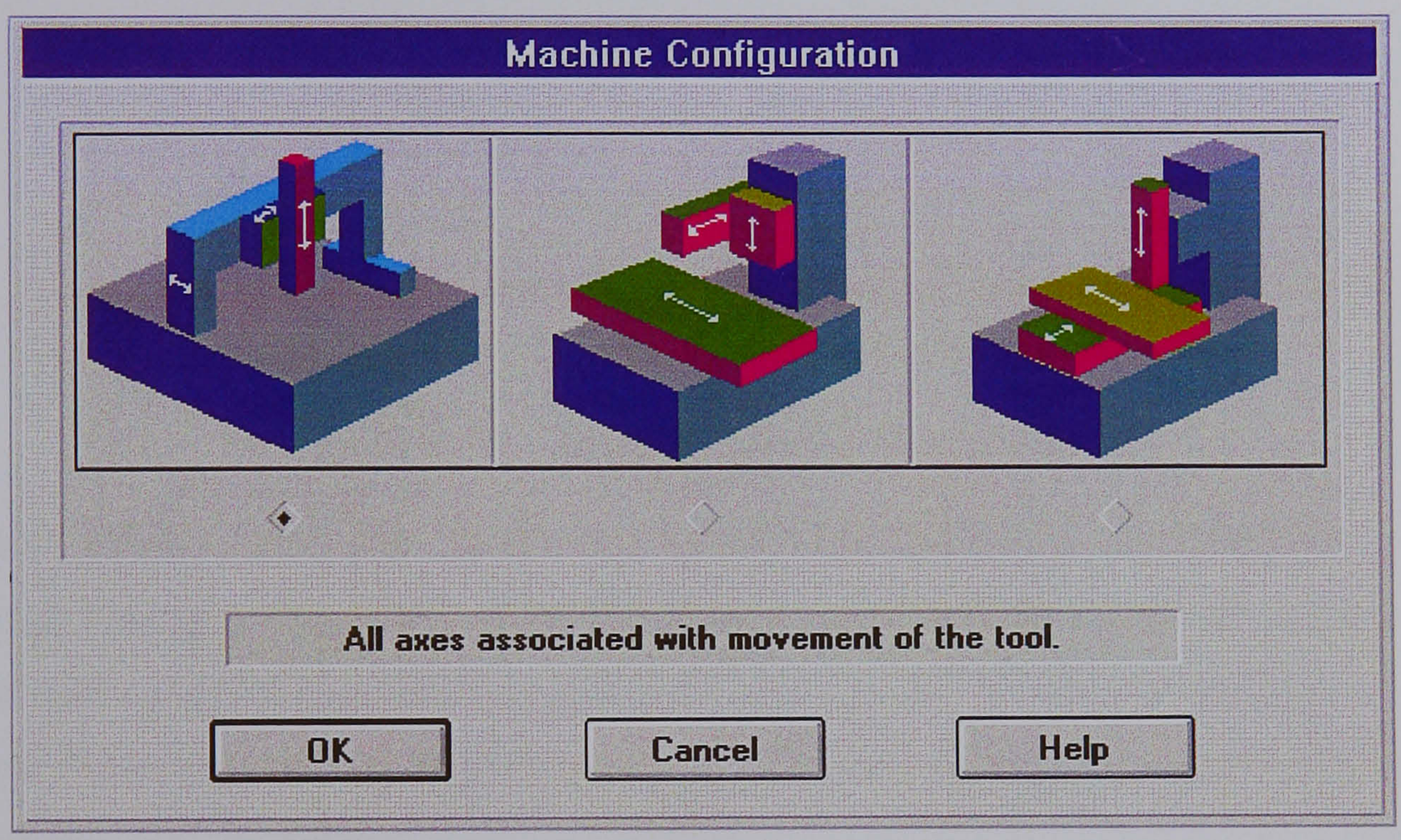


**Figure 3.7: Configuration selection screen**

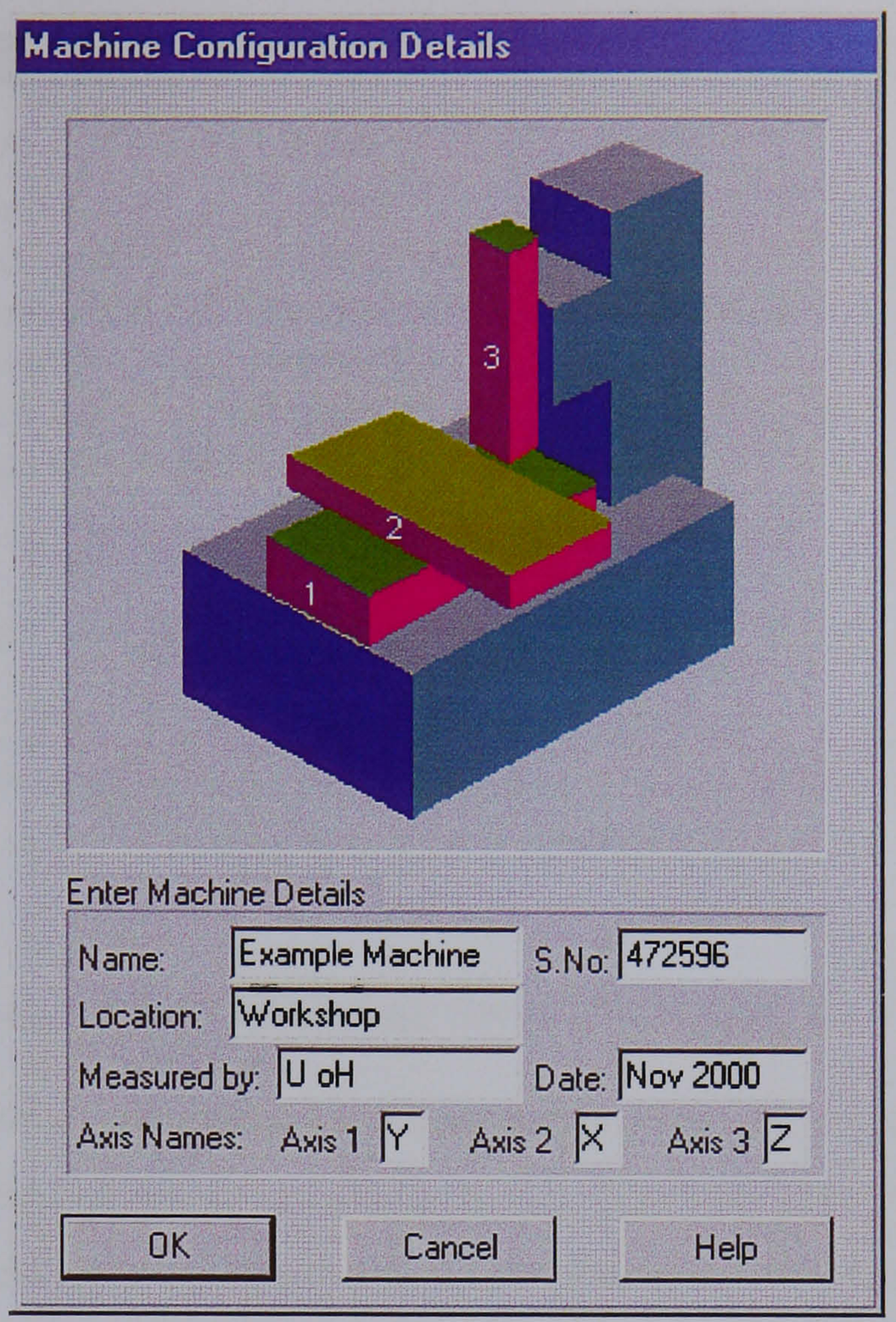


**Figure 3.8: Machine specification screen**

The next screen (figure 3.8) defines the specific configuration of the machine to allow meaningful interpretation of the input data. This screen allows the input of machine details and the naming of the axes, which is critical for correct application of the error model. In the example shown in figure 3.8, the bottom axis is Y, the middle axis is X and the top axis is Z. The notation for this machine would be YX**w**Z**t**.

Once the configuration has been set the relevant measurements for the error components can be loaded through an interactive screen (figure 3.9) before analysis is undertaken.

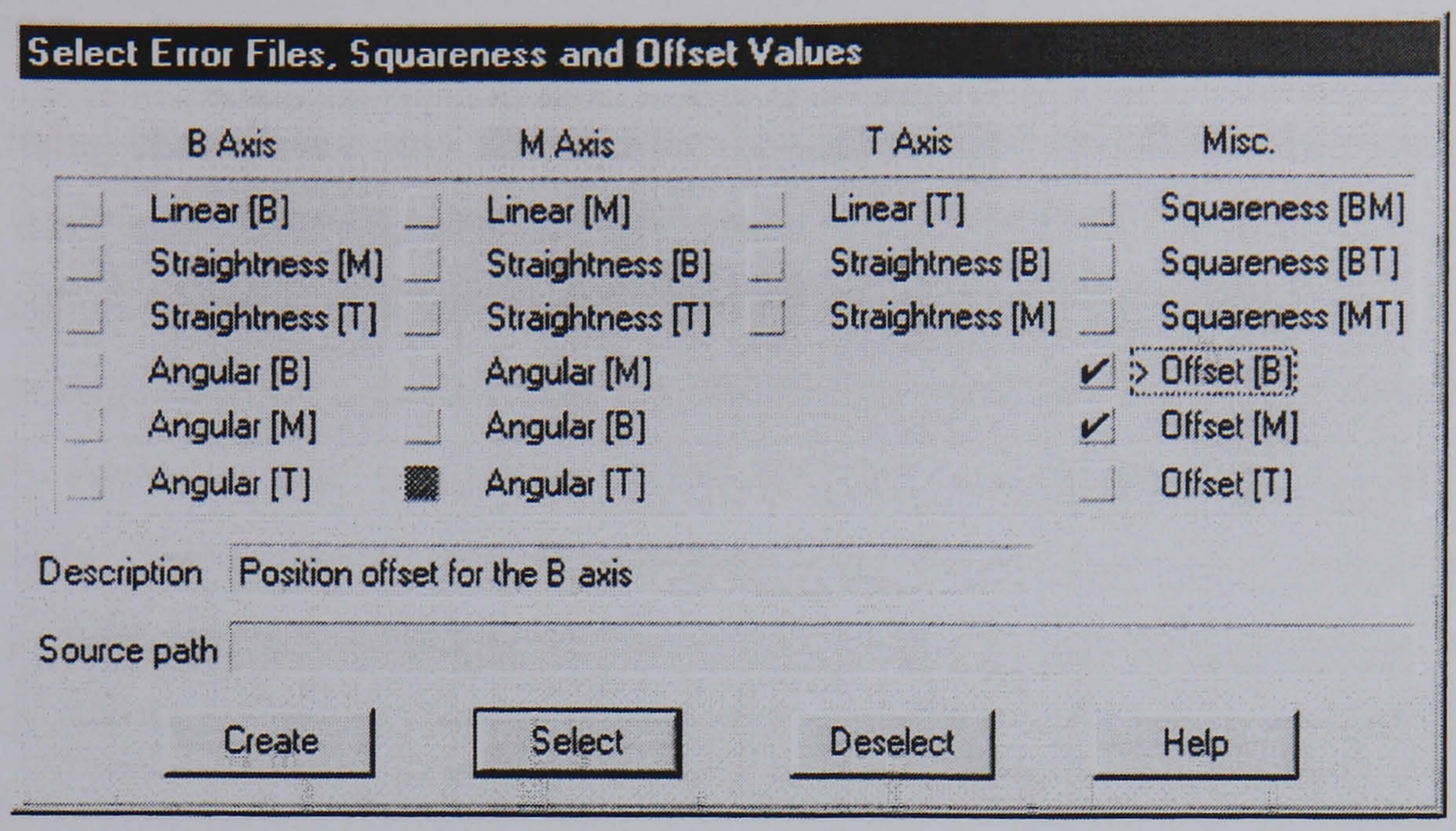


**Figure 3.9: Error selection screen**

## 3.12 Method of incorporating new analysis in ESP

The exclusion of unnecessary terms in the geometric model is a valuable method of limiting the time required to calibrate a machine. It has therefore been decided to maintain this functionality by deciding at the front end of the software the level of model required and so determine the number of inputs. This requires an input box to select one of the five combinations of tool offset and compensation described in section 3.10.

It then becomes important to determine the required output from the analysis. If a particular problem is to be addressed, such as a job with a unique tool length at a single orientation, then this specific analysis should be performed. However, the program may be used to determine the performance of a machine with an indexable head, capable of a range of orientations, using a variety of probe-lengths. In this case it will be essential to carry out the analysis for a much larger number of instances and quote the worst-case as the overall accuracy of the machine, for that particular job.

If the latter case is to be considered some restrictions must be made in order to ensure the calculation time is not prohibitive. It was decided that volumetric error should be calculated in 90 degree increments about the spindle axis, and 45 degree increments in the perpendicular plane. This compromise should trap the most significant errors due to the head, but not increase calculation time to an impractical level. Additionally, the tool length is selectable and a separate volumetric accuracy should be quoted for each tool length.

### 3.12.1 ESP software changes

The following changes are only relevant for the case where tool offsets are required. For a standard three-axis Cartesian machine tool where measurement at the MCP is required, the initial decision screen will ensure that the standard methodology is applied. It is also worth noting that when passing a machine off the volumetric assessment should be determined for the MCP. Problems due to tooling should not be the responsibility of the machine manufacturer. These changes are designed to help the machine user to understand the capability of the device in question.

As discussed above, when considering the effect of the tool offset additional information is required to determine the errors at the end of the tool. It is therefore necessary to supply the additional information to the simulation program. This can be achieved by providing additional inputs on the relevant user screen, an example of which is shown as figure 3.10.

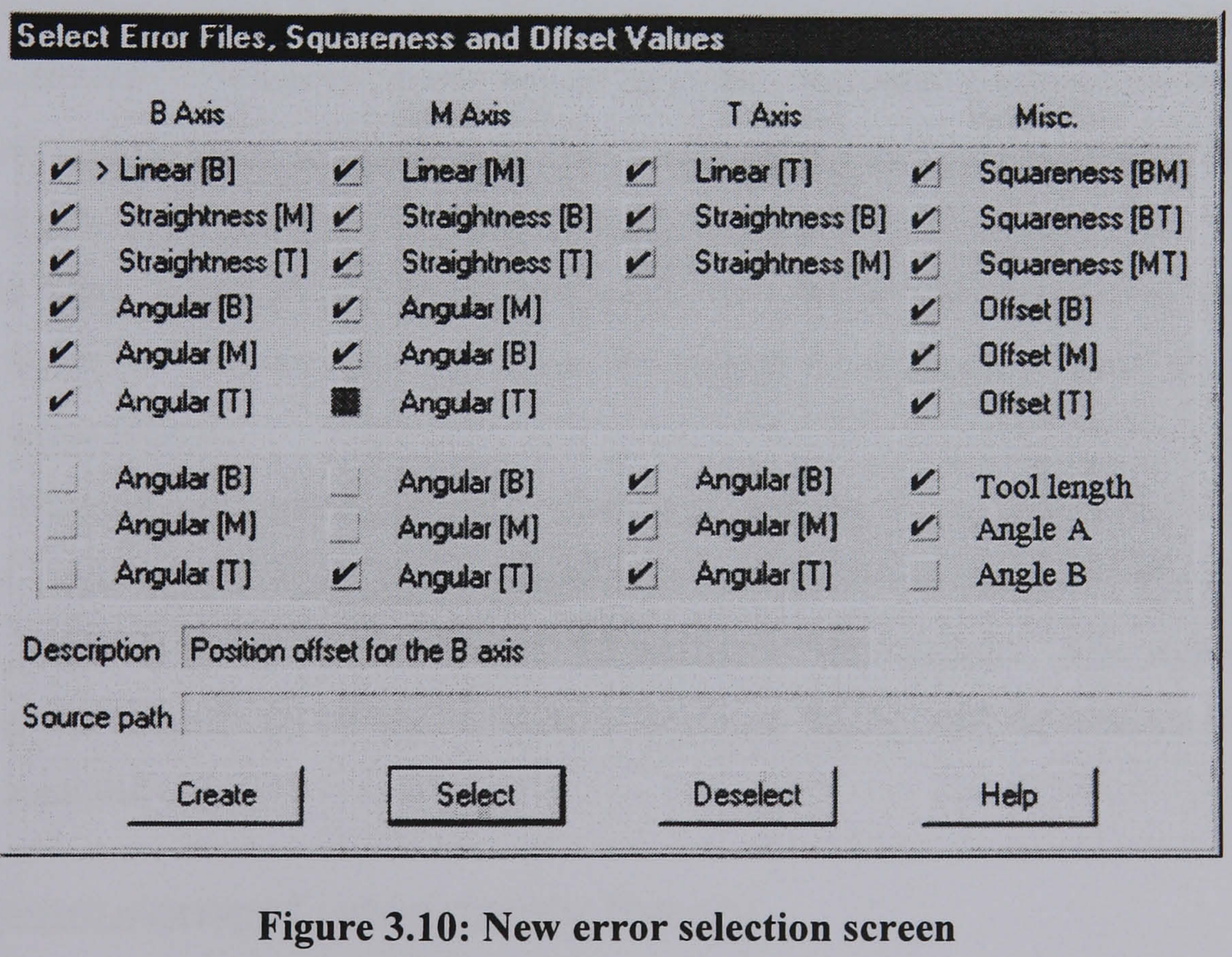


**Figure 3.10: New error selection screen**

Figure 3.10 is a typical representation of a machine in which all three axes move the tool (for example a gantry structure) for a machine with compensation for the errors at the MCP. The standard inputs, which appear above the dividing line, are concerned with calculating

the volumetric error at the MCP. Below the separating line are the errors relevant to the tool extension.

Figure 3.10 shows the selections (those boxes which are ticked) for a machine without volumetric compensation. In a machine where there is no volumetric compensation the additional angular components for the 'B' and 'M' axes are unnecessary, since the angles affecting probe error are of the same value as those affecting position at the MCP. However the angular error 'M angular error about T', whose effect is normally measured as part of the 'M axis straightness in the B direction' must now be measured individually. It also becomes necessary to measure all the 'T' axis angular errors.

Those unchecked components in figure 3.10 would be inactive for a machine with compensation for errors at the TCP, since the information for the model is the same as that provided in the upper half of the screen.

The chosen value of tool length and the relevant angles of the tool head must be provided to permit calculation at the tool tip. It is possible to select the orientation of the tool by specifying angles A and B. This allows a single calculation of the errors for that specific orientation. Without these values set, the software performs a number of calculations with different orientation to give an indicative figure for the performance of the machine by giving the worst case volumetric accuracy for all orientations.

The final output from the software indicates the overall worst-case volumetric accuracy figure for the machine. This can be printed in a standard form showing the individual error sources.

As suggested in section 1.11, the volumetric accuracy figure is only an "estimate of the answer." An important part of this research is to evaluate the quality of this estimation given the uncertainty of the individual measurement uncertainties. The approach for quantifying the uncertainty of the volumetric accuracy figure will be constructed in the following sections.

## 3.13 Measurement uncertainty theory

The effects that give rise to uncertainty in measurement can be classified as either random or systematic. The effect of random sources of uncertainty can be reduced by performing statistical analysis on a series of repeated measurements. However, a systematic uncertainty will not be better understood by simply repeating the same measurement. It is necessary to

perform different measurements or undertake uncertainty budget calculations to identify such uncertainties.

A source of uncertainty in a measurement is classified under one of two types. 'Type A' evaluations are the uncertainty estimates using statistics, usually from repeated readings. 'Type B' estimates come from other information. Bell [59] gives examples of these as past experience, calibration certificates, manufacturer's specifications, calculations, published information and from common sense. He further cautions against identifying 'Type A' with 'random' and 'Type B' with 'systematic', since this simplification is not always the case.

All contributing uncertainties must be expressed in the same units and at the same confidence level in order that they may be combined. This is achieved by converting each into an individual 'standard uncertainty', u(y), which can be thought of as 'plus or minus one standard deviation'. This gives the uncertainty of an average, not just the overall spread of values.

The uncertainty of the mean for a Type A measurement is calculated from the estimated standard deviation, s, and the number of measurements in the set, n, by equation 3.17

$$u = \frac{s}{\sqrt{n}} \qquad \text{Equation 3.17}$$

Where less readings are available (Type B uncertainties) it is often necessary to assume a rectangular distribution. If 'a' is half the width of the upper and lower limits, the standard uncertainty for the distribution is found from equation 3.18

$$\frac{a}{\sqrt{3}} \qquad \text{Equation 3.18}$$

Although rectangular distributions are quite common, if it is known or strongly suspected that another distribution is more appropriate, then the better model should be adopted.

Individual standard uncertainties calculated by Type A or Type B evaluations can be combined validly by 'summation in quadrature.' [59] The result of this is called the 'combined standard uncertainty', and is denoted $u_c$ or $u_c(y)$.

For problems where a result is the sum of a series of measured values this is calculated by equation 3.19

$$u_c = \sqrt{u_1^{\,2} + u_2^{\,2} + \ldots + u_n^{\,2}} \qquad \text{Equation 3.19}$$

Where $u_1$, $u_2$, …, $u_n$ are the individual uncertainties.

For cases where a result is a combination of multiplying or dividing two measurements it is more convenient to perform the uncertainty calculation in terms of 'fractional uncertainties.' If $D_{RESULT}$ is calculated from any combination of multiplication and division of $D_1$, $D_d$,…,$D_n$, then the uncertainty of the final result is given by equation 3.20.

$$\frac{u(D_{RESULT})}{D_{RESULT}} = \sqrt{\left(\frac{u(D_1)}{D_1}\right)^2 + \left(\frac{u(D_2)}{D_2}\right)^2 + \ldots + \left(\frac{u(D_n)}{D_n}\right)^2} \qquad \text{Equation 3.20}$$

Where $u(D_1)$, $u(D_2)$, …, $u(D_n)$ are the individual uncertainties for each of $D_1$, $D_d$,…,$D_n$ respectively.

Equation 3.19 and equation 3.20, which calculate the combined uncertainty for a measurement are only true if the individual uncertainties are independent. If more complex relationships exist, further analysis is required.

The combined uncertainty, $u_c$, can be related to the common concept of 'one standard deviation.' In order to allow the uncertainty to be quoted at different confidence levels, the expanded uncertainty, U, is calculated from the combined uncertainty and a coverage factor, k, according to equation 3.21.

$$U = ku_c \qquad \text{Equation 3.21}$$

For a normal distribution, the coverage factor k = 2 provides a 95% confidence.

As previously stated, Type A uncertainties are evaluated by the statistical analysis of a series of observations. The standard ISO repeatability test for an axis requires multiple runs, which can indeed be considered as a series of observations. It is clear that the measured repeatability from a series is not independent of the uncertainty attributed the measurements.

For example, the contributors to the uncertainty of measuring straightness using a laser interferometer with short-range optics are dominated by beam disturbance (table 3.1).

These figures are quoted for a measurement range of three hundred microns from alignment. The 'Device' uncertainty is dependent upon the measurement range. A second set of figures has been produced in the same report to illustrate the case of a measurement range of two millimetres. Under these conditions, the combined uncertainty is dominated by the uncertainty of the device, which is 6.0μm. It is clear that the measurement range should be incorporated in any calculation of the uncertainty of a straightness measurement.

**Table 3.1: Uncertainty contributors for Straightness [63]**

| **Contributor** | u (μm) | |
|---|---|---|
| Device | 1.1 | |
| Alignment | 0.0 | |
| Thermal Drift | 0.3 | |
| Air Disturbance | 4.2 | |
| **Combined uncertainty** | 4.3 | **Expanded uncertainty = ±9μm** |

### 3.13.1 Bayesian approach

When evaluating uncertainties in machine calibration, some contributing factors can be evaluated by repeated measurement runs as Type A uncertainties. However, some uncertainties are associated with the set-up of the measurement equipment. It would be impractical to repeatedly set-up the equipment in order to produce a satisfactorily large sample population so Type B evaluations are employed. However, these can tend to be over-prudent estimations so it would be valuable if experience could be used to modify the estimates. Phillips, *et. al.* [80] propose the use of Bayesian theory for situations where prior information is available. The method is based upon equation 3.22 and equation 3.23.

$$y = y_m\left(\frac{\gamma^2}{1+\gamma^2}\right) + y_{pe}\left(\frac{1}{1+\gamma^2}\right) \qquad \text{Equation 3.22}$$

$$\text{where} \qquad \gamma = \frac{u_{pe}}{u_{cm}}$$

$$\frac{1}{u_c^2} = \frac{1}{u_{cm}^2} + \frac{1}{u_{pe}^2} \qquad \text{Equation 3.23}$$

where

y is the best estimate of the measurand including prior information.

$y_m$ is the best estimate of the measurand without including prior information.

$y_{pe}$ is the best estimate of the measurand based upon prior information.

$u_{cm}$ is the combined standard uncertainty of the measurement without using prior information.

$u_{pe}$ is the standard deviation of the probability distribution which describes the measurand based on historical information.

Equation 3.22 in effect allows us to obtain the best estimate of the uncertainty from a weighted average of the current measurement and historical data from previous measurements. The use of this theory means that using historical data can never cause the uncertainty value to increase.

It can be seen that if the historical information comes from a broad measurement distribution then $u_{pe} >> u_{cm}$, so $\gamma \to \infty$. From equation 3.22 we get $y \approx y_m$ which gives $u_c \approx u_{cm}$ by equation 3.23. In other words, if the historical information does not reduce the uncertainty of the measurement then the uncertainty of the measurement will approach the uncertainty for a single measurement.

Conversely, if the historical data is shown to be very good then $u_{pe}$ will be very small, and so $\gamma << 1$. In this case, equation 3.22 reduces to $y \approx y_{pe}$, giving $u_c \approx u_{pe}$ from equation 3.23.

When using this method we produce a different expanded uncertainty. This difference, $\Delta U$, is given as a function of the unadjusted expanded uncertainty, $U_m$ by equation 3.24.

$$\Delta U = U_m\left(1-\sqrt{\frac{\gamma^2}{\gamma^2+1}}\right) \qquad \text{Equation 3.24}$$

This method of adjusting the uncertainty on the basis of historical information is very interesting and could be of great benefit where repeated measurements are made on similar machines. However, equation 3.22 and equation 3.23 rely on the prior and measurement distributions being Gaussian. Furthermore, unless the historical data is 'randomly sampled' it will not provide a good example of uncertainty. For example, this method could not be used for estimating the uncertainty of measurement on a standard workshop machine if historical data was predominately from machines in a temperature-controlled environment. Making a pre-requisite of using this methodology that the historical data be appraised for appropriateness before each analysis would remove standardisation and increase the analysis complexity. This is certainly not desirable if the benefit in reduced uncertainty were not significant. However, the method could be applied where similar machines in similar environments are measured using similar set-ups. The historical data could then be used to reduce the uncertainty for any future measurements on that installation type.

### 3.13.2 Machine repeatability

An important quality of a machine is its repeatability. For linear positioning, the repeatability can be evaluated by statistical methods. ISO 230-2 [14] prescribes that a minimum of five measurement runs be taken along an axis, the error band of two standard uncertainties for the data then describes the uni-directional repeatability of the axis. If the measurement data is acquired in both directions, a bi-directional repeatability can be calculated.

The old British standard for accuracy and repeatability (BS 3800-2) employed statistical methods for determining the repeatability of angularity and straightness. This idea was rejected by ISO since, for such parameters, the statistics provide information about the uncertainty of measurement, rather than the physical repeatability of the machine.

This is supported by analysis carried out on machines at the University of Huddersfield. The positioning repeatability of an axis can vary in performance from

machine to machine and so this is often used as the main indicator of machine repeatability. Due to the mechanical construction of a machine, the repeatability of angular errors is usually very good. For this reason the volumetric accuracy figure which has been given uses a mean average of any multiple data runs to provide a single figure for the volumetric accuracy. However, this figure provides no indication of the repeatability with which the volumetric accuracy is achievable. It has always been assumed that this figure is governed by the linear positioning repeatability of the axes.

It is here suggested that any available information regarding the repeatability of each of the geometric errors be combined using a similar statistical approach to that suggested in section 3.13. Further, it is noted that an element of the repeatability figure for the geometric error must be due to the uncertainty of the measurement. Therefore, it would not provide an accurate figure if the measurement uncertainty were added to the repeatability figure determined by repeated measurements. As such, it is proposed that the figures for measured repeatability and measurement uncertainty be combined using the statistical regime proposed in the following sections.

## 3.14 Method of incorporating measurement uncertainty in ESP

Based upon the sources of measurement uncertainty proposed by Knapp [63] and the principles of calculating uncertainty discussed in this section, the following pseudo-code has been produced for calculation of volumetric uncertainty in ESP. Most of the individual uncertainties are calculated from equation 3.18, assuming a rectangular distribution, the remainder are derived from repeated measurement runs according to equation 3.17.

An important contributory source of measurement uncertainty derives from thermal drift. Table 3.2 shows a lookup table presented by Knapp [63] for typical thermal drifts during testing.

**Table 3.2: Thermal drift values**

| Time | Displacement (μm) | Angle (μm/m) |
|---|---|---|
| 5 minutes | 0 | 0 |
| 15 minutes | 1 | 3 |
| 30 minutes | 2 | 5 |
| 60 minutes | 5 | 10 |

### 3.14.1 Linear position – laser interferometer

**u(device) = u(calibration)**

where

- u(calibration) is the standard uncertainty of the calibration of the laser as provided on the calibration certificate. If there is no calibration certificate, u(calibration) is given by the specification of the manufacturer.

**u(alignment) = (alignment / measuring length) /(2 * √3)**

where

- alignment is the maximum positional misalignment perpendicular to the axis under measurement
- the measuring length is retrieved from the data

**u(thermal drift) = thermal lookup**

where

- thermal lookup is from table 3.2. The test duration can be retrieved from the data file

**u(workpiece expansion) = √(temperature measurement uncertainty$^2$ +...**

**expansion coefficient uncertainty$^2$)**

where

**temperature measurement uncertainty =...**

**measuring length * thermal expansion coefficient * temperature change / (2 * √3)**

**expansion coefficient uncertainty =...**

**measuring length * expansion coefficient uncertainty *...**

**maximum difference to 20°C / (2 * √3)**

- measuring length is obtained from data file
- thermal expansion coefficient is specified for material used in encoder
- temperature change is derived from data file since it is likely to rise during test
- the uncertainty of the thermal expansion coefficient is quoted as 0.7°C [79]
- the maximum difference to 20°C is calculated from the data file

then

**U = k * √( u$^2$(device) + u$^2$(alignment) + u$^2$(thermal drift) + u$^2$(workpiece expansion))**

where

- k is the coverage factor, depending upon the required confidence level (normally 2)

It is important to note that the uncertainty value derived from this process has units of microns per metre, so the uncertainty of any data increases with measurement length.

### 3.14.2 Angular – differential precision levels

**u(device) = √2 * unit uncertainty**

where

- unit uncertainty is specified by the manufacturer

**u(alignment) = negligible**

- if alignment between device and axis is small

**u(cross talk) = (maximum angle * measurement length / footprint length) / (2 * √3)**

- if alignment between device and axis is small

where

- maximum angle (in μm/m) is retrieved from data
- measurement length is the measured axis stroke, retrieved from the data
- footprint length is part of the device specification

if the number of measurement runs is less than 5

**u(thermal drift) = thermal lookup**

where

- thermal lookup is from table 3.2. The test duration can be retrieved from the data file

otherwise

**u(thermal drift) = s/√n** (according to equation 3.17)

where

- s is the standard deviation for the data
- n are then number of samples

then

**$U = k * \sqrt{(u^2(device) + u^2(cross\ talk) + u^2(thermal\ drift))}$**

where

- k is the coverage factor, depending upon the required confidence level (normally 2)

### 3.14.3 Angular – laser interferometer, angular optics

**u(device) = (measurement range * range accuracy +…**

**measurement length * length accuracy) / (2 * √3)**

where

- measurement range is the range of angular values retrieved from the data
- range accuracy is quoted (0.4%)
- measurement length is the measured axis stroke, retrieved from the data
- length accuracy is quoted (0.5μm/m)

**u(alignment) = negligible**

- if alignment between laser and axis is small

**u(cross talk) = (maximum angle * measurement length / beam offset) / (2 * √3)**

if alignment between device and axis is small

where

- maximum angle (in μm/m) is retrieved from data
- measurement length is the measured axis stroke, retrieved from the data
- beam offset is determined by the distance between the reflectors in the laser optics and forms part of the device specification

if the number of measurement runs is less than 5

**u(thermal drift) = thermal lookup**

where

- thermal lookup is from table 3.2. The test duration can be retrieved from the data file

otherwise

**u(thermal drift) = s/√n** (according to equation 3.17)

where

- s is the standard deviation for the data
- n are then number of samples

then

$$U = k * \sqrt{(2 * u^2(device) + u^2(cross\ talk) + u^2(thermal\ drift))}$$

where

- k is the coverage factor, depending upon the required confidence level (normally 2)

### 3.14.4 Angular – calculated from two linear measurements

The uncertainty associated with this method of measuring the angular errors is a function of the individual uncertainty of measuring a single linear file. The uncertainty calculation is given by:

**u(linear measurements) = U(linear position) √2 / 2**

$$\frac{u(angle)}{angle} = \sqrt{\left(\frac{u(linear\_measurements}{linear\_measurements}\right)^2 + \left(\frac{u(displacement)}{displacement}\right)^2}$$

where

- u(displacement) is the uncertainty of the displacement between the two linear measurement runs.
- displacement is the distance between the measurement runs

then

**U = k * u(angle) * angle**

where

- k is the coverage factor, depending upon the required confidence level (normally 2)

### 3.14.5 Straightness – short-range laser optics

**u(device) = (u(optical reference) + 1% * measurement range) / (2 * √3)**

where

- u(optical reference) = 3μm (quoted)
- measurement range is determined from data file

**u(alignment) = (measurement range – cos(max angle) * measurement range) / (2 * √3)**

where

- max angle = $1^{o}$ (quoted)
- measurement range is determined from data file

if the number of measurement runs is less than 5

**u(thermal drift + air disturbance) = (thermal lookup +...**

**air disturbance * reduced influence *...**

**magnifying factor * number of beams) / (2 * √3)**

where

- thermal lookup is from table 3.2. The test duration can be retrieved from the data file
- air disturbance = 1μm (quoted)
- reduced influence because beam is not the basis = 0.1
- magnifying factor due to optical arrangement = 36.0
- number of beams (two forward and two return) = 4

otherwise

**u(thermal drift + air disturbance) = s/√n** (according to equation 3.17)

where

- s is the standard deviation for the data
- n are then number of samples

then

**U = k * √(u²(device) + u²(alignment) + u²(thermal drift + air disturbance))**

where

- k is the coverage factor, depending upon the required confidence level (normally 2)

### 3.14.6 Squareness – mechanical square

**u(device) = √((square edge A)² + (square edge B)² +...**

**(squareness * measuring length / (2 * √3))² )**

where

- square edge A, square edge B and squareness are given by the calibration certificate for the square

**u(alignment) = (uncertainty of alignment / measuring length) / (2 * √3)**

where

- an indicative uncertainty of alignment of 1mm is quoted by Knapp [63]

then

$$U = k * \sqrt{(u^2(device) + u^2(alignment))}$$

where

- k is the coverage factor, depending upon the required confidence level (normally 2)

### 3.14.7 Volumetric uncertainty

For the software to calculate an uncertainty figure, additional information would be required when inputting data at the file selection screen (figure 3.10). The equipment used for measuring each geometric facet would be selected at the same time as the error file. In this way the uncertainty for each geometric component could be calculated from the appropriate algorithm from section 3.14.1 to 3.14.6 and the relevant information in the data file.

The total volumetric uncertainty would then be calculated by synthesis using the measurement algorithms specified in section 3.09 as the basis. Two methods are proposed and tested in section 4.01. One simply utilises the existing algorithms as they stand to perform the synthesis. However, it makes sense to utilise a statistical approach.

Since each of the uncertainties has already been converted to an expanded uncertainty, it is appropriate to perform the analysis by taking the square root of the sum of the square of each uncertainty acting in each axis direction. There is no need to multiply a coverage factor since this has already been performed when calculating the individual expanded uncertainties. The uncertainty at any given point is then the vector sum of the three axial uncertainties.

## 3.15 Summary

The method of synthesising the effect of geometric errors throughout the working volume for a machine has been developed during previous research projects. The current research has taken the principles involved and extended them to machines with a tool offset from the end of the ram.

The research has further considered the problem of applying this method to machines with volumetric compensation. This has required a re-specification of the measurement procedures, the production of new algorithms for calculating the errors and specifying new functionality in software used to calculate the volumetric accuracy of the machine.

The basic premises of the Swiss contribution to the ISO committee [63] regarding uncertainty of measurement for positioning errors in numerically controlled machines have been evaluated and generalised. Further to this, the methods have been re-examined to incorporate the information available from the data files. In general, the following philosophy is proposed by this research for calculating the combined uncertainties for each geometric error:

I. Those uncertainty contributors that derive from changes between equipment set-up are calculated from first principles and incorporate measurement-specific parameters. In general, the equations lend themselves to a rectangular distribution and so $u_c$ is calculated by equation 3.18.
II. Those uncertainty contributors that derive from changes between measurement runs are estimated from multiple measurement runs in accordance with equation 3.17.

It is not proposed that a Bayesian approach (section 3.13.1) be applied to the individual uncertainties within the ESP software. However, the uncertainty of a machine with historical data could be adjusted by applying equation 3.24 to the generated uncertainty value if analysis of the quality of the prior information proved satisfactory.

An uncertainty for the total geometric displacement error for each axis can be produced by synthesising the effect of the individual geometric uncertainties. A volumetric uncertainty can then be produced by performing a vector sum on the three resultant axis uncertainties.

The work covered in this chapter successfully achieves the objectives set in section 1.14 (a) and presents the methods required for satisfying 1.14 (b). Chapter 4 will confirm the realisation of the objective of section 1.14 (a) by validating the simulation software against compensated machines with tool offset and against coordinate measuring machines. It will also complete the objective of 1.14 (b) by performing the necessary simulation of volumetric uncertainty.

# Chapter 4 Validation of Redesigned ESP

In the previous chapter, a method of evaluating the positioning capability of a Cartesian machine by synthesis of the individual error components was described. Enhancements were then made to this by consideration of the additional effect on accuracy when the machine operates with a tool offset from the end of the ram. Models were then produced to calculate the effect of the errors at the end of the tool for analysing machines whose errors have been reduced by application of electronic compensation. A new version of an error simulation program (ESP) was designed and measurement protocol devised to allow efficient assessment of Cartesian machines by the synthesis method. In this chapter, the results of measuring two turning machines (TM1 & TM2) and two coordinate measuring machines (CMM1 & CMM2) are analysed using a new version of ESP that has been created during the course of this work.

Section 4.01 will provide a worst-case volumetric uncertainty based upon a number of assumptions of individual error uncertainties for geometric measurements. This analysis was undertaken using a special version of ESP written to perform the statistical calculations as described in the previous chapter. Finally, a volumetric uncertainty figure is produced for the four machines used in the validation in order to provide representative data.

# 4.01 Uncertainty of measurement of geometric errors

A report from Knapp [63] to the International Standards Committee provides a list of suggested measurement uncertainties for the error components used to calculate volumetric accuracy. The values for linear measurement are intended for inclusion in the next revision of the ISO standard [79]. The uncertainty figures arise from a series of assumptions, given in table 4.1.

**Table 4.1: Assumptions for measurement uncertainty calculation**

| Uncertainty description | Assumption | Effect |
|---|---|---|
| Air disturbance on beam of light | 1μm | |
| Max angular error | 300μm/m | |
| Max straightness error | 50μm | |
| Max deviation from 20°C | 5°C | |
| Nominal thermal expansion coefficient | 12μm/m°C | |
| Thermal drift during 5 minutes | 0μm | 0μm/m |
| Thermal drift during 15 minutes | 1μm | 3μm/m |
| Thermal drift during 30 minutes | 2μm | 5μm/m |
| Thermal drift during 60 minutes | 5μm | 10μm/m |

In practice, the method of determining the individual geometric uncertainties (section 3.14.1 to 3.14.6) will be utilised. However, to provide the expected worst-case uncertainty the data provided by Knapp has been used for the simulation of the volumetric uncertainty.

## 4.01.1 Measurement uncertainty values

Based upon the assumptions of table 4.1, Knapp proposes the following values for the measurement of uncertainty for each geometric error (table 4.2). The figure is specific for each error and the piece of equipment used to perform the measurement. It should be noted that the laser-based measurements are assumed to be on the Hewlett Packard laser system, no corresponding values are presented for other laser equipment, such as the Renishaw system. It is assumed that the uncertainties will be of a similar magnitude.

**Table 4.2: Measurement uncertainty values for a measuring length of one metre**

| Geometric Measurement | Uncertainty |
|---|---|
| Positioning | ±8μm/m |
| Roll (precision level) | ±4μm/m |
| Pitch (precision level) | ±5μm/m |
| Angular (laser with angular optics) | ±4μm/m |
| Straightness (0,350mm) | ±9μm |
| Squareness (square) | ±10μm/m |

### 4.01.2 Method of simulation in analysis software

For the purpose of this evaluation, a set of Renishaw error files was generated using the Renishaw software. The magnitude of the errors was that of the stated measurement uncertainty for that quantity. These files were then input to the ESP. A gantry structure with three axes of one metre length was used in this simulation.

#### 4.01.2.1 Files

**a. Linear**

An error file with three linear targets at 0mm, 500mm, 1000mm. The error at each target was set to 0μm, 4μm and 8μm respectively, the magnitude of the measurement uncertainty for this quantity being eight microns per metre. The error on the reverse run was set to -8μm/m to allow comparison.

**b. Angular**

An error file with three linear targets at 0mm, 500mm, 1000mm. The error at each target was set to 4μm/m, being the magnitude of the measurement uncertainty for this quantity. The error on the reverse run was set to -4μm/m to allow comparison.

**c. Straightness**

When performing a straightness measurement the laser is often slightly misaligned with the axis of motion. The residual 'slope error' is a measurement error and is normally removed by means of a least squares or end-point fit. For the uncertainty analysis an error file with five targets was used to generate a trapezoidal error form. The targets were -0.001mm, 0.000mm, 500.000mm, 1000.000mm, 1000.001mm. The error rose from 0μm to 4μm over the first micron and then returned to 0μm over the last micron. The error profile was

reversed for the reverse run to allow comparison. By using this error profile, an end-point fit on the data resulted in a 4μm straightness error over the majority of the axis length.

**d. Squareness**

This is a single-valued error and was set at 10μm/m for each axis.

### 4.01.3 Simulation of volumetric uncertainty using pure addition

The wBMTt (All axes associated with movement of the tool) configuration was selected for initial investigation, since this is the most commonly used configuration on CMMs.

The error files, described above, were input for the three axes. The measurement offsets were left at zero. This provides the worst-case scenario for the measurement uncertainty. The simulation was then run over the full $1m^3$ working volume, and then over a $0.3m^3$ volume from the origin. The detailed results of these simulations can be found in Appendix A.

The simulation was then run again with the offsets set at 500mm for all axes, to represent another realistic measurement set-up. Again, the simulations were performed over a $1m^3$ and $0.3m^3$ working volume. In this case, the smaller working volume was about the measurement lines. The detailed results of these simulations can also be found in Appendix A.

Table 4.3 shows the results of the uncertainty evaluation. As expected, the uncertainty figure is much larger for the $1m^3$ volume. It is, however, interesting to note the significant reduction in uncertainty that can be achieved by choosing a central axis position for measurement rather than an extreme of travel. This is because the uncertainty is related to the distance over which the measurement is taken.

**Table 4.3: Uncertainty by directly adding geometric uncertainties**

| | $1m^3$ | $0.3m^3$ |
|---|---|---|
| Measured at Origin | 60.0 | 11.1 |
| Measured Centrally | 43.0 | 11.1 |

### 4.01.4 Volumetric uncertainty using statistical approach

A special version of ESP was created. This allowed the error component in each axis to be calculated from the square root of the sum of the square of each of the uncertainties acting

in that direction. The volumetric uncertainty was then calculated as the vector sum of these uncertainties. The 'All axes associated with movement of the tool' configuration was again selected for investigation.

The error files (described in section 4.01.2.1) were input for the three axes. The measurement offsets were left at zero. This provides the worst-case scenario for the measurement uncertainty. Simulations identical to the previous subsection were run, the detailed results of which can be found in Appendix A.

The volumetric uncertainty figures arrived at by this method are presented in table 4.4. Again, the uncertainty figure is much larger for the $1m^3$ volume and selection of the mid-point for the origin can reduce the overall uncertainty. This value of ±26.2μm for the volumetric uncertainty across a one meter cubed volume can be compared with that of linear positioning uncertainty of ±8μm.

**Table 4.4: Uncertainty by statistical approach**

| | $1m^3$ | $0.3m^3$ |
|---|---|---|
| Measured at Origin | 26.2 | 18.0 |
| Measured Centrally | 19.7 | 19.7 |

### 4.01.5 Further consideration

A further consideration raised by Bell [59] is that of rounding errors during computation. Although this has been proffered as a source of uncertainty it should really be classified as an error in the same way that misuse of a laser would produce incorrect results. For that reason, such computational 'uncertainties' are not considered in the same way as discussed in the previous section. Instead, the problem of rounding during computation has been addressed by performing all calculations after scaling all displacement values into microns before operating upon them.

A greater uncertainty in the volumetric accuracy figure derives from the assumption that the machine is rigid-body. However, to consider the non-rigid effect is a non-trivial problem that cannot be sufficiently simplified to be incorporated in this analysis. The influence of any non-rigid effect can be minimised by careful choice of measurement position. [81, 82]

# 4.02 Volumetric errors of two-axis turning machines

## 4.02.1 Introduction

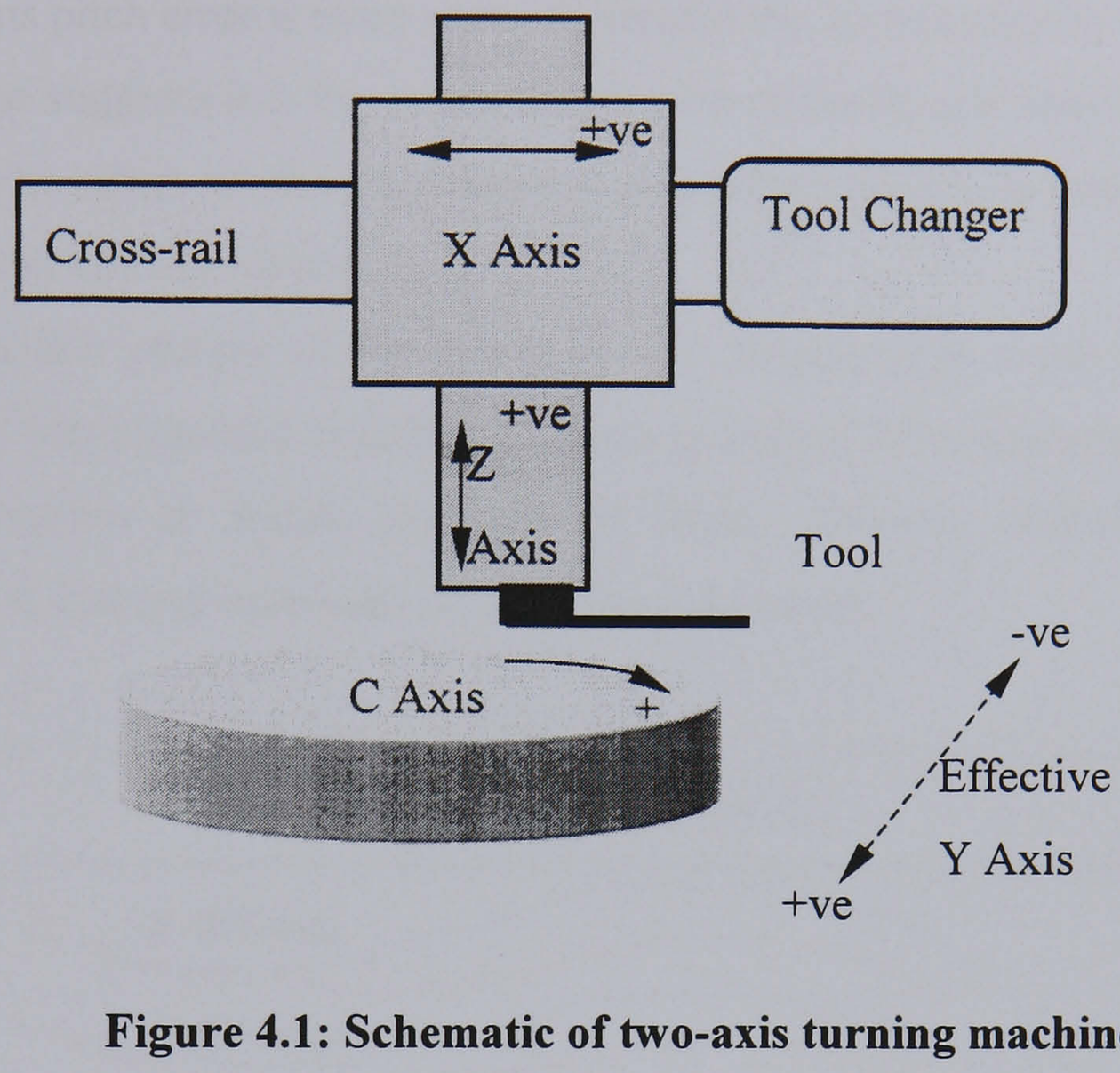


**Figure 4.1: Schematic of two-axis turning machine**

A collaborating company has two turning machines (TM1 and TM2) each with a tool moved by an X and Z-axis and the workpiece moved using a rotating C-axis. Much of the work carried out on these machines utilises a turning tool of significant length in a direction parallel to the X-axis. In addition to this, in-process probing and machine-checking by probing an artefact (gold standard) are also carried out in a position offset from the base of the ram.

A two-axis version of the volumetric compensation system that has been created at the University of Huddersfield [77], has been applied to both machines to compensate for errors in the X and Z-axes at the MCP.

In the following discussion reference is made to an imaginary Y-axis, which is perpendicular to the X and Z-axes. Since there is no Y-axis it is not possible to correct errors in this direction.

### 4.02.2 Investigation of X-axis pitch error on TM1 – test 1

For this configuration of machine and probing system the major contributory effect to residual inaccuracies would arise from the X-axis pitch error. For this reason, the error was investigated in some detail on TM1 using both direct and indirect measurement.

The X axis pitch error is more correctly termed the X-axis angular error about the Y-axis. As the name suggests it is the unwanted rotation of the X-axis about the Y-axis as the X axis moves. The effect of this pitch error is to produce an X-axis positioning error that varies as a function of Z-axis position.

To get a full picture of the effect of the X-axis pitch error the X-axis linear positioning error was measured at different Z-axis positions. Five measurements were made without compensation at Z-axis positions of 0mm, -200mm, -400mm, -600mm and -800mm. Figure 4.2 shows the results of these measurements.

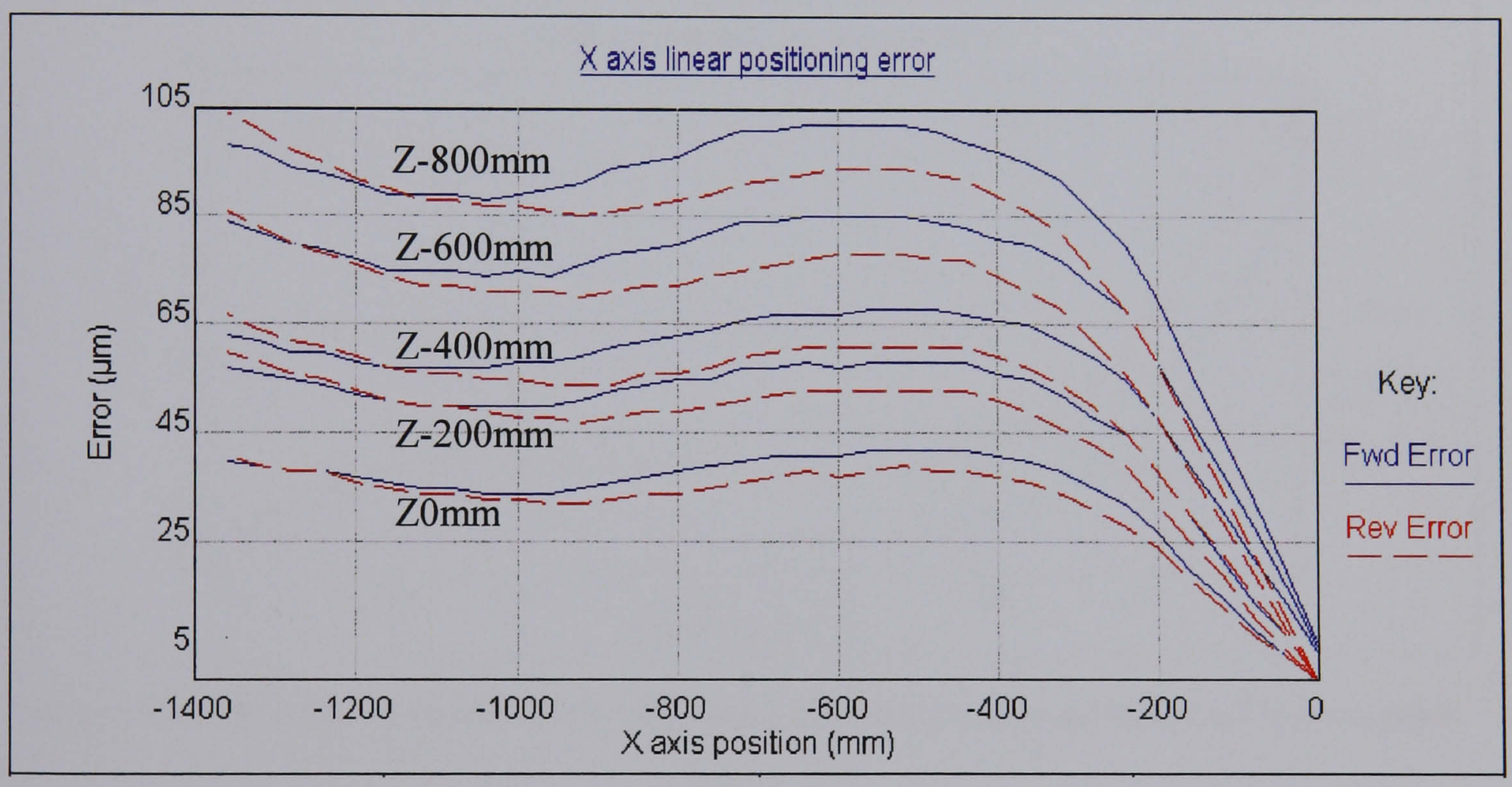


**Figure 4.2: X-axis linear positioning error measured at different Z-axis positions without compensation (TM1)**

It can be seen from figure 4.2 that, as expected, the X axis linear positioning error gets progressively worse with increasing extension of the Z axis. The maximum amplitude of the error increases from 42µm to 104µm, and the maximum reversal error increases from 4µm to 12µm.

The angular error data used in the compensation system was derived from the above X-axis linear positioning measurements using the software described in section 3.08.1. The pitch error was calculated by subtracting the linear positioning error with the Z-axis at the origin from the linear positioning error with Z at full extension and dividing the result by the Z-axis displacement of –800mm. The calculated X-axis pitch error is shown in figure 4.3, plotted with the measured value of the error. In calculating the pitch error the datum (i.e. the point at which the pitch error is zero) was set with X at –560mm, as this is the point where the table to Z-axis squareness was measured. In the graph, a positive pitch error is clockwise rotation of the tool if the machine is viewed from the front. The pitch error has a total range of -9μm/m (-1.9arc sec) to 71μm/m (14.6arc sec). The good correlation between the traces shows that the use of two linear measurements for calculation of angular error provides good correspondence with normal measurement techniques.

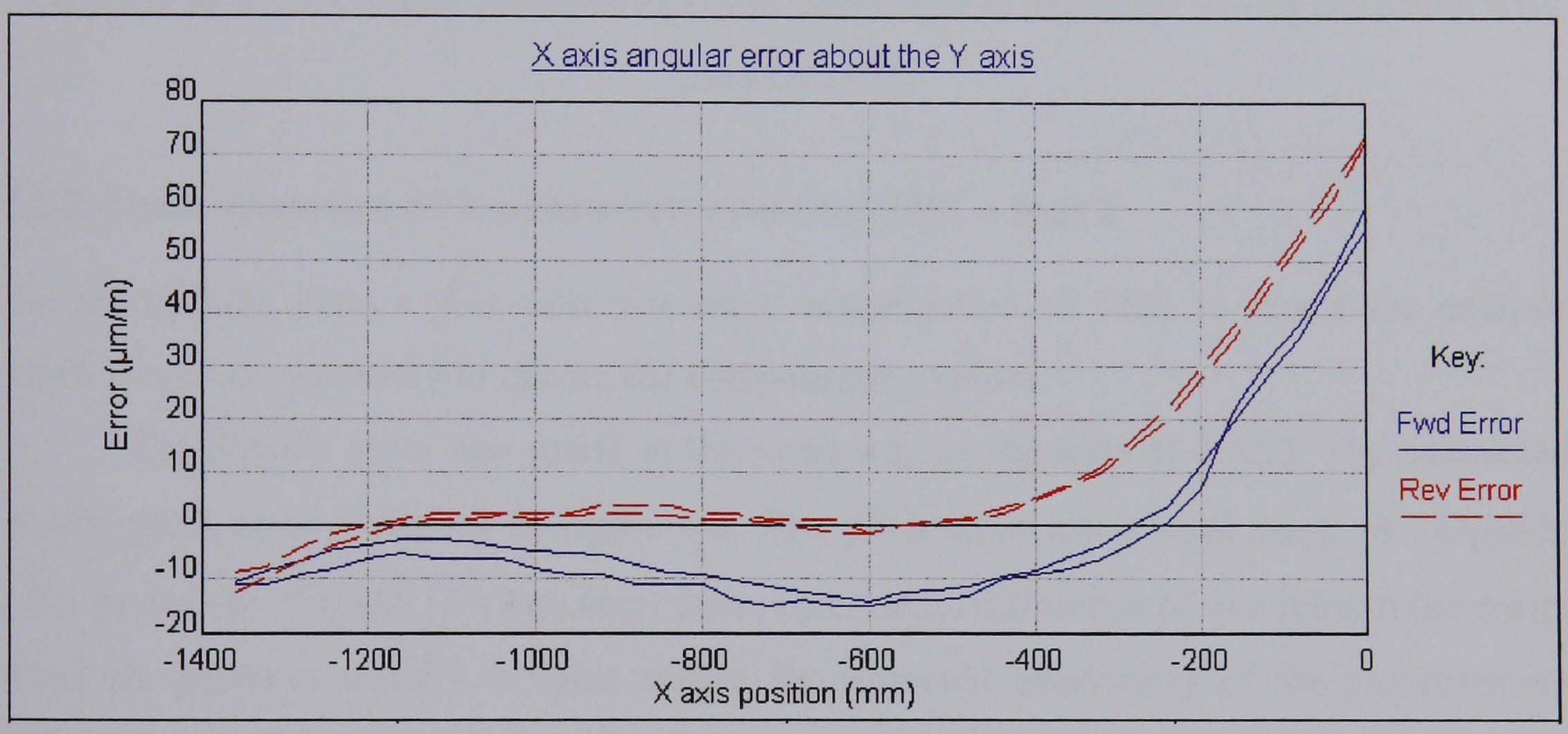


**Figure 4.3: Comparison between calculated and direct measurement of X-axis pitch error (TM1)**

To determine the effectiveness of the compensation the X-axis linear positioning error was re-measured with the compensation active, at Z-axis positions of 0mm, -400mm and -800mm. The results of these measurements are shown in figure 4.4. These are plotted to the same scale as figure 4.2 to provide a visual indication of the improvement achieved. It can be seen from this graph that the linear positioning error and reversal error have been greatly reduced and are similar for all three Z-axis positions. The range of error for the three Z-axis positions is -3μm to 5μm.

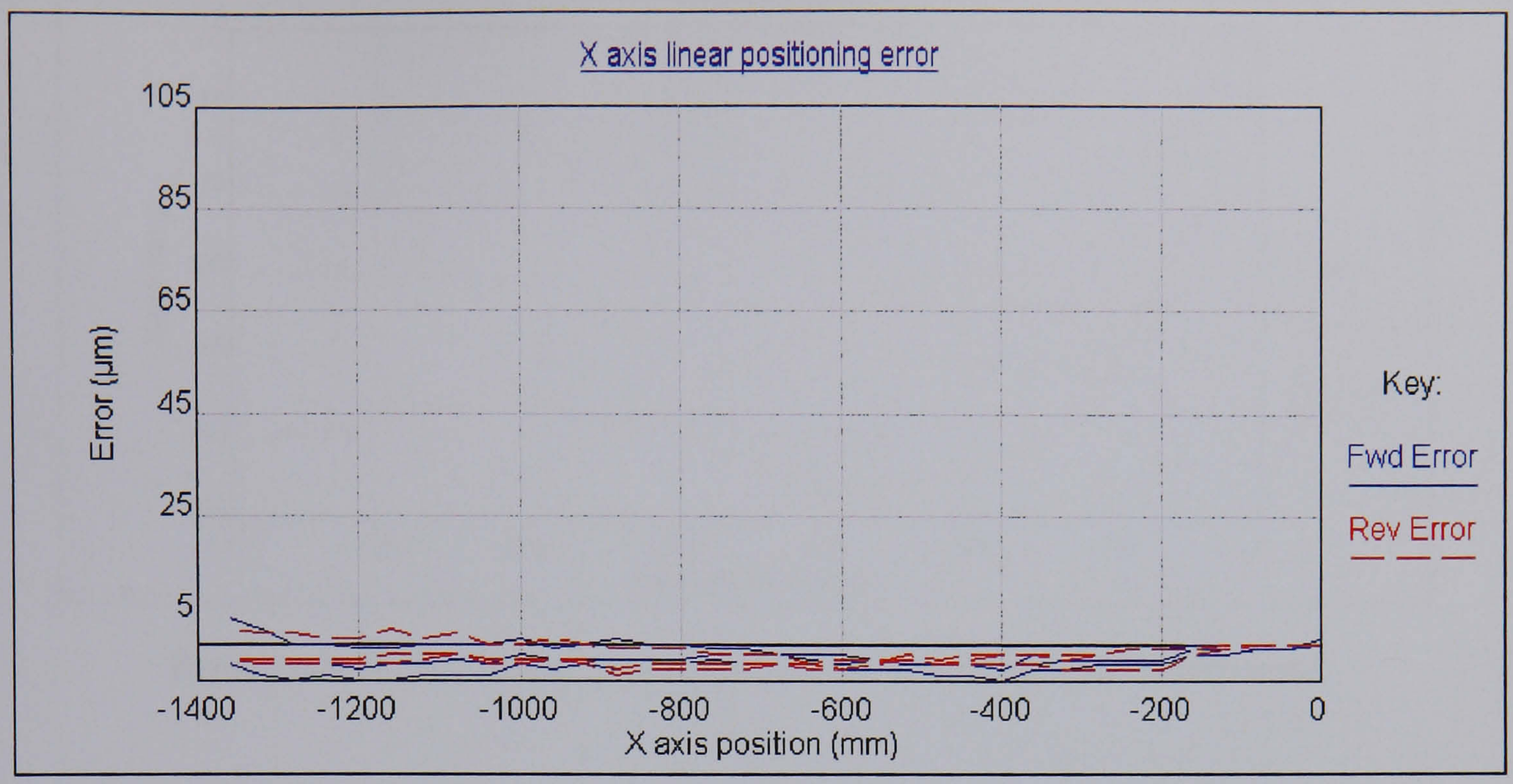


**Figure 4.4: X-axis linear positioning error measured at different Z-axis positions with compensation**

### 4.02.3 Investigation of X-axis pitch error on TM1 – test 2

An opportunity arose a year after the initial investigation of TM1 to repeat the analysis when it became necessary to update the compensation values.

The angular error was found in the same way as the tests of 4.02.2. The calculated X-axis pitch error is shown in figure 4.6. The pitch error has a total range of -10µm/m (-2.1arc sec) to 72µm/m (14.9arc sec). This represents a difference of one micron per metre from the previous result – a value within the expected uncertainty of the measurement device.


**Figure 4.5: X-axis linear positioning error resulting from pitch error**

Again, the effectiveness of the compensation for the X axis linear positioning error was determined by re-measuring with the compensation active with the Z-axis at the home position. The results (figure 4.7) are plotted to the same scale as figure 4.5 to provide a visual indication of the improvement achieved. It can be seen from this graph that the linear positioning error and reversal error have been greatly reduced and are similar as for the reference position. The range of linear error resulting from the pitch has been reduced from 55µm to 7µm.

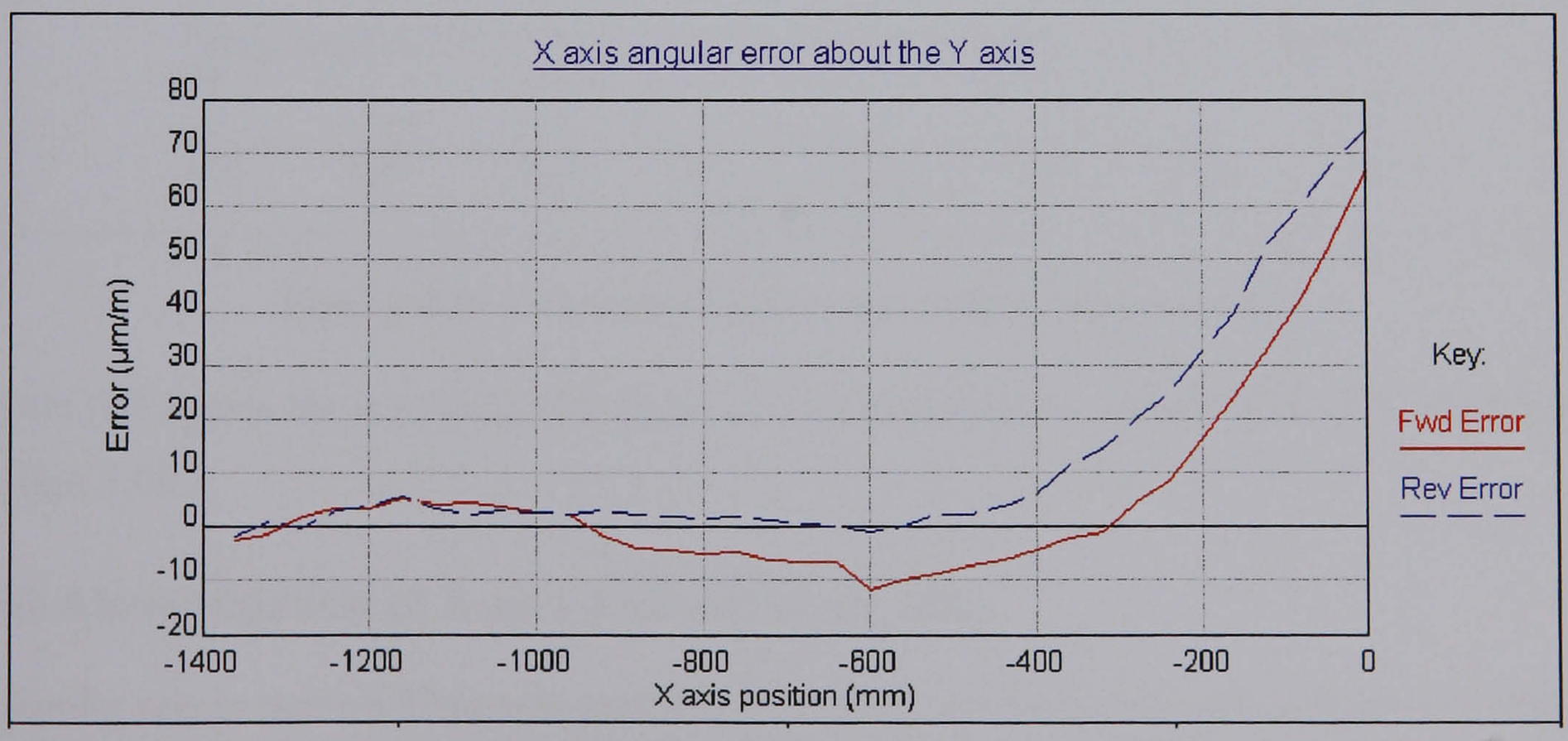


**Figure 4.6: X-axis pitch error calculated from the X-axis linear positioning error**

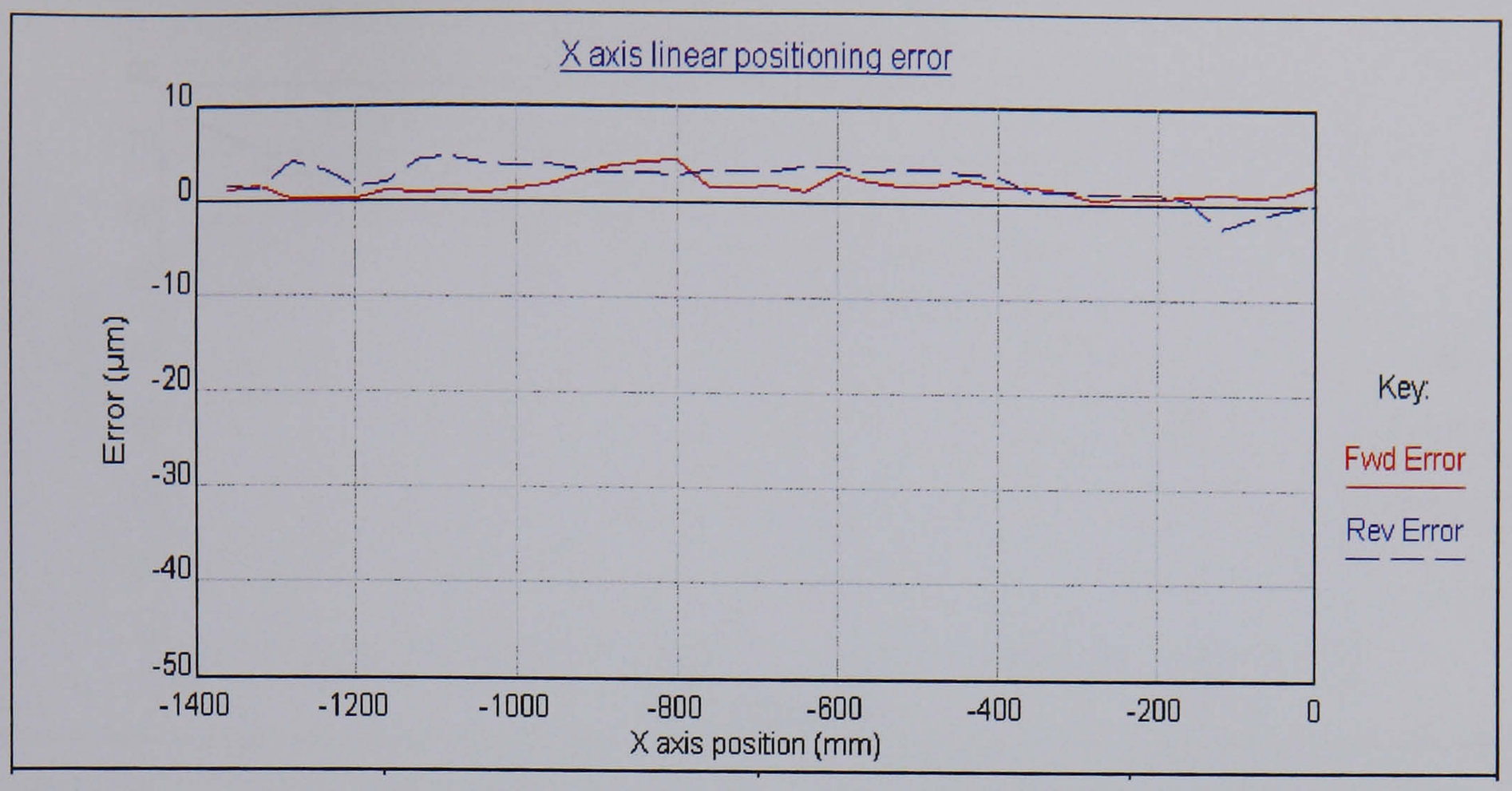


**Figure 4.7: X-axis linear positioning error resulting from pitch error after compensation**

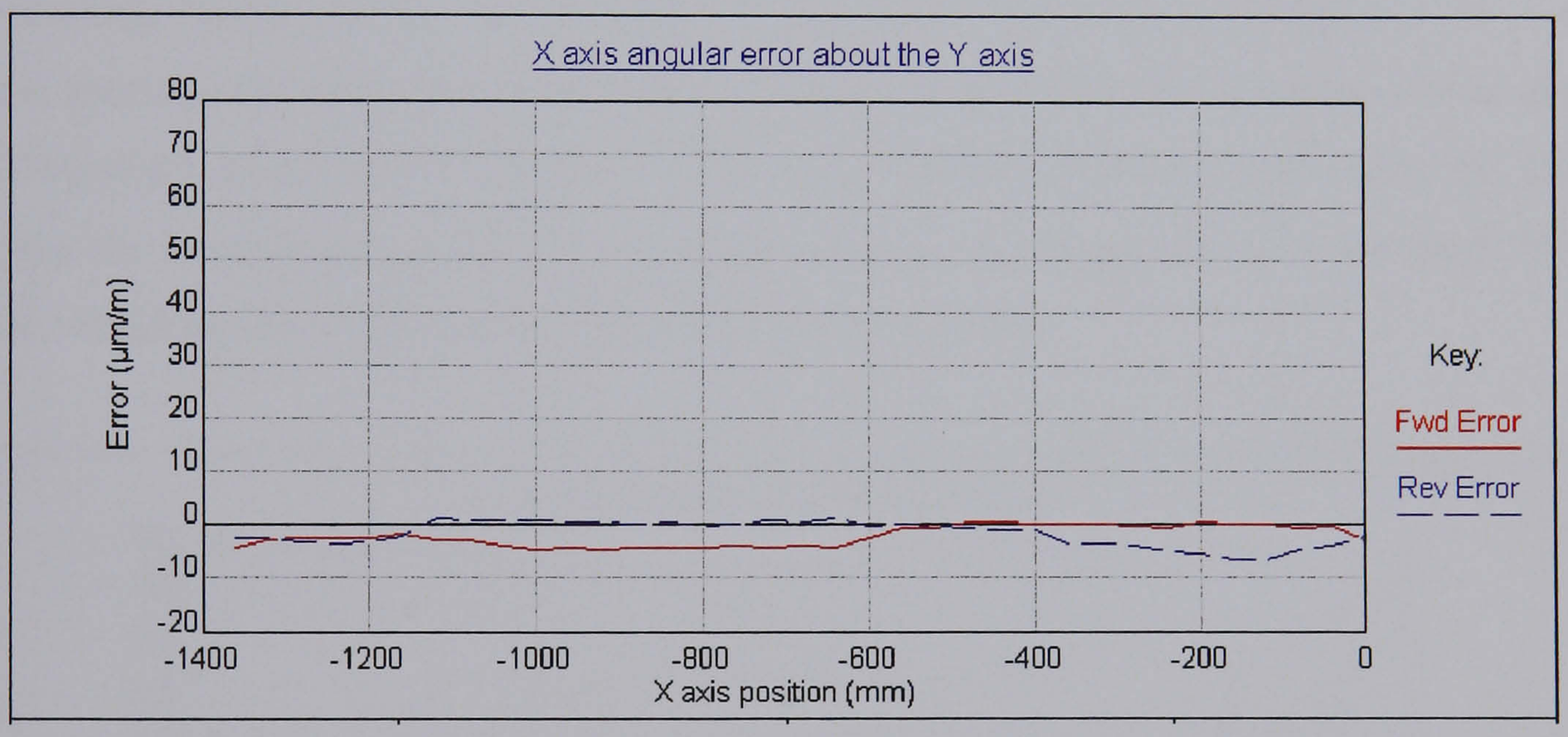


**Figure 4.8: Calculated pitch error after compensation**

Figure 4.8 shows the residual pitch slope after compensation, calculated by the methods of section 3.08.1.

### 4.02.4 Investigation of X-axis pitch error on TM2

A similar test to that on TM1 was performed on TM2. It can be seen from figure 4.9 that the linear positioning error resulting from X-axis pitch had a maximum value of 75µm, with maximum reversal of 11µm.


**Figure 4.9: X-axis linear positioning error measured with the Z-axis at –800mm**

The pitch error data used in the compensation system was derived from these X-axis linear positioning measurements. The calculated X-axis pitch error is shown in figure 4.10 on the same graph as the error measured using the angular optic. The pitch error has a total range of -20µm/m (-4.1arc sec) to 72µm/m (14.9arc sec), which is identical to the values for TM1. Again, the correspondence between calculated and measured angular error has been found to be within the uncertainty of the measurement device used.

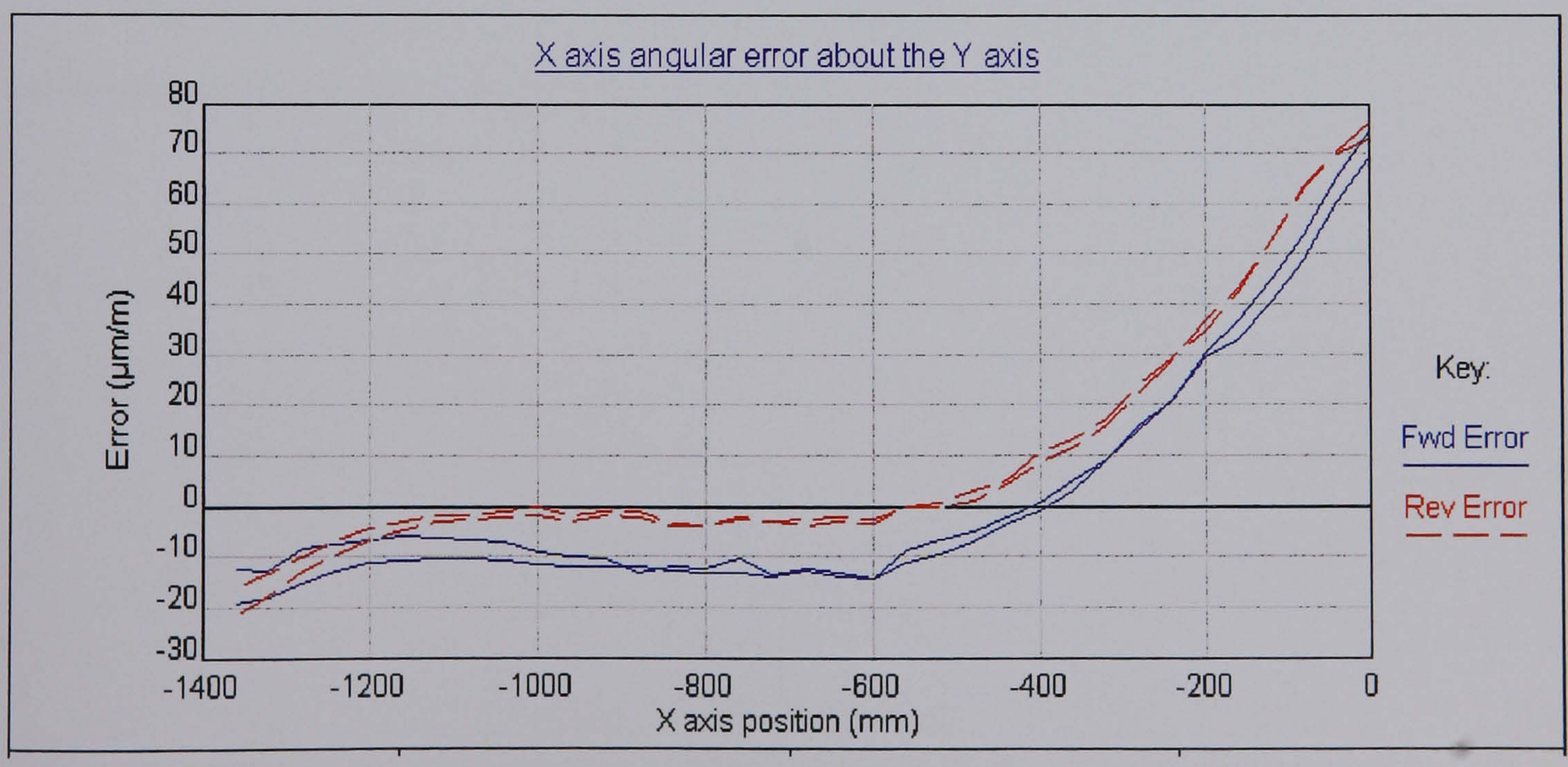


**Figure 4.10: Comparison between calculated and direct measurement of X-axis pitch error (TM2)**

Figure 4.11 shows the effectiveness of compensation for this geometric error. The range of error for the three Z-axis positions is -7µm to 5µm.

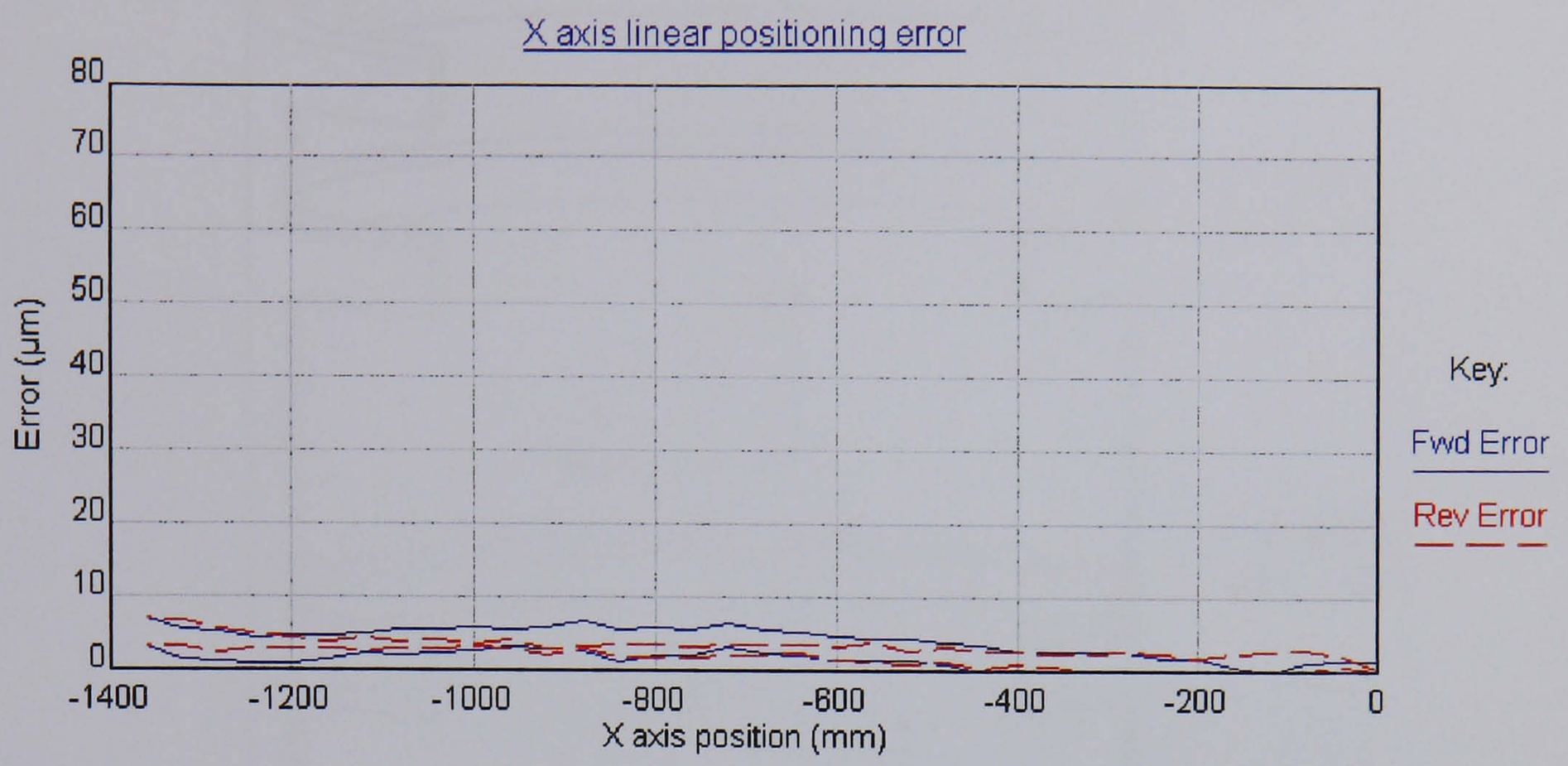


**Figure 4.11: X-axis linear positioning error measured at different Z-axis positions with compensation**

### 4.02.5 Comparison with artefact probing

The company uses an artefact probing technique to monitor the health of the machines. There is a separate artefact for TM1 and TM2, which have both been independently measured on a DEA CMM.

On these machines, the probe used to measure features on an artefact is mounted perpendicular to the tool, parallel to the X-axis.

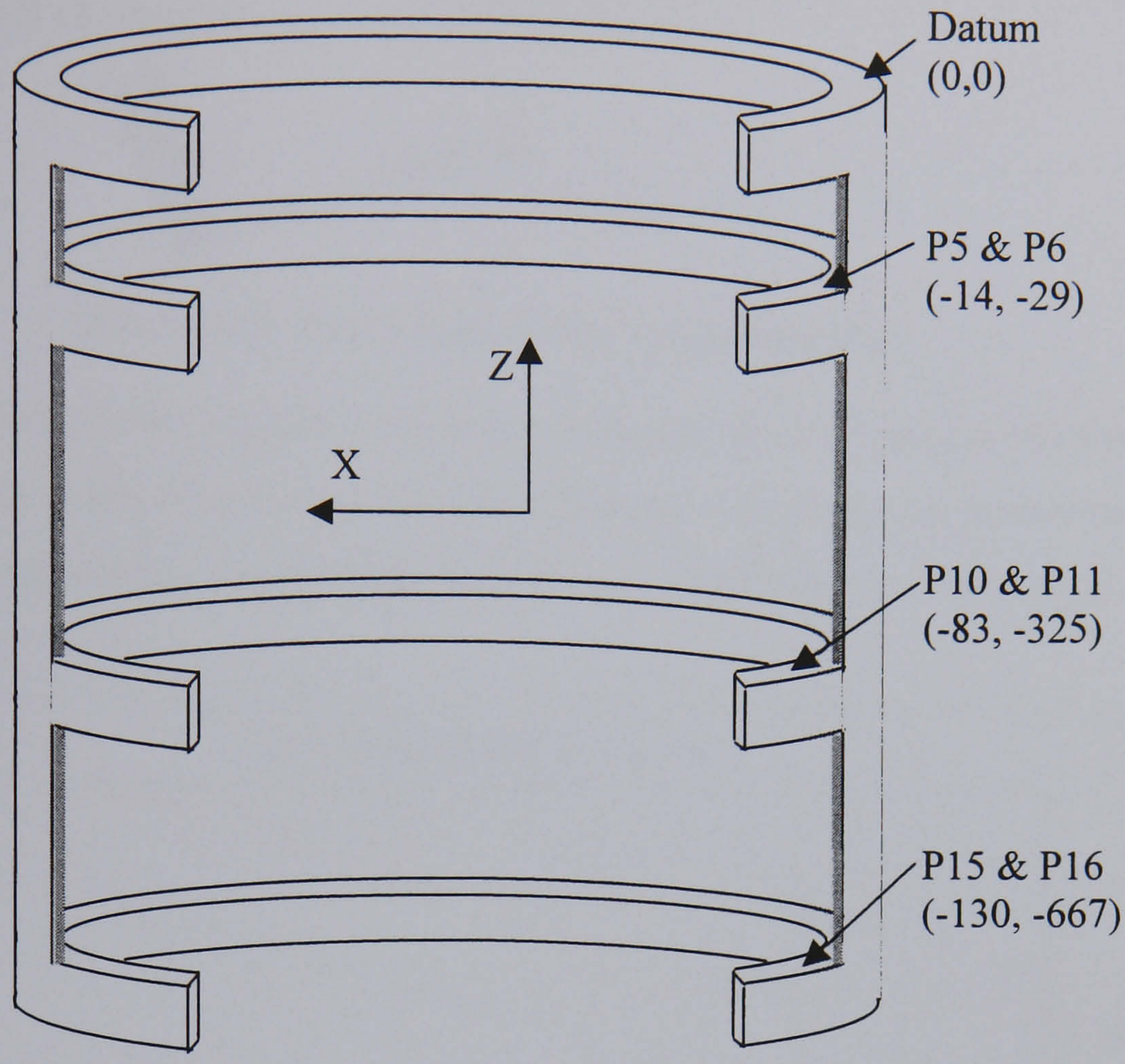


**Figure 4.12: Schematic of probed artefact**

The majority of measurements are taken in the X-direction since this is the critical dimension for the turning application, but two probing positions verify Z-axis positioning. The surface of the component is probed to provide a reference point, with measurements in the Z-axis direction at the points shown in figure 4.12 being used to check the machine.

The distance from MCP to the TCP is 170mm or 270mm depending upon probe. Comparisons between the predicted errors at the probing positions and the measured errors have been made. However, consideration should be given to the probing errors in both the probe and artefact that could cause disparity between the two sets of results. The uncertainty introduced by the artefact includes measurement uncertainty of the calibrated values from the DEA CMM and the quality of surface finish which could lead to non-repeatability (includes contamination of probed surface).

### 4.02.5.1 Z-axis rotation about the Y axis (Z-axis yaw)

Since electronic compensation has been applied only for those errors manifested at the end of the ram, the angular effect of the Z-axis rotation about the Y-axis could have a significant

effect upon the probing. The Z-axis error will be a function of the magnitude of the angular error and the length of the offset between MCP and TCP.

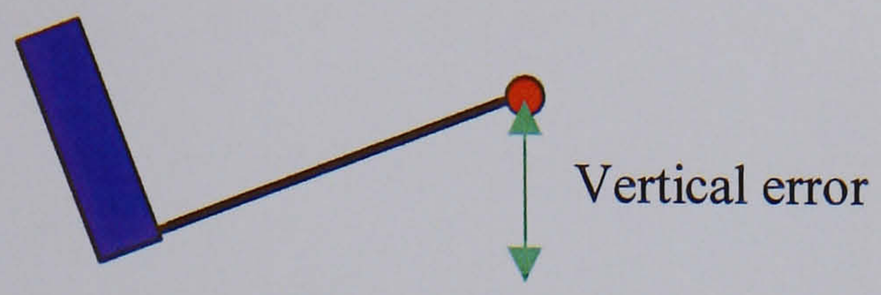


**Figure 4.13: Error induced by rotational effect**

Figure 4.14 is the plot of the angular error at the probing position (X-axis at –675mm). This shows a magnitude of the error of approximately 23µm/m. Given that the probe extension is 230mm, this would produce a worst-case Z-axis linear positioning error of 5.3µm over the length of the axis.

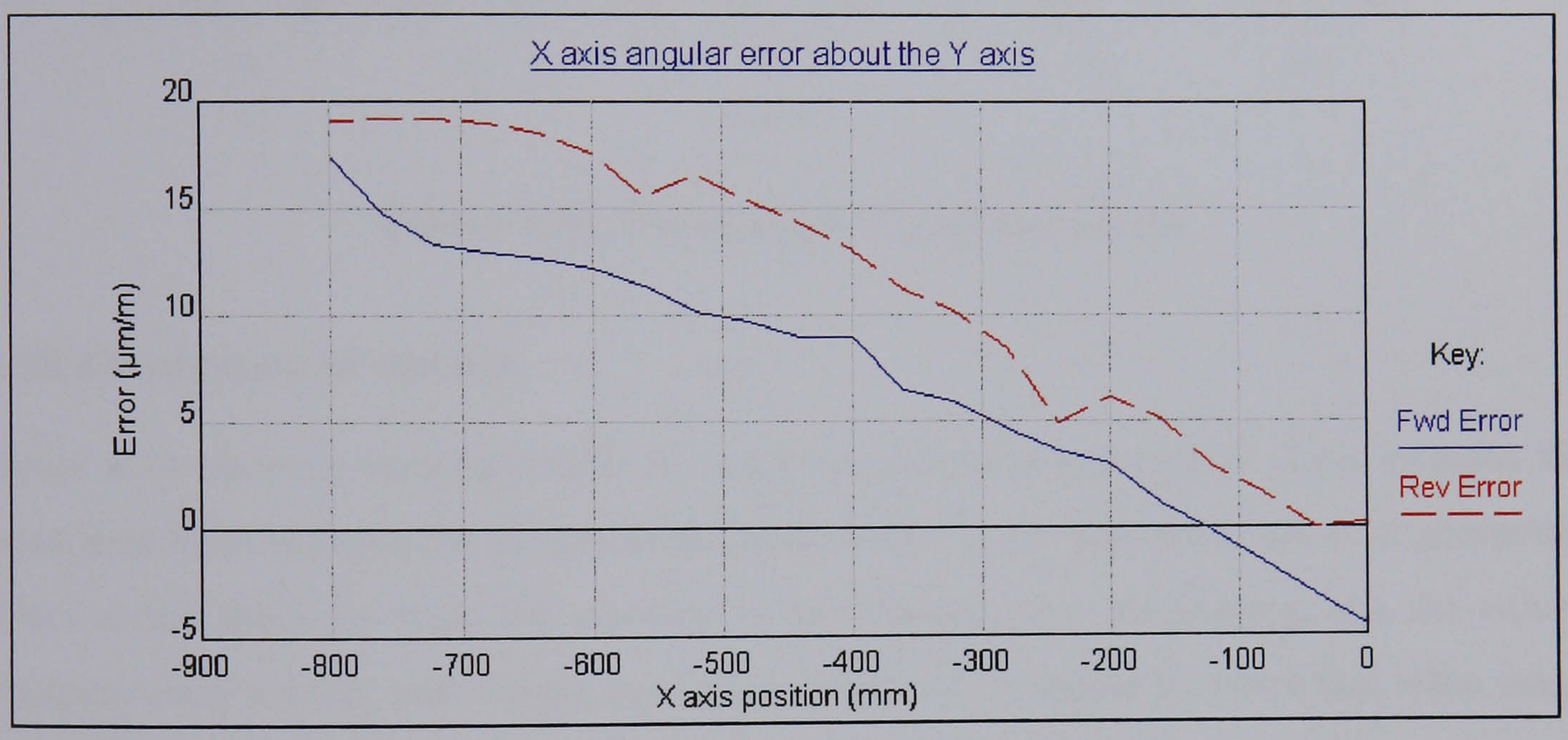


**Figure 4.14: X-axis rotation about the Y-axis**

## 4.02.5.2 Probe results

A possible source of error is in the probing itself. In an attempt to validate the probing results two measurement cycles were performed with one probe (MP2) and three cycles were performed using an 'identical' probe (MP1). Since these probes are nominally the same, probing results should produce similar results. Figure 4.15 show the comparison between the two probes.

The results are within 10µm for all points on the artefact except P16. The reason for the disparity at this point was unclear so point P16 was ignored for further analysis.

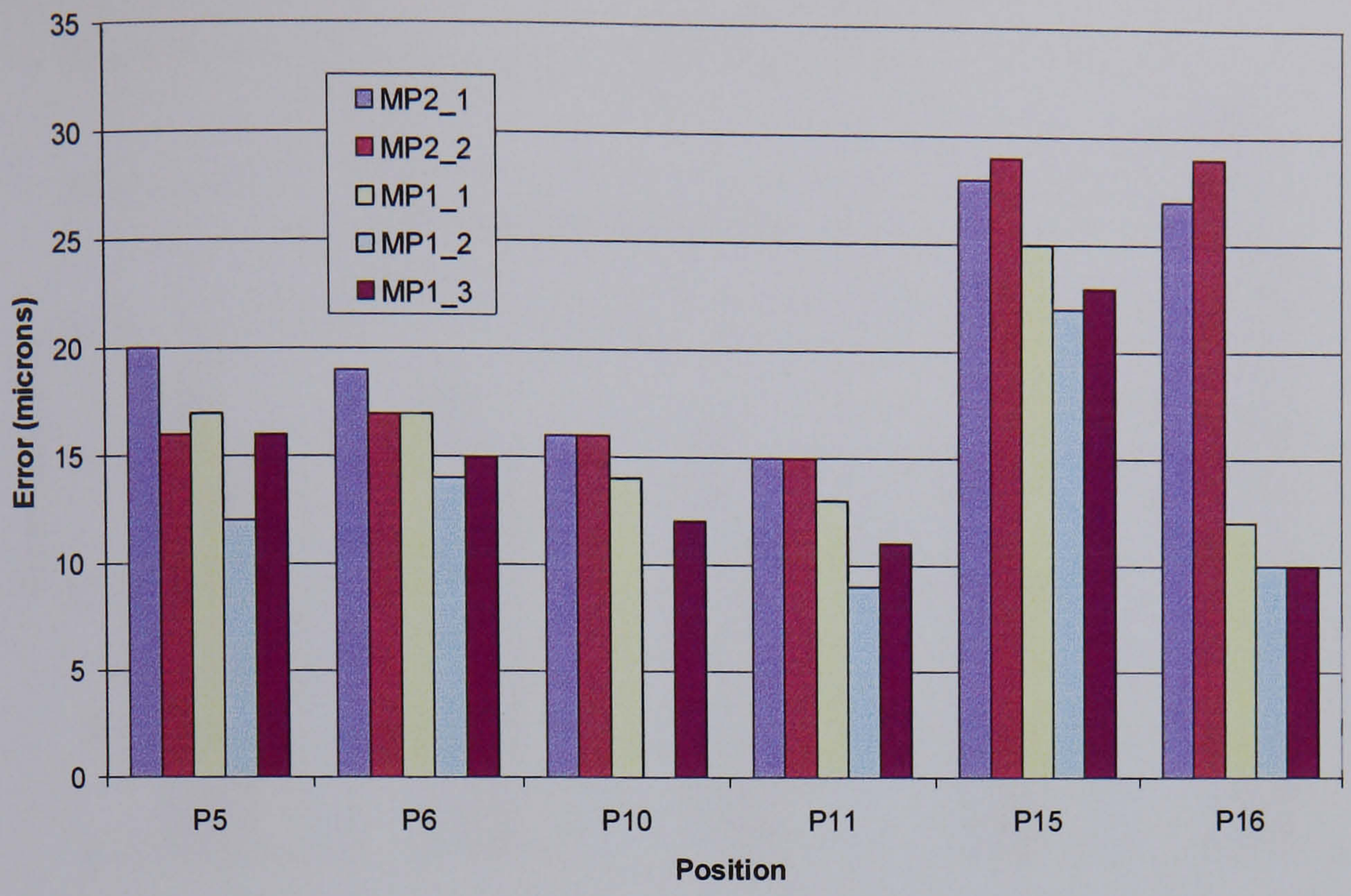


**Figure 4.15: Comparison of probing results**

### 4.02.6 Summary of results

Figure 4.16 shows a comparison of all results at the probing positions. This includes the mean data from both probes (as presented in figure 4.15), the calculated effect of geometric errors at the probe tip with the machine at the relevant axis coordinates, and the values obtained using a probe with longer tool offset (probe 3). It should be noted that when using the longer probe no data is available at the P15 position.

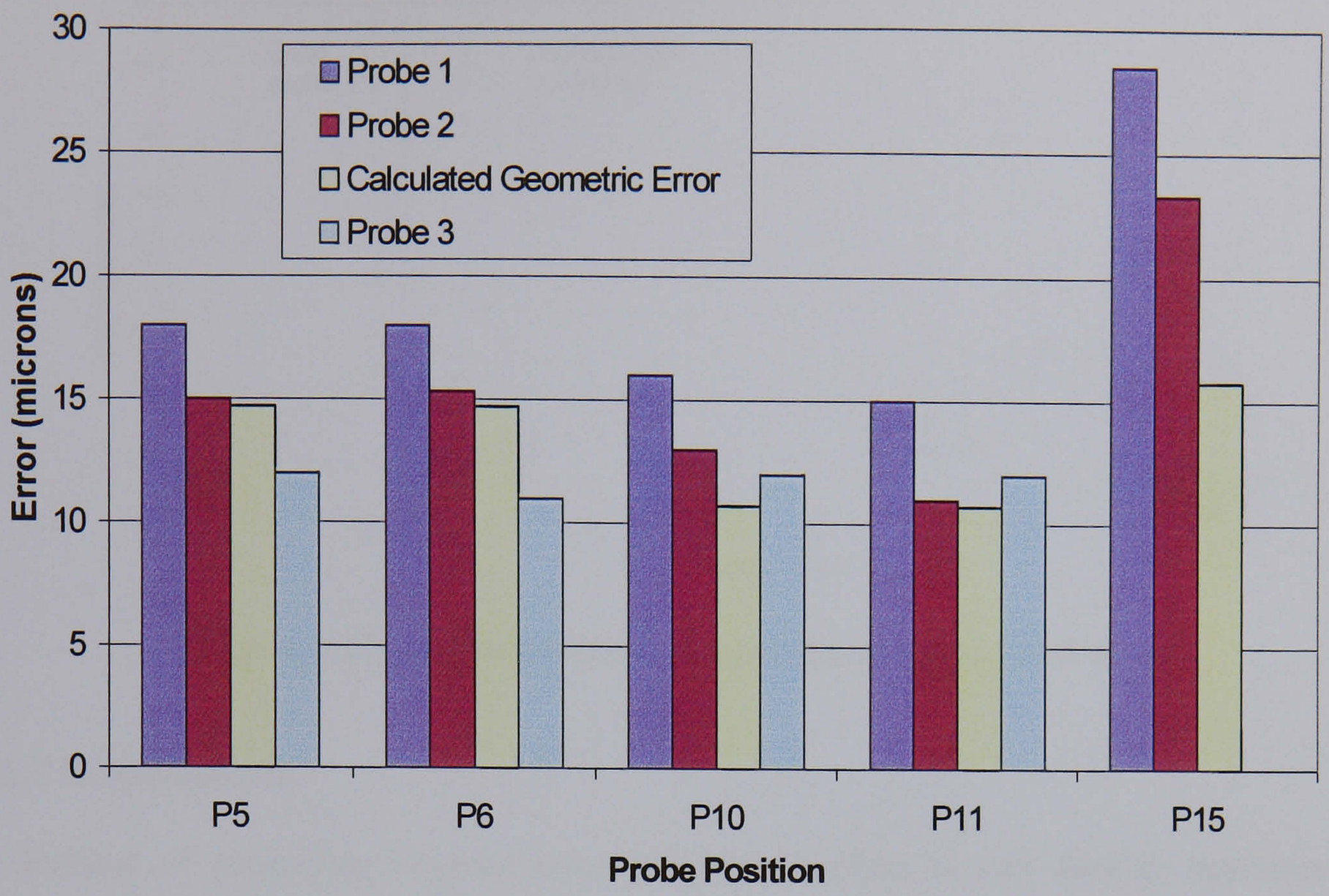


**Figure 4.16: Comparison of results**

The predicted errors derived from the model are very good, being within the spread of probing results at all but point P15. The reasons for the relatively poor performance were not clearly understood, but it is believed that this may be the influence of non-rigid effects. At this point the Z-axis is at a significant extension and so is not as well supported by the guideways as it is at the top.

The discepancy between the longer probe and  probes could be explained by the cyclic effect in the linear positioning of the Z-axis. As seen in figure 4.17, the cyclic effect when using the T10 probe would produce a positive error in the probe measurement. However, the cyclic effect of the ballscrew would produce a negative error in the probe results for the short probe, which potentially cancels some of the other errors.

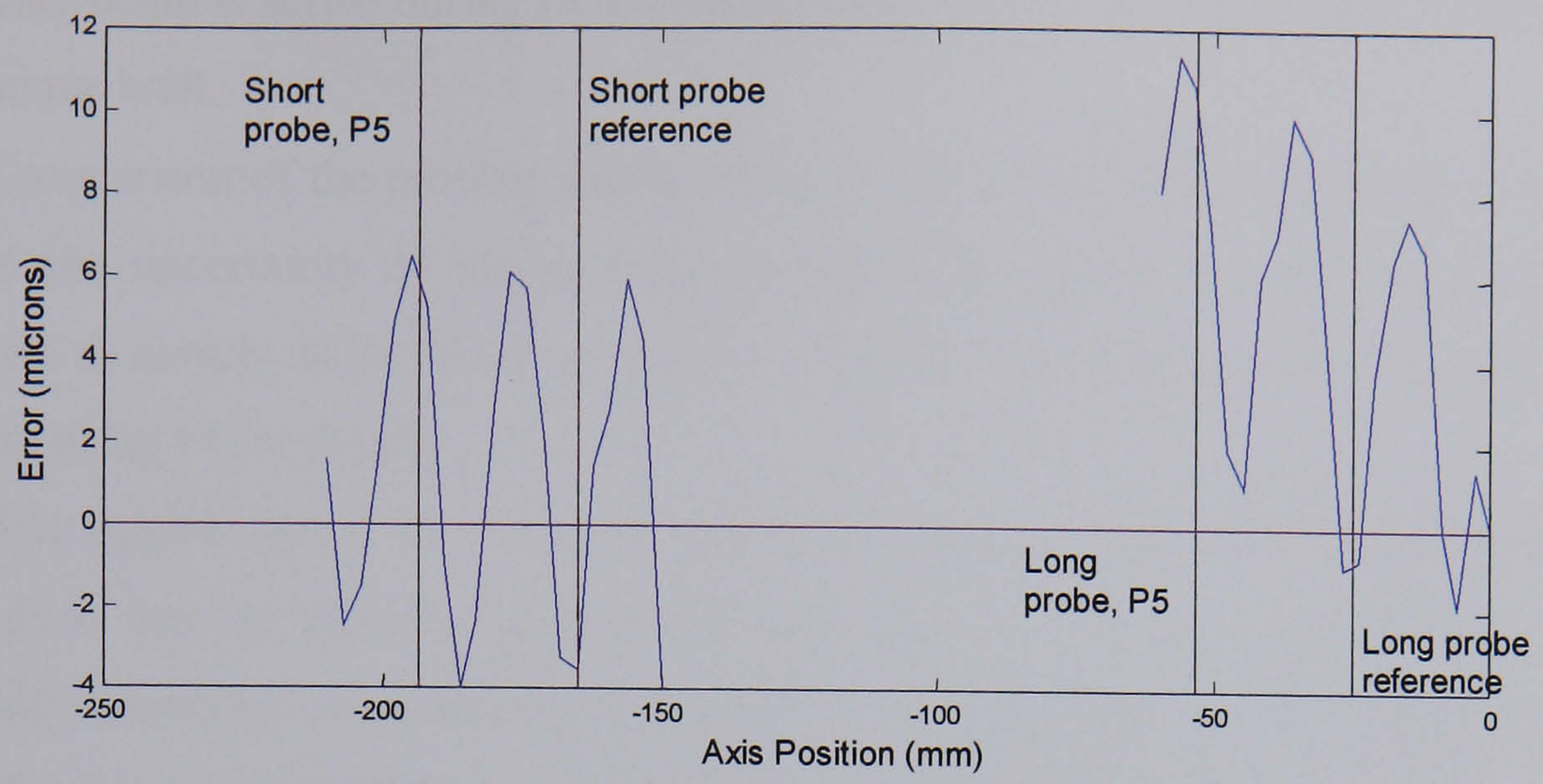


**Figure 4.17: Z-axis position measurement using 3mm step**

### 4.02.7 Conclusions

The method of measuring angular error has been applied to two similar machines and repeated on one of them. In each case the results were similar (table 4.5).

**Table 4.5: Comparison of angular measurements on TM1 and TM2**

| | Method | TM1 (test 1) | TM1 (test 2) | TM2 |
|---|---|---|---|---|
| Maximum error without compensation | Measured | 73 μm/m | 74 μm/m | 75 μm/m |
| | Calculated | 71 μm/m | 72 μm/m | 72 μm/m |
| Maximum error with compensation | Calculated | 6 μm/m | 1 μm/m | 5 μm/m |
| Minimum error without compensation | Measured | -12 μm/m | -14 μm/m | -21 μm/m |
| | Calculated | -9 μm/m | -10 μm/m. | -20 μm/m |
| Maximum error with compensation | Calculated | -6 μm/m. | -7 μm/m | -6 μm/m |

A potential concern was the change in environment between each of the measurement runs when calculating the angular errors. Because measurement practices were adopted that minimise environmental change (machine is not heated) and environmental compensation

for the laser beam is active during measurement these effects were negligible. This validates the technique well.

Comparison of the probing results with the calculated errors at the end of the probe is within the uncertainty of the probing process. The results for P15 and P16 do not correspond as closely as for the other points, but there is some uncertainty over the probing at this extension of the Z-axis.

The magnitude of the residual X-axis pitch error after compensation has been applied show that the effect of mechanical slope on a tool offset cannot be ignored when calculating volumetric performance. The range of residual slope on TM1 would produce a positioning error over the stroke of the amplifier of over nine microns.

## 4.03 Volumetric errors of Gantry CMM 1

CMM1 is a gantry machine supported by four pairs of pillars (figure 4.18), manufactured by a collaborating establishment. This structure had recently been assembled, but final levelling and adjustments for mechanical misalignments had not been performed. This results in a machine with an accuracy that would be considered very poor for a CMM. However, these large errors are very useful for accentuating the effects of angular errors. Additionally, this machine has strokes of 4.4 m, 2.8 m and 800 mm, in the X-, Y- and Z-axes respectively. These large traverses will amplify any angular error components greatly, thus providing clear demonstrative results.

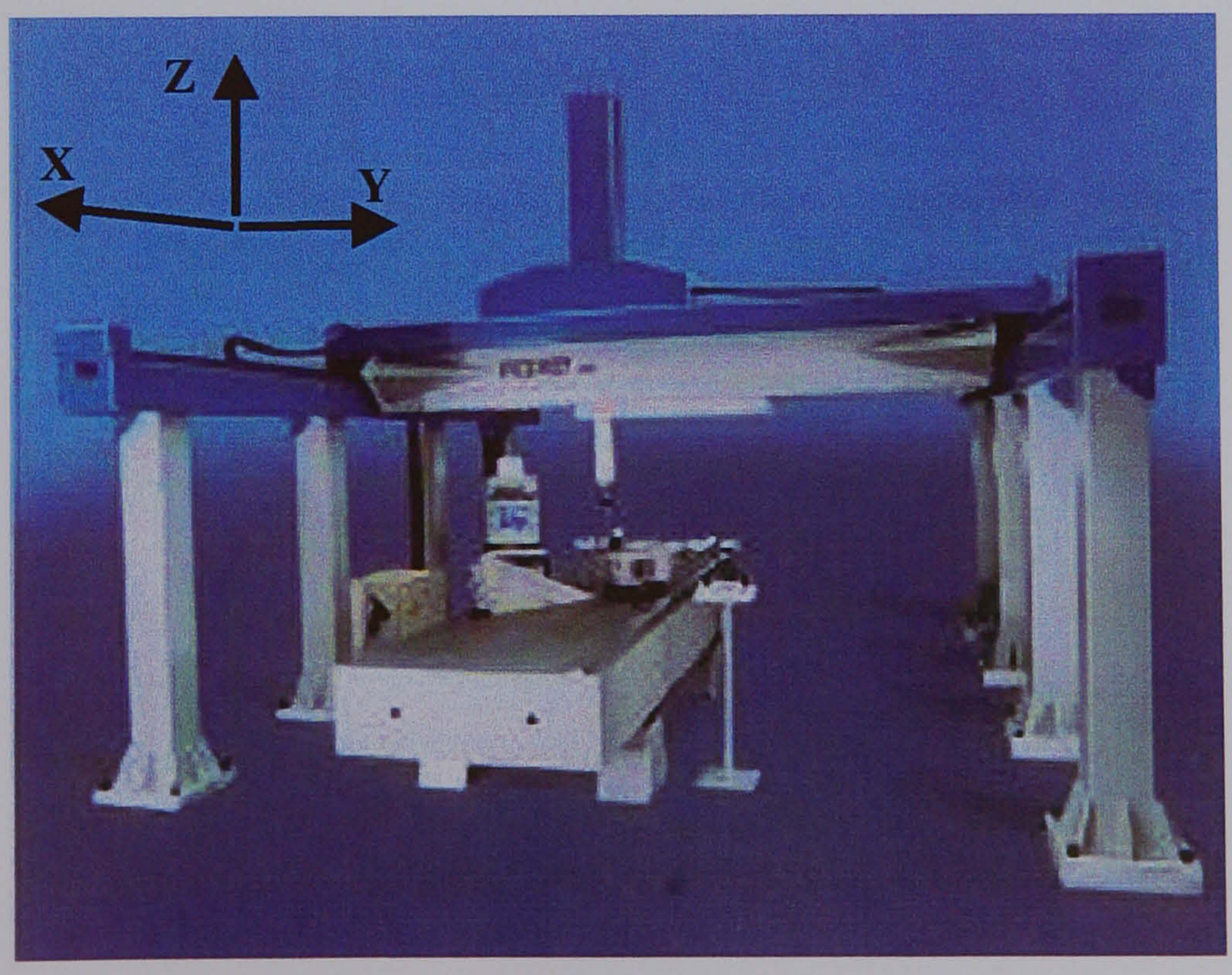


**Figure 4.18: Multi-pillar gantry CMM**

The results of the simulation (Appendix B) show that the volumetric accuracy of the machine was approximately 4.3mm with the Y-axis at –220 mm and the other two axes at their origins. The main contributory factor is the total displacement error for the Y-axis, which has a range of 7.8mm. A large percentage of this derives from a very poor squareness between the X- and Y-axes – something that would normally be significantly reduced during installation and commissioning.

### 4.03.1 Y-axis rotation about the Y-axis

Y-axis roll, which is more correctly termed Y-axis rotation about the Y-axis, has been measured with a range of fifteen arc-seconds (figure 4.19). This error has the effect of producing an X-axis position error as a function of Z-axis position (figure 4.20) and Z-axis position error as a function of X-axis position (figure 4.21).

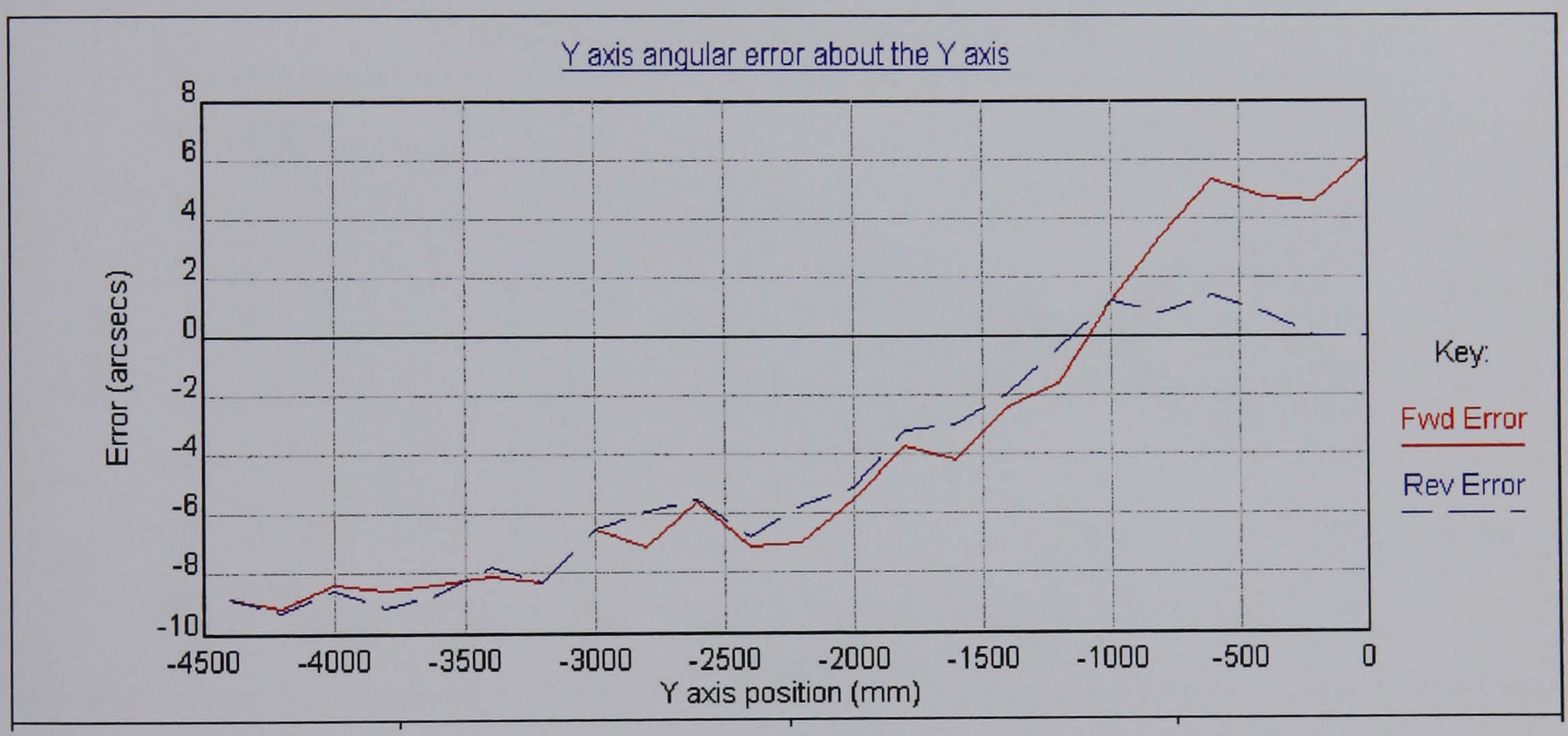


**Figure 4.19: Y-axis roll (CMM1)**

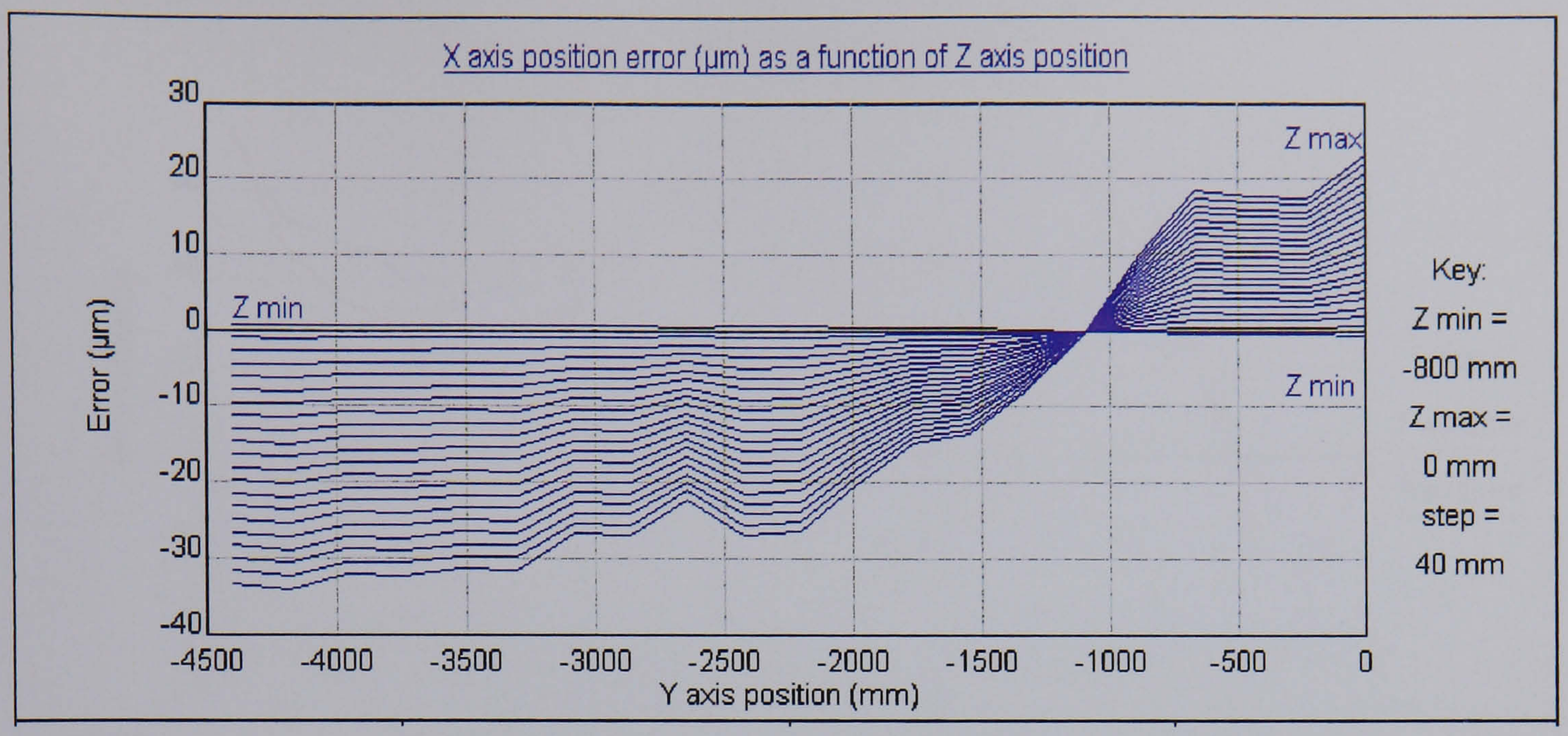


**Figure 4.20: X-axis position error as a result of Y-axis roll (CMM1)**

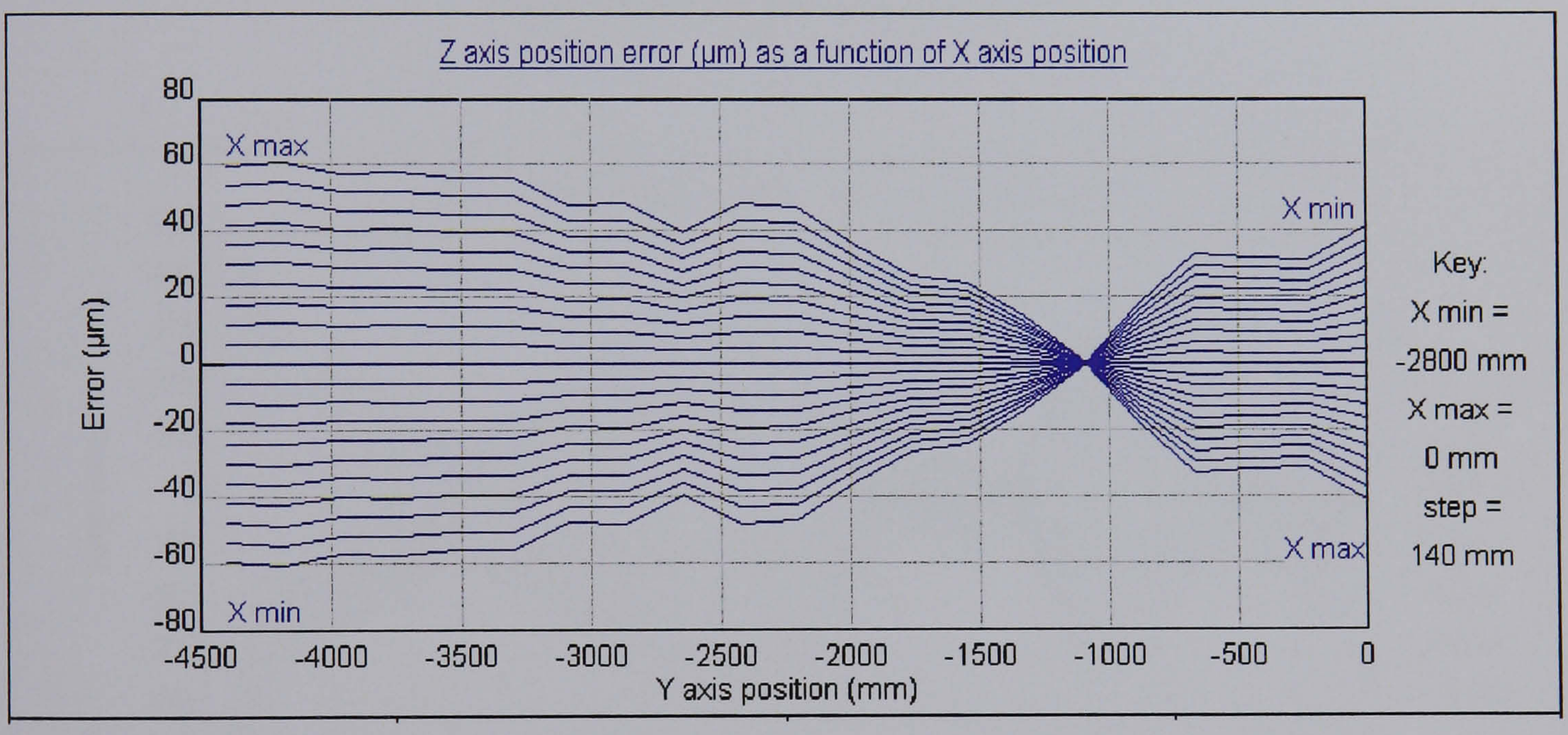


**Figure 4.21: Z-axis position error as a result of Y-axis roll (CMM1)**

## 4.03.2 Y-axis rotation about the Z-axis

The majority of the X-axis error, when discounting linear positioning and squareness errors, derives from Y-axis yaw, or Y-axis rotation about the Z-axis (figure 4.22). Figure 4.23 shows that the resultant error in the Y-axis, due to motion of the X-axis, has a range of one millimetre.

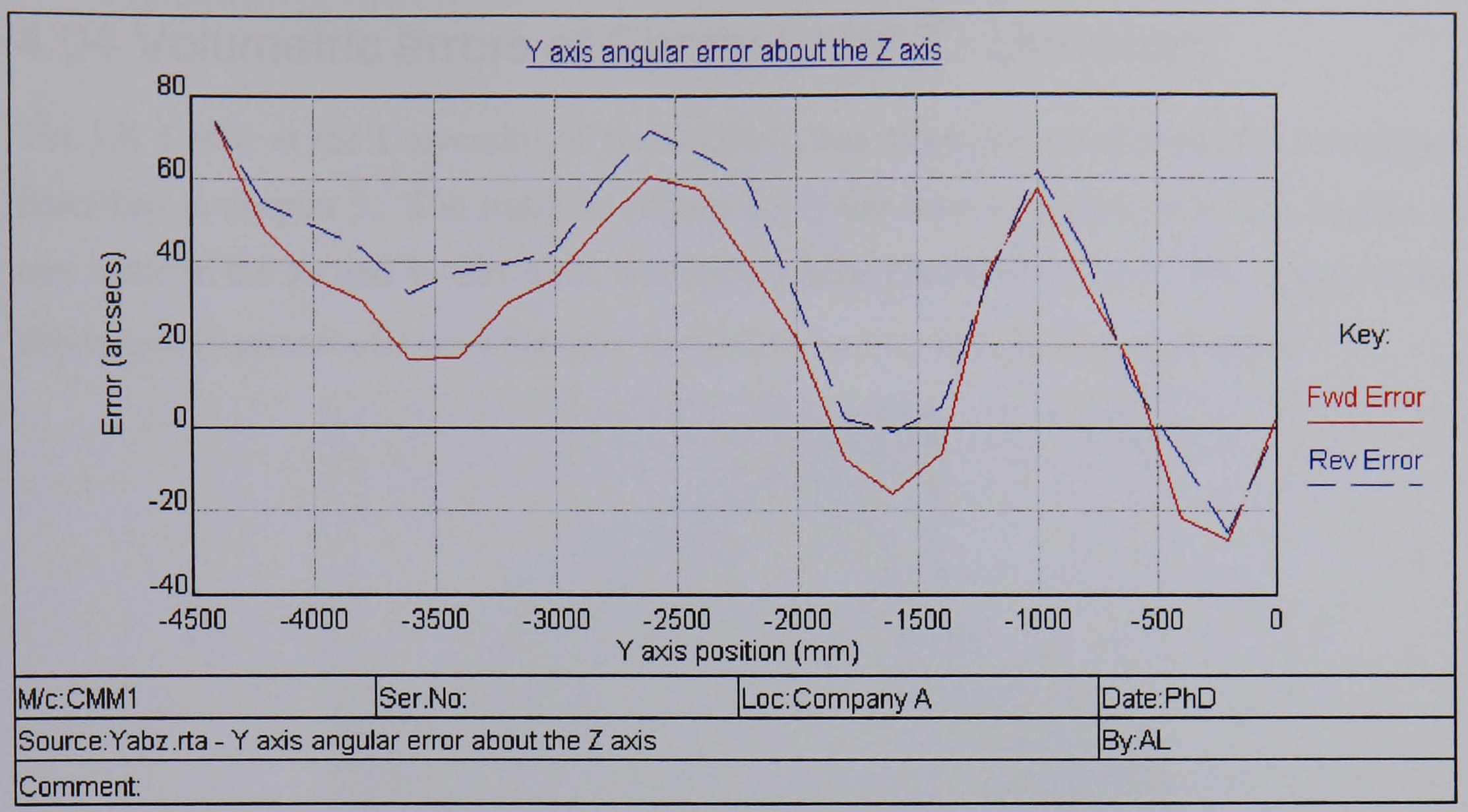


**Figure 4.22: Y-axis yaw (CMM1)**

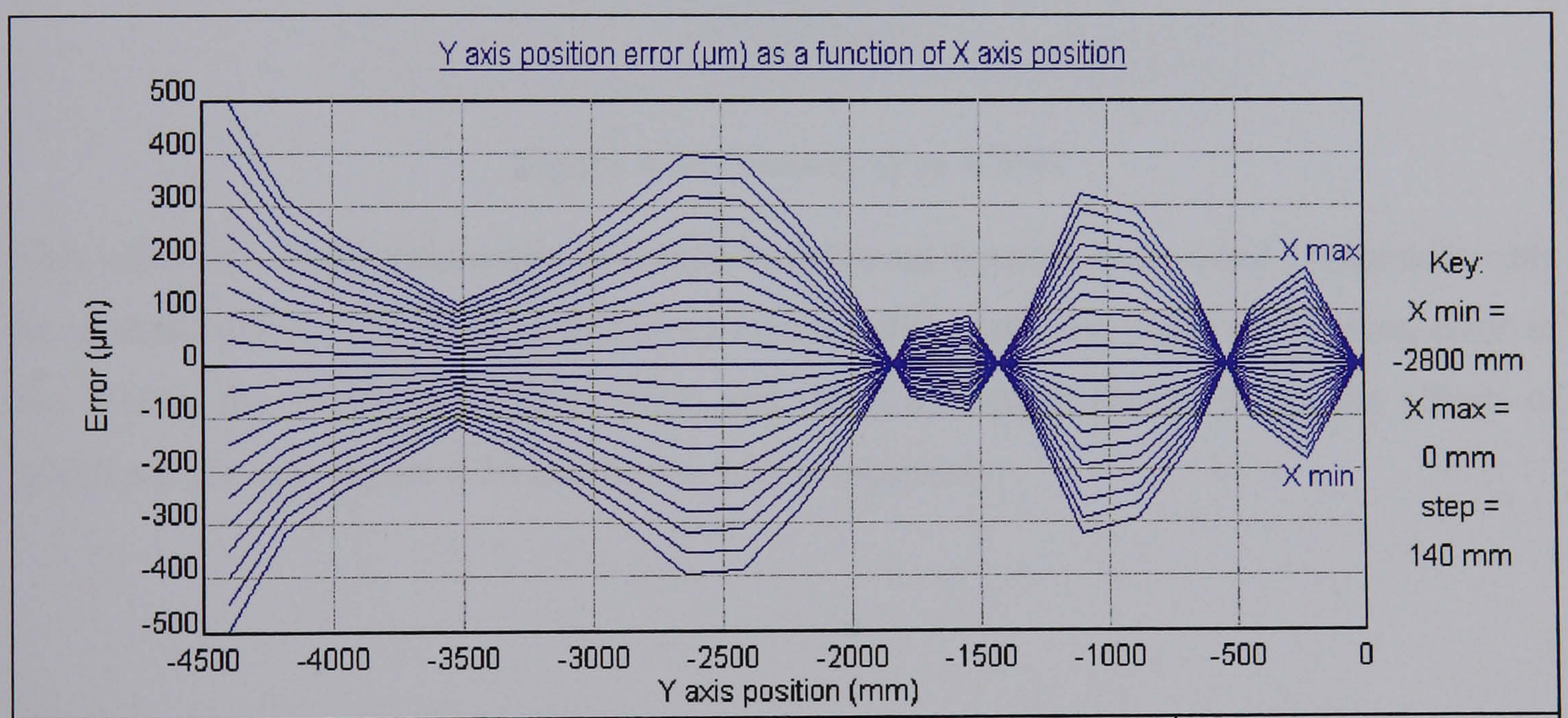


**Figure 4.23: Y-axis position error as a result of Y-axis yaw (CMM1)**

The shape of the errors in figure 4.23 indicates the complexity of the angular error manifestation. The Y-axis is supported by posts in a number of places and it is apparent that this influences the angular error. Although the magnitude of the errors are not typical for this type of machine, the trends may be found to correspond with a finished machine. This would indicate that some mechanical redesign is necessary. Alternatively, the errors can be compensated through software correction.

## 4.04 Volumetric errors of Gantry CMM 2 - University

The LK CMM at the University of Huddersfield has been measured using the techniques described in chapter 3. The machine (figure 4.24) has been measured over axis lengths of one metre in the X- and Y- direction, and three hundred millimetres in Z. The results of the simulation (Appendix C) show that the device has a volumetric accuracy of 18μm.

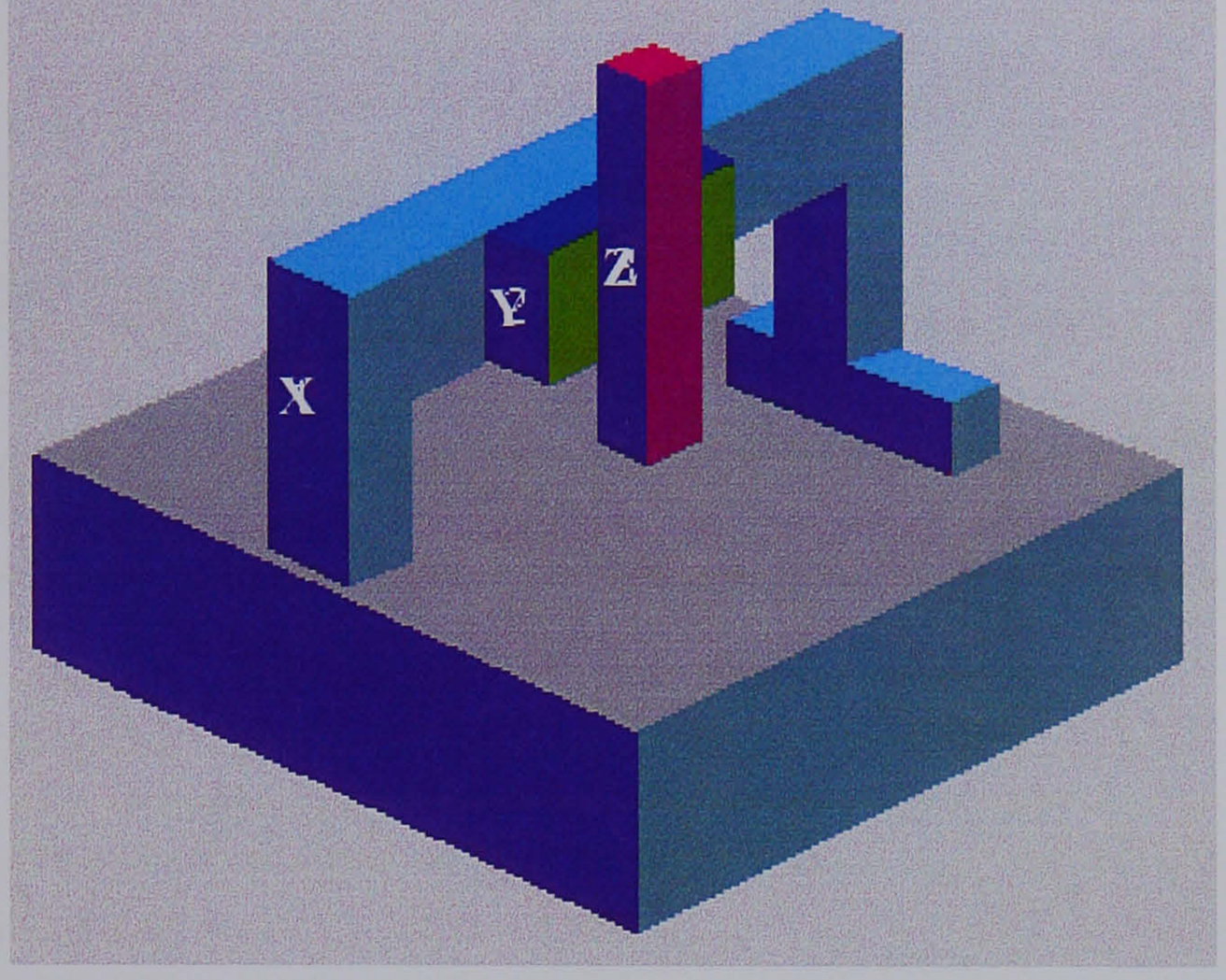


**Figure 4.24: Gantry type CMM**

This relatively small volumetric accuracy is achieved because each error component only has a small effect. The main contributory errors derive from the linear positioning error of the X-axis, the Y-axis roll (figure 4.25) and the X-axis pitch (figure 4.27), the effects of which are given in figure 4.26 and figure 4.28 respectively.

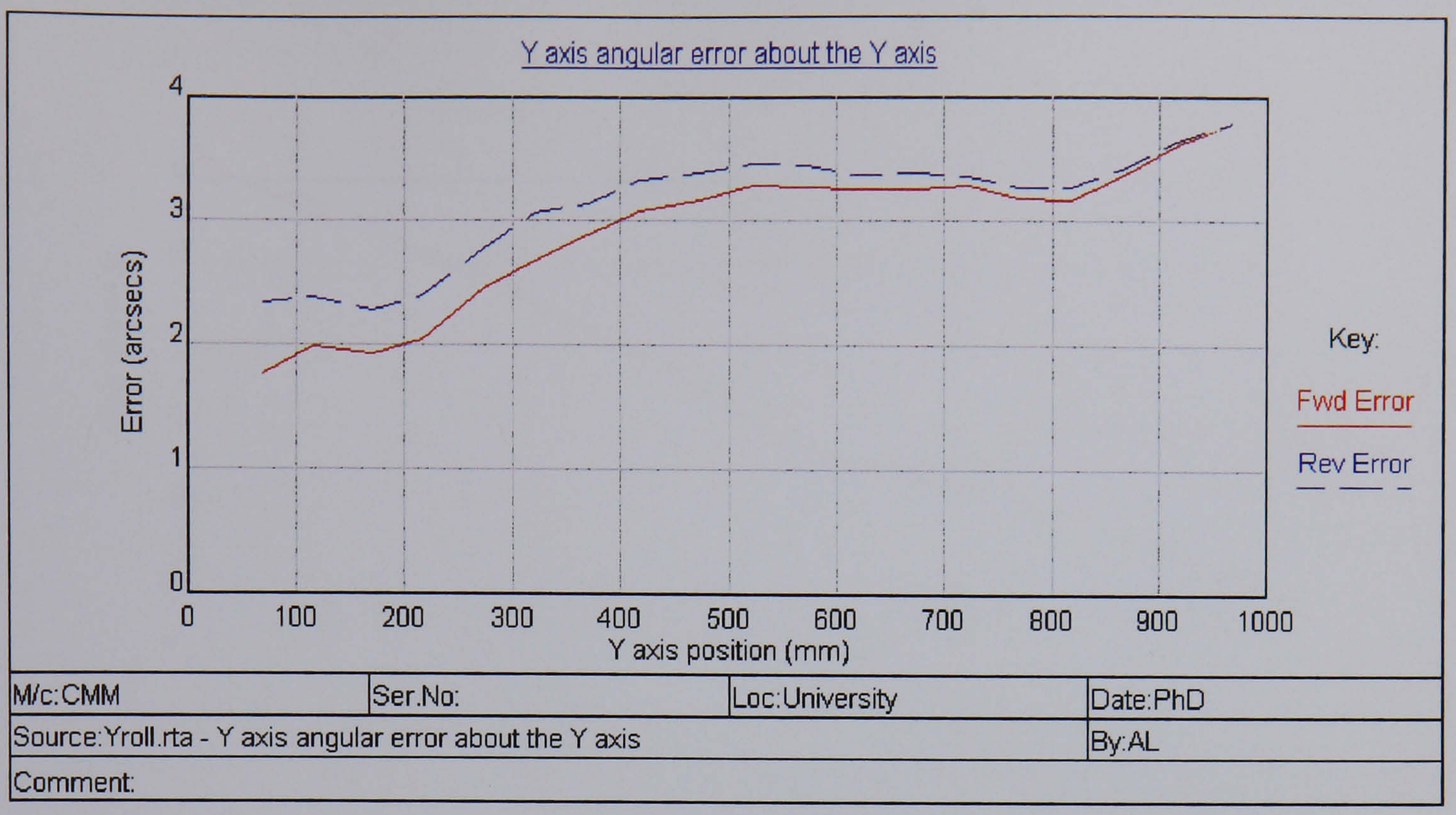


**Figure 4.25: Y-axis roll (CMM2)**

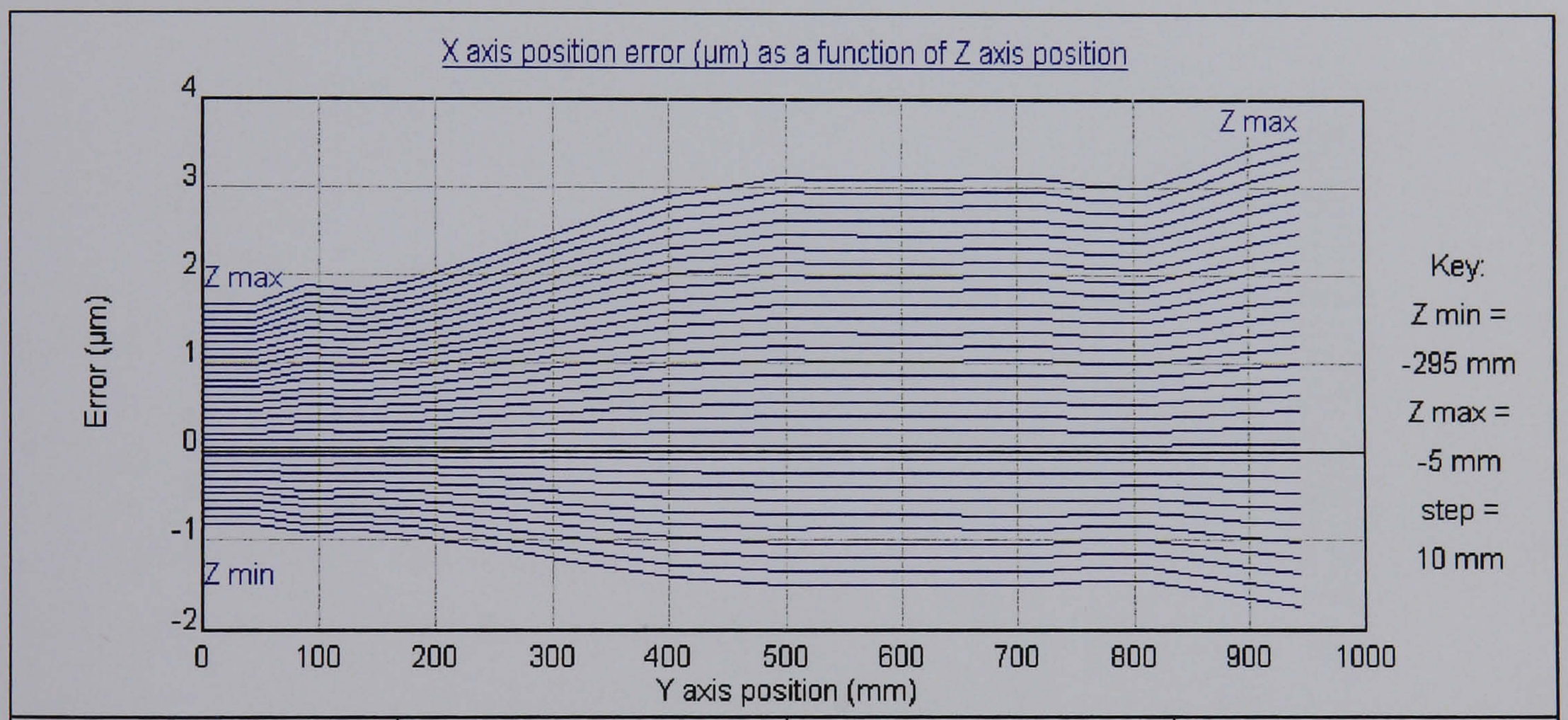


**Figure 4.26: X-axis positioning error as a result of Y-axis roll (CMM2)**

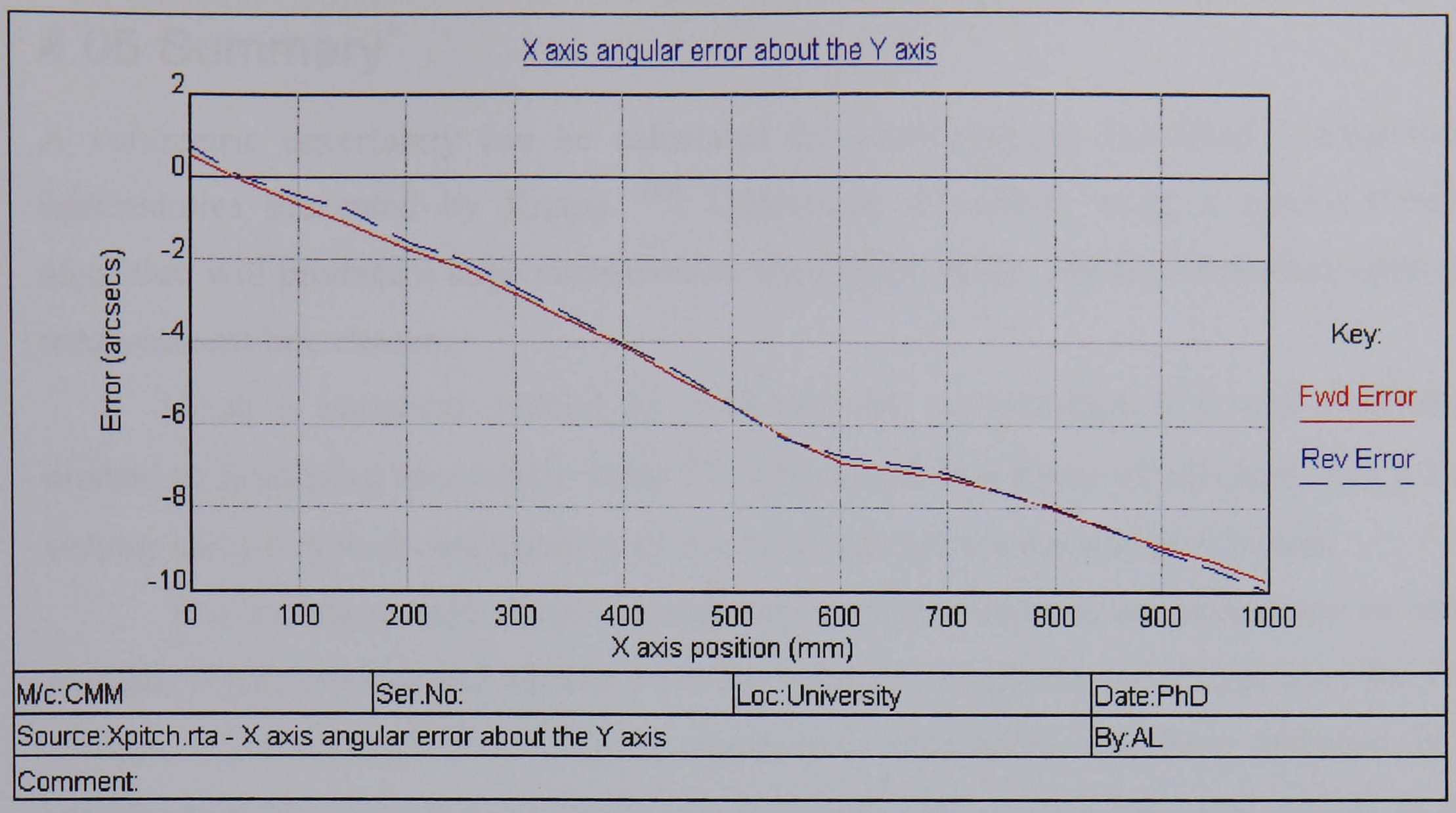


**Figure 4.27: X-axis pitch (CMM2)**

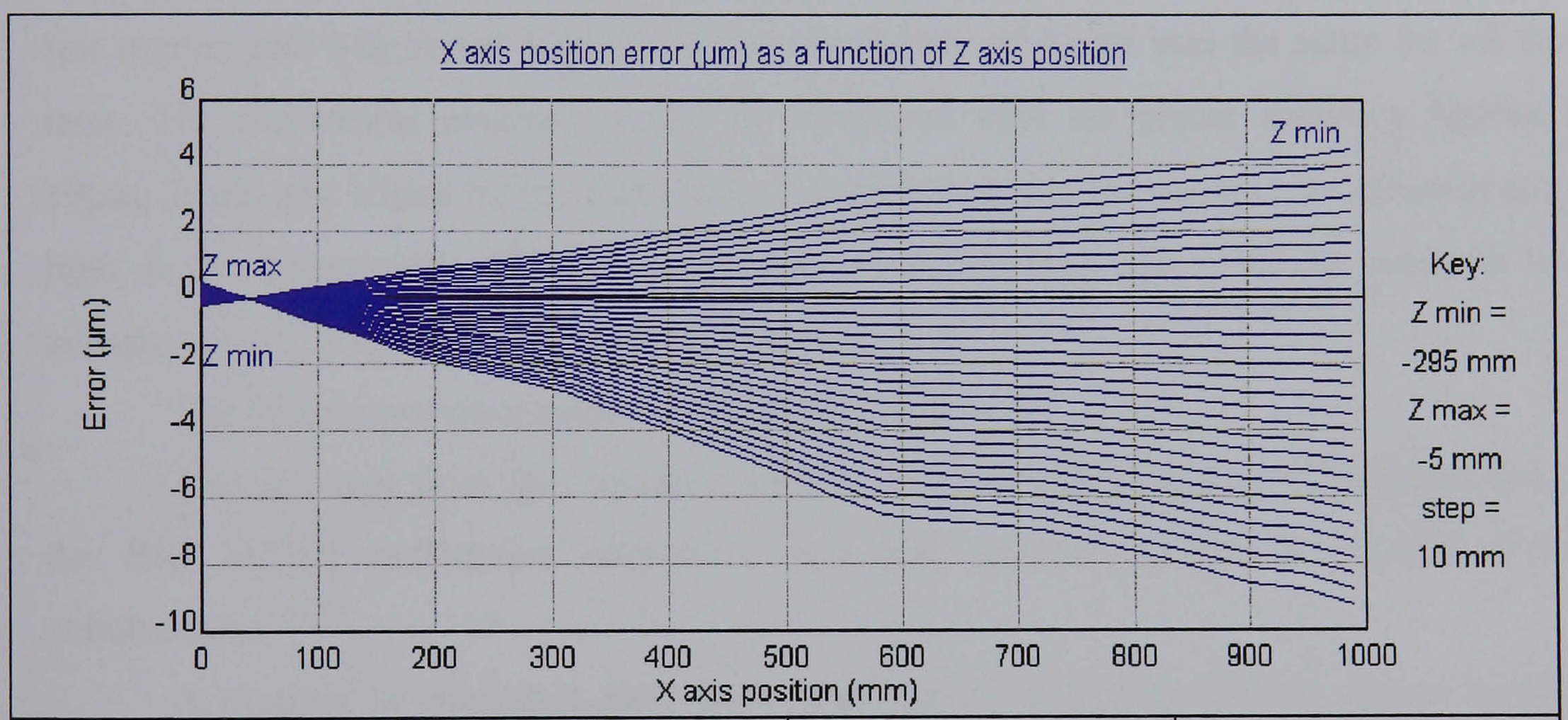


**Figure 4.28: X-axis positioning error as a result of X-axis pitch (CMM2)**

The performance of CMM2 shows a typical volumetric accuracy for a CMM of this configuration and specification. When calibrated by the supplier only the linear accuracy for each axis is quoted as being ±5µm.

The volumetric performance of this device required quantification, since it is to be used as the reference device for validating the LaserTrace measuring device, as discussed in chapter 5, chapter 6 and chapter 9.

## 4.05 Summary

A volumetric uncertainty can be calculated by combining the individual measurement uncertainties presented by Knapp. [63] Combining all effects using a purely additive algorithm will produce a large measurement uncertainty value, which is dependent upon the measurement line chosen.

Using a statistical method of combining the uncertainties is a well-established method of producing uncertainty value [64]. This produces a figure of ±26.2μm over a $1m^3$ volume using a typical configuration of machine and typical measurement devices.

This statistical method has subsequently been used to calculate uncertainty on other machine configurations and obtains a similar value of volumetric uncertainty over the $1m^3$ volume. This method of calculating volumetric uncertainty has been included in a specification for updated error simulation software. This method has been applied to the turning machines analysed in section 4.02. Because of the similarity in configuration and test regime and was found that the planar uncertainty of 11μm was the same for all three tests. The theoretical uncertainty can be compared with the planar accuracy figures of 19μm, 21μm and 15μm for the three tests. It can be seen that the variance in values is not as high as the uncertainty, which may indicate that historical data could be used, in such circumstances, to refine the uncertainty estimate.

The volumetric uncertainty for the two CMMs was

The findings from this research activity have been postulated for consideration by the BSI MTE/1 calibration committee and also offered to the EC funded project collaborators. [2, 3]

A number of machines have been investigated during the course of this research work. Those included in this thesis show the applicability of the techniques to both machine tools and coordinate measuring machines. In particular two similar machines (TM1 and TM2) have been assessed using ESP during the course of this research. It has been found that the results are similar for both machines and that this does not change significantly over time. This information is not only confirmation of the repeatability of the measurement and analysis techniques, but the relatively small variation in results indicates that the uncertainty of measurement does not compound to produce a great uncertainty in the volumetric result. Gathering repeated information in this way can lead to evaluation of the uncertainties by Type A methods for a greater number of the uncertainty sources.

CMM1 has shown the effect that angular errors can have on a machine with long axes. It also highlights the influences that structural elements can have on machine performance and the need for error avoidance before error compensation is considered. CMM2 shows a typical result for a coordinate measuring machine with relatively small errors and amplifier axes of one metre or less. The volumetric accuracy figure of 18μm is comparable to a recent calibration report measuring up to 5μm positional error in each axis. The volumetric uncertainty for the machine is found to be 14μm.

The work covered in this chapter successfully validates the synthesis methods described in chapter 3. The results of measuring CMM2 using traceable equipment means that the machine can be used as a benchmark for validating the performance of the LaserTrace system in conformance with objective 1.14 (d). This system will provide an alternative method of measuring Cartesian machines, but will also be applicable to non-Cartesian systems. This work is covered in the following five chapters.

# Chapter 5 Preliminary Investigation of Laser Tracking

## 5.01 Introduction

The work in the previous chapters has introduced and validated a method by which the volumetric performance of a Cartesian machine can be assessed by combining measured geometric errors for each of the three axes. It furthers the applicability of the technique by evaluating the additional effect when considering tool offset. The techniques have then been expanded to include machines with volumetric compensation active.

This synthesis method provides excellent data for quantifying overall performance. However, the strength of the system is its ability to provide interpretation of the geometric error data to highlight the most significant error sources, for which mechanical adjustment may be possible. If correction cannot be successfully achieved, the shape of the output graphs indicates which regions of the machine have constant errors, allowing the machine to be used more effectively by avoiding these areas if possible.

A drawback of this technique is the amount of time required to collect the error data for calculation of the error grid. Depending upon the length of the axes, a full measurement of the twenty-one error sources could take up to a week. Furthermore, this technique is only applicable to a machine with Cartesian axes.

A convenient method of obtaining error grid data would be by measuring the errors directly. There are various means discussed in chapters 1 and 2 by which this could be achieved. The method selected for analysis during this project is the LaserTrace scanning laser, which could be used to measure the error map of either Cartesian or non-Cartesian machines directly.

Tracking lasers have potential for the fast, automatic gathering of static calibration data for measuring the position of the end effector for robotic systems. There are two fundamental designs for tracking laser measurement systems. The first uses a tracking laser interferometer, which provides displacement and angular measurement data, giving a polar coordinate measurement. The second provides only angular data, which requires multiple laser units to allow measurement of the position of a target by triangulation. One such system is LaserTrace.

LaserTrace is inappropriate for many measurement tasks in standard form, due to the low accuracy achievable. The collaborating company who supplied the system measured a static accuracy of no better than one millimetre and ten millimetres dynamically for a volume of less than one cubic metre. These values stand as benchmarks for the testing work of this project. Furthermore, the system requires a complex method of calibration before it can be utilised. In order to improve upon the accuracy and ease of use of the LaserTrace system new models have been devised and tested on CMM2. The results of the LaserTrace have been compared with the measured accuracy of CMM2 from section 4.04.

## 5.02 Standard for laser tracking

It is important for companies wishing to conform to ISO 9000 that any metrology equipment they use be calibrated to a traceable standard.

Traceability and measurement uncertainty for laser interferometer trackers was discussed by NIST in America [35]. Laser tracking systems suffer the same difficulties as all 3 dimensional metrology devices when estimating uncertainty since the error mechanisms and their propagation through the system are very complex and often task-specific. Some methods of quantifying error are comparison, usually artefact based, virtual instrument or uncertainty budgeting. [83]

The virtual instrument is a simulation of the error propagation of the device, which is used in tandem with a model of all non-instrument related error sources to give an overall uncertainty for a measurement. The simulation can be run for each task for which the device

is to be used to determine the uncertainty for that measurement. This method of determining the error uncertainty relies on the integrity of the model and the accuracy with which parameters are estimated.

Because of the complexity of the problem, the traceability and standardisation of laser tracking equipment remains at the working group stage. [84]

## 5.03 Description of LaserTrace

### 5.03.1 Description of a LaserTrace laser pod

LaserTrace is a laser-based position measurement device designed for measurement in two or three dimensions, depending upon configuration. The calibration system is a non-contact device with the only constraint on the machine being the mass of the target retroreflector, which is mounted at the tool tip, or end effector. This constraint may not prove at all prohibitive, since the mass of approximately three hundred and fifty grams may only be a fraction of the load incurred when using a tool or carrying a part.

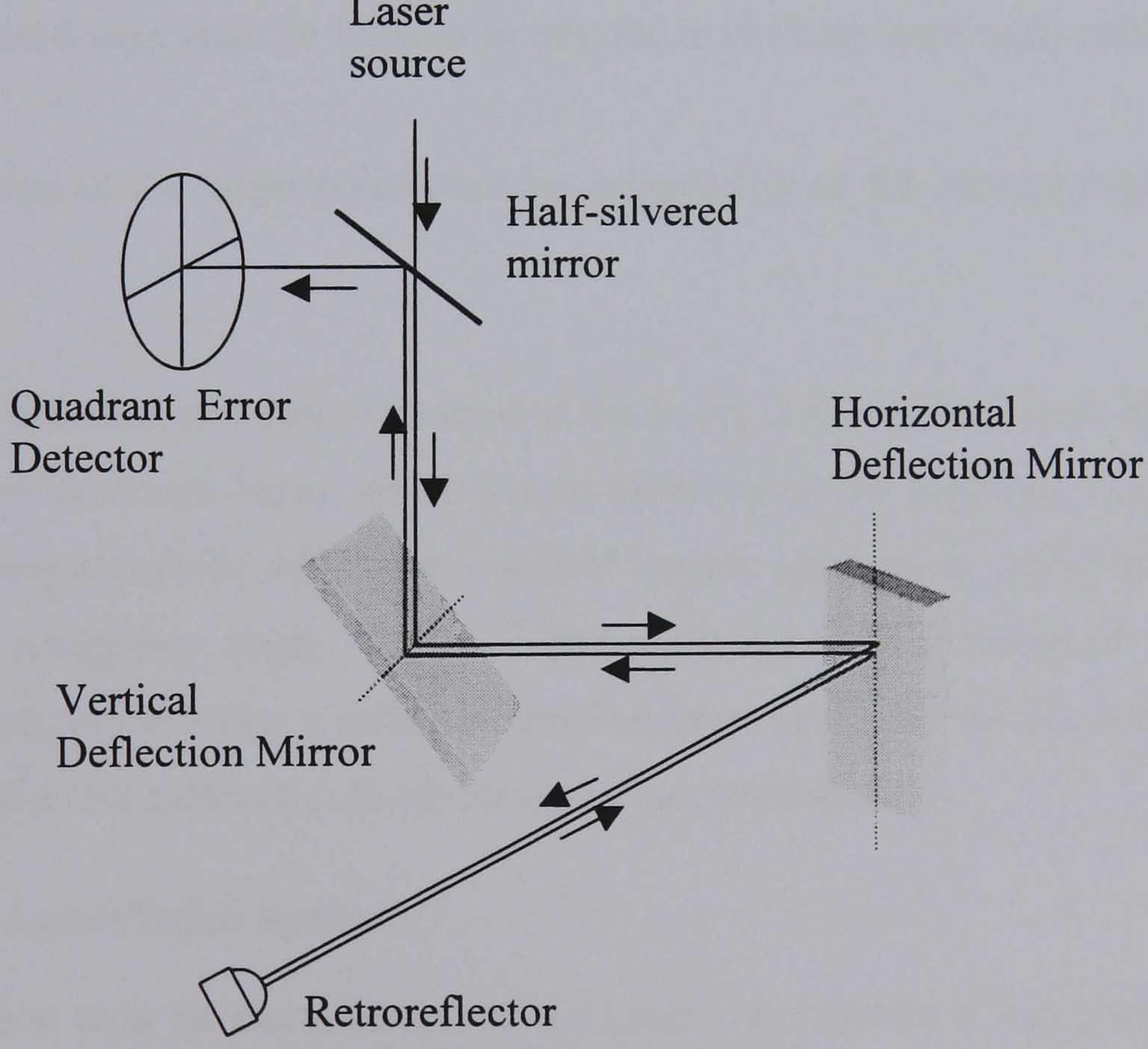


**Figure 5.1: Schematic of LaserTrace System**

A schematic of the LaserTrace is shown in Figure 5.1. Each LaserTrace pod contains one fixed half-silvered mirror and two actuated mirrors, which allow the emergent beam to be deflected vertically and horizontally. The emergent beam is then directed to a retroreflector (usually corner cube or cat's eye) which, if it is struck centrally, returns the beam along the same path. Any deviation of the incident beam from the optical centre of the target results in the return beam being offset from, but parallel to, the incident beam. The return beam is deflected by the mirrors until it impinges upon a quadrant error detector, the signal from which is converted into an actuation signal for the mirrors which are servoed to bring the beam onto the optical centre of the target. It is by this control loop that the laser maintains its monitoring of the optic – this process is called "tracking." A 16-bit resolver mounted on the axis of rotation measures the rotation of each of the actuated mirrors.

### 5.03.2 Specification of target optic

The target must conform to the following requirements [85]:

1. The reflected rays must be parallel to the incident ones. An afocal system is therefore required.
2. The reflected rays must be located to provide a tracking error with respect to a target point.
3. The position of the target point must be independent of the viewing angle or tracking error.

Glass prism retroreflectors cannot be used as the target in this system since they modify the polarisation of the return beam, which causes problems in the feedback loop. The air-path corner-cube retroreflectors, which are available for this application, suffer the disadvantage of a narrow acceptance angle – a 22.5° half-angle cone. The choice of target for this application was the cat's eye, a reflector based on glass parabolic mirrors, which has a 112° acceptance cone, but suffers the disadvantage of increased mass.

### 5.03.3 Dual LaserTrace system

After discussion with the manufacturer of the LaserTrace system it was possible to contact other users of the system. [86, 87] In both cases, the pods were being used individually to provide limited information on deflection of structures. However, the purpose of this research is to use a system with two lasers to provide full three-dimensional position measurements.

The LaserTrace system that is used for this research employs two laser tracking pods (figure 5.2). The position of the targeted reflector can then be found by triangulation. Determining the errors between measured and programmed position at a grid of points over the working volume will produce an error map.

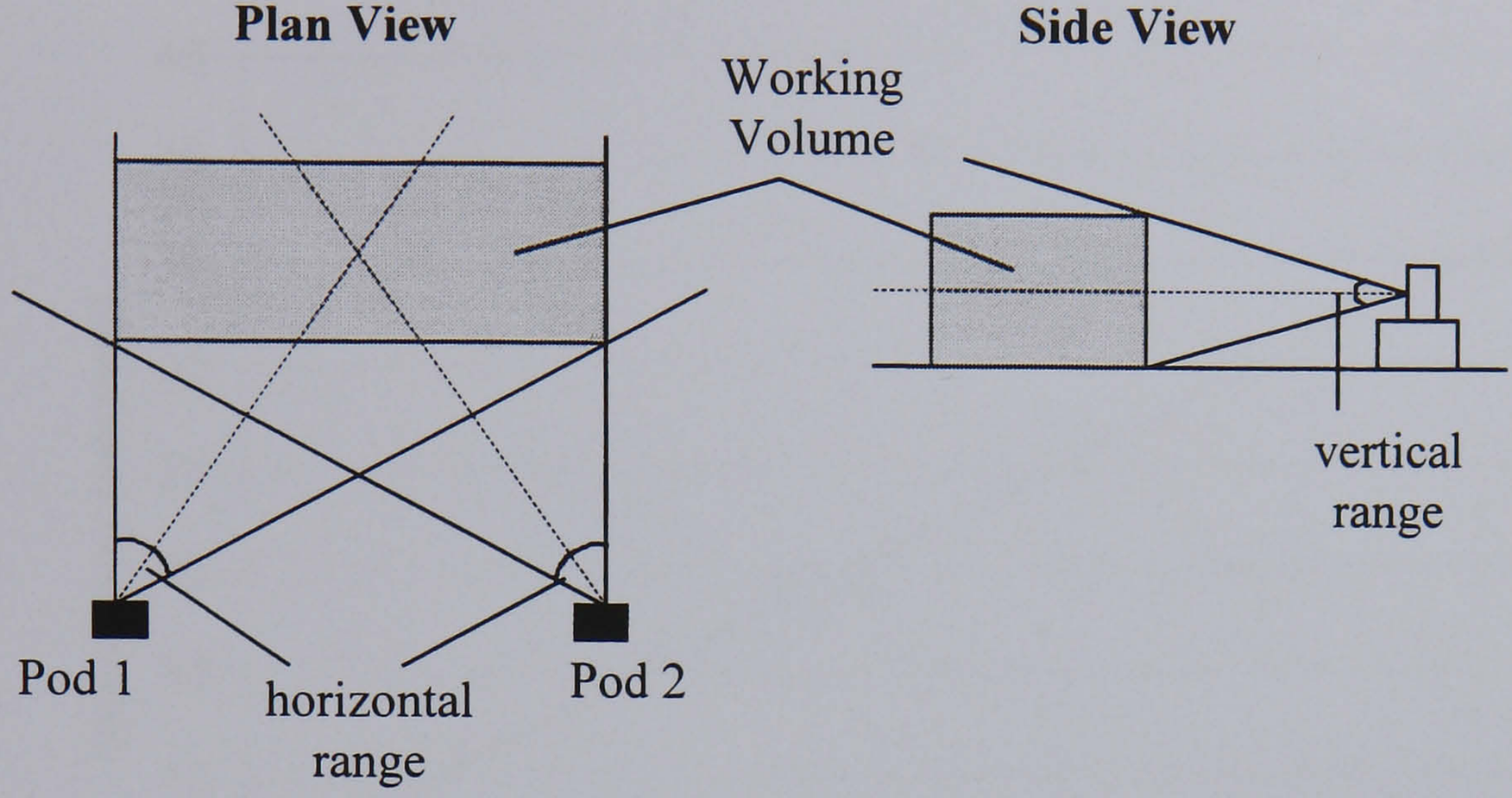


**Figure 5.2: Configuration of a LaserTrace system**

The method of computing position measurement from encoder readings is based upon mathematical rotation and translation of pod positions. Two matrices $M_{WP}$ and $M_{PW}$ are defined to allow transformation between local pod coordinates, P, and world coordinates, W. These transformation matrices can therefore be defined by:

$$\left.\begin{aligned} M_{PW} \times P &= W \\ M_{WP} \times W &= P \end{aligned}\right\} \qquad \text{Equation 5.1}$$

Determining the coefficients of the transformation matrices is not trivial since no direct length measurement is available. There is also no direct knowledge of the relative position and orientation of the two pods. For the RoboTrak system, which is based on a similar principle of trilateration, the distance between encoder devices can then be calibrated by pulling the cords from one encoder to the next. Such a measurement is not possible with the two LaserTrace pods because of their configuration. An iterative method is required to determine position and orientation, the accuracy of this procedure being dependent upon the quality of data and the conditioning of the equations that describe the system.

The methods that have previously been adopted to define pod position and orientation used a beam of known fixed length to establish the conversion factor from encoder data to length measurement. However, this method is complex and time-consuming

to implement. The calibration is also based upon a small number of data points and so is susceptible to measurement noise.

### 5.03.4 System resolution

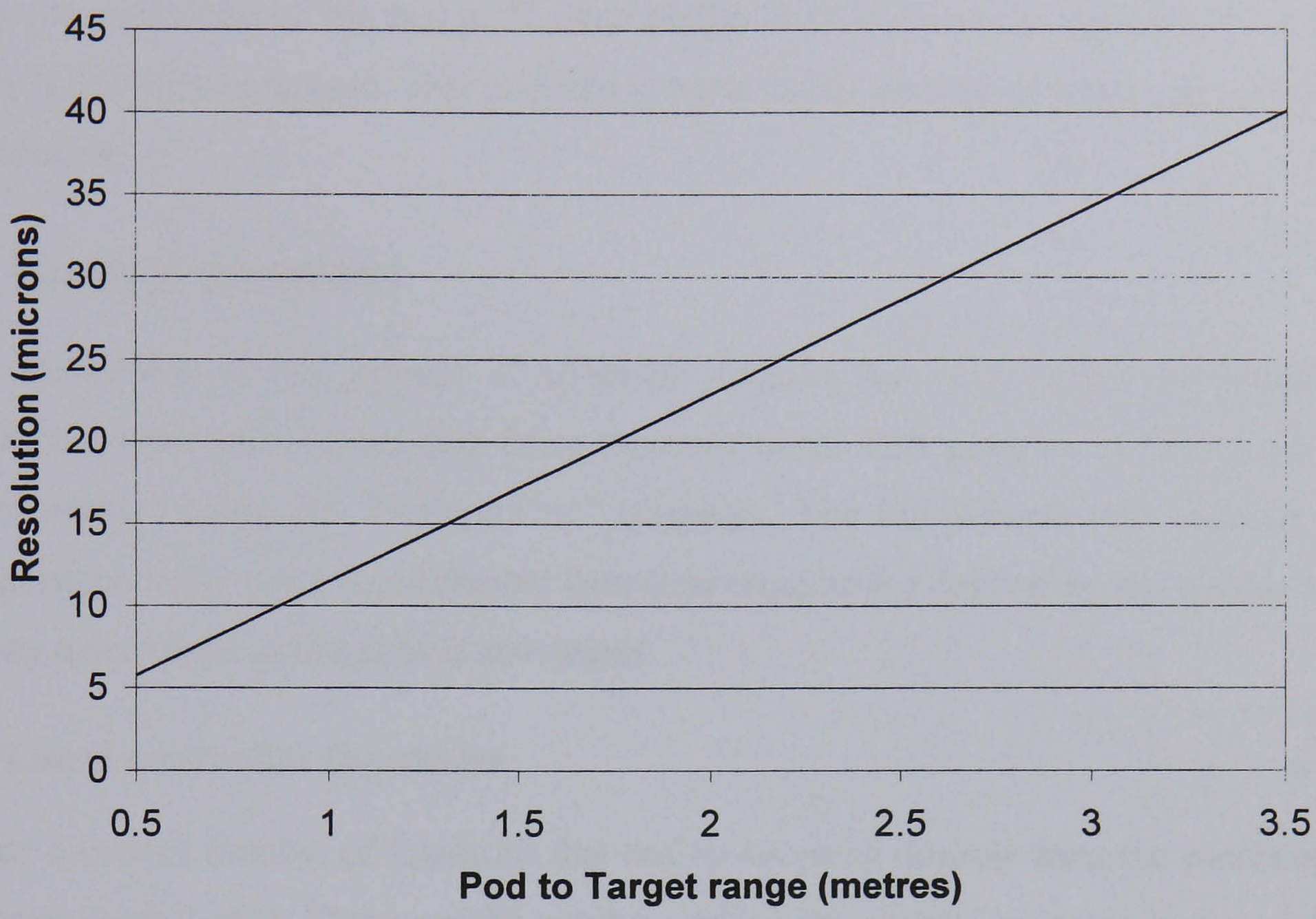


**Figure 5.3: Calculated resolution of LaserTrace with distance**

Any performance gain attainable on the LaserTrace is limited by the resolution of the encoders on the steering mirrors. The resolution of a LaserTrace pod is quoted at 2.2 arc-seconds, or 12μm at 1m range, the repeatability being ±1 least significant digit (resolution). The field of view of the LaserTrace has been measured as being approximately 43° for both vertical and horizontal deflections. The tracking rate of the system is up to 5 radians per second or $5ms^{-1}$ at 1m.

The range for each pod is quoted between half and one hundred metres. As can be seen from figure 5.3 the resolution of the system quickly degrades with range. For a calibration where the pods are 1.5metres from a working volume of 1 cubic metre the resolution at the furthest extremity will be of the order of 28μm.

It should be noted that the quoted resolution is for each local encoder measurement for a single pod, not for the three-dimensional measurement of a dual trace system.

### 5.03.5 Pod timing

A potential problem with the system is that, since multiple units are used, data must be acquired from both pods when the optic is in a single position. If a command to take a measurement is made it must be simultaneous for all pods. If a command to accumulate data is made the cycle time of the two pods must be the same to ensure a 'data set' for a given position is correctly measured. This problem is particularly significant when taking dynamic measurements.

## 5.04 Control program

During the course of this project, a computer program has been written to control the LaserTrace system and acquire data from the laser units. This program is DOS-based and has been written using the 'Borland C++' language. The functionality has evolved from basic operation to the more sophisticated functions required for calibrating the system which were only determined as the project developed.

### 5.04.1 Local controller functions

There are a limited number of functions that can be accessed directly from the panels on the LaserTrace control unit. These can be used to debug the control program and to provide feedback regarding track-status, encoder values, etc.

#### 5.04.1.1 Interface controls

An RS232 or GPIB interface is available for interfacing to the external control computer. For this project the GPIB interface was used because of the relatively high data transfer rate that can be achieved when compared with the RS232 connection. Additionally, all data for both pods is transferred using a single interface card. This provides a simple method of synchronising commands.

A list of the controls and feedback are given in appendix D.2 . The feedback includes the current hexadecimal value for each of the four encoders, the status of the laser track and a latching switch to indicate when the laser has been in track mode.

### 5.04.2 List of available remote operation commands

Appendix D.2 contains a full list of the commands understood by the LaserTrace system, the usage and the syntax. These are summarised in table 5.1.

Of these commands, the ability to gain track is one of the most important functions, since otherwise no data can be obtained. It was found that on numerous occasions track would be lost due to the line of sight to the optic being broken by other equipment or the need for human access. The 'search' or 'search window' commands of table 5.1 were used to scan for a track by effectively selecting a range of possible encoder values and scanning through them until a track could be established. This is further described in appendix D.2.13 and appendix D.2.17 .

**Table 5.1: LaserTrace command list**

| Command | Usage |
|---|---|
| Status | Current state of laser |
| Log Data | Commence logging |
| Find Track | Enters track at a defined position |
| Set Horizontal | Sets the horizontal beam position to defined value |
| Set Vertical | Sets the vertical beam position to defined value |
| Read Horizontal | Reads the current horizontal beam position |
| Read Vertical | Reads the current vertical beam position |
| Read Both | Reads the current horizontal and vertical beam positions |
| Laser On/Off | Switches the laser source on or off |
| Strobe Mode | Allows strobing of commands |
| Position | Puts the laser into position mode |
| Number Format | Sets the number format into decimal or hexadecimal |
| Range | Sets the range (gain of the axis controllers) |
| Search | Searches about a point for a track |
| Track | Enters track mode, if this is possible |
| Search Window | Searches within a defined window to obtain track |
| Read All Data | Reads status and current horizontal and vertical positions |
| Abort | Aborts data logging |

### 5.04.3 LaserTrace control program

The LaserTrace control program is driven through a number of simple menus. This approach was chosen to maximise the possible data throughput. It was decided that no advantage could be gained by using a windows-based approach.

When the program initially runs it provides the choice of resetting the lasers and if this is selected it allows the range of operation to be set. This, in effect, sets the servo-loop gain of each pod. When the program was first written the lasers were automatically reset each time the program ran. However, but it became apparent through usage that this was not desirable. For example, temporarily quitting the control program to copy data files does not require a change in the physical set-up of the system. With the new functionality, the lasers can maintain track even while the program is not running, allowing data to be acquired as soon as the program is restarted.

The main control functions are then provided through the control menu (figure 5.4) and are discussed in the following subsections.

```
Input Choice:
        1 - Gain track
        2 - Read Position
        3 - Drive lasers to specified position
        4 - Status
        5 - Get track about last position.
        C - Continuous encoder readings.
        T - Colect Calibration Data.
        D - Calibration data, without pause.
        V - Collect Validation data.
        r - Reset Laser

        M - Monitor track
        q - Quit

              A - Encoders averaged over 20 samples.
```

**Figure 5.4: LaserTrace control program main menu**

#### 5.04.3.1 Gain track

"Gain track" utilises the 'search window' command of table 5.1 to search within a specified region for the cat's eye. This has pre-defined values which provide a convenient sized window around the centre of the laser pod ranges. The parameters were chosen to allow rapid resumption of track on program start-up or if the optic had moved significantly after track had been lost.

If this menu item is chosen a further menu allows the user to search for track on either or both lasers, or to abort the function if it was chosen by mistake. Having attempted to find track the system reports whether this has been successful.

### 5.04.3.2 Read position

"Read position" is used to read the current encoder values for both pods and display them on the screen.

### 5.04.3.3 Drive lasers to specified position

"Drive lasers to specified position" drives a laser to a stipulated position, which can be specified as absolute encoder values in either decimal or hexadecimal number format. Alternatively, the encoder values can be incremented in either direction using the arrow keys.

### 5.04.3.4 Status

"Status" returns the status of both pods. Information is relayed as to whether the laser is in track mode, on target, has been on target, etc. This information is useful when attempting to set-up the system. A full listing of the possible statuses appears in the error handling function of appendix E.1 .

### 5.04.3.5 Get track about last position

"Get track about last position" performs a similar task to 'Gain track' of section 5.04.3.1. However, this search is carried out focussed on the last encoder values. If track has been lost and the optic has not moved it is more efficient to localise the search about this point. Alternatively, the 'Drive' function (5.04.3.3) can be used to move the laser beams to a known position before a search is attempted. This function returns the status of the track after operation.

### 5.04.3.6 Continuous encoder readings

"Continuous encoder readings" records encoder values continuously. This can be used to capture data dynamically, either with the optic moving, or to monitor the optic while stationary.

### 5.04.3.7 Collect calibration data

"Collect calibration data" calls the routines for capturing calibration data required for solving the transformation of equation 5.1. This function is further explained in section 9.01.2.

From this menu it is possible to call the main menu. This is important for restoring track, or establishing current track status. Quitting from the main menu returns to this menu. Quitting this menu concludes the calibration data collection procedure and returns the user to the main menu.

### 5.04.3.8 Calibration data, without pause

"Calibration data, without pause" was specifically written for the 'Machine Checking Gauge' (MCG) method of calibrating the LaserTrace (chapter 8). Instead of moving the MCG to discrete points for each sphere of data, the readings were 'swept' continuously.

### 5.04.3.9 Collect validation data

"Collect validation data" was written to obtain validation data for the LaserTrace calibration. Cartesian positions are entered and the LaserTrace encoder values captured. This allows comparison of the values.

From this menu it is possible to call the main menu. This is important for restoring track, or establishing current track status. Quitting from the main menu returns to this menu. Quitting this menu concludes acquisition of the validation data and returns the user to the main menu.

### 5.04.3.10 Reset laser

"Reset laser" resets the LaserTrace controller pods and registers, allows the range to be entered and resets the beams to the centre of their operational range.

### 5.04.3.11 Monitor track

"Monitor track" is used to continuously monitor whether the LaserTrace is still in track mode. If track is lost the PC gives a warning. This function can be used to check line-of-sight during a programmed machine move.

#### 5.04.3.12 Quit

"Quit" exits the program.

#### 5.04.3.13 Encoders averaged over a defined number of samples

"Encoders averaged over a defined number of samples" continuously monitors the encoder value, but averages the results over a hard-coded number of samples. This function is used for static measurements and was incorporated to overcome encoder flutter (see section 5.05.2).

## 5.05 Testing

### 5.05.1 Reference standard for testing

To validate any work on the LaserTrace a standard of reference must be established. The work on Cartesian machine error evaluation (chapter 3) enables a traceable standard for a Cartesian machine to be defined.

CMM2 was chosen for testing because it is known to have relatively small errors and is kept in an environmentally controlled room. In addition, the machine is readily available for other tests. It was therefore ideal for validating the LaserTrace against a known machine. Errors determined by calibration data from the LaserTrace can be compared with those from the laser interferometer. Those errors that are attributable to the laser system, rather than the machine under test, can then be identified.

A full calibration was undertaken on the CMM (section 4.04), giving the simulation results included as Appendix C. The results show that the CMM has a volumetric accuracy of 18μm. Such an accuracy is sufficient when required to validate the LaserTrace with its expected performance being no better than 100μm.

### 5.05.2 Encoder flutter

At each target position there should be a unique combination of the four encoders. However, this was not found to be the case since the encoder values were seen to fluctuate with the optic stationary.

A possible cause of encoder changes would be if the relative position and orientation of the pods does not remain constant throughout the test. This can only be achieved by providing a solid base for each pod. At the collaborating establishment solid concrete

plinths were used for each pod, however this renders the system non-portable. Tripods of sufficient stability were therefore purchased to damp any vibration. Although this reduced the fluctuations when compared to mounting the pods on stools there remained a residual fluctuation. This was not eliminated when mounting the pods on the granite bed of the CMM. It therefore became apparent that some of the fluctuations derived from a different source.

It was surmised that the change in readings was related to the control loop of the tracking system. Tests were carried out with the optic held stationary at varying displacements from the pods to determine if this affected the amount of flutter.

Figure 5.5, figure 5.6 and figure 5.7 give the change in the number of encoder counts against number of samples for different optic positions. The shape of the graphs shows that an average value for the encoder value would give a good representation for the line of sight. It is usual practice for measurement lasers to operate using a 'short term average' because of effects such as air blowing the beam or vibration of the optic. Such averaging has been applied to the LaserTrace for static testing.

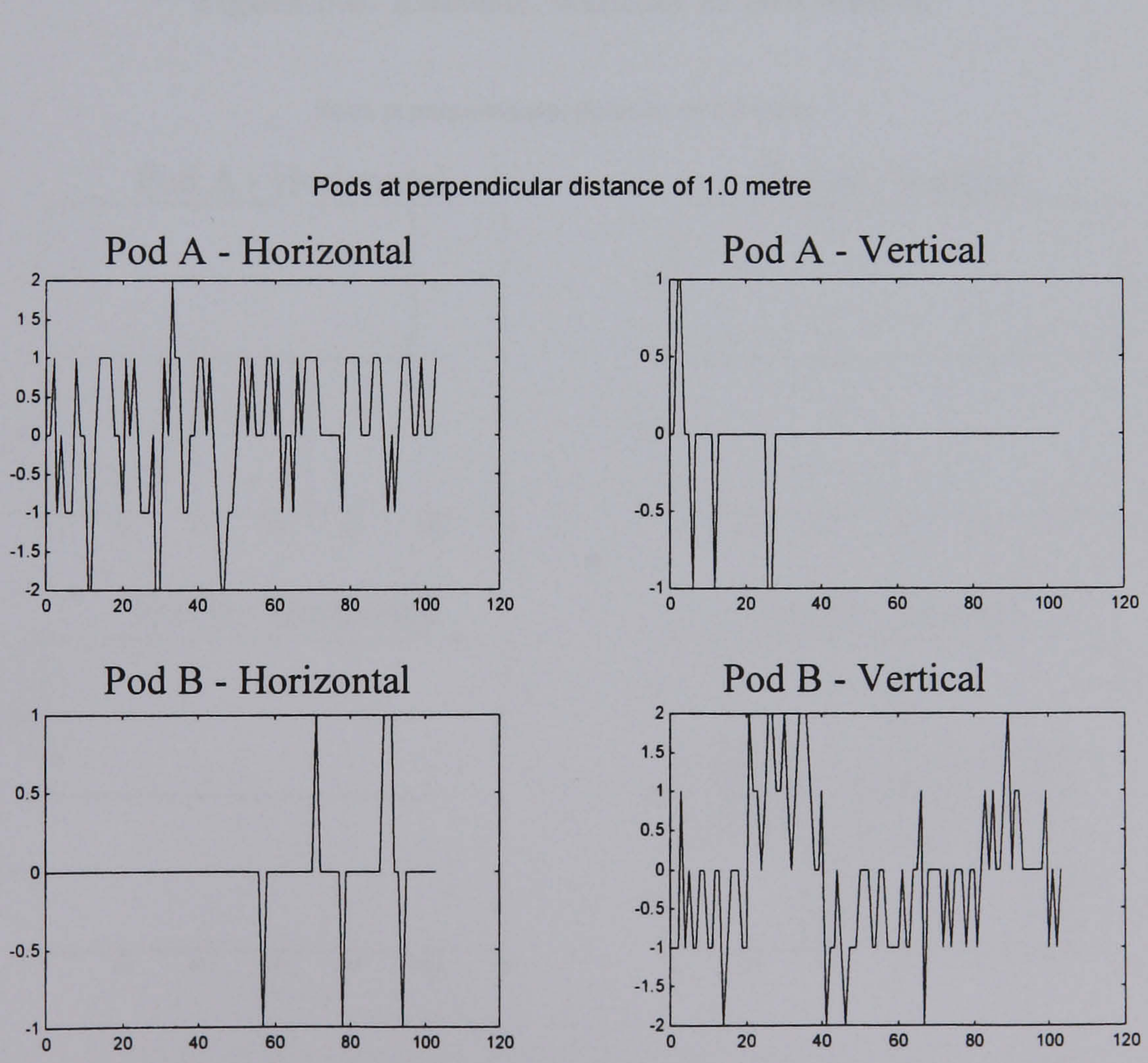


**Figure 5.5: Encoder stability at one metre**

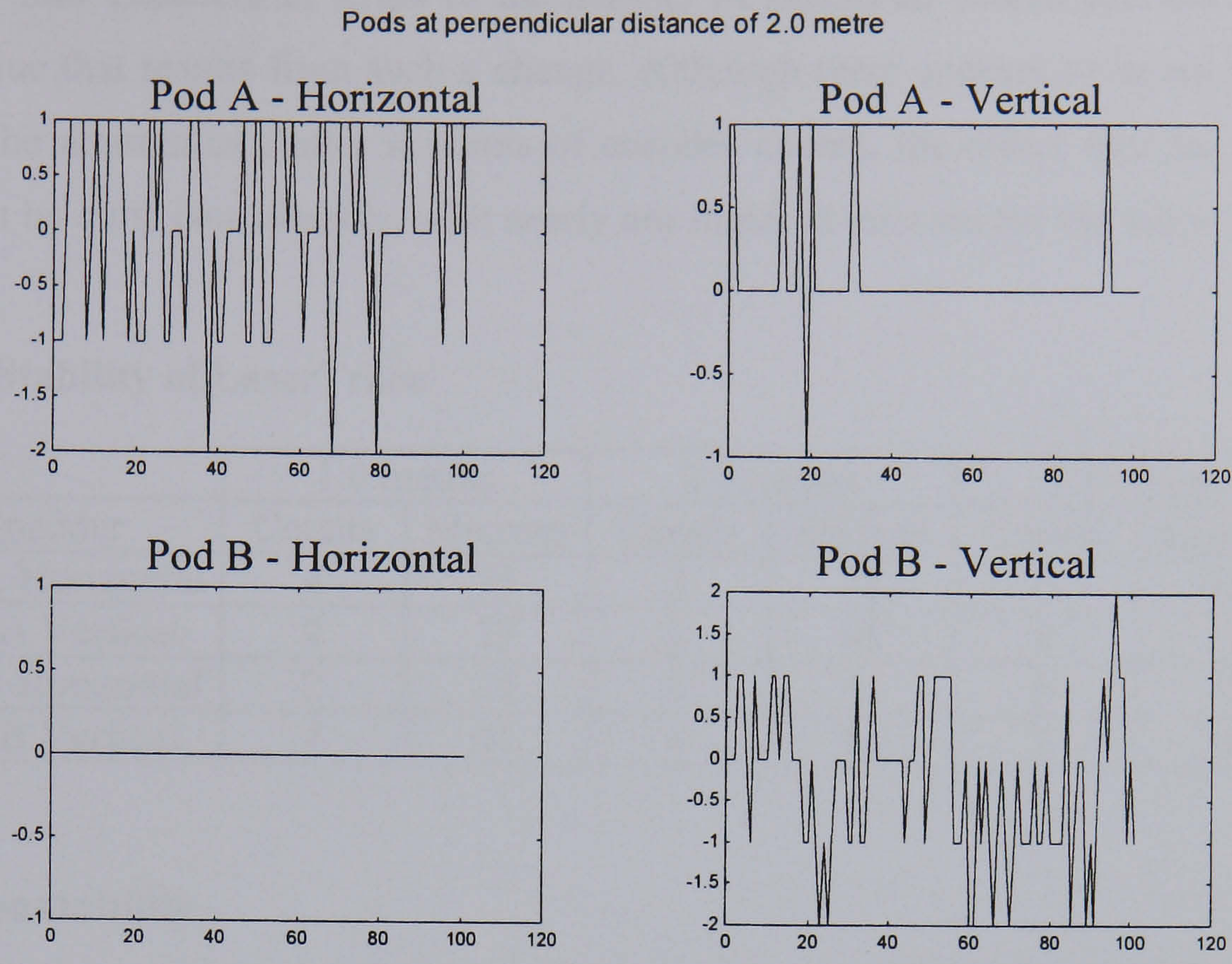


**Figure 5.6: Encoder stability at two metres**

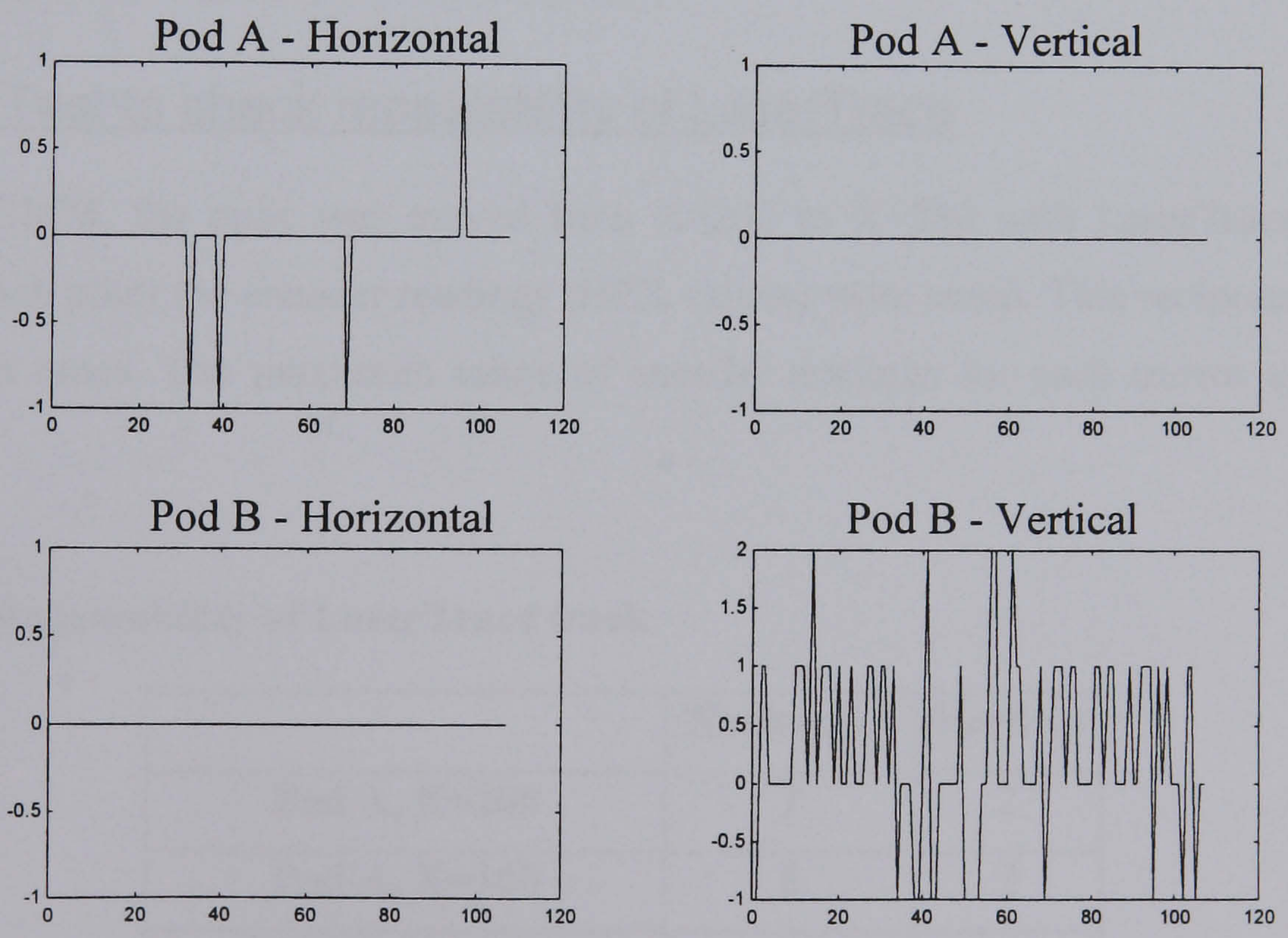


**Figure 5.7: Encoder stability at 2.8 metres**

Table 5.2 summarises the results in terms of the range of encoder values at different displacements from the laser pods for each of the pods. It shows the amount of flutter for

each of the four encoders in terms of the number of measured counts and the calculated position value that results from such a change. Although there appears to be no significant change in the amount of flutter in terms of encoder counts, the effect this has at greater distance can be quite considerable, with nearly one hundred microns for the worst case.

**Table 5.2: Stability of LaserTrace**

| | 1.0 metres | | 2.0 metres | | 2.8 metres | |
|---|---|---|---|---|---|---|
| Encoder | Counts | Microns | Counts | Microns | Counts | Microns |
| Pod A Horizontal | 4 | 55 | 3 | 72 | 2 | 66 |
| Pod A Vertical | 2 | 27 | 2 | 48 | 0 | 0 |
| Pod B Horizontal | 2 | 27 | 0 | 0 | 0 | 0 |
| Pod B Vertical | 4 | 55 | 4 | 96 | 3 | 99 |

### 5.05.3 Repeatability

Critical to the success of any measurement device is the repeatability of the readings that can be acquired. The two main repeatability factors that required evaluation were the repeatability with which the beam found the centre of the optic and the repeatability of the measured angles for a given position of the optic.

#### 5.05.3.1 Test to check repeatability of LaserTrace

Using the CMM, the optic was moved from X=200 to X=300 with LaserTrace in track mode. At each point the encoder readings (HEX values) were noted. This reciprocation was repeated ten times. The maximum range of encoder readings for each mirror appears as table 5.3.

**Table 5.3: Repeatability of LaserTrace track**

| | **Horizontal** | **Vertical** |
|---|---|---|
| **Pod A, X=200** | 7 | 2 |
| **Pod A, X=300** | 8 | 2 |
| **Pod B, X=200** | 0 | 1 |
| **Pod B, X=300** | 0 | 2 |

It can be seen the greatest difference occurs within the horizontal mirror of pod A. The configuration of the lasers meant that this mirror had the greatest change during the test. This mirror also displayed the greatest amount of flutter in the tests of section 5.05.2.

### 5.05.3.2 Repeatability of track

With the optic stationary, the LaserTrace was repeatedly commanded to find track, the encoder values were noted and the beam broken. The repeatability of attaining track was excellent, being a maximum of only two counts in variation after averaging.

## 5.06 Calibration

The previous tests did not produce direct three-dimensional measurement since the conversion from angular data had not been established. The transformation between local and world data is only possible by calibration. This can be achieved in three stages. The first level is that of the system components. Resolver offset and mirror range are calibrated by experimentation immediately after manufacture. The second level is to calibrate the relative position of the optical elements within each local unit.

An indirect method is used by Mayer, *et. al.* [89], rather than trying to measure the relative location of the optical elements directly. A single retroreflector is moved along a known path to known positions on this path. The relative position between the path and the subsystem is not known. The path is generated by a precision linear slideway with an accurate linear encoder (specification not given). The position of the lines of sight are then calculated assuming no assembly errors. The model is then modified using numerical optimisation techniques to reduce any error between calculated and known position on the path.

Mayer, *et. al.* [90] performs the calibration of the photo-detector with the target. This ensures that any optical aberrations in the target optics are accounted for in the detector response model. A ten-micron resolution x-y translation stage is used to move the target at known displacement while tracking is non-operational. The detector outputs are monitored and its model parameters adjusted according to the known target offsets. This test is performed at selected target distances from the sub-system in order to account for the effect of beam diameter variation and returned beam divergence due to aberrations in the target.

Mayer's determination of the relative position and orientation of the two sub-systems at a test site uses an indirect method. It involves the measurement of two targets at

a calibrated displacement in addition to a set of random and unknown 3D positions. All six degrees of freedom are determined from this information. The bar is made of carbon fibre which has a temperature expansion coefficient of $-0.7 \times 10^{-6}/^{\circ}C$, thus providing good position stability.

Mayer claims that an overall calibration of the present system reveals a repeatability of better than ± 0.1mm in x, y, z directions for one standard deviation based on 30 tests. The tests were repeated at twenty nominal positions along a straight-line precision slideway equipped with a linear optical encoder. The total distance between the positions was 800mm.

## 5.07 Summary

The LaserTrace system has been investigated and PC-based control software has been written to exploit the control available. This has allowed testing of the system for repeatability of readings for given positions of the target optic and for regaining track. In both cases, the angular encoders provided results repeatable to two counts. However, it has been found that the encoders fluctuate while monitoring a static target. The effect of this flutter has been calculated to be up to 100μm at the extremity of the working volume (2.8m from the pod). The distribution of the measurement data indicates that an average reading will significantly reduce the variation.

Some methods of calibrating the LaserTrace system to find the matrix coefficients of **equation 5.1** have been researched. These involve additional hardware and time-consuming experimentation. The following chapter describes an attempt to produce a simple, efficient method of calibration requiring no additional hardware.

# Chapter 6 Photogrammetry Calibration Of LaserTrace

## 6.01 Introduction

The investigation of chapter 5 has indicated the level of inconsistency in the LaserTrace encoders. It has been found that each encoder can vary by up to four counts on a stationary target. With short-term averaging, the uncertainty for each encoder falls to ±1 encoder reading, translating to ±33μm at the extremity of the test machine. This provides an indication of the possible performance achievable from the LaserTrace system, although the final repeatability and resolution must be considered as a combination of the performance of all four encoders.

The data in encoder values is not directly meaningful for measuring a machine. It is therefore necessary to model the system and calibrate the model parameters in order to convert encoder counts to a three-dimensional position.

Mayer's technique (section 5.06) is time consuming, which is a large drawback when considering that a calibration of the system must take place each time the laser pods are moved. A more efficient method of system calibration has been sought. The remainder of this chapter describes an attempt to use the principles of photogrammetry to achieve this goal.

# 6.02 Theory of photogrammetry

## 6.02.1 Principles of perspective projection

The photogrammetry technique is used to determine the position of an object by measurement of images rather than by direct distance measurement. The particular principle of interest for this project is that of 'close range photogrammetry', which is used to measure objects whose extent is less than 100m.

The LaserTrace system is similar in configuration to a pinhole camera, which has no focussing, and so no lens distortion. Some correction needs to be made for the deflection due to refraction when the laser beam passes through the pod window, but the basic concept could be applied.

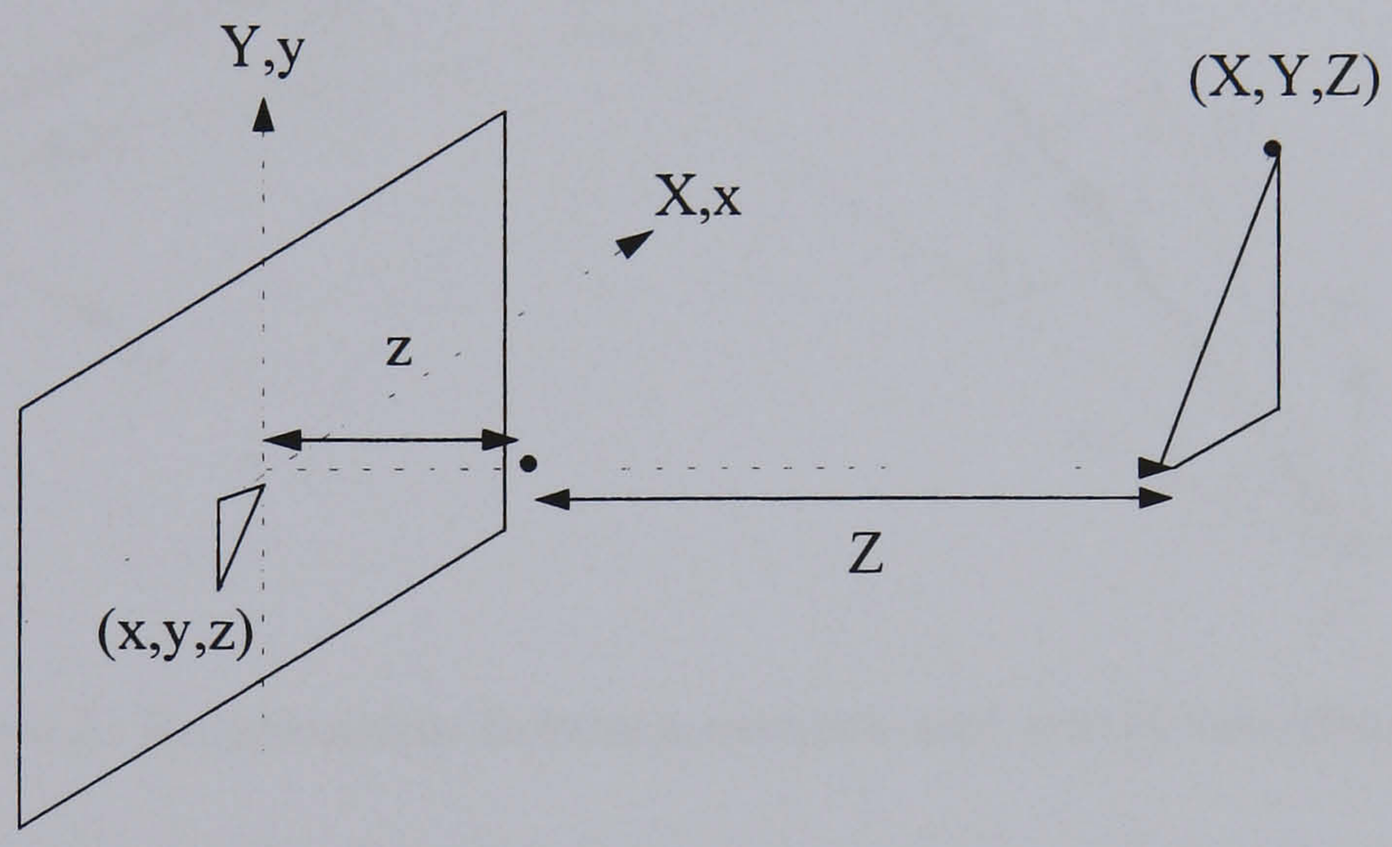


**Figure 6.1: Principle of perspective projection**

Figure 6.1 show the principle of perspective projection which uses similar triangles to determine world position from measured data. Equation 6.1 defines the relationship between world and camera coordinates using the above principle:

$$\left.\begin{aligned} \frac{x}{z} &= \frac{X}{Z} \\ \frac{y}{z} &= \frac{Y}{Z} \end{aligned}\right\} \qquad \text{Equation 6.1}$$

Since z is a known, fixed length this leaves three unknown values and two equations. A single camera can only be used to take measurements in a single plane. The combination of two or more cameras allows measurements in three dimensional space.

Figure 6.2 shows that a single point, P, will have different coordinates for each camera. The position measured by each camera has to be transformed to a single position reading in a common coordinate frame. This is achieved by performing rotation and translation of the data from one of the cameras in order to bring it to the same frame as the other.

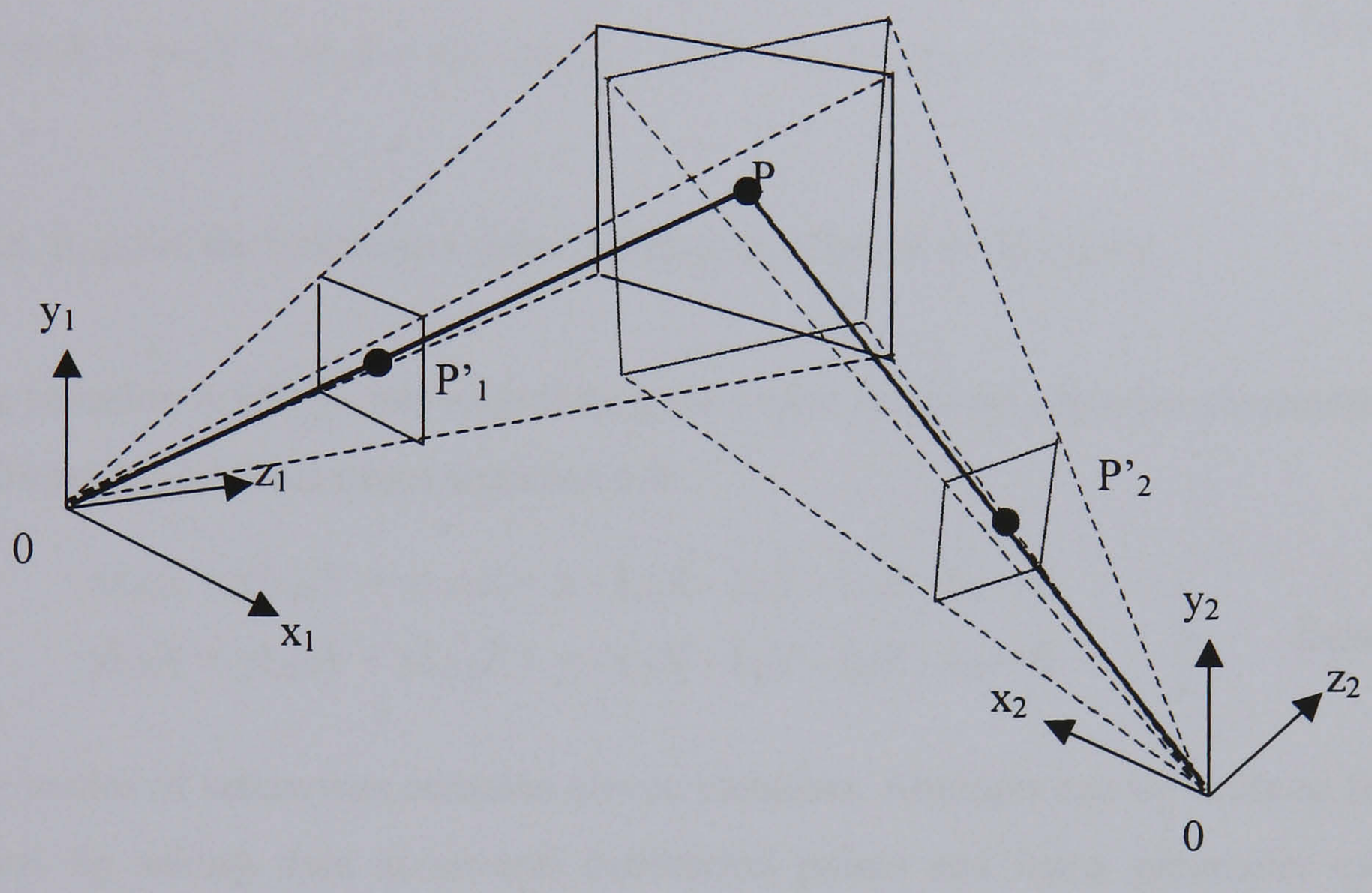


**Figure 6.2: Relationship between camera and world coordinates**

In practice the transformation is made using a matrix which rotates about the x, y and z-axes in order by $\alpha$, $\beta$, and $\gamma$. The matrix is given by equation 6.2.

$$R_{\alpha,\beta,\gamma} = \begin{pmatrix} r_{11} & r_{12} & r_{13} \\ r_{21} & r_{22} & r_{23} \\ r_{31} & r_{32} & r_{33} \end{pmatrix} \qquad \text{Equation 6.2}$$

Where:

$r_{11} = \cos\alpha.\cos\beta$ $\quad r_{12} = \cos\alpha.\sin\beta.\sin\gamma - \sin\alpha.\cos\gamma$ $\quad r_{13} = \cos\alpha.\sin\beta.\cos\gamma + \sin\alpha.\sin\gamma$

$r_{21} = \sin\alpha.\cos\beta$ $\quad r_{22} = \sin\alpha.\sin\beta.\sin\gamma + \cos\alpha.\cos\gamma$ $\quad r_{23} = \sin\alpha.\sin\beta.\cos\gamma - \cos\alpha.\sin\gamma$

$r_{31} = -\sin\beta$ $\quad r_{32} = \cos\beta.\sin\gamma$ $\quad r_{33} = \cos\beta.\cos\gamma$

### 6.02.2 Direct linear transformations

The approach used to calibrate the lasers is based upon the above theory and that of the "Direct Linear Transform" (DLT) as proposed by Abdel-Aziz *et. al.*[91]. This attempts to linearise the camera equations by combining the unknown parameters.

Equation 6.1 and equation 6.2 combine to give the following non-linear equation 6.3:

$$\left.\begin{aligned} xr_{31}X + xr_{32}Y + xr_{10}Z + xp_z - zr_{11}X - zr_{12}Y - zr_{13}Z - zp_x = 0 \\ yr_{31}X + yr_{10}Y + yr_{10}Z + yp_z - zr_{21}X - zr_{22}Y - zr_{23}Z - zp_y = 0 \end{aligned}\right\} \quad \text{Equation 6.3}$$

Where $\{p_x\ p_y\ p_z)$ is the unknown vector defining translation to the origin.

Dividing equation 6.3 by $p_z$ and substituting for a new vector of unknown parameters, L, we get the Direct Linear Transform equation 6.4:

$$\left.\begin{aligned} xL_9X + xL_{10}Y + xL_{11}Z + x - L_1X - L_2Y - L_3Z - L_4 = 0 \\ yL_9X + yL_{10}Y + yL_{11}Z + y - L_5X - L_6Y - L_7Z - L_8 = 0 \end{aligned}\right\} \quad \text{Equation 6.4}$$

The new vector of unknowns contains eleven elements. Attempts can be made to find these parameters by taking data at several calibration points and using parameter estimation techniques. Theoretically, six data points are required since two equations are given at each point. In practice, better results may be obtained by taking a larger number of points and using a least-squares method to select the best-fit parameters.

## 6.03 Application of photogrammetry to LaserTrace

A DOS-based computer program was designed and written in Borland C++ to perform the analysis on-line by taking encoder readings directly from the LaserTrace controller and converting them to world coordinate measurements.

The program is designed to perform a system calibration function where data points are recorded and loaded into the DLT equation 6.4. In this application x and y are determined from the tangent of the measured angles and the fixed distance, z. The L matrix of estimated parameters is then used to calculate positions from encoder readings throughout the working volume.

### 6.03.1 Accuracy tests

Calibration data was taken to verify the photogrammetry method. The optic was then placed at several points within the working volume of the CMM and measurement from the LaserTrace compared with the command position of the CMM.

Figure 6.3 shows typical results from this calibration method. The results were disappointing with the error in each axis being as much as 5mm within a one metre cube.

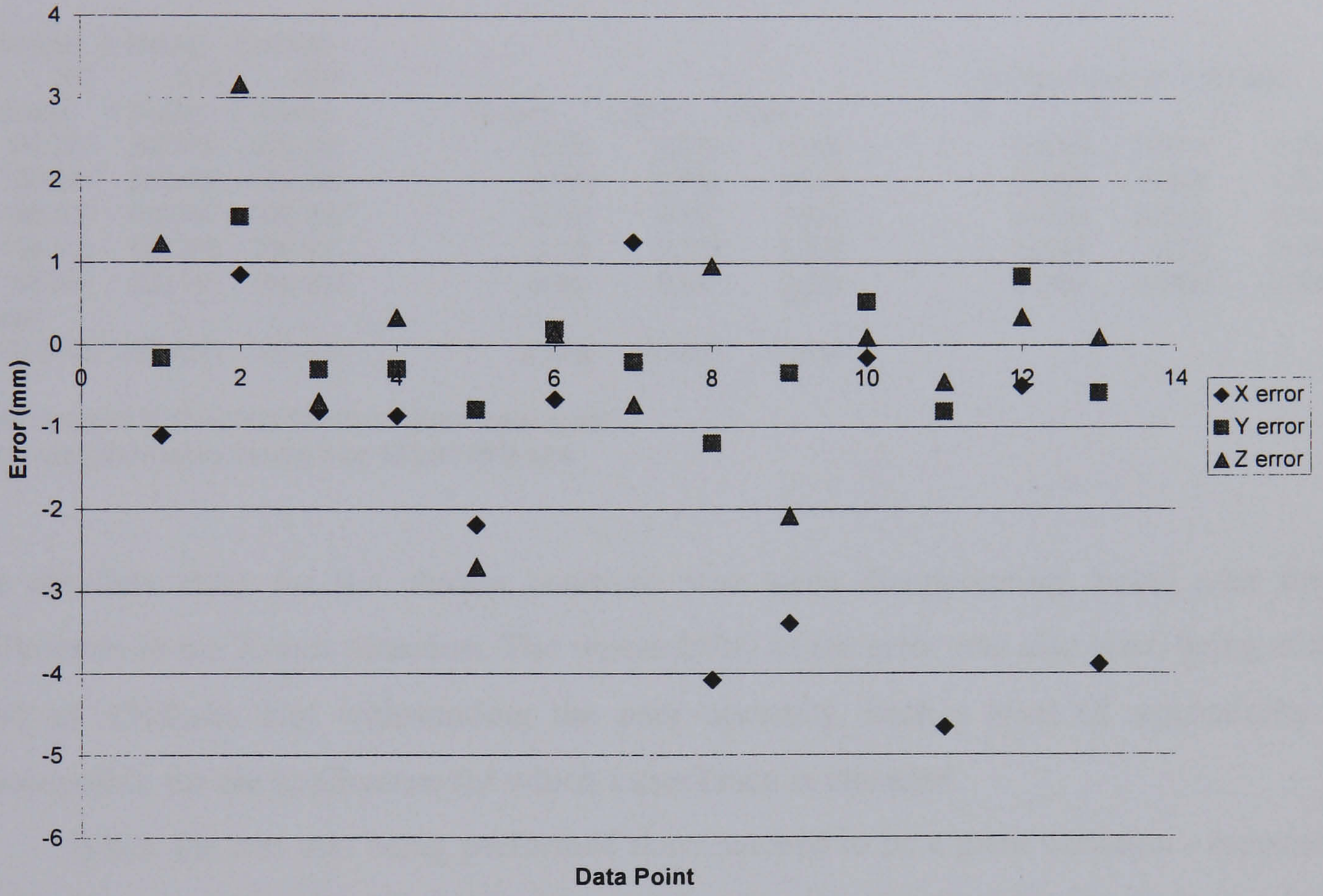


**Figure 6.3: Results of photogrammetry calibration**

Tests were made to determine the repeatability of the position data derived from this calibration technique. The optic was run on the CMM exclusively in the X direction from 200mm to 300mm. A single measurement was taken at each point and compared to the commanded position. This was repeated to provide repeatability results (table 6.1).

## Table 6.1: Repeatability on X-axis

| X (actual) | Y (actual) | Z (actual) | | | | | | |
|---|---|---|---|---|---|---|---|---|
| 300 | 500 | -300 | | | | Deviation of error from mean | | |
| X (trace) | Y (Trace) | Z (Trace) | X (err) | Y (err) | Z (err) | X | Y | Z |
| 298.813 | 499.792 | -299.046 | -1.187 | -0.208 | 0.954 | 0.1826 | 0.0352 | 0.0052 |
| 299.043 | 499.836 | -299.054 | -0.957 | -0.164 | 0.946 | -0.0474 | -0.0088 | 0.0132 |
| 298.926 | 499.814 | -299.02 | -1.074 | -0.186 | 0.98 | 0.0696 | 0.0132 | -0.0208 |
| 298.984 | 499.825 | -299.042 | -1.016 | -0.175 | 0.958 | 0.0116 | 0.0022 | 0.0012 |
| 299.212 | 499.869 | -299.042 | -0.788 | -0.131 | 0.958 | -0.2164 | -0.0418 | 0.0012 |
| Mean | | | | | | | | |
| 298.9956 | 499.8272 | -299.041 | -1.0044 | -0.1728 | 0.9592 | | | |
| X (actual) | Y (actual) | Z (actual) | | | | | | |
| 200 | 500 | -300 | | | | Deviation of error from mean | | |
| X (trace) | Y (Trace) | Z (Trace) | X (err) | Y (err) | Z (err) | X | Y | Z |
| 197.277 | 500.272 | -299.391 | -2.723 | 0.272 | 0.609 | -0.4028 | -0.0814 | 0.005 |
| 196.914 | 500.199 | -299.358 | -3.086 | 0.199 | 0.642 | -0.0398 | -0.0084 | -0.028 |
| 196.709 | 500.157 | -299.398 | -3.291 | 0.157 | 0.602 | 0.1652 | 0.0336 | 0.012 |
| 196.812 | 500.178 | -299.391 | -3.188 | 0.178 | 0.609 | 0.0622 | 0.0126 | 0.005 |
| 196.659 | 500.147 | -299.392 | -3.341 | 0.147 | 0.608 | 0.2152 | 0.0436 | 0.006 |
| Mean | | | | | | | | |
| 196.8742 | 500.1906 | -299.386 | -3.1258 | 0.1906 | 0.614 | | | |

Test designed to show repeatability of Laser Trace system.
Test was peformed by varying X by 100mm for 5 runs.

The absolute error for the chosen positions was again disappointing, being over three millimetres in the X-axis direction. The repeatability of the error was also poor, being of the order of ±300μm. Not withstanding the poor accuracy, such a level of repeatability is unacceptable for the application for which LaserTrace is intended.

While the test was being performed there seemed to be a great variation - especially in the X-axis. A further test was performed by running the CMM exclusively in the Z direction between 200cm and 300cm. A single measurement was taken at each point and compared to the commanded position.

It can be seen (table 6.2) that the X-axis repeatability is of a similar magnitude to the previous test, although the overall error range has improved. The reason for this is that the X-axis remains stationary.

**Table 6.2: Repeatability of Z-axis**

| X (actual) | Y (actual) | Z (actual) | | | | | | |
|---|---|---|---|---|---|---|---|---|
| 300 | 500 | -300 | | | | Deviation of error from mean | | |
| X (trace) | Y (Trace) | Z (Trace) | X (err) | Y (err) | Z (err) | X | Y | Z |
| 298.928 | 499.814 | -299.036 | -1.072 | -0.186 | 0.964 | 0.0095 | 0.0035 | 0.00775 |
| 299.103 | 499.848 | -299.019 | -0.897 | -0.152 | 0.981 | -0.1655 | -0.0305 | -0.00925 |
| 298.847 | 499.804 | -299.055 | -1.153 | -0.196 | 0.945 | 0.0905 | 0.0135 | 0.02675 |
| 298.872 | 499.804 | -299.003 | -1.128 | -0.196 | 0.997 | 0.0655 | 0.0135 | -0.02525 |
| Mean | | | | | | | | |
| 298.9375 | 499.8175 | -299.028 | -1.0625 | -0.1825 | 0.97175 | | | |
| X (actual) | Y (actual) | Z (actual) | | | | | | |
| 300 | 500 | -200 | | | | Deviation of error from mean | | |
| X (trace) | Y (Trace) | Z (Trace) | X (err) | Y (err) | Z (err) | X | Y | Z |
| 298.398 | 499.867 | -198.354 | -1.602 | -0.133 | 1.646 | 0.37425 | 0.07725 | 0.051 |
| 298.571 | 499.901 | -198.313 | -1.429 | -0.099 | 1.687 | 0.20125 | 0.04325 | 0.01 |
| 299.253 | 500.032 | -198.277 | -0.747 | 0.032 | 1.723 | -0.48075 | -0.08775 | -0.026 |
| 298.867 | 499.977 | -198.268 | -1.133 | -0.023 | 1.732 | -0.09475 | -0.03275 | -0.035 |
| Mean | | | | | | | | |
| 298.7723 | 499.9443 | -198.303 | -1.22775 | -0.05575 | 1.697 | | | |

Test designed to show repeatability of Laser Trace system.
Test was peformed by varying Z by 100mm for 5 runs.

## 6.04 Summary

The results obtained from this method were not as accurate as expected. It is known that the model did not fully compensate for beam deflection, but the worst errors appeared to derive from noise in the data. Figure 6.4 shows a variation in calculated X-coordinate of 1.25mm when the tracked optic remained stationary and no averaging of encoder value is used. This calibration method appears very sensitive to the encoder fluctuations due to the limited number of samples used in calibrating the system. This resulted in repeatability worse than 300μm for a given measurement point – an unacceptable deviation.

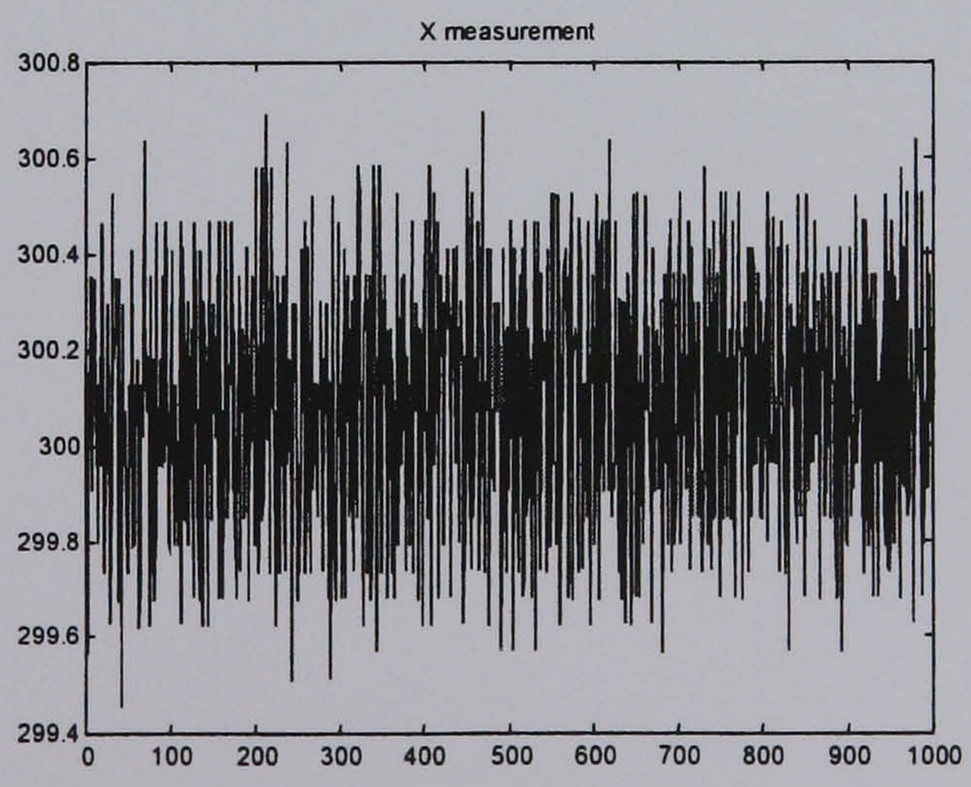


**Figure 6.4: Value of X-coordinate calculated from LaserTrace data**

Due to the sensitivity of the photogrammetry method to its calibration data, it became apparent that a new approach was required. The advantages of adopting a simplified approach were far outweighed by the inaccuracies that the approximations produced. A new model and calibration strategy, based upon a more accurate model of the pods has been devised. The building of the model is described in the following chapter, with the method by which it can be exploited described in chapter 8. Chapter 9 then validates this work, and so achieves objective 1.14 (d).

# Chapter 7 Model of LaserTrace from First Principles

The results of the previous chapter indicate that a more sophisticated method of data capture and analysis will be required to solve the problem of calibrating the LaserTrace. However, if this is only achieved by time-consuming methods requiring complex dedicated hardware then little advantage will be gained. By modelling the system from first principles, it will be possible to evaluate the requirements of any measurement system for finding the transformation parameters.

## 7.01 Calculation of target position from mirror angles

This derivation of the models assumes that a local Cartesian coordinate frame can be defined for each of the LaserTrace pods. The axes of rotation of the two mirrors and their mutual normal define this frame (figure 7.1). The angles of rotation, $\theta$ and $\phi$, are given as outputs by the LaserTrace controller.

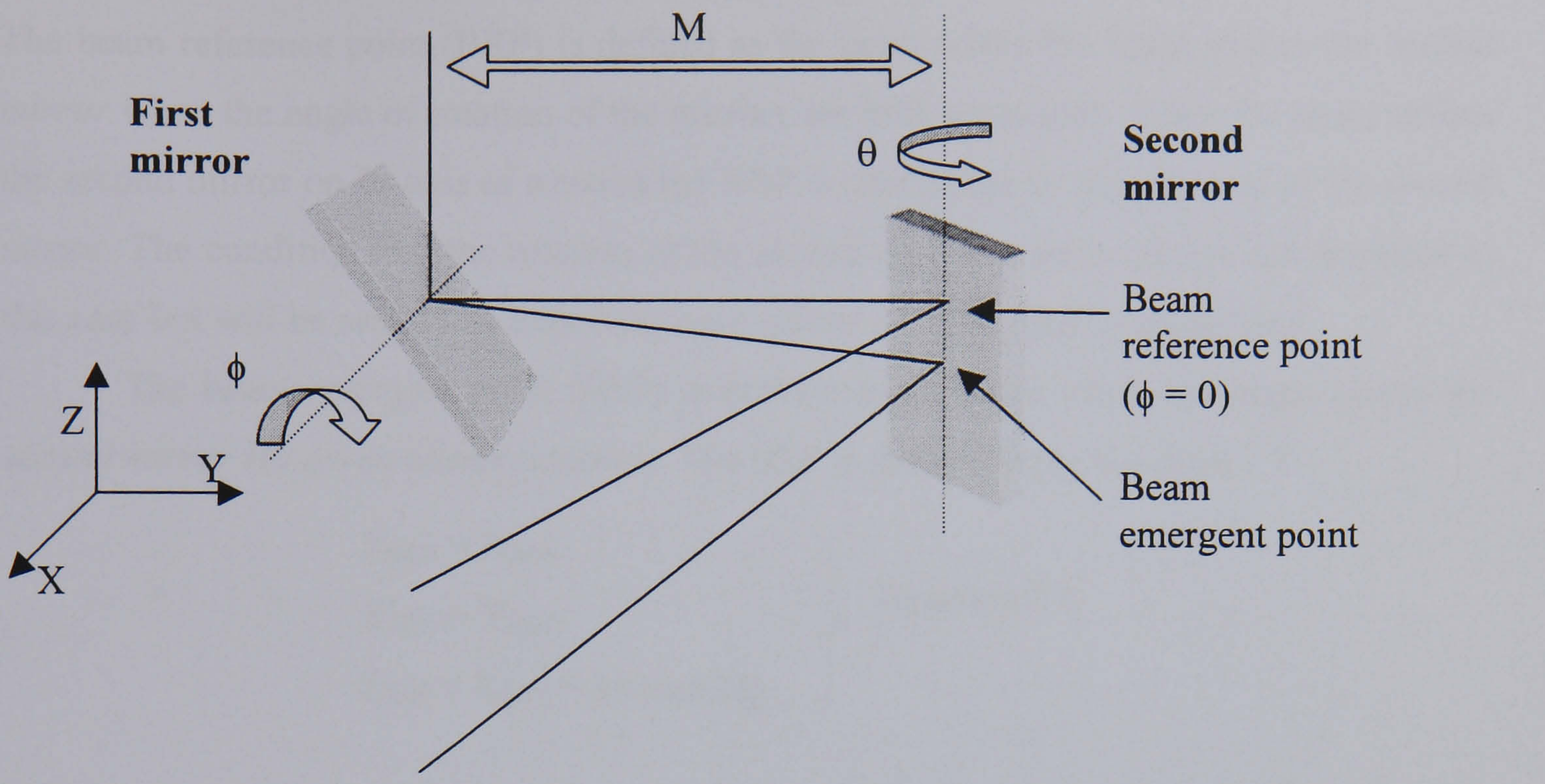


**Figure 7.1: LaserTrace internal mirror configuration**

### 7.01.1 Determination of beam emergent point

Initially assume the local coordinate frame of each pod is aligned with the world Cartesian frame. The frame is defined such that the rotational axis of the first mirror is parallel to the world X-axis, that of the second mirror is parallel to the world Z-axis and the mutual normal of the axes of rotation of mirrors is parallel to the world y-axis (figure 7.1 and figure 7.2).

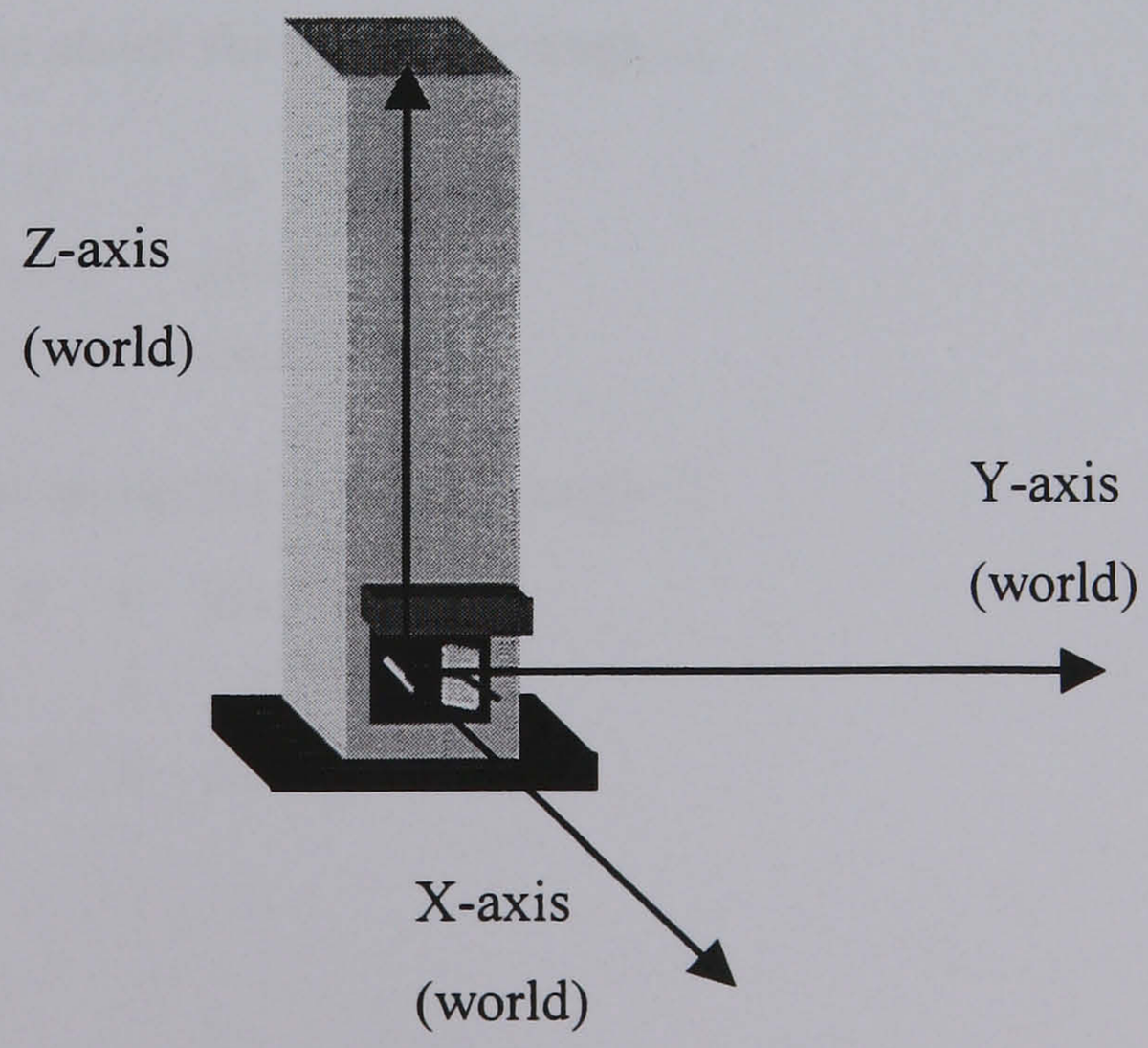


**Figure 7.2: Pod aligned with world axes**

The beam reference point (BRP) is defined as the point where the beam strikes the *second mirror* when the angle of rotation of the mirrors are both set to zero. Since the beam strikes the second mirror on its axis of rotation the BRP is unaffected by any rotation of the second mirror. The condition that the rotation of the second mirror is set to zero is not essential in this case but will be seen to be important once mirror misalignment is introduced.

The beam emergent point (BEP) is defined as the point where the beam leaves the *second mirror* for given mirror rotations. The BEP is defined using equation 7.1:

$$\left.\begin{aligned} X_{BEP} &= X_{BRP} \\ Y_{BEP} &= Y_{BRP} \\ Z_{BEP} &= Z_{BRP} + M\times\tan(2\phi) \end{aligned}\right\} \text{Equation 7.1}$$

These equations are a function of four quantities: the X, Y & Z coordinates of the reference point and the mirror separation (M). The emergent point changes for varying values of the vertical rotation, $\phi$, but is unaffected by the horizontal rotation, $\theta$. M is a fixed quantity, determined during the manufacture of the pod. The reference point is fixed for each set-up of the dual LaserTrace system, and only varies when a pod is moved.

These calculations are subject to rotation since, in general, the local coordinate frame of the pods will not be coincident with the world Cartesian frame. This transformation requires the standard rotation matrices associated with rotation about the major axes, using the right-hand rule.

**Rotation of a point about the X axis by angle $\alpha$**

$$R_\alpha = \begin{bmatrix} 1 & 0 & 0 \\ 0 & \cos\alpha & -\sin\alpha \\ 0 & \sin\alpha & \cos\alpha \end{bmatrix} \qquad \text{Equation 7.2}$$

**Rotation of a point about the Y axis by angle $\beta$**

$$R_\beta = \begin{bmatrix} \cos\beta & 0 & \sin\beta \\ 0 & 1 & 0 \\ -\sin\beta & 0 & \cos\beta \end{bmatrix} \qquad \text{Equation 7.3}$$

**Rotation of a point about the Z axis by angle γ**

$$R_\chi = \begin{bmatrix} \cos\gamma & -\sin\gamma & 0 \\ \sin\gamma & \cos\gamma & 0 \\ 0 & 0 & 1 \end{bmatrix} \qquad \text{Equation 7.4}$$

These rotations are performed about the reference point, so they have the effect of moving the emergent point but have no effect upon the reference point. The rotations introduce three further *fixed* parameters affecting the calculation of the emergent point: rotation about the X, Y and Z axes. Because the lasers are likely to be turned towards the centre of the volume, the rotation about Z is likely to be a major adjustment. Usual practice would be to set the lasers reasonably level, so the rotations about X and Y are likely to be minor corrections.

### 7.01.2 Determination of beam intersection

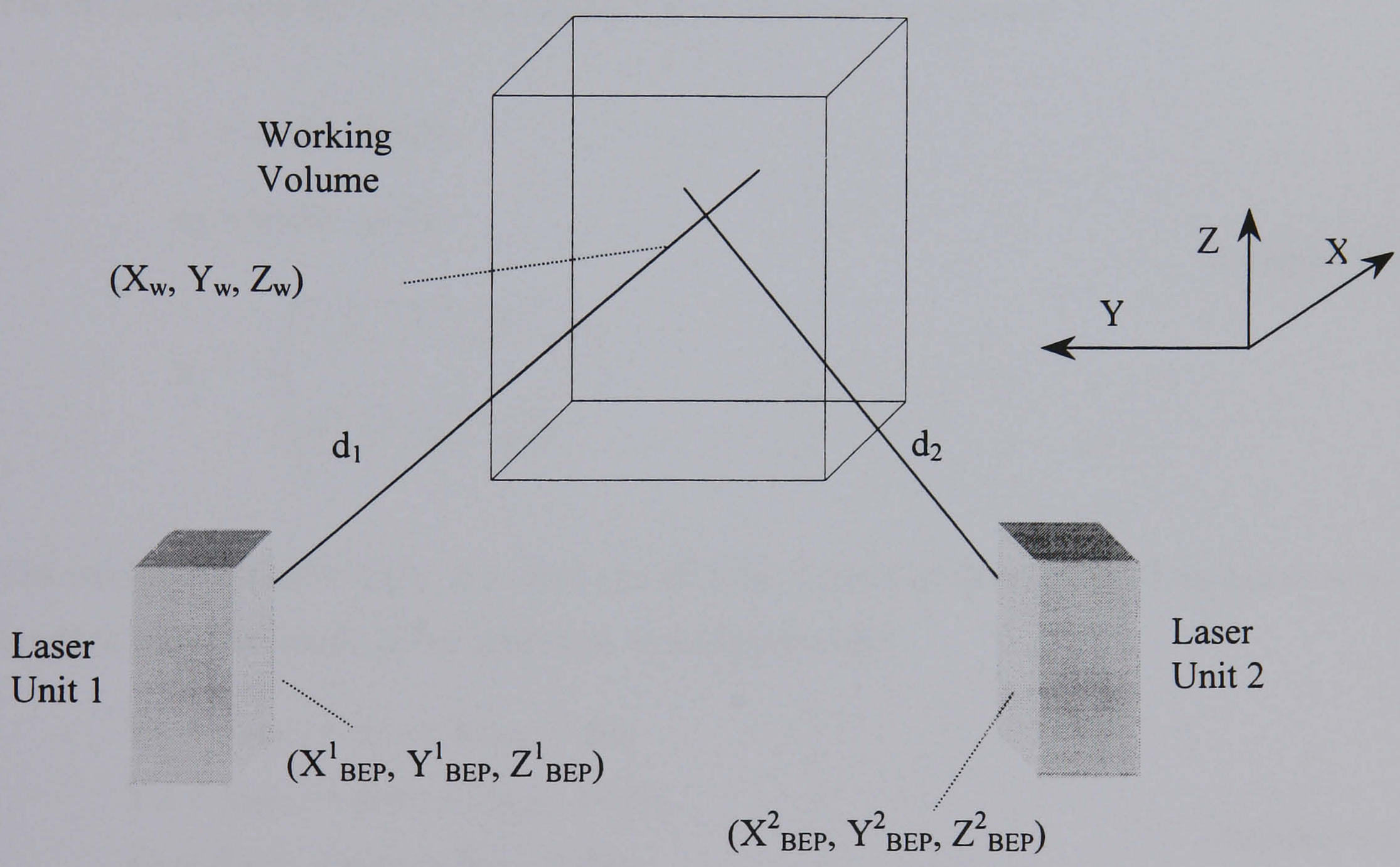


**Figure 7.3: Dual LaserTrace system**

The target position at any given moment in time is defined as the point where the laser beams intersect. The methodology adopted to determine the point of intersection utilises direction cosines. The principle is that for a vector $\vec{P} = (Px \quad Py \quad Pz)$ the direction cosines are defined by equation 7.5.

$$\left.\begin{aligned} \cos(\alpha) &= \frac{Px}{\| \vec{P} \|} \\ \cos(\beta) &= \frac{Py}{\| \vec{P} \|} \\ \cos(\partial) &= \frac{Pz}{\| \vec{P} \|} \end{aligned}\right\} \quad \text{Equation 7.5}$$

Also, we have

$$\cos^2(\alpha) + \cos^2(\beta) + \cos^2(\partial) = 1 \quad \text{Equation 7.6}$$

For the LaserTrace the direction cosines, l, m, n are given by equation 7.7.

$$\left.\begin{aligned} l &= \cos 2\phi . \cos 2\theta \\ m &= \sin 2\theta . \cos 2\phi \\ n &= \begin{cases} \sqrt{1 - l^2 - m^2} & \phi > 0 \\ -\sqrt{1 - l^2 - m^2} & \phi < 0 \end{cases} \end{aligned}\right\} \quad \text{Equation 7.7}$$

The world coordinates (Xw, Yw, Zw) can then be defined in terms of the direction cosines for each pod, the length of the beam and its emergent point.

$$\left.\begin{aligned} X_W &= X_{BEP,1} + d_1 l_1 = X_{BEP,2} + d_2 l_2 \\ Y_W &= Y_{BEP,1} + d_1 m_1 = Y_{BEP,2} + d_2 m_2 \\ Z_W &= Z_{BEP,1} + d_1 n_1 = Z_{BEP,2} + d_2 n_2 \end{aligned}\right\} \quad \text{Equation 7.8}$$

These can be rearranged to produce equations relating the difference in emergent points in terms of the direction cosines:

$$\left.\begin{aligned} l_1 d_1 - l_2 d_2 &= {}^2X_{BEP} - {}^1X_{BEP} \equiv dX_{BEP} \\ m_1 d_1 - m_2 d_2 &= {}^2Y_{BEP} - {}^1Y_{BEP} \equiv dY_{BEP} \\ n_1 d_1 - n_2 d_2 &= {}^2Z_{BEP} - {}^1Z_{BEP} \equiv dZ_{BEP} \end{aligned}\right\} \quad \text{Equation 7.9}$$

The above direction cosines must be rotated about z, y and x, in that order, to resolve them to the world coordinate frame. The l, m and n which are used in the following discussion are these corrected values.

Equation 7.9 can be represented in matrix format for manipulation purposes:

$$\begin{pmatrix} l_1 & -l_2 \\ m_1 & -m_2 \\ n_1 & -n_2 \end{pmatrix} \begin{pmatrix} d_1 \\ d_2 \end{pmatrix} = \begin{pmatrix} dX_{BEP} \\ dY_{BEP} \\ dZ_{BEP} \end{pmatrix} \equiv A\vec{d} = \vec{x} \qquad \text{Equation 7.10}$$

Rewrite equation 7.10 in the form of equation 7.11 and solve for the unknown vector, $\vec{d}$, using a least squares method.

$$\vec{d} = \left(A^T A\right)^{-1} A^T \vec{x} \qquad \text{Equation 7.11}$$

Measurement data input in equation 7.9 will then yield two sets of calculated world coordinates. These coordinates do not agree due to measurement and computational resolution. The pair of values comprise the ends of the normal common to each beam (figure 7.4), with the mean of this yielding the final XYZ value of the target (equation 7.12).

$$\begin{aligned} X_W &= (X_{BEP,1} + d_1 l_1 + X_{BEP,2} + d_2 l_2)/2 \\ Y_W &= (Y_{BEP,1} + d_1 m_1 + Y_{BEP,2} + d_2 m_2)/2 \\ Z_W &= (Z_{BEP,1} + d_1 n_1 + Z_{BEP,2} + d_2 n_2)/2 \end{aligned} \qquad \text{Equation 7.12}$$

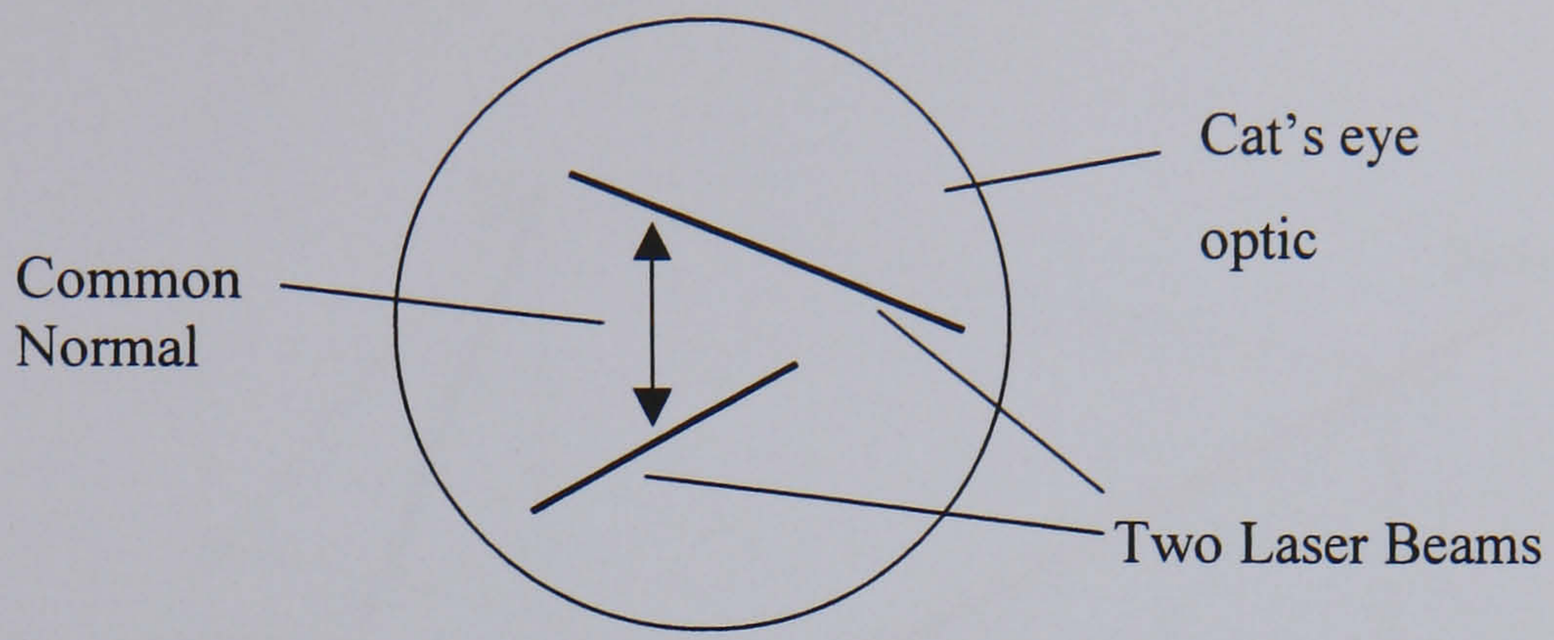


**Figure 7.4: The cat's eye retroreflector**

## 7.02 Effect of refraction

An important effect that must be included in the model is the refraction of the laser beam as it passes through the glass window once it has been deflected by the second mirror.

The beam leaves the second mirror with angle $\psi_1$ and is subject to refraction which deflects the beam to angle $\psi_2$ whilst within the glass medium. This then returns to the original angle when it returns to the air. The effect is an offset in the X-coordinate of the emergent beam in the local coordinate frame (figure 7.5).

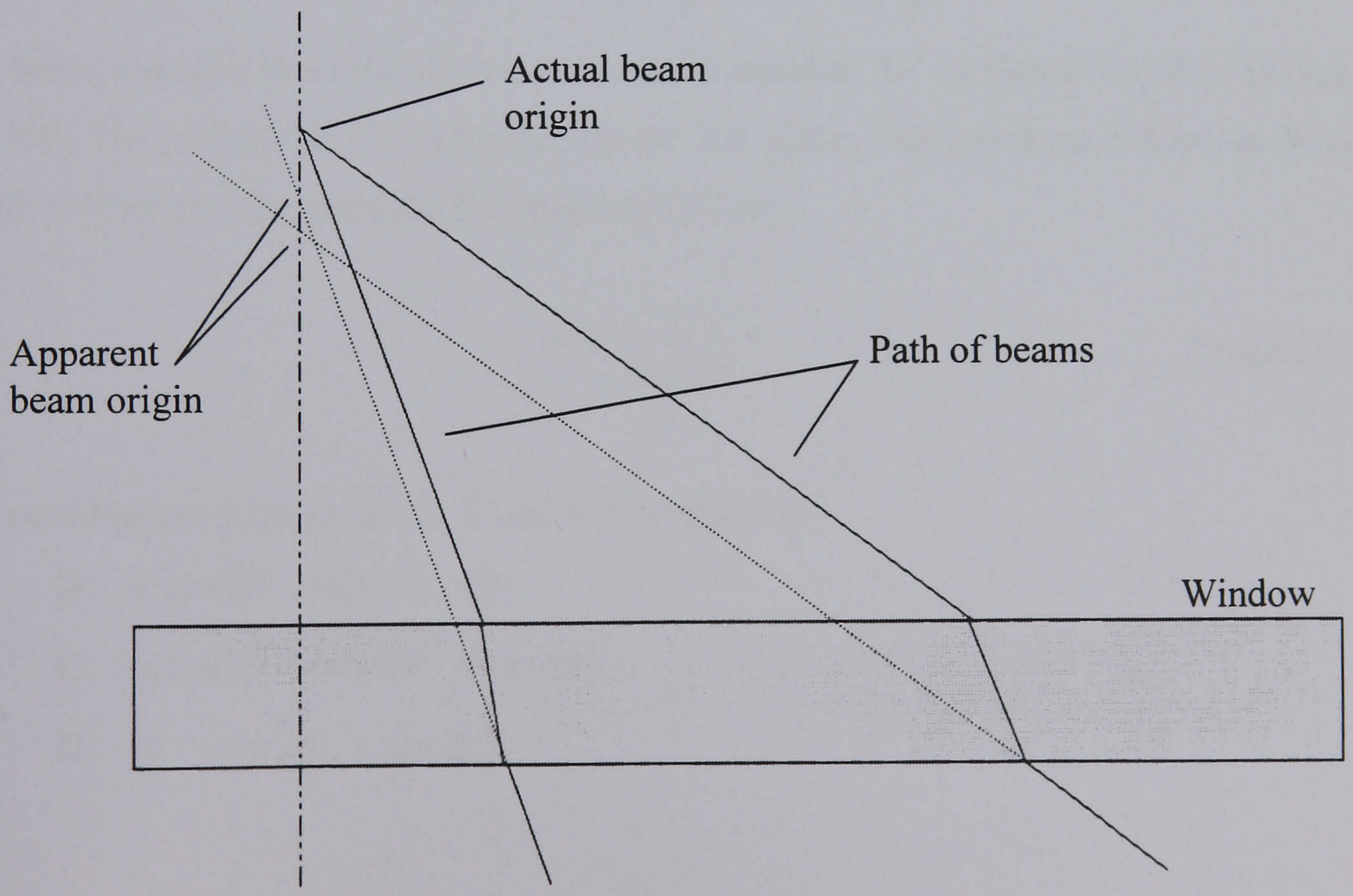


**Figure 7.5: Offset caused by refraction**

## 7.02.1 Determination of Emergent Angle, Ψ

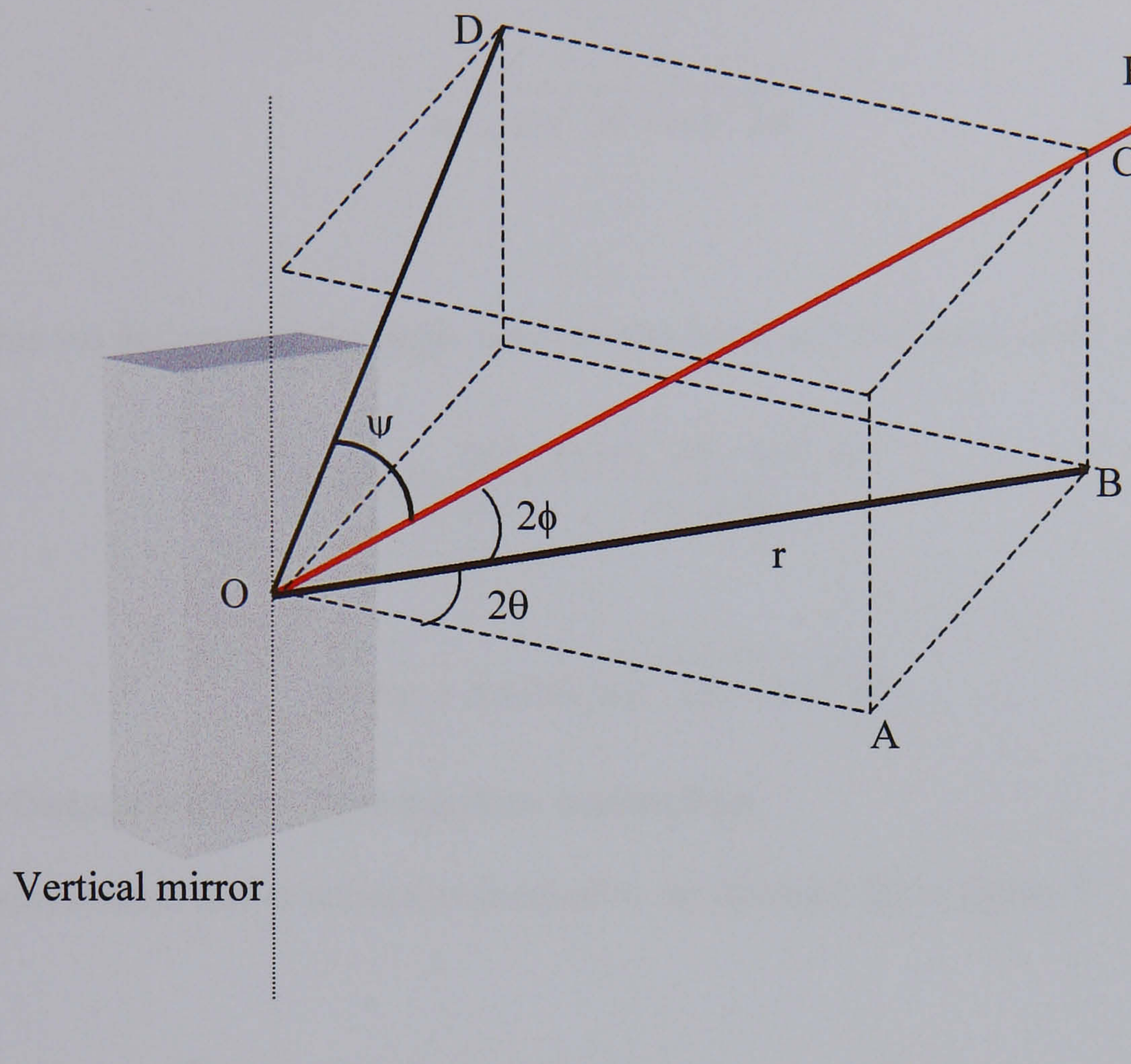


**Figure 7.6: Emergent beam angle**

The beam emerges from the mirror at the point labelled 'O' in figure 7.6, thus giving the line OC. The projection of this beam onto the XY plane, OB, has been defined as being of length r. From this we calculate the length of OC as:

$$OC = \frac{r}{\cos 2\phi} \qquad \text{Equation 7.13}$$

The coordinates of the points B, C and D are therefore:

B: $(r\cos 2\theta \quad r\sin 2\theta \quad 0)$

C: $(r\cos 2\theta \quad r\sin 2\theta \quad r\tan 2\phi)$

D: $(0 \quad r\sin 2\theta \quad r\tan 2\phi)$

Using Pythagoras to obtain length OD:

$$OD = \sqrt{r^2 \sin^2 2\theta + r^2 \tan^2 2\phi} \qquad \text{Equation 7.14}$$

$$\equiv r\sqrt{\sin^2 2\theta + \tan^2 2\phi}$$

From this we deduce that the angle between the beam and the plane of the mirror is:

$$\cos\psi = \frac{OD}{OC} \equiv \frac{r\sqrt{\sin^2 2\theta + \tan^2 2\phi}}{r/\cos 2\phi} \qquad \text{Equation 7.15}$$

hence

$$\cos\psi = \cos 2\phi \sqrt{\sin^2 2\theta + \tan^2 2\phi} \qquad \text{Equation 7.16}$$

### 7.02.2 Determination of refraction correction

The displacement due to refraction is equal to the distance JK in figure 7.7.

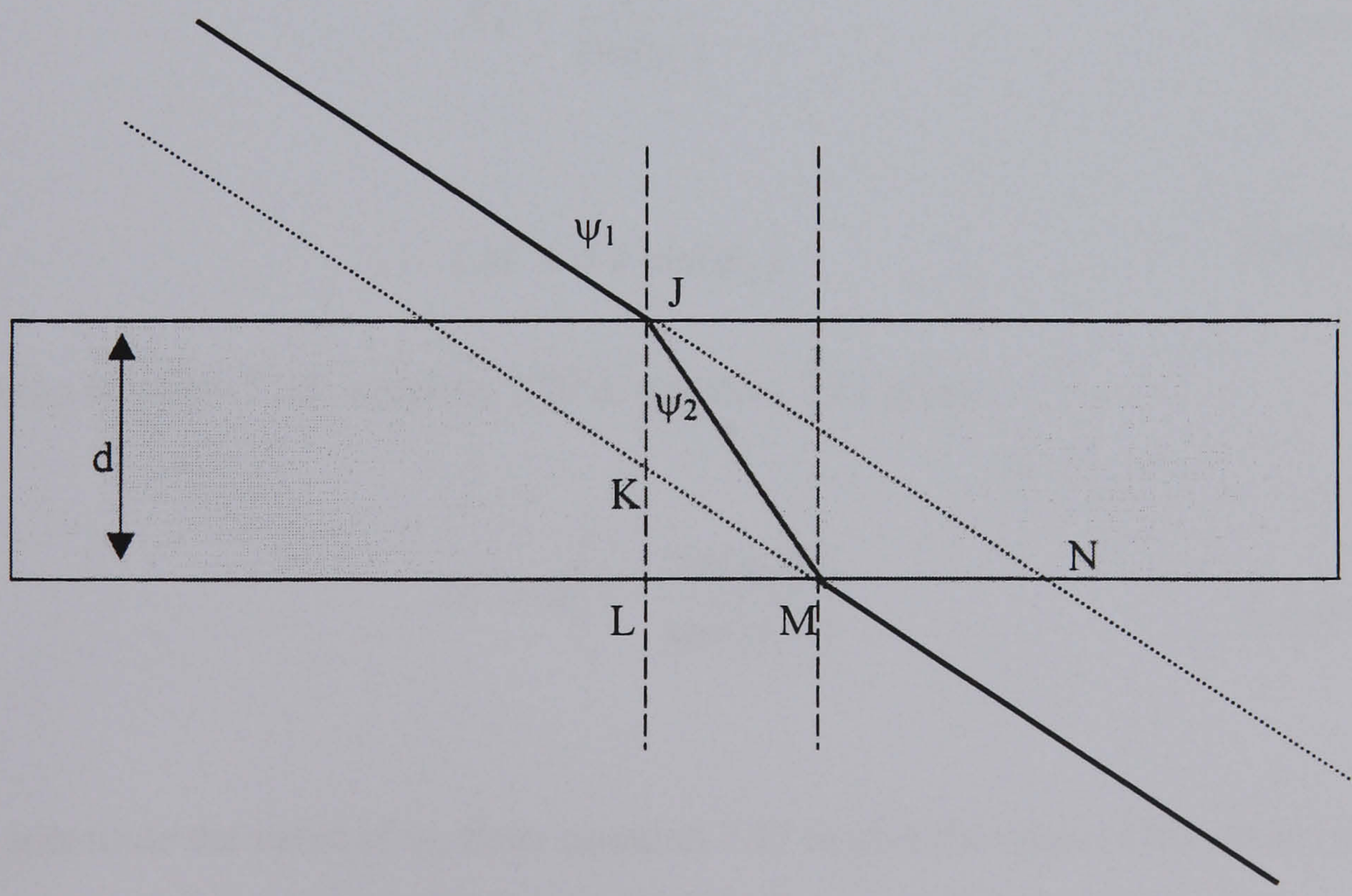


**Figure 7.7: Beam path through glass**

Critical to determination of the effect of the refraction is the 'relative refractive index', μ, defined by equation 7.17

$$\mu = \frac{\sin(\psi_1)}{\sin(\psi_2)} \qquad \text{Equation 7.17}$$

Where $\psi_1$ is the angle of incidence and $\psi_2$ is the angle of refraction. This is known as *Snell's law*. Note that the refractive index value depends on the wavelength of the light.

We need to determine the distance JK in terms of the known glass width, d, and known angle of incidence, $\psi_1$.

Now

$$JK = d - KL \qquad \text{Equation 7.18}$$

find KL

$$\tan(\tfrac{1}{2}\pi - \psi_1) = \frac{KL}{LM} \qquad \text{Equation 7.19}$$

$$KL = \frac{LM}{\tan(\psi_1)} \qquad \text{Equation 7.20}$$

But

$$LM = d \times \tan(\psi_2) \qquad \text{Equation 7.21}$$

Combining equation 7.18, equation 7.20 & equation 7.21 gives:

$$JK = d\left(1 - \frac{\tan(\psi_2)}{\tan(\psi_1)}\right) \qquad \text{Equation 7.22}$$

Finally substitute the value of $\psi_2$ from equation 7.17 to give the value of the offset, JK.

$$JK = d\left(1 - \frac{tan(sin^{-1}(sin(\psi_1)/\mu))}{tan(\psi_1)}\right) \qquad \text{Equation 7.23}$$

Equation 7.23 gives the offset as a function of the known constants d and μ, and the variable $\psi_1$, which is calculated using equation 7.16.

The resultant correction is applied to the emergent point for each calculation of encoder angles by adjusting equation 7.1 such that:

$$\left.\begin{aligned} X_{BEP} &= X_{BRP} + JK \\ Y_{BEP} &= Y_{BRP} \\ Z_{BEP} &= Z_{BRP} + M\times\tan(2\phi) \end{aligned}\right\} \qquad \text{Equation 7.24}$$

## 7.03 Calculation of mirror angles from given target position

Given a target position in the world Cartesian coordinate frame the four mirror rotations can be calculated using the reverse model. This model is dependent on the same six parameters for each pod discussed in section 7.01. The method of obtaining the values of the angles employs iterative methods.

### 7.03.1 Method

1) Make an estimate of the initial value of the angles θ and ϕ.

The estimate of the angles can be any legal value, though the solution will be found more rapidly by using a closer guess. In practice the procedure is not sensitive to this initial guess and since the procedure is not computationally intensive there is not a large cost associated with a poor initial estimate.

2) Begin Loop

a) Calculate the beam's emergent point (BEP) using equation 7.24:

$$\left.\begin{aligned} X_{BEP} &= X_{BRP} + JK \\ Y_{BEP} &= Y_{BRP} \\ Z_{BEP} &= Z_{BRP} + M\times\tan(2\phi) \end{aligned}\right\}$$

b) Now calculate a new value of the angles using equation 7.25, which have been derived from trigonometric techniques. Coordinates with the 'world' subscript refer to the target position in the world Cartesian frame.

$$\left.\begin{aligned}\theta_n &= \frac{1}{2\cdot 0}\tan^{-1}\left(\frac{Y_{world}-Y_{BEP}}{X_{world}-X_{BEP}}\right)\\ \phi_n &= \frac{1}{2\cdot 0}\tan^{-1}\left(\frac{(Z_{world}-Z_{BEP})\times\cos(2\theta_n)}{X_{world}-X_{BEP}}\right)\end{aligned}\right\}$$ Equation 7.25

c) Calculate direction cosines according to equation 7.7. These direction cosines are then rotated by the *known* values of pod rotation about the X- and Y- axes. The adjusted values of the direction cosines are then used in equation 7.26 to calculate the estimated values of θ and ϕ

$$\left.\begin{aligned}\theta_n &= \frac{1}{2\cdot 0}\tan^{-1}\left(\frac{m}{n}\right)\\ \phi_n &= \frac{1}{2\cdot 0}\cos^{-1}\left(\frac{l}{\cos(2\theta)}\right)\end{aligned}\right\}$$ Equation 7.26

d) Compare the new values of the angles with the values obtained from the previous iteration. The calculations within the loop are then repeated until the results of successive iterations are within a pre-defined tolerance. It was found that this method could successfully achieve a result with double precision accuracy within 15 iterations.

Once values of θ and ϕ have been found in the local coordinate frame the angles are converted to world angles by subtracting the rotation of the pods about the world Z-axis.

## 7.04 Full model

The models described in the above sections rely upon the internal geometry being perfectly aligned, with no manufacturing errors. The practical construction of the LaserTrace units introduces errors into the model such as misalignment of the mirrors.

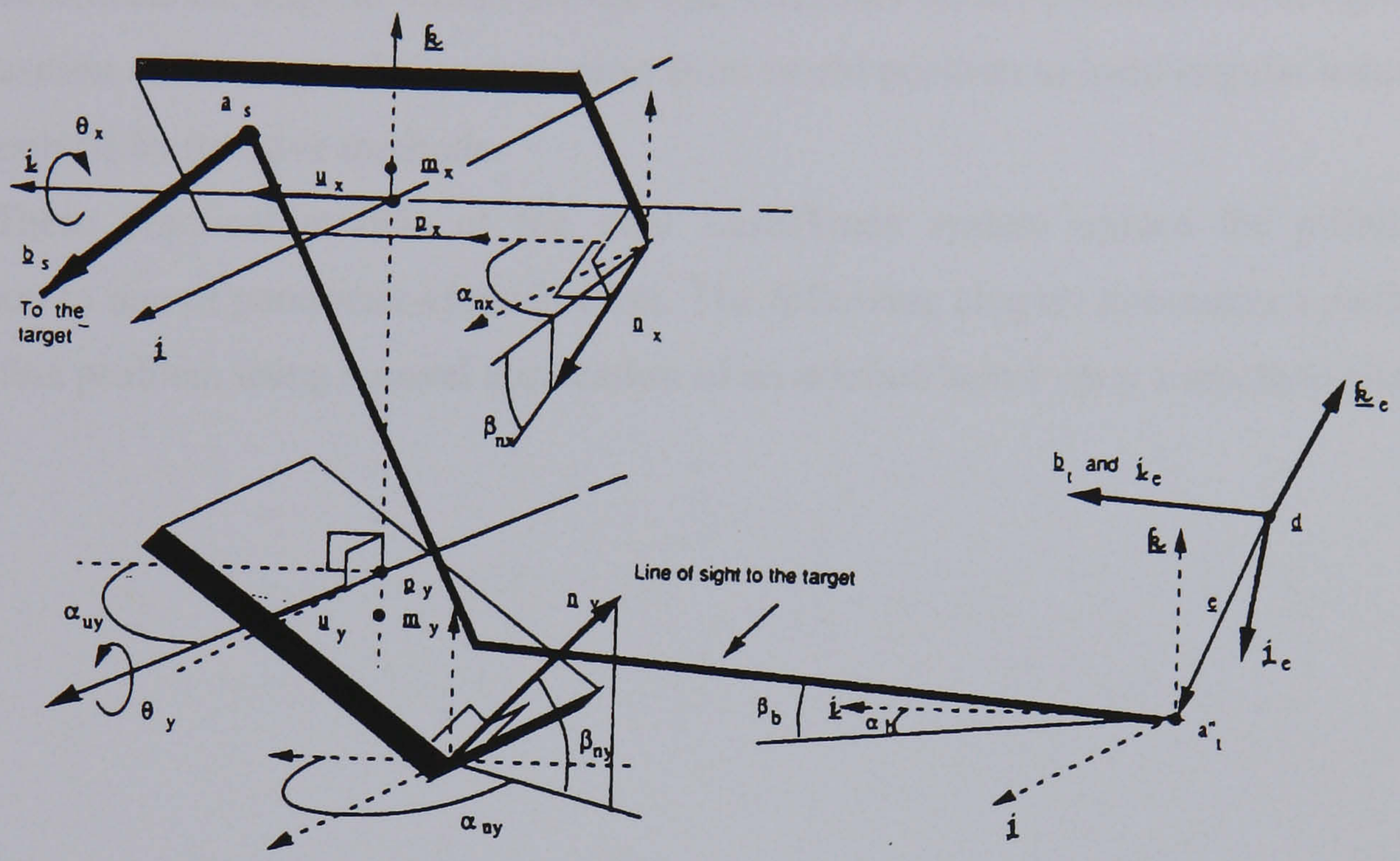


**Figure 7.8: Diagram of head geometry**

A full model of the head makes no assumption about the accuracy of the manufacture of the head. The thirteen parameters in each head are shown in figure 7.8.

Mayer, *et. al.* [88] developed the ideal model of the tracking laser head, although without the refraction of the glass panel. These equations are used to calculate the offset $\underline{a}$ and direction $\underline{b}$ of the line of sight to the target centre. Although this model would potentially reduce the errors in the calibration, it is not well-suited to the parameter estimation method chosen for this problem (chapter 8). Freeman [92] has noted, by simulation, that using this technique on a system with such a large number of parameters will not yield a satisfactory result within a realistic timescale for this type of application. It is also expected that the error introduced by ignoring construction inaccuracies will be outweighed by the uncertainties in the measurement data.

## 7.05 Summary

Two models of the dual LaserTrace system, described in section 5.03, have been found from first principles. The forward model is used to calculate the world position of the tracked target given the angle of rotation of the four mirrors in the system. The reverse model is used to determine the angular values for the four encoders on the actuated mirrors given the world position of the target. This conversion from world position to local angular values can only be solved by iterative methods.

These practical models of the dual LaserTrace system reduce the problem of calibration to one of parameter-identification. The following chapter introduces a method of solving this problem using a novel application of an artefact based upon a machine-checking gauge.

# Chapter 8 Machine Checking Gauge Application to Parameter Identification

## 8.01 Parameter identification

The forward model of the LaserTrace, as derived in section 7.01, allows the calculation of the position of the tracked target from measured angular data. The model contains six parameters for each subsystem that vary for each set-up of the LaserTrace system, namely:

| | | |
|---|---|---|
| i) | X position | Of reference point |
| ii) | Y position | |
| iii) | Z position | |
| iv) | Rotation about X | World axes |
| v) | Rotation about Y | |
| vi) | Rotation about Z | |

These values are fixed throughout a calibration exercise, but are changed every time the lasers are moved. This includes the case where they are accidentally disturbed during experimentation.

The remainder of this chapter discusses the method by which these parameters can be estimated by processing of experimental data. The procedure used for parameter estimation relies on a novel utilisation of the machine checking gauge (MCG) technique for acquiring calibration data.

## 8.02 Machine Checking Gauge (MCG)

### 8.02.1 Principle of the MCG

The Renishaw MCG (figure 8.1a) is a device used to check machines such as CMMs by constraining a probing anvil to movements a known distance from a fixed point. A kinematic joint (figure 8.1b) on the MCG arm rotates about a pivot ball on the MCG column. The MCG arm is slightly negatively balanced so the probing ball supports the fingers of the gauge without causing false triggering due to the force exerted by the MCG arm. The CMM can then be commanded to probe the anvil of the MCG. All points probed are distant from the centre of the pivot ball by the calibrated length of the MCG arm.

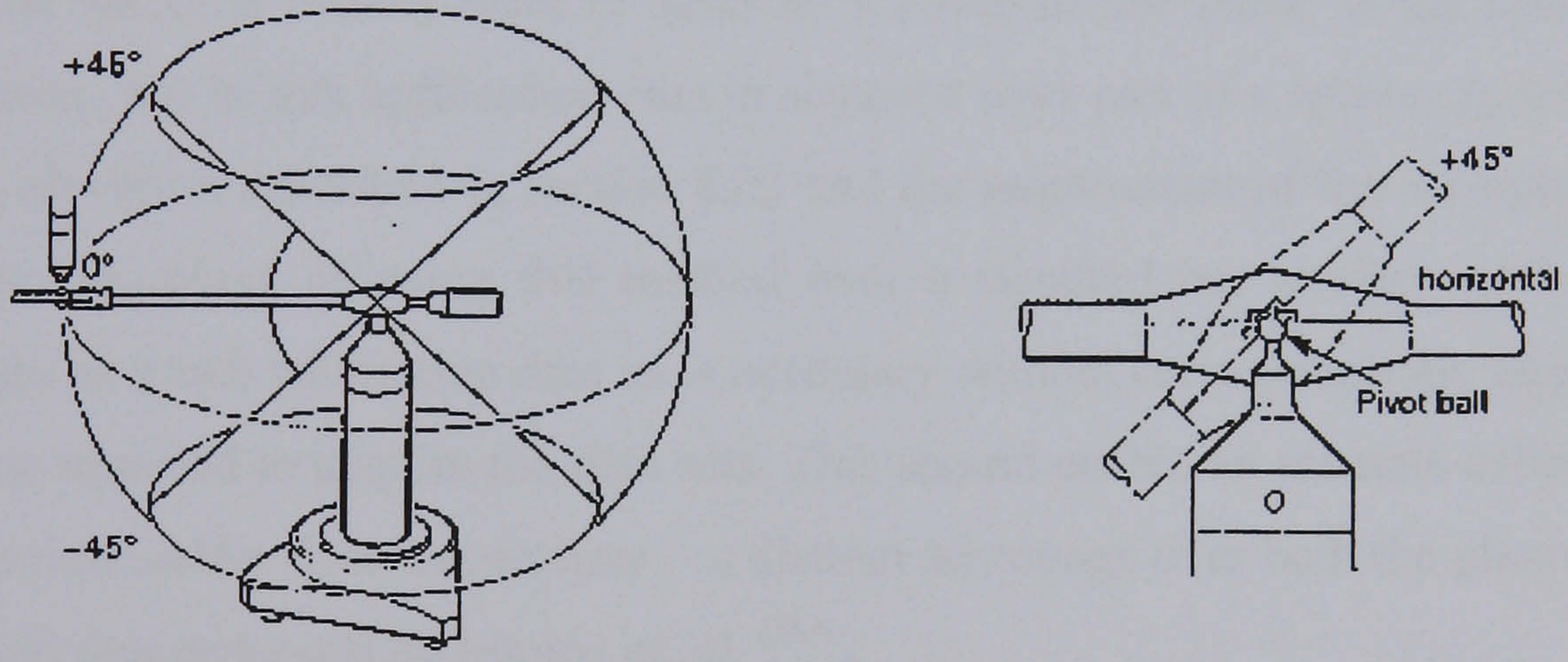


**a: MCG** **b: Kinematic joint**

**Figure 8.1: Machine Checking Gauge**

The arm of the MCG is limited to an elevation of ±45° from horizontal. Operation over this range ensures that the kinematic joint does not become unseated. It is essential that the kinematic location does not move since the centre of rotation must be a fixed point. The manufacturer, Renishaw Plc, [10] states that the "total gauge error is ±0.5μm." This value can be taken to include the uncertainty figure, which is not individually specified by the manufacturer.

### 8.02.2 Adaptation of MCG for LaserTrace application

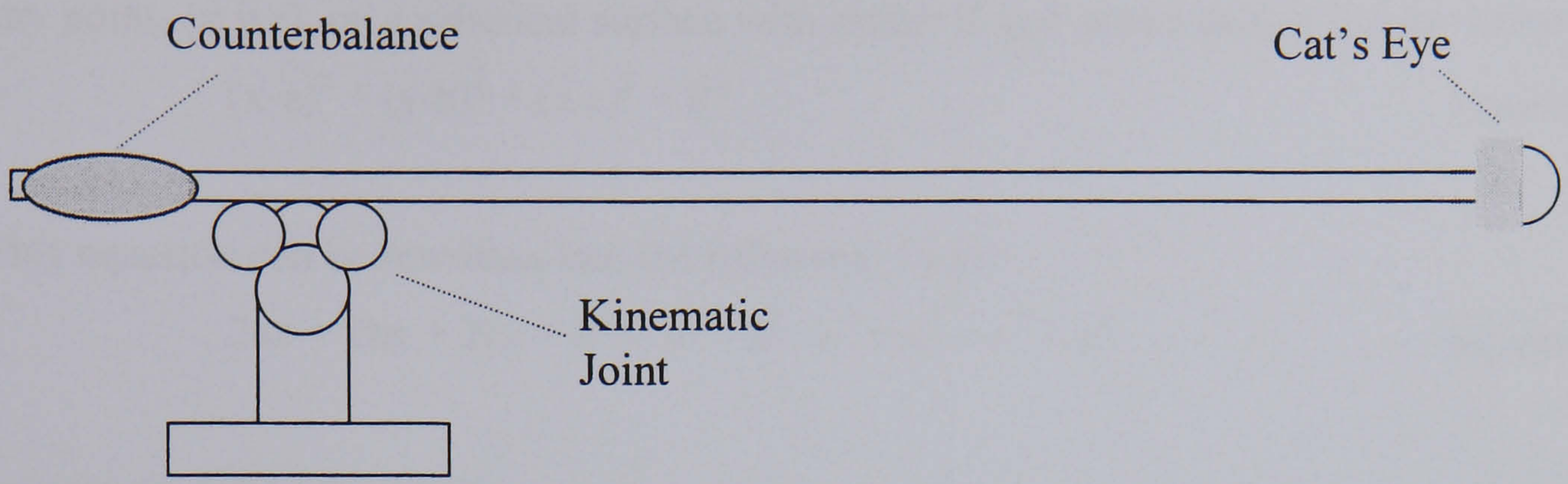


**Figure 8.2: Pod calibration artefact**

The principle of the MCG to sweep out points on a sphere of fixed centre has been applied to the calibration of the LaserTrace system. The calibration artefact (figure 8.2) is similar to the MCG except that the probing anvil is replaced by a cat's eye retroreflector which can be tracked by the LaserTrace. The artefact is also somewhat larger than a standard MCG since it is required to support the mass of the target.

The MCG is usually used to describe a circle in one plane of the machine under investigation, but in this application data is acquired over part of a sphere, restricted by the limits on elevation described in section 8.02 and the requirement of line of sight from both pods. The advantage of using this method over a standard bar artefact is the ability to accumulate as much calibration data as is necessary without correspondingly large increases in the time required to acquire the data sets. This should enable an accurate calibration even if a few points suffer from uncertainty – a distinct advantage over both the photogrammetry method and that proposed by Mayer, *et. al.* [88]

### 8.02.3 Calibration of MCG centre

For this method to work the MCG sphere centre must be accurately known. CMM2 (section 5.05.1) is used to define the world Cartesian coordinate frame for the testing and validation work. It was therefore valid to use the CMM to probe the pivot point to determine the centre of the subscribed sphere. In practice, the centre of the sphere will be used to define the datum for the calibration. Eight points were probed on the surface of the sphere and the method of section 8.02.3.1 used to find the sphere centre, which we denote ($a_{pivot}$, $b_{pivot}$, $c_{pivot}$). The calculation of the radius of the pivot ball was compared with the known dimension to validate the calibration.

### 8.02.3.1 Calculation of the centre of a sphere

Any point, (x,y,z), on a spherical surface with radius R and centre (a,b,c) can be written as

$$(x-a)^2 + (y-b)^2 + (z-c)^2 = R^2 \qquad \text{Equation 8.1}$$

This equation can be rewritten into the following form:

$$2ax + 2by + 2cz + R^2 - a^2 - b^2 - c^2 = x^2 + y^2 + z^2 \qquad \text{Equation 8.2}$$

Rewrite the left hand side by

$$F(x,y,z) = P_1.x + P_2.y + P_3.z + P_4 \qquad \text{Equation 8.3}$$

Determine the four parameters $P_1,\ldots, P_4$ which minimise the average error given by equation 8.4 for all data points on a given sphere. Algorithms for solving this problem, such as Powell's, simplex or a least squares method, can be found in 'Numerical Recipes in C' [93].

$$\{F(x,y,z) - x^2 - y^2 - z^2\}^2 \qquad \text{Equation 8.4}$$

The best fitting sphere will have centre

$$(a,b,c) = (\tfrac{1}{2} P_1, \tfrac{1}{2} P_2, \tfrac{1}{2} P_3) \qquad \text{Equation 8.5}$$

and radius

$$R = \sqrt{(P_4 + a^2 + b^2 + c^2)} \qquad \text{Equation 8.6}$$

## 8.03 Calibration of MCG arm-length

The arm length must also be found by probing on the CMM. The radius of the MCG sphere is defined by the distance from the pivot centre to the centre of the optic. To obtain the length of the MCG arm the kinematic joint was located on one of the balls defining the sphere centres. The counterbalance of the arm was held in a v-block in such a way that the arm was unlikely to move during probing, but without imposing such constraint that it might affect the seating of the kinematic joint. The centre of the optic, ($a_{optic}$, $b_{optic}$, $c_{optic}$), was then found by probing eight times and applying the calculation of 8.02.3.1. Again, the calculated radius was used to validate the measurement data.

To ensure the optic did not move during the probing procedure the encoder values on the LaserTrace were captured before and after the probing operation. If these values

agreed (within the repeatability of the system) it could be said that the optic had not moved. To validate this procedure it was repeated at different, arbitrary positions. The data used to determine the arm length could also be used as static validation points.

Pythagoras' formula was then used to determine the overall arm length, $R_{MCG}$.

$$R_{MCG} = \sqrt{\left(a_{pivot} - a_{optic}\right)^2 + \left(b_{pivot} - b_{optic}\right)^2 + \left(c_{pivot} - c_{optic}\right)^2} \qquad \text{Equation 8.7}$$

During the testing phase a single cats eye optic was available for all testing. This meant that the optic used for the artefact had to be removed for use as the measurement target throughout the working volume. As such, the length of the artefact arm changed each time it was used. In a final system, this artefact would have a fixed, known length and a separate optic would be used for calibration of the machine under investigation.

## 8.04 The need for multiple MCG spheres

A number of spheres are required to use the MCG principle for parameter identification. A single sphere has three degrees of freedom of rotation about its centre (figure 8.3a), so rotational parameters cannot be identified from a single set of data. Two spheres will have a line common to their centres, about which rotations cannot be evaluated (figure 8.3b). It can therefore be seen that three spheres, whose centres are not coincident or co-linear, are required for parameter identification.

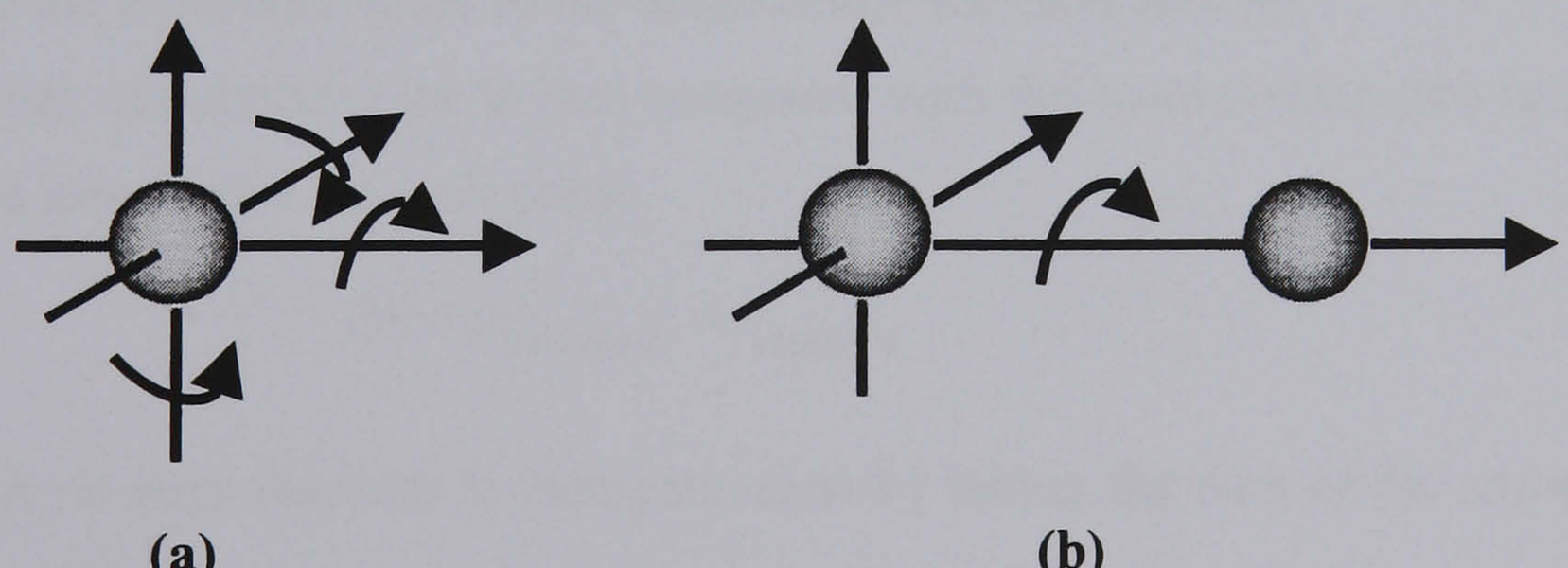


**Figure 8.3: Rotational symmetry of spheres**

Theoretically, if a single datum is known, only two spheres will be required to fix all parameters. However, this method is highly susceptible to error, especially in the presence of measurement noise, since a single point is being used to fix all parameters.

In practice, the position of the spheres should be chosen so as to cover as much of the working volume as possible. In addition, the choice of points on the surface of the spheres should also provide the greatest coverage possible. Combining these philosophies will result in the most general calibration values.

For the validation experiments all sphere centres were measured using the CMM as described above. For calibration of other machines a calibrated jig that defines the sphere centres would be manufactured. The orientation of this jig would define the coordinate frame for the calibration.

## 8.05 Parameter identification theory

With the MCG located on the kinematic seating, the beams from each pod are made to track the target, ensuring the centre of the optic is on the line of sight of both units. Angular data for each pod is captured and stored for analysis.

The forward model, derived in section 7.01, is used to calculate the world position of the target for each data set. The sphere radius this measurement would produce can be calculated using Pythagoras:

$$r = \sqrt{dX^2 + dY^2 + dZ^2}$$ Equation 8.8

Where dX, dY, dZ are the difference between the known coordinates of the MCG pivot point and the measured value of the target centre for each data set.

This calculated value is then compared with the known value (the length of the arm) to give an error value for each point.

$$\Delta r = r_{calculated} - r_{measured}$$ Equation 8.9

An objective error function is then generated by taking the sum of the squares of the error for N data points:

$$E = \sum_{k=1}^{k=N} \Delta r_k$$ Equation 8.10

### 8.05.1 Optimisation

A Nelder and Meade downhill simplex method is used to vary the values of the twelve unknown parameters to attempt to minimise the total error function. This is a

multidimensional minimisation technique that requires only function evaluations, not derivatives, as required in other downhill methods. The method is very robust in so far as it never diverges, but may not produce the correct values for the parameters due to the presence of local minima of the objective function, or even a flat valley which will not produce a unique minimum value.

Despite the drawbacks of this optimisation technique it was proven to find an acceptable solution during the modelling stage of development, even when noise was introduced in the input data. For a problem such as this, which required relatively small computation time, the inefficiency of the method was deemed acceptable.

The simplex method requires an initial estimate of the unknown parameters from which to calculate an initial objective function. It was important for this technique to be practical that the method be relatively insensitive to this 'seed point.' It was found that these approximations must be within 10mm for position and $5^{o}$ for angular measurements to allow the optimisation to succeed. This is acceptable.

## 8.06 Experimental practices

Different methods were used to acquire data from the three spheres necessary for parameter identification. Initially the MCG arm was moved to several points on each sphere (approximately 20) and angular values measured at each point. For the arm to be held stationary a magnet was used as an adjustable counterbalance.

This method produced good calibration data, but was found to be time consuming for taking larger quantities of data on each sphere and when the inclusion of a fourth sphere was investigated. To reduce the time required to acquire the calibration data, points were measured dynamically as the arm moved about the available spheres. This allowed many hundreds of data sets to be acquired on each sphere in a fraction of the time taken when static capture was used.

The potential drawback of dynamic, rather than static, data acquisition is the susceptibility to noise in the measurements. As outlined in section 5.03.5 there is a potential problem when acquiring dynamic data due to the lack of a common timing system between the two pods. As such, the data from each pod for a single sample may not represent a single position in the world coordinate system. This would produce unacceptable levels of uncertainty in the calibration data. Similarly, short-term averaging of the readings cannot be

performed if the target is moving. Therefore the fluctuations in the encoder remain untreated.

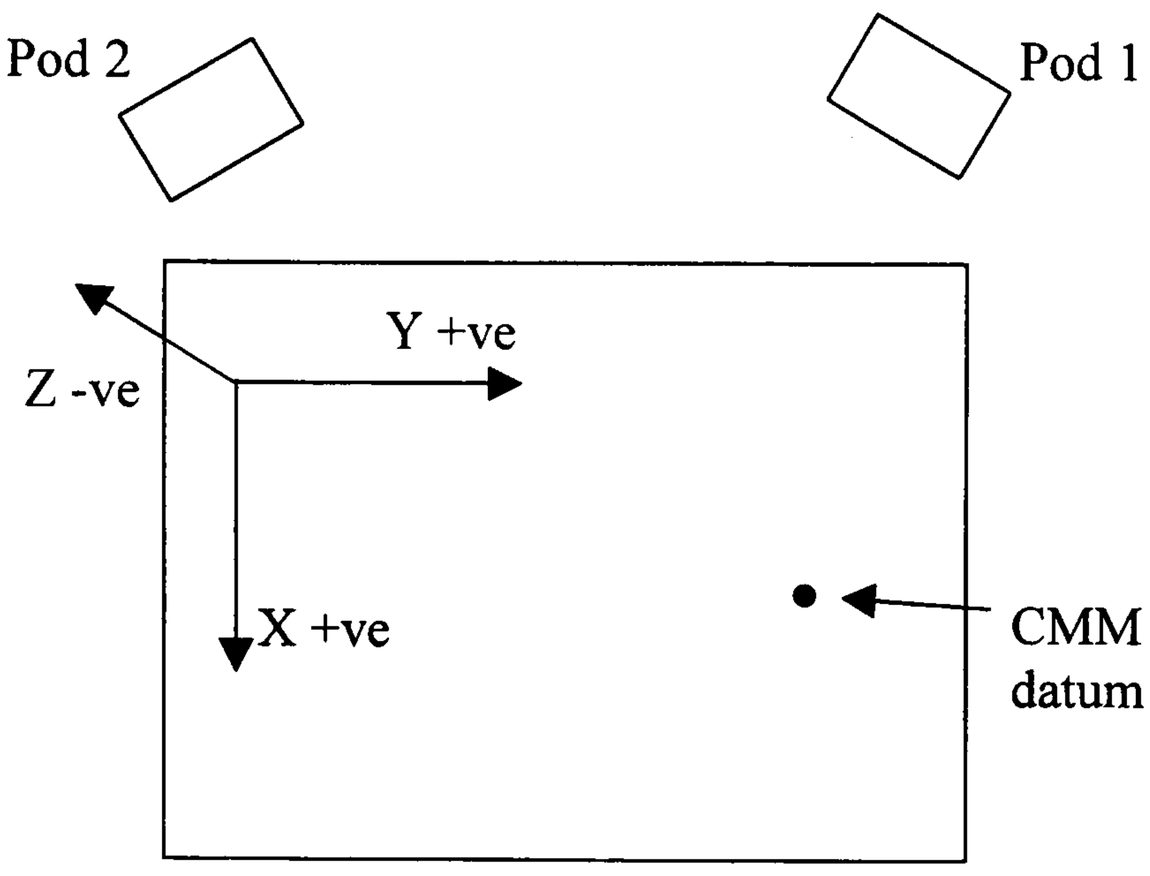


**Figure 8.4: Plan of test set-up**

Figure 8.5 to figure 8.7 show different views of a typical test set-up. Each axis is labelled, with the scale being the position, in millimetres, from the CMM datum. The asterisk indicates the centre of the pivot of one of the calibration spheres and the each circle represents the potential radius that can be described in the given plane. Each measurement point (for this example test) is then marked with a point-mark. It can be seen from the diagrams that, in this test, four spheres were used and the calibration points represent a good coverage of both the Z- and Y-axes. Calibration data is necessarily more sparse in the X-axis because of the position of the measurement posts.

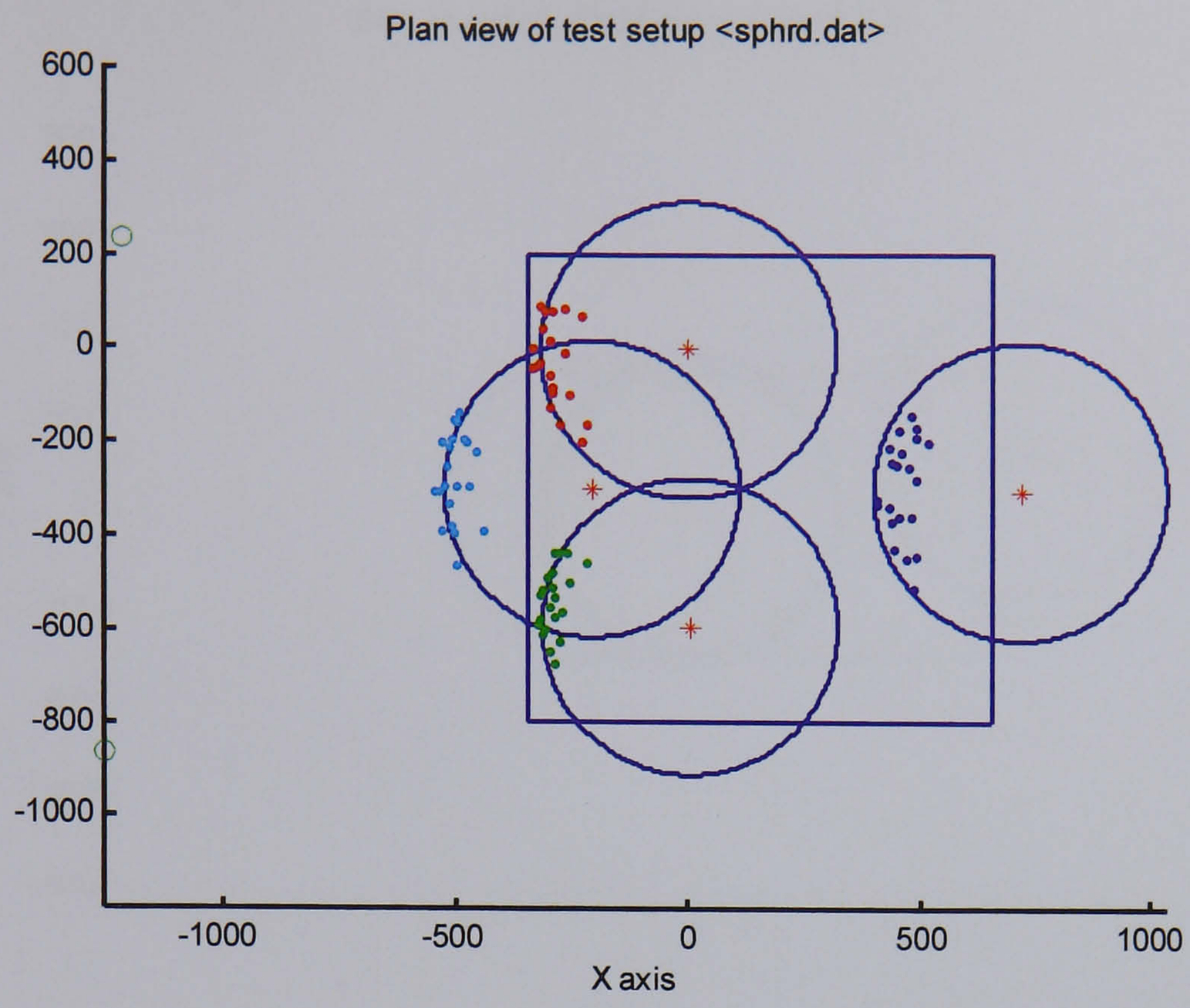


**Figure 8.5: Side elevation of typical calibration set-up**

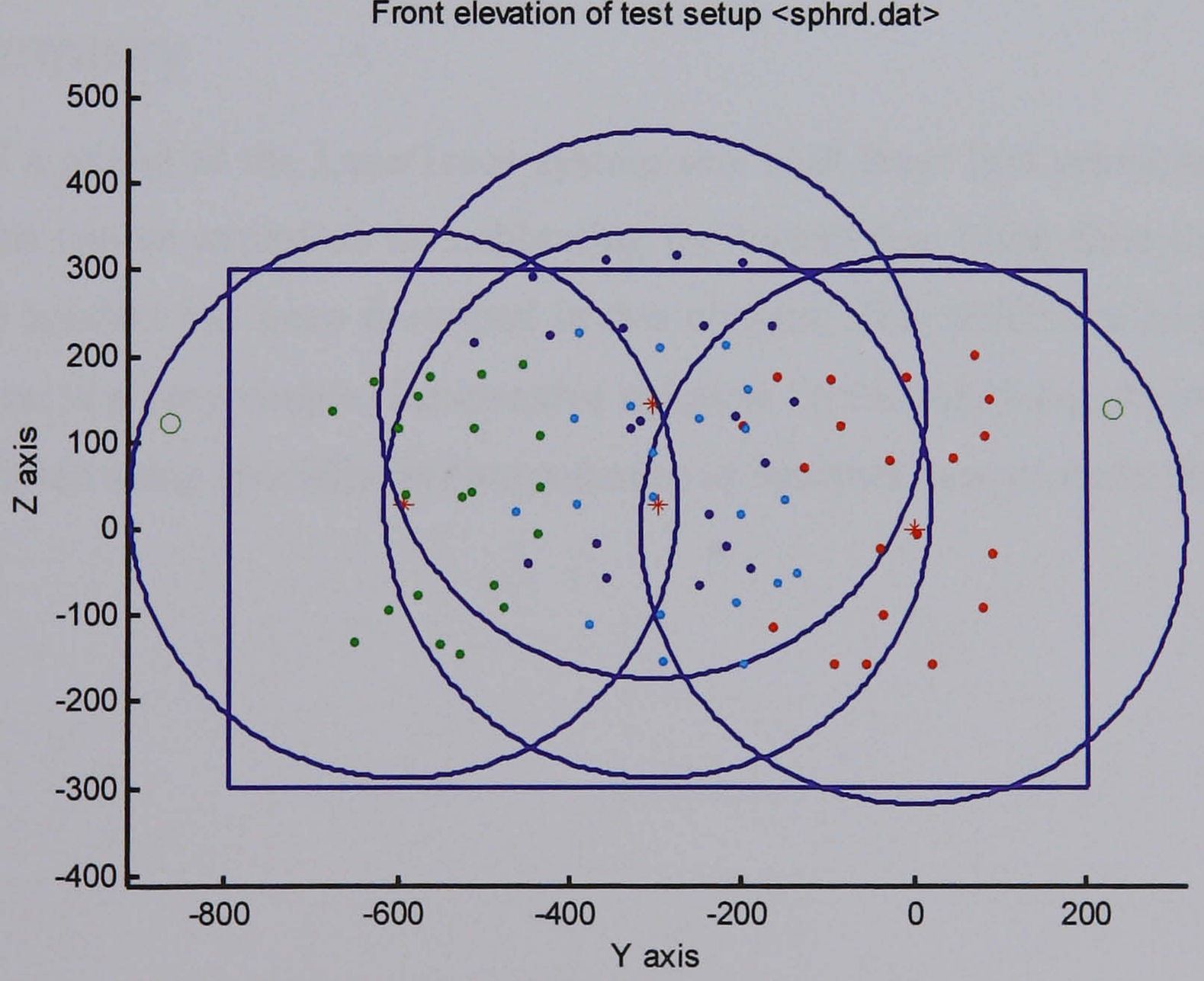


**Figure 8.6: Front elevation of typical calibration set-up**

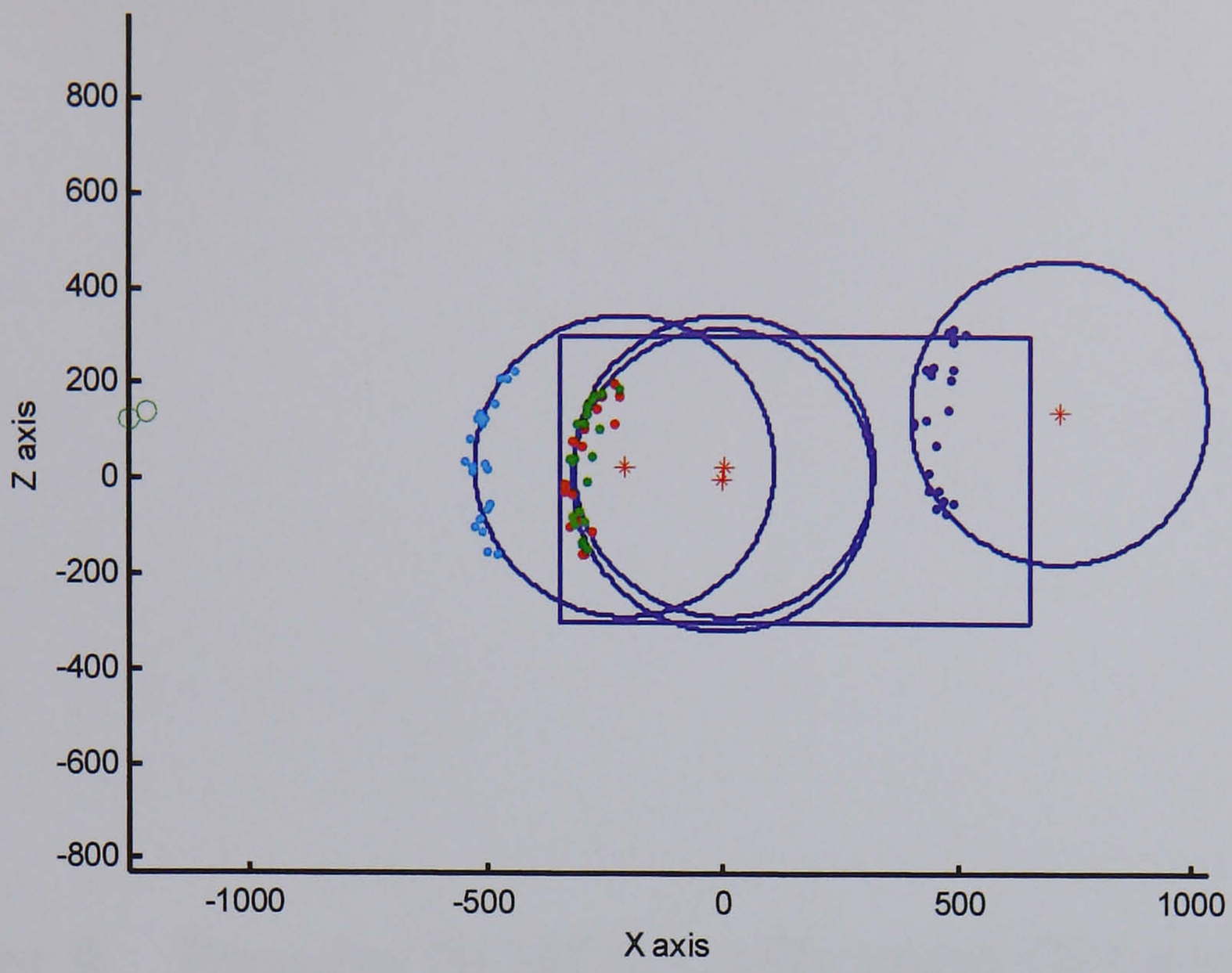


**Figure 8.7: Plan view of typical calibration set-up**

## 8.07 Summary

In chapter 7 a model of the LaserTrace system was built from first principles. The method by which this can be exploited for calibrating the LaserTrace using data obtained from an MCG-based artefact has been described in this chapter. This additional hardware required for calibration is a very simple, inexpensive solution. In the following chapter, this method will be validated using specially written software to interpret measurement data.

# Chapter 9 Results Of MCG Calibration Of LaserTrace

## 9.01 Validation of optimisation

### 9.01.1 Introduction

This calibration was performed to validate the use of the Machine Checking Gauge (MCG) artefact for obtaining LaserTrace calibration data. During the modelling stage described in the previous chapter, software was written to test the model and optimisation routines for this method of calibration. It was essential to perform analysis on simulated data in order to validate the integrity of the mathematical routines. All analysis on practical data conducted within this chapter was performed off-line using the same routines that had been used during the modelling phase of this project.

### 9.01.2 Calibration method

For this testing CMM2 (section 4.04) was used to collect comparative measurement data and to measure the positions of the sphere centres. The CMM Cartesian axes define the world coordinate system. Figure 9.1 shows the general set-up of the pods.

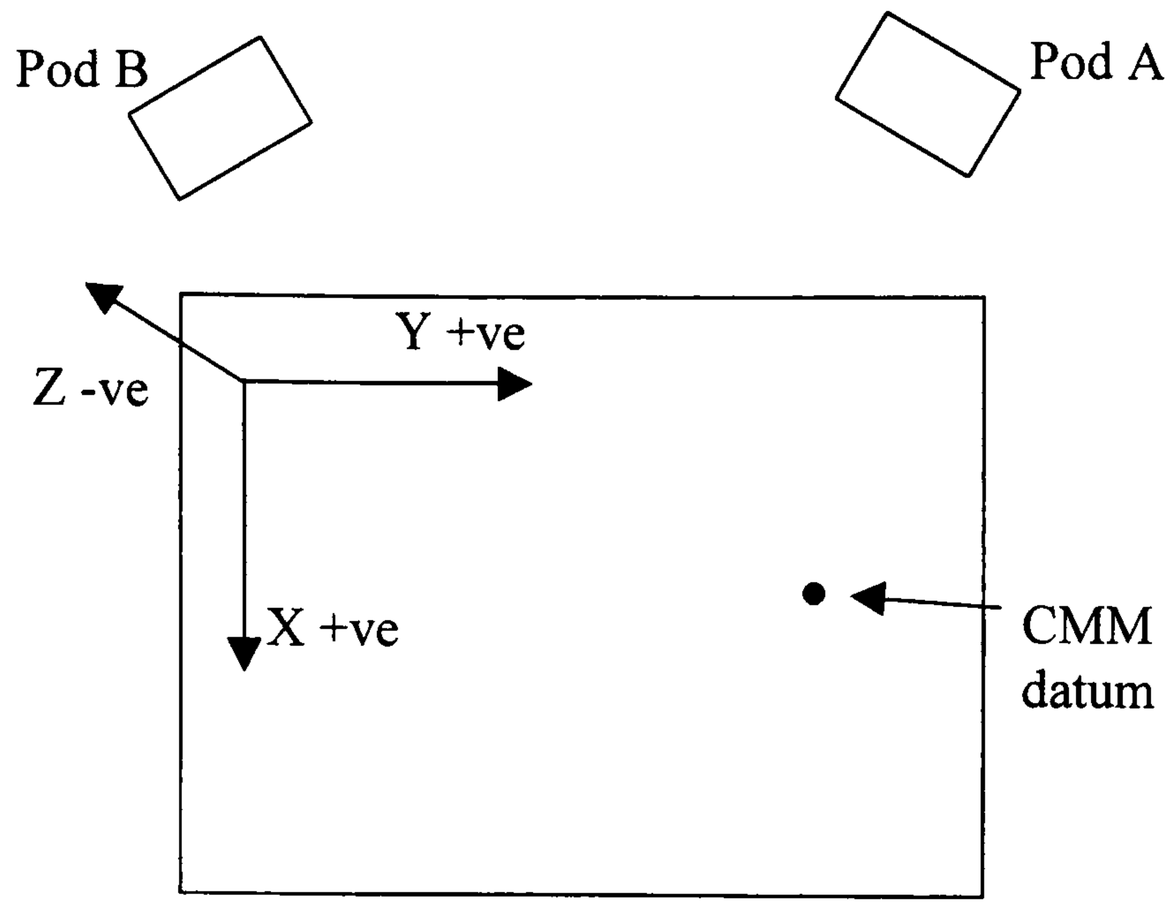


**Figure 9.1: Plan of test set-up**

Calibration data was taken using four sphere centres. The X, Y, Z position of their centres and the number of data points per sphere are given in table 9.1. This distribution of sphere positions was chosen to give the greatest coverage over the working volume. This was achieved by overlapping of the spheres so those points within a sphere were calibrated by one or both of the other spheres. A pictorial representation of the coverage is included in the previous chapter as Figure 8.5 to figure 8.7. Some areas of the working volume will not contain calibration points since three spheres could not tessellate the cubic volume. It was anticipated that if the calibration lost accuracy in these areas the working volume would have to be re-defined, or a shorter arm used to obtain calibration points in these regions. The *Z* coordinate of the sphere centres was governed by the height of the mounting posts. All posts were fixed directly to the granite bed during this experiment, reducing uncertainty over movement of sphere centres.

**Table 9.1: Position of sphere centres for experiment**

| Sphere | X | Y | Z | Points |
|---|---|---|---|---|
| 1 | 0.008 | 0.210 | 0.001 | 21 |
| 2 | 3.346 | -593.211 | 29.696 | 21 |
| 3 | 716.276 | -303.200 | 144.884 | 21 |
| 4 | -207.730 | -297.835 | 29.703 | 21 |

Figure 9.2 shows the menu for calibration data called from within the DOS control program (section 5.04.3.7). Data is associated with a particular MCG centre location, which is entered by using the 'change sphere centre' menu item and inputting the current coordinates. Performing this operation defines a new sphere centre and the 'Sphere Number' will increment. A number of readings are then taken for this 'sphere' by pressing a key at each target point, the amount of readings captured is monitored on the screen.

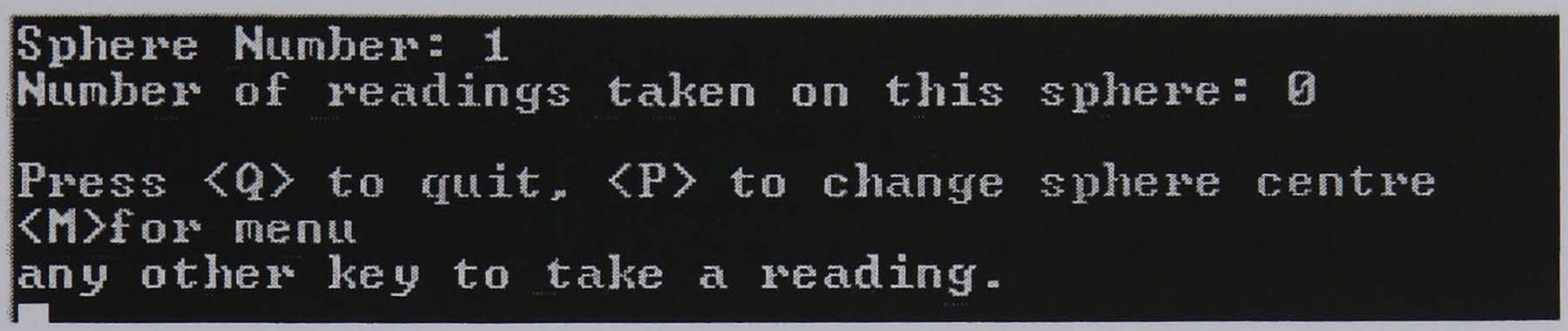


**Figure 9.2: LaserTrace calibration data collection menu**

The optimisation was performed on 12 parameters, with the *m* value being fixed at 30.000 mm. The variable parameters are the X, Y and Z positions of each pod and their three rotations about the world axes. A test was performed to determine the approximate values of these parameters by lining the lasers up 'by eye' and making calculations using the trigonometry described in the following subsection. As stated in section 8.05.1, the initial 'seed' parameter estimates need to be within 10mm and 5° for the optimisation to be successful. Additionally, during the testing phase work it was desirable to have a good estimate of the parameters in order to validate the technique.

### 9.01.2.1 Initial estimation of parameters

Figure 9.3 shows the points used for estimating the parameters of the model for a single laser. With the pod located at point O, the laser is levelled using a bulls-eye spirit level. The laser is then commanded down two distinct lines with the first mirror angle $\phi = 0^{o}$.

(Definition of mirrors is given in figure 7.1.) Normally the lines were chosen such that the second mirror of the laser be at angle $\theta = A = 0^o$ (represented by the line OH) and $\theta = B = \pm 20^0$ (represented by the line OF).

The CMM was then moved to positions such that the laser was centred on a target. Target points were then produced in pairs, such that the nominal X-coordinates of E and G were the same, as were those of F and H. The Cartesian coordinates of the CMM at each point were then recorded. The following analysis was then used to determine the position of the pod, $(O_x, O_y, O_z)$, the rotation of the pod about the Z-axis in world coordinates, rotz, and the rotation of the pods about the X- and Y- axes ($R_x$ and $R_y$).

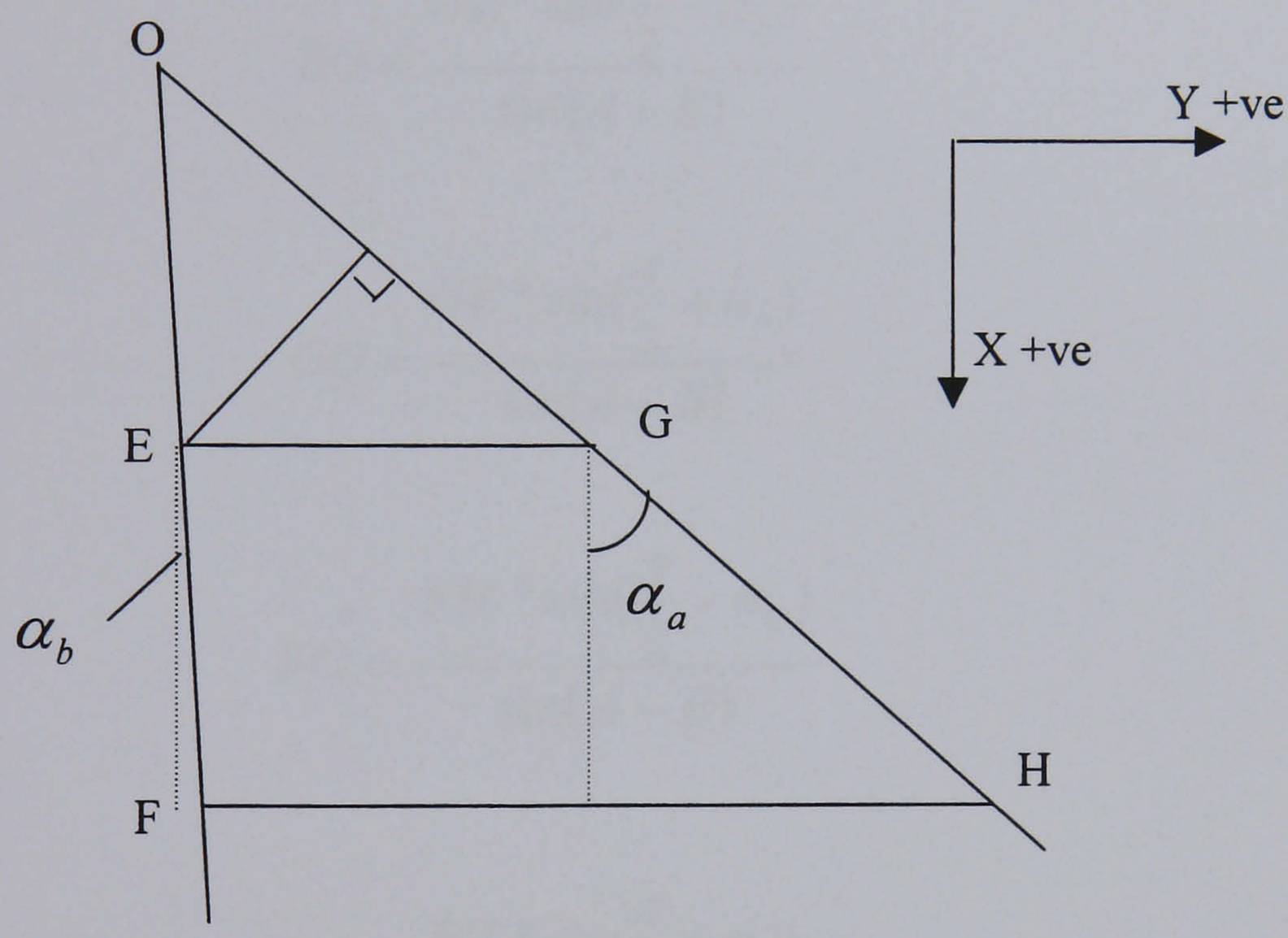


**Figure 9.3: Test points for estimating parameters**

$$\alpha_a = \frac{F_Y - E_Y}{F_x - E_x} \qquad \text{Equation 9.1}$$

$$\alpha_b = \frac{H_Y - G_Y}{H_x - G_x} \qquad \text{Equation 9.2}$$

$$rotz = \frac{\alpha_a + A + \alpha_b + B}{2} \qquad \text{Equation 9.3}$$

$$HG = \sqrt{\left(H_y - G_y\right)^2 + \left(H_x - G_x\right)^2}$$ Equation 9.4

$$FE = \sqrt{\left(F_y - E_y\right)^2 + \left(F_x - E_x\right)^2}$$ Equation 9.5

$$FH = H_y - F_y$$ Equation 9.6

$$GE = G_y - E_y$$ Equation 9.7

$$EO = \frac{GE * \sin(\frac{\pi}{2} - \alpha_b)}{\sin(A - B)}$$ Equation 9.8

$$GO = \frac{GE * \sin(\frac{\pi}{2} + \alpha_a)}{\sin(A - B)}$$ Equation 9.9

$$FO = \frac{FH * \sin(\frac{\pi}{2} - \alpha_b)}{\sin(A - B)}$$ Equation 9.10

$$HO = \frac{FH * \sin(\frac{\pi}{2} + \alpha_a)}{\sin(A - B)}$$ Equation 9.11

Then compare FE + EO with FO and compare HG + GO with HO to ensure they are within tolerance.

$$O_{x_1} = F_x - FO * \sin(\frac{\pi}{2} - \alpha_a)$$ Equation 9.12

compare with a second calculation for the same value

$$O_{x_2} = H_x - HO * \sin(\frac{\pi}{2} - \alpha_b)$$ Equation 9.13

$$O_x = \frac{O_{x_1} + O_{x_2}}{2}$$ Equation 9.14

$$O_{y_1} = F_y + FO * \sin(\alpha_a)$$ Equation 9.15

compare with a second calculation for the same value

$$O_{y_2} = H_y + HO * \sin(\alpha_b)$$ Equation 9.16

$$O_y = \frac{O_{y_1} + O_{y_2}}{2}$$ Equation 9.17

$$O_z = \frac{E_z + F_z + G_z + H_z}{4}$$ Equation 9.18

A computation is then performed to ensure that, within tolerance,

$$A - B = \alpha_a + \alpha_b$$ Equation 9.19

The local rotation of the pod about its y-axis is then given by equation 9.20.

$$R_y = \tan^{-1}\left(\frac{H_z - G_z}{\sqrt{(H_y - G_y)^2 + (H_x - G_x)^2}}\right)$$ Equation 9.20

A good estimation of the local rotation of the pod about its x-axis is then given by equation 9.21.

$$R_x = \tan^{-1}\left(\frac{G_z - E_z}{G_y - E_y}\right) \qquad \text{Equation 9.21}$$

### 9.01.3 Optimisation results

The final estimates reached by the optimisation are compared with the estimated values obtained from the method described above (table 9.2).

**Table 9.2: Change in parameter value after optimisation**

| Parameter | Pod 1 | | Pod 2 | |
|---|---|---|---|---|
| | Original | Final Value | Original | Final Value |
| X | -1218.00 | -1217.807 | -1253.00 | -1233.896 |
| Y | 235.00 | 234.424 | -864.00 | -860.490 |
| Z | 140.00 | 139.706 | 122.00 | 120.080 |
| m (fixed) | 30.00 | 30.000 | 30.00 | 30.000 |
| rotz | -27.00 | -27.251 | 28.00 | 32.495 |
| rotx | 0.00 | 0.129 | 0.00 | -0.151 |
| roty | 0.00 | 0.019 | 0.00 | -0.123 |

The difference between the measured estimate of each parameter and the value obtained from the optimisation are given in table 9.3. The greatest change in parameter was for the X coordinate value of the second pod.

**Table 9.3: Difference between measured and calculated value for parameters**

| Parameter | Pod 1 | Pod 2 |
|---|---|---|
| X | -0.193 | -19.104 |
| Y | 0.576 | -3.510 |
| Z | 0.294 | 1.920 |
| m (fixed) | 0.000 | 0.000 |
| rotz | 0.251 | -4.495 |
| rotx | -0.129 | 0.151 |
| roty | -0.019 | 0.123 |

That there is a discrepancy is unsurprising. The method of 'measuring' the pod positions is susceptible to error since the laser was aligned 'by eye' and the calculation relied on simplified trigonometry, assuming features were at right angles. Secondly, noise in the data would affect the results, giving some error in the estimated parameters. The model being used for this simulation was the simple one, assuming the laser had been manufactured with all mirrors correctly aligned. Since this is not the case, some error can be expected in the reverse model.

However, the magnitude of the discrepancy is somewhat surprising. A likely reason is that the optimisation has found a local minima that does not match the actual values of the physical parameters, but compensates for other features in the model. As was stated in section 8.05.1, the Nelder and Meade optimisation method can find local minima. Although the parameters found by the optimisation do not exactly match the values obtained by measurement, this does not mean that the calibration is invalid. In fact, these values best define actual points in the working volume. The following section describes the validation of this calibration by testing random points within the working volume and comparing them with the known position, as measured by the CMM.

## 9.02 Validation of calibration

To validate the calibration it is necessary to compare calculated and measured coordinates in the working volume. This was achieved by probing the cat's eye in ten positions within the calibrated working volume on the CMM bed (table 9.4). The CMM was used to probe the cat's eye, thus determining the centre of the optic. At each point, the encoder readings required to find the centre of the optic were recorded for both pods. Using the model and the parameters obtained from the above calibration, these encoder readings can be converted to position measurements.

**Table 9.4: Measured position of test points**

| Point | X | Y | Z |
|---|---|---|---|
| 1 | -123.876 | -288.242 | 57.040 |
| 2 | 266.070 | -363.858 | 57.073 |
| 3 | 153.803 | -594.386 | 122.020 |
| 4 | -151.560 | 38.935 | 122.010 |
| 5 | 475.965 | -178.672 | 57.083 |
| 6 | 773.937 | -345.735 | 122.121 |
| 7 | 109.975 | -497.464 | 57.049 |
| 8 | -136.903 | -256.429 | 201.951 |
| 9 | 374.456 | -385.530 | 120.762 |
| 10 | 248.962 | -282.658 | 201.930 |

### 9.02.1 Results of measurement

Figure 9.4 shows the error between the LaserTrace calculation and the known CMM position at each point.

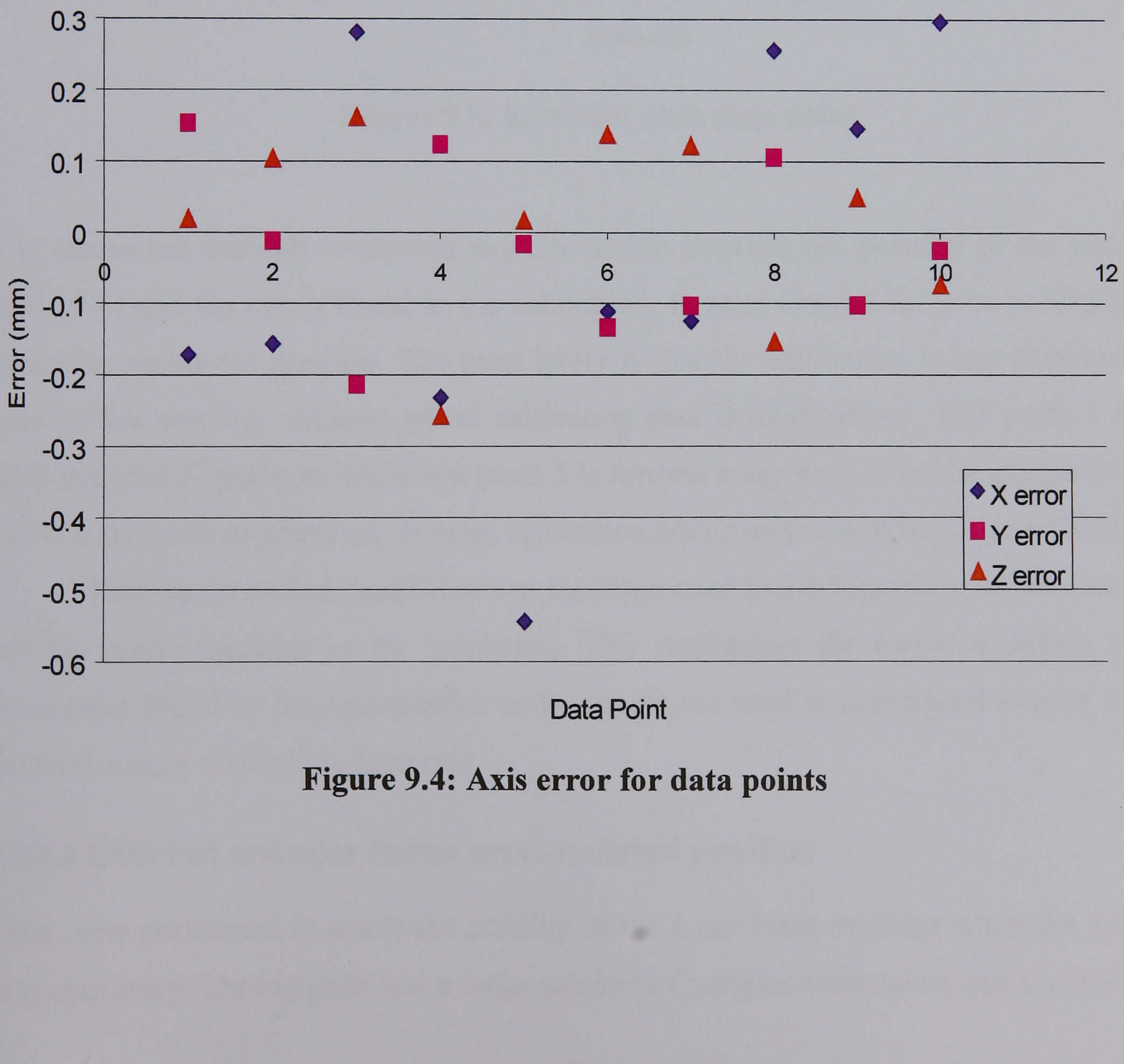


**Figure 9.4: Axis error for data points**

The errors in each axis are less than 300 μm for each data point, except for the X value for point 5. Figure 9.5 shows the volumetric errors at each of the ten data. Positions 3 and 5 have the worst volumetric errors, with the remainder being within 300μm.

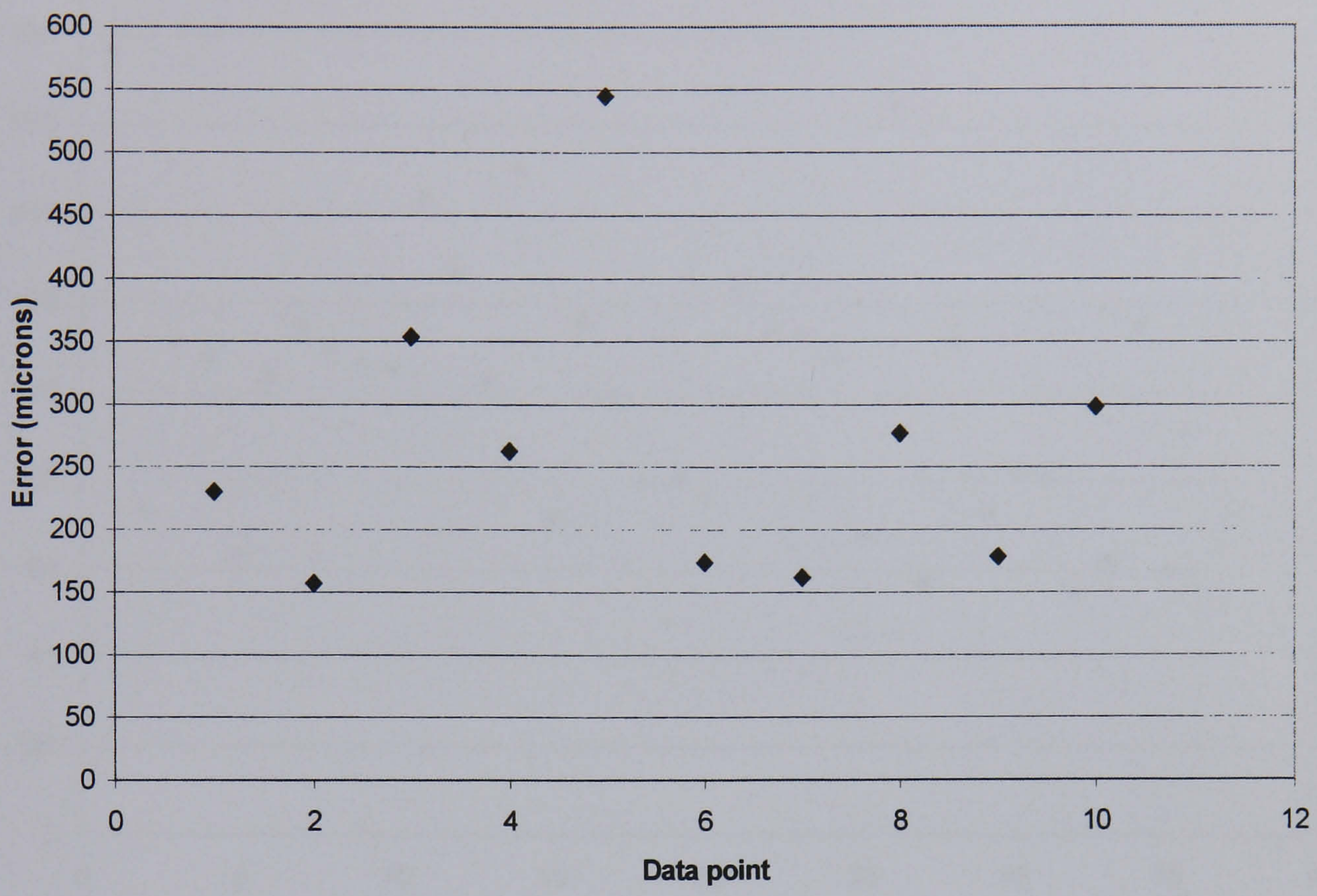


**Figure 9.5: Error for each data point**

It is somewhat difficult to discern any correlation between the position of the test points (table 9.4) and the errors found in the calibration. Several reasons for poor performance at particular points are possible. The most likely is that the calibration is less accurate at the limit of the working volume, where calibration data is more sparse. Test point 3 has the most extreme *Y*- position, while test point 5 is furthest away in X. It is also possible that the *best* results occur at points on, or near, calibration points on the surface of the MCG sphere.

There is no evident trend between the large error in the X position of the second pod and the errors manifest in the validation. This emphasises the earlier assertion that the parameters found by the optimisation technique do not need to correspond exactly with the physical values which they represent.

### 9.02.2 Effect of encoder flutter on calculated position

Tests were performed to assess the stability of the LaserTrace readings while the optic was held stationary. During each test a large number of samples were taken and converted into

position measurements. It can be seen (figure 9.6) that the effect of encoder fluctuation on the volumetric measurement can be over 150μm.

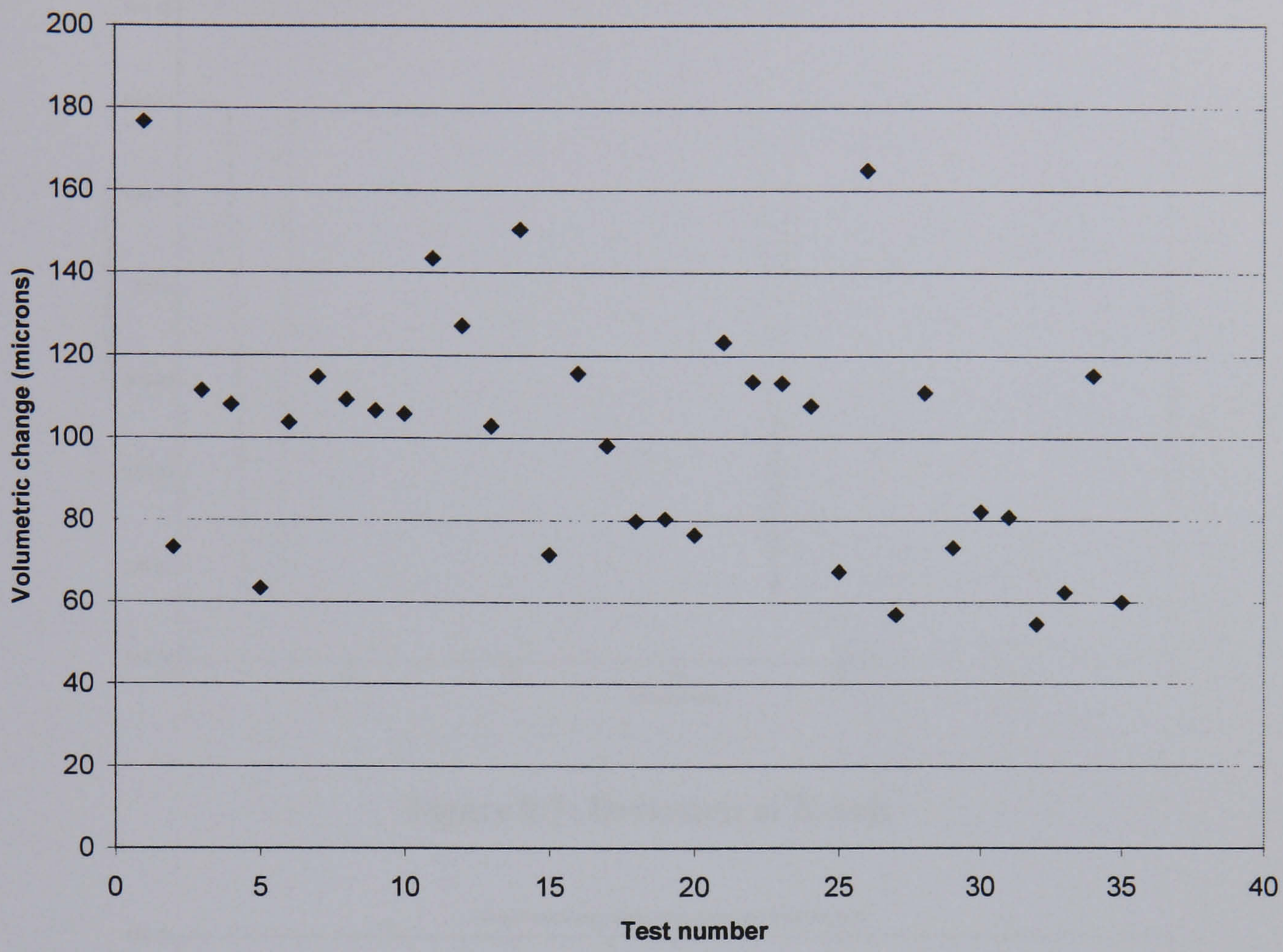


**Figure 9.6: Calculated positional deviation because of encoder flutter**

Figure 9.7 shows the deviation experienced in the X-axis during this test. It can be clearly seen that the deviation is due mainly to a few 'data spikes.' However, the variation in reading in the Z-axis (figure 9.8) is seen to be much more variable. However, even in this instance it can be seen that an average value would produce good results. The quantisation of the results is due to the resolution of the measurement device at a given distance from the laser, as discussed in section 5.03.

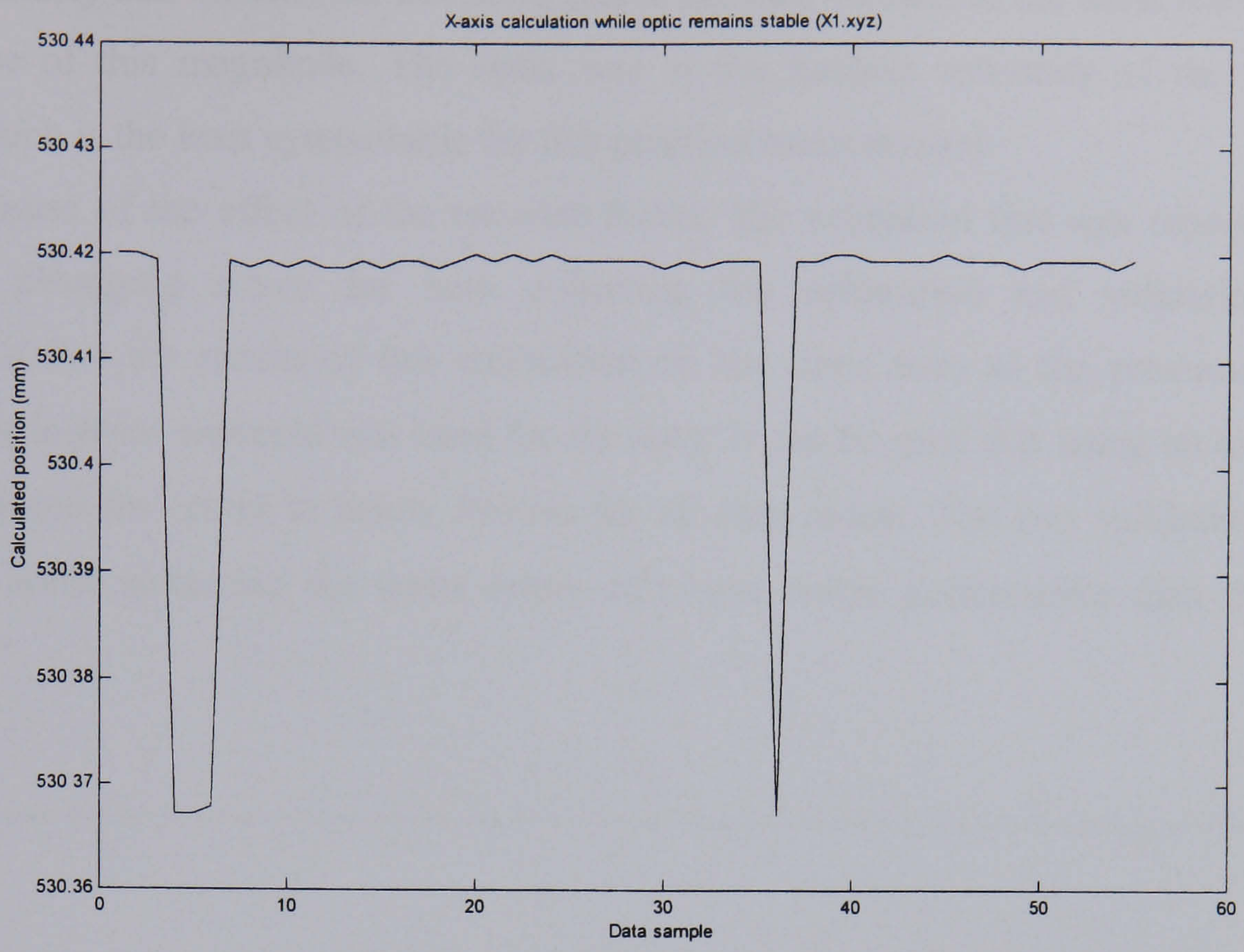


**Figure 9.7: Deviation of X-axis**

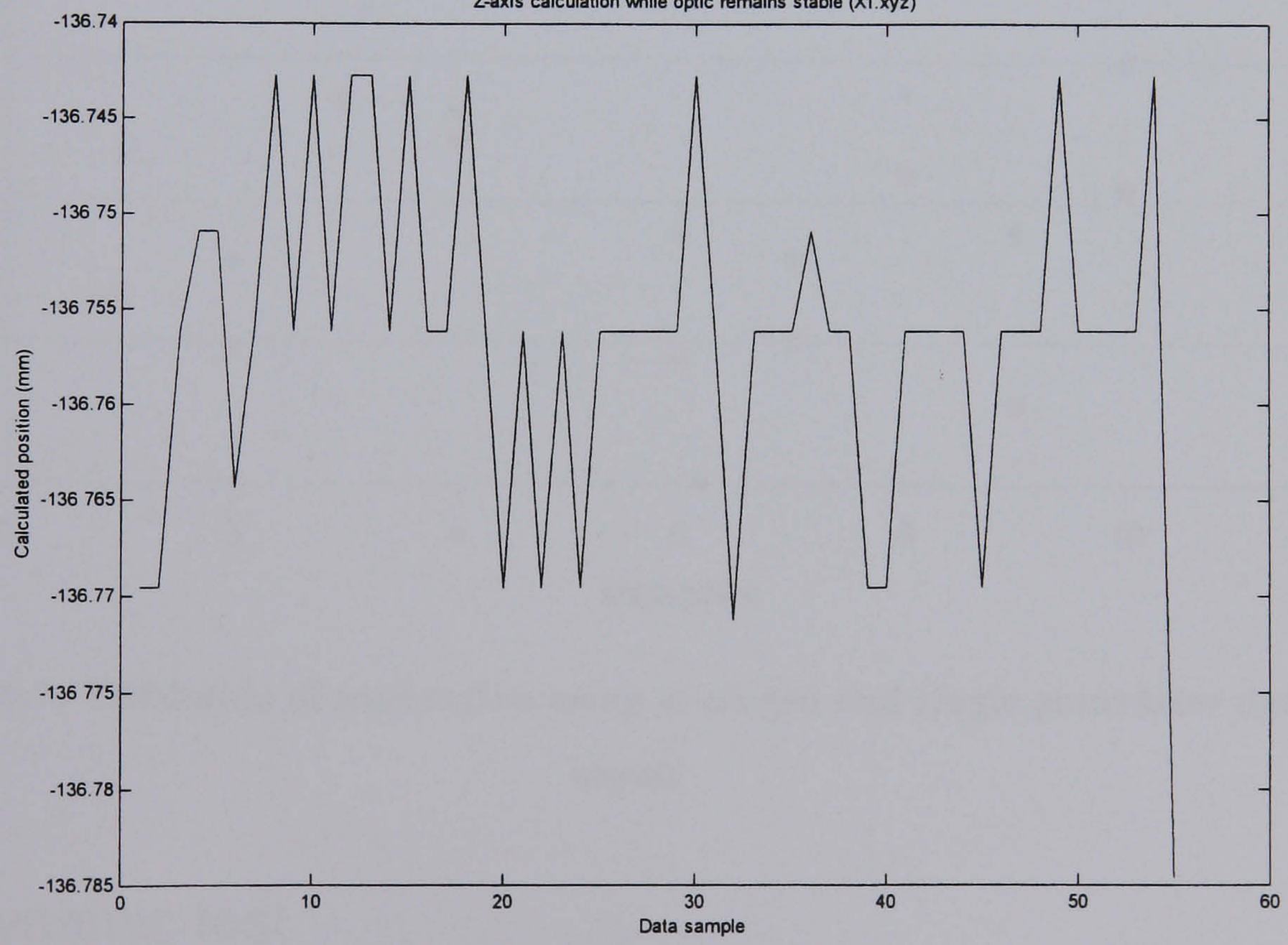


**Figure 9.8: Deviation of Z-axis**

It seems unlikely that the encoder deviation can be reduced further, so the static error will be found to be of this magnitude. The optic was at the furthest extremity of the working volume, which is the least sympathetic for this position measurement.

Because of the effect of the encoder flutter, the validation test was repeated with short-term averaging active for both collecting the calibration and validation data. Figure 9.9 shows the results of this calibration on the same axes as the previous results where a single-point captured was used for the data. It can be seen that using an averaging capture reduced the errors to below 500µm for all data points. The two validation points previously noted as having the worst errors still have worse performance than the other points.

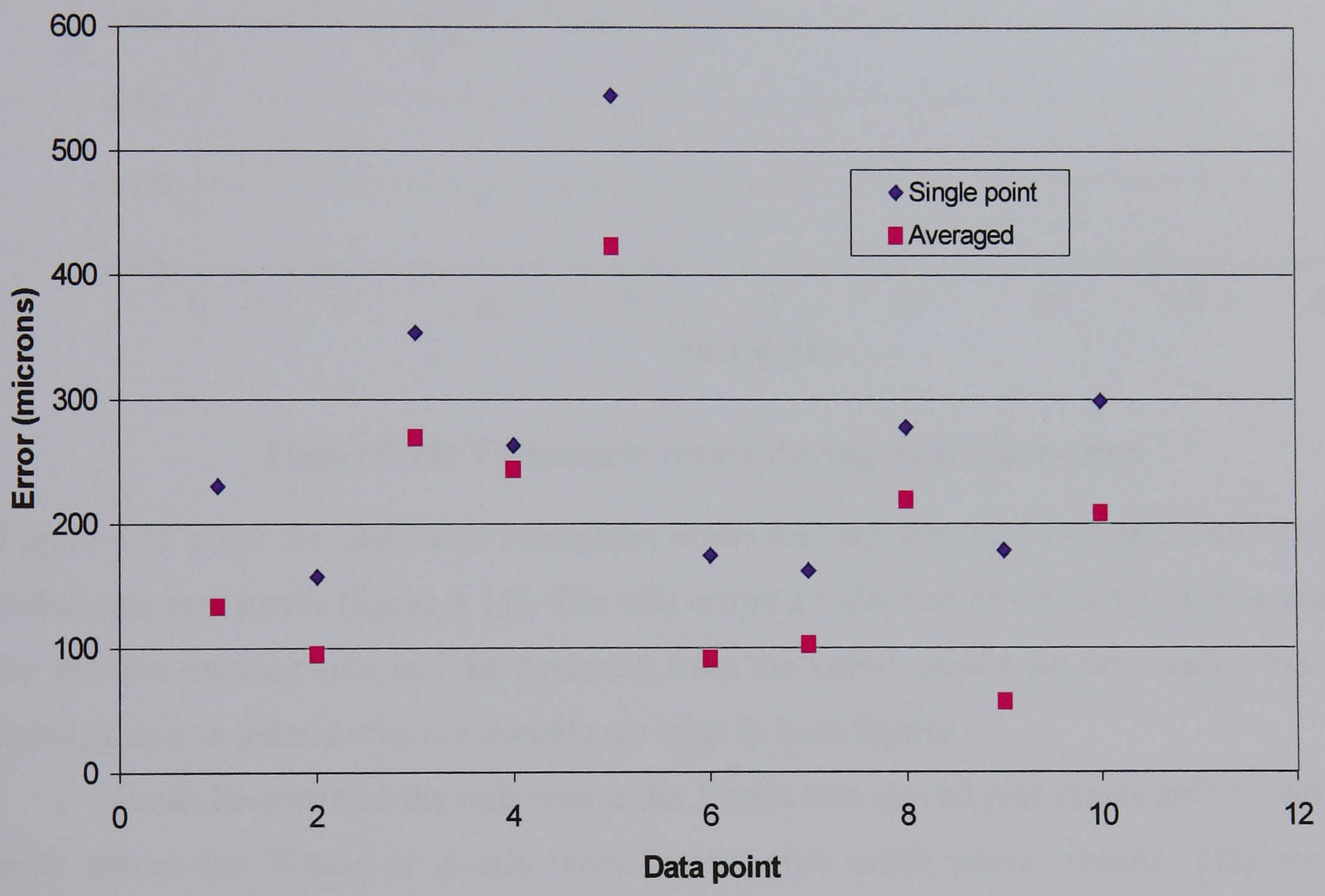


**Figure 9.9: Validation of calibration using averaged and single point laser data for inputs**

## 9.03 Dynamic test

Some work was performed to assess the dynamic capability of the system using this calibration technique. It is expected that this method will produce relatively poor results due to the problems of flutter and of timing discussed previously (section 5.03.5). For these tests

one of the axes was moved at one metre per minute, with the other axes commanded to remain stationary.

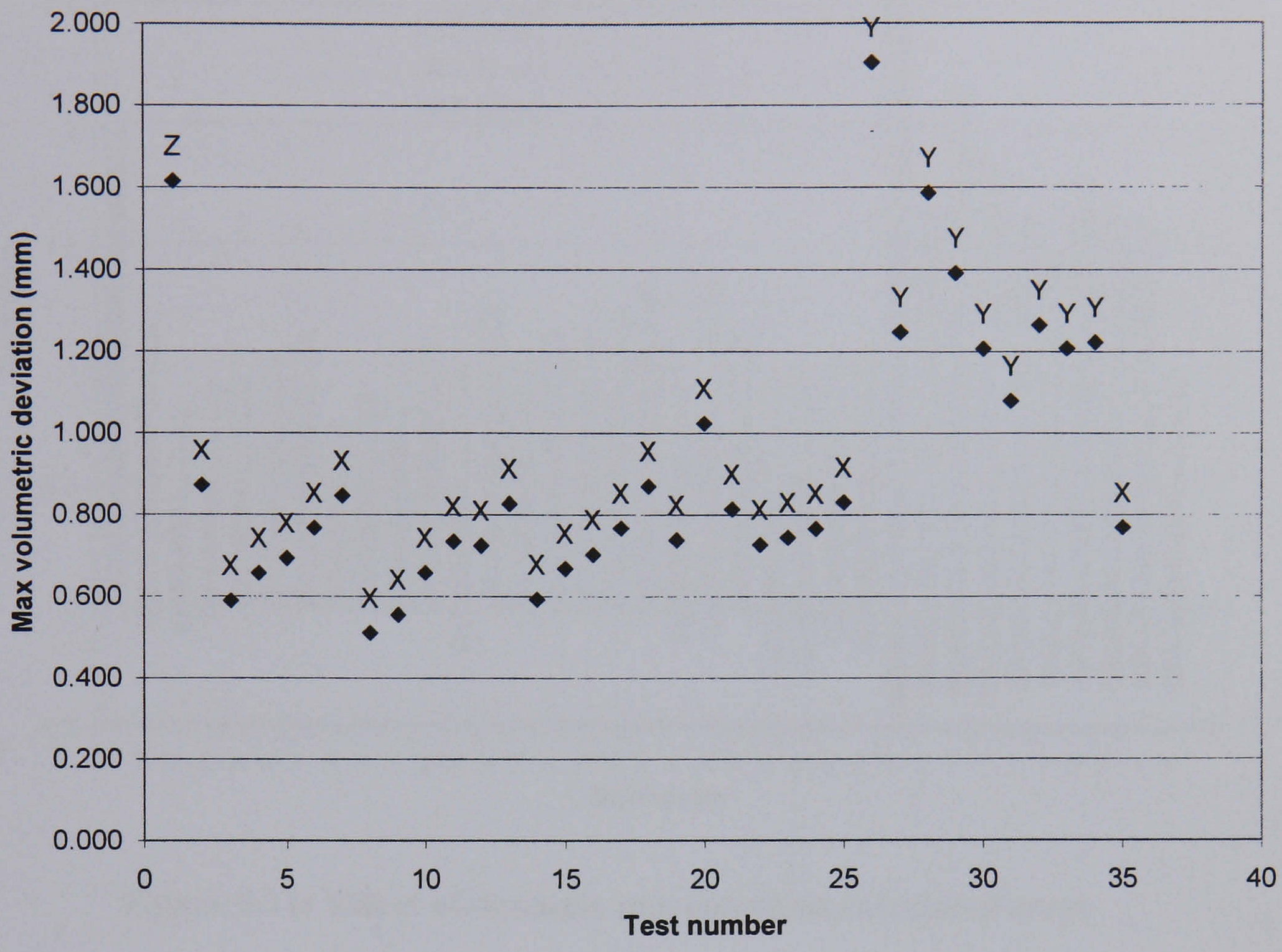


**Figure 9.10: Volumetric errors during dynamic motion**

Figure 9.10 gives the calculated volumetric errors for each test, which is calculated from the individual axis errors (figure 9.11). The axis errors are defined as the range of measurement for the non-moving axes and the deviation from the known stroke for the moving axis. The moving axis is listed as the horizontal axis label in both figures.

It can be seen that the tests where the X-axis was moved give reasonable results. The tests where the Y-axis or Z-axis were moved give much poorer results. This result is intuitive since tracking of movement in the X-axis direction requires less angular movement of the mirrors than in either of the other two axis directions.

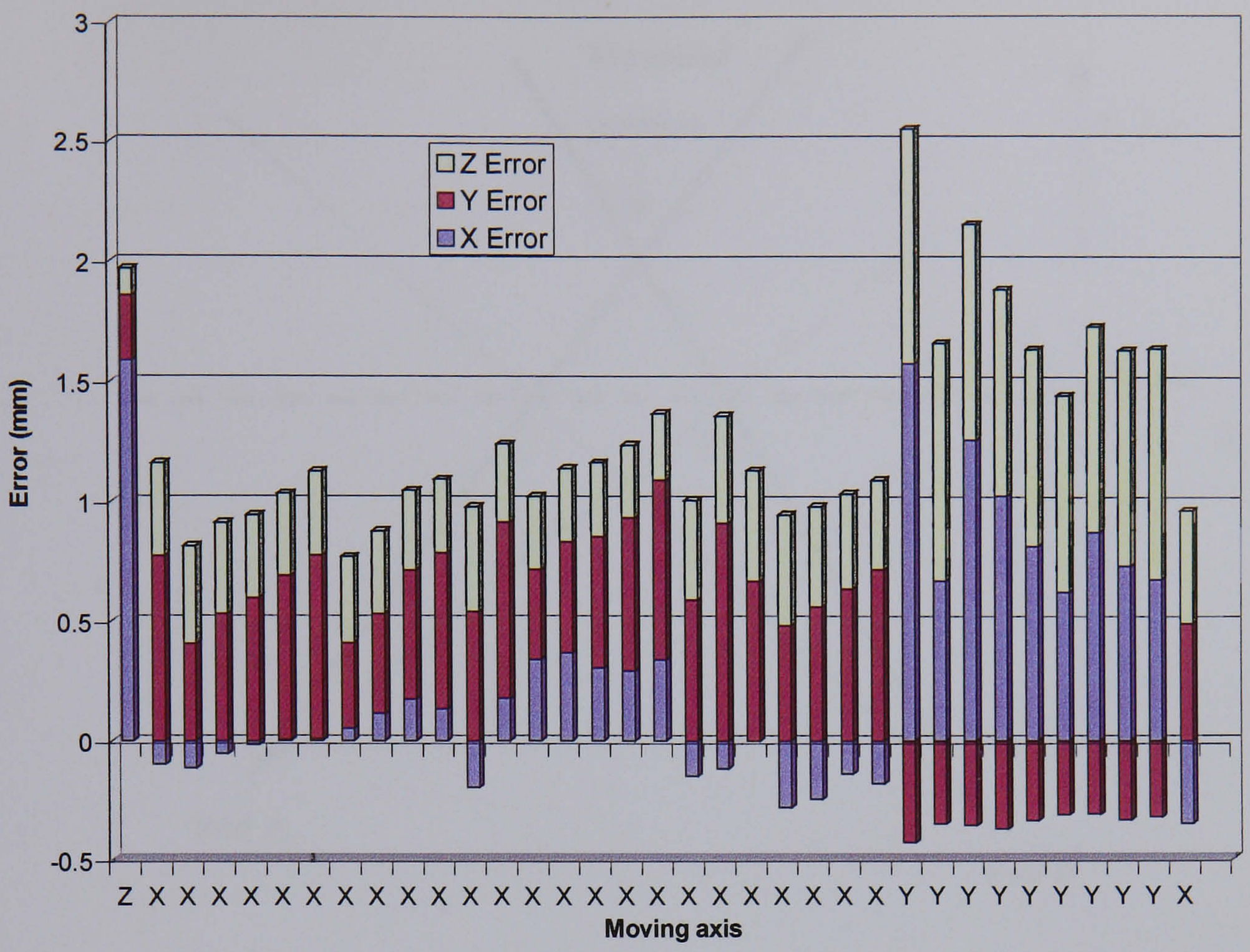


**Figure 9.11: Effect of dynamic movement on calculated error**

Figure 9.11 shows that when the Y-axis is moved, the position of the X-axis is poorly estimated. This is consistent with error introduced due to a lag in readings. Figure 9.12 shows the case where pod A triggers while the optic is at $Y_1$ while pod B triggers when at $Y_2$. The calculated point of intersection of the laser beams is shown on the diagram to be offset in both the Y- and X-axes.

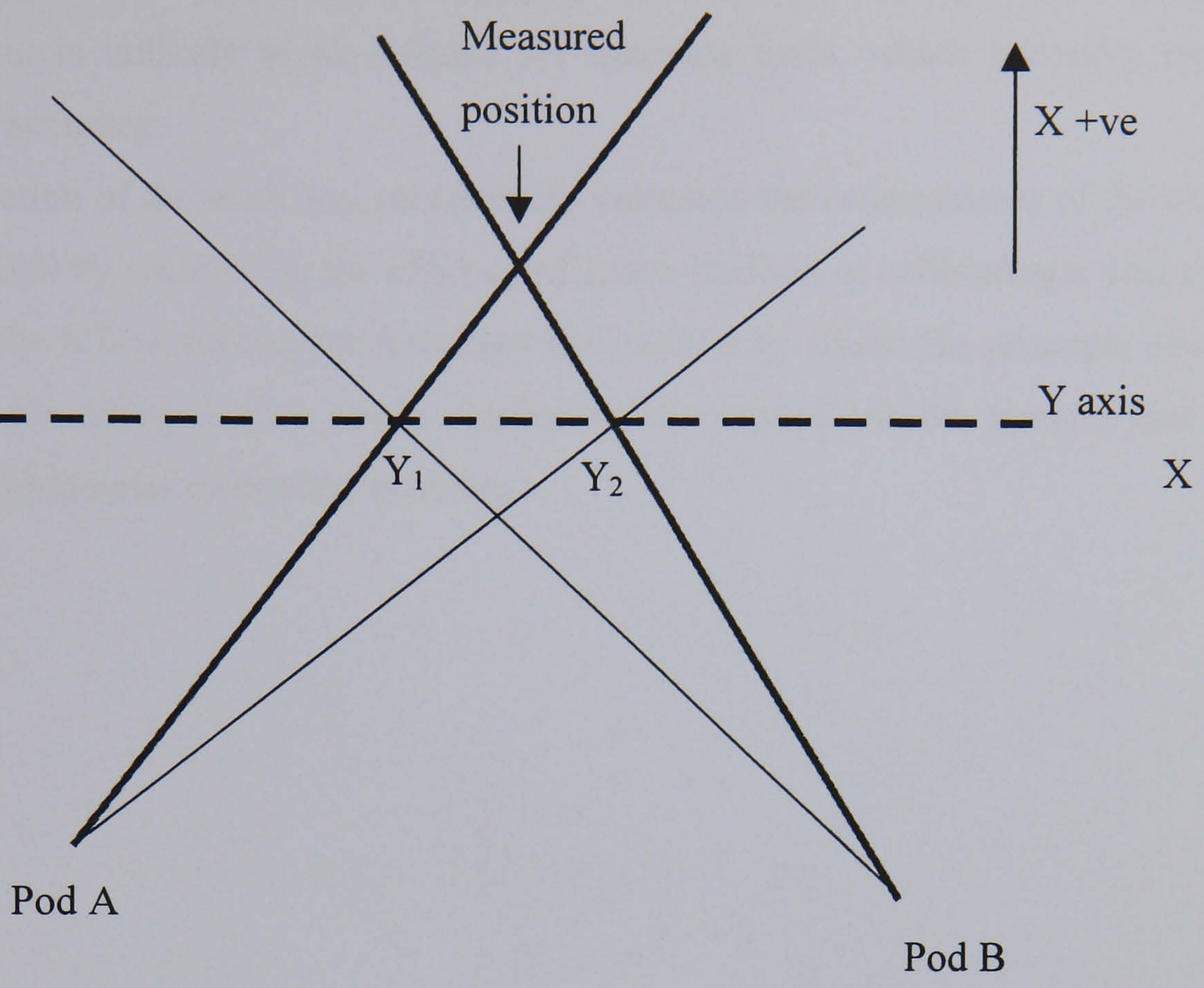


**Figure 9.12: Error due to non-coincident pod triggering**

## 9.04 Summary

The calibration model and technique for calibrating the LaserTrace using an MCG artefact has been shown to give very good results. Compared with the benchmark of one millimetre stationary accuracy and ten millimetres dynamic accuracy the new calibration has shown to give better than fifty percent reduction in errors. The large amount of calibration data available with very little increase in calibration time has a significant effect upon the repeatability of calibration data. The use of averaged data for each target position provides improved performance and does not significantly increase the amount of time required for data collection.

The accuracy benefits of this method have been limited by the resolution of the encoders and the need for the values of the encoders to change as the laser attempts to maintain 'track'. These limitations outweigh the effect of the simplification of the model by assuming perfect manufacture of the laser head. For a machine with better resolution and feedback control such simplifications are likely to become the dominant factor.

The improved performance of the dual LaserTrace system means that it can be used for measurement of Cartesian or non-Cartesian machines whose positioning capability

needs be known to no better than one millimetre. As such, it is appropriate for many robot applications, but is unlikely to be suitable for machine tools, which generally require a higher level of accuracy.

This section of the work has successfully validated the requirements of the objective of section 1.14 (d) by confirming the efficacy of a new method of calibrating a dual tracking laser system. The following chapter discusses the method by which the principle developed in this and the preceding chapter can be applied to other non-Cartesian systems that can be simplified to a parameter estimation problem.

# Chapter 10 Application Of MCG Techniques To Non-Cartesian Machines

The MCG method of collecting calibration data has been shown to be successful for solving the LaserTrace model. The accuracy of the calibrated system was limited by the resolution and stability of the encoder values. The calibration was found more robust than other techniques since the volume of data can minimise the effects of measurement noise. Since the LaserTrace is a non-Cartesian system, it may be supposed that this method of calibration could be applied in a similar way to non-Cartesian machines provided their models were known.

## 10.01 Non-Cartesian manipulators

A joint project between the Precision Engineering Centre at the University of Huddersfield and an industrial collaborator investigated the design, calibration and performance of non-Cartesian machines. The company intended to manufacture a three-legged machine whose configuration is an adapted form of the hexapod (a diagram of a typical hexapod appears as figure 10.1).

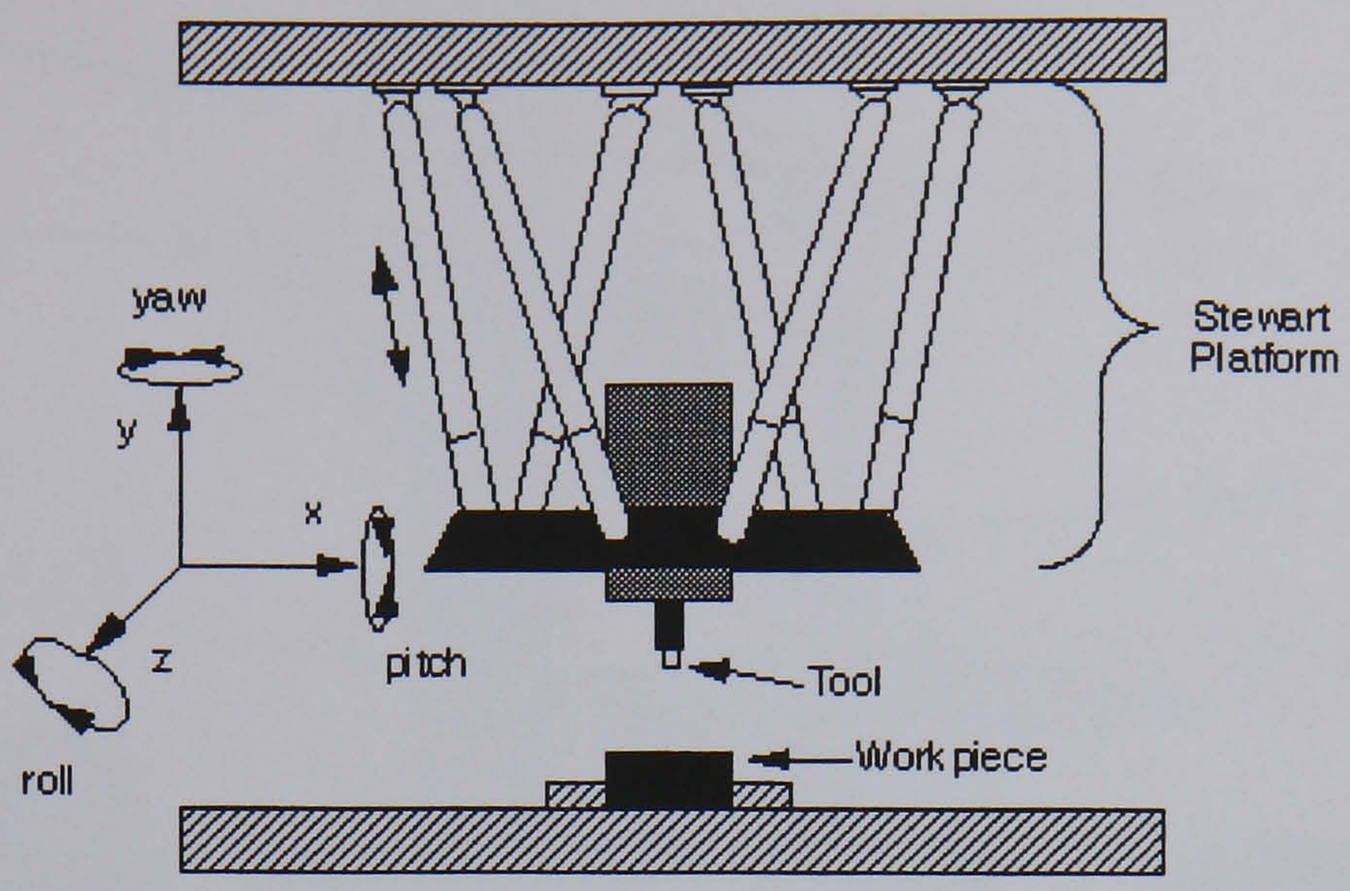


**Figure 10.1: Typical machine of hexapod configuration**

For commercial reasons, the company requires that the machine be calibrated by the end-user without the need for an expensive, dedicated calibrator. With a knowledge of the full model of the system it should be possible to use a standard MCG to perform the calibration.

## 10.02 Description of the UMD

The Universal Measuring Device (UMD) was produced by the company as a prototype test device (figure 10.2). This is a manual machine consisting of a hollow aluminium column fixed to a granite base. Three pivoting 'barn doors' are mounted at the top of the column, two of which operate in the horizontal direction and the third operating in the vertical. The hollow aluminium doors have three pairs of carbon fibre 'stays' attached to them which in turn support a quill, which is also made from carbon fibre. A touch-trigger probe is attached to the bottom of the quill in order to take measurements from the system. The quill and probe remain nominally vertical at all times. Figure 10.2 provides a photograph of the system in operation, probing a ballplate calibration artefact, which is discussed in section 10.06.

The position of the probing point is measured in a coordinate frame defined by the angles of the three barn doors. Position feedback is provided by one-micron resolution tape scales mounted on aluminium arcs, which are fastened to the doors. As a barn door moves the scale pass over a static reader head, which is mounted on the column structure. The amount of movement of the scale can then be converted into an angular displacement for that barn door. These angles are denoted as 'p' and 'q' for the horizontal doors, and 'r' for the vertical door.

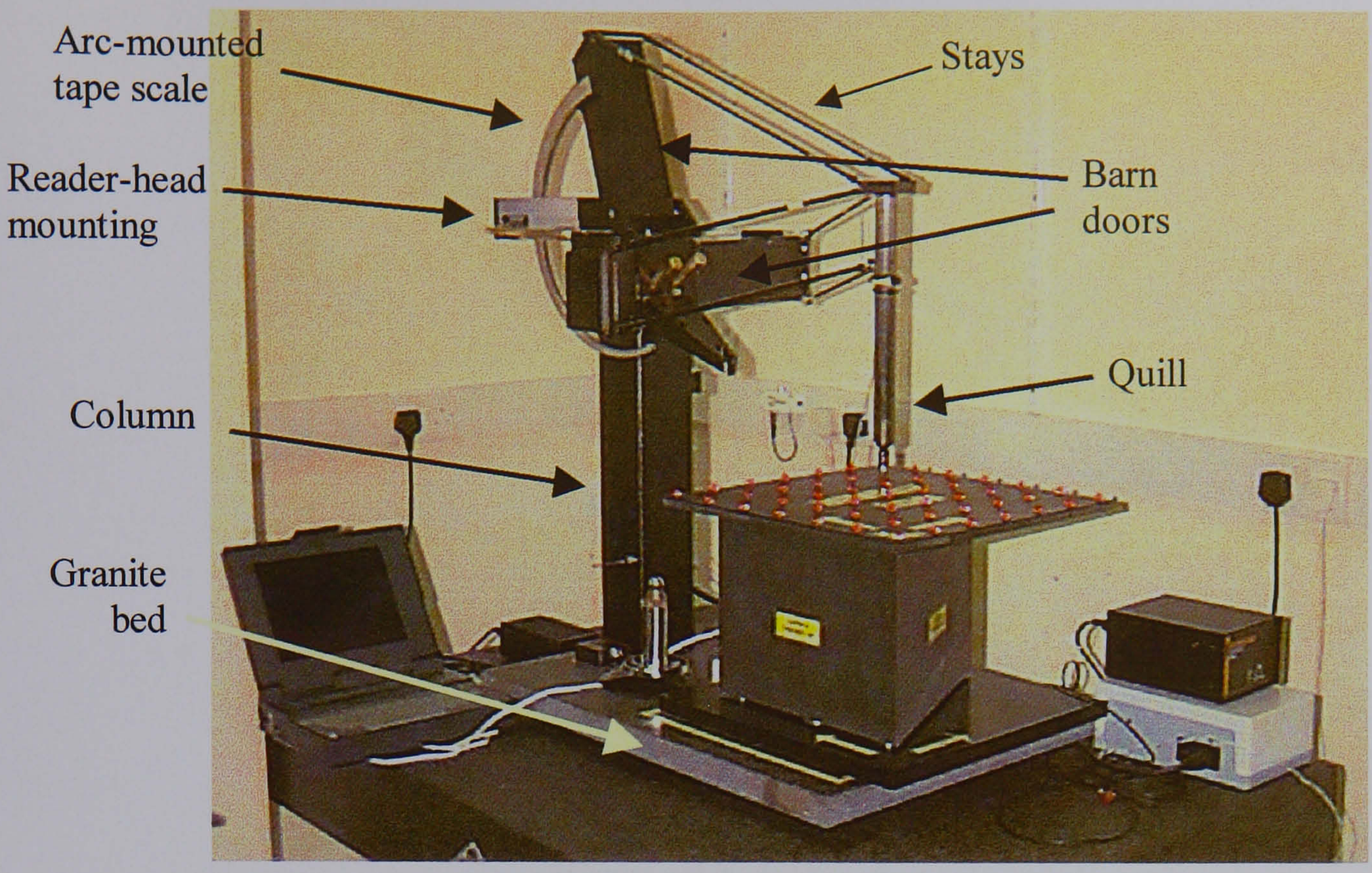


**Figure 10.2: UMD manual non-Cartesian machine**

A simplified diagram of the operation of the UMD is given in figure 10.3. This depicts a single barn door (operating in the vertical) with the UMD in two positions. The door pivots about the hinge at the top of the column, while each of the stays has cup-and-ball joints that provide pivot points at the end of the barn door and at the top of the quill. The stays are made of carbon fibre and the steel balls are glued into recesses using an epoxy resin (figure 10.4). Figure 10.3 further depicts the arc, on which a tape-scale is mounted, passing over the stationary reader head during motion.

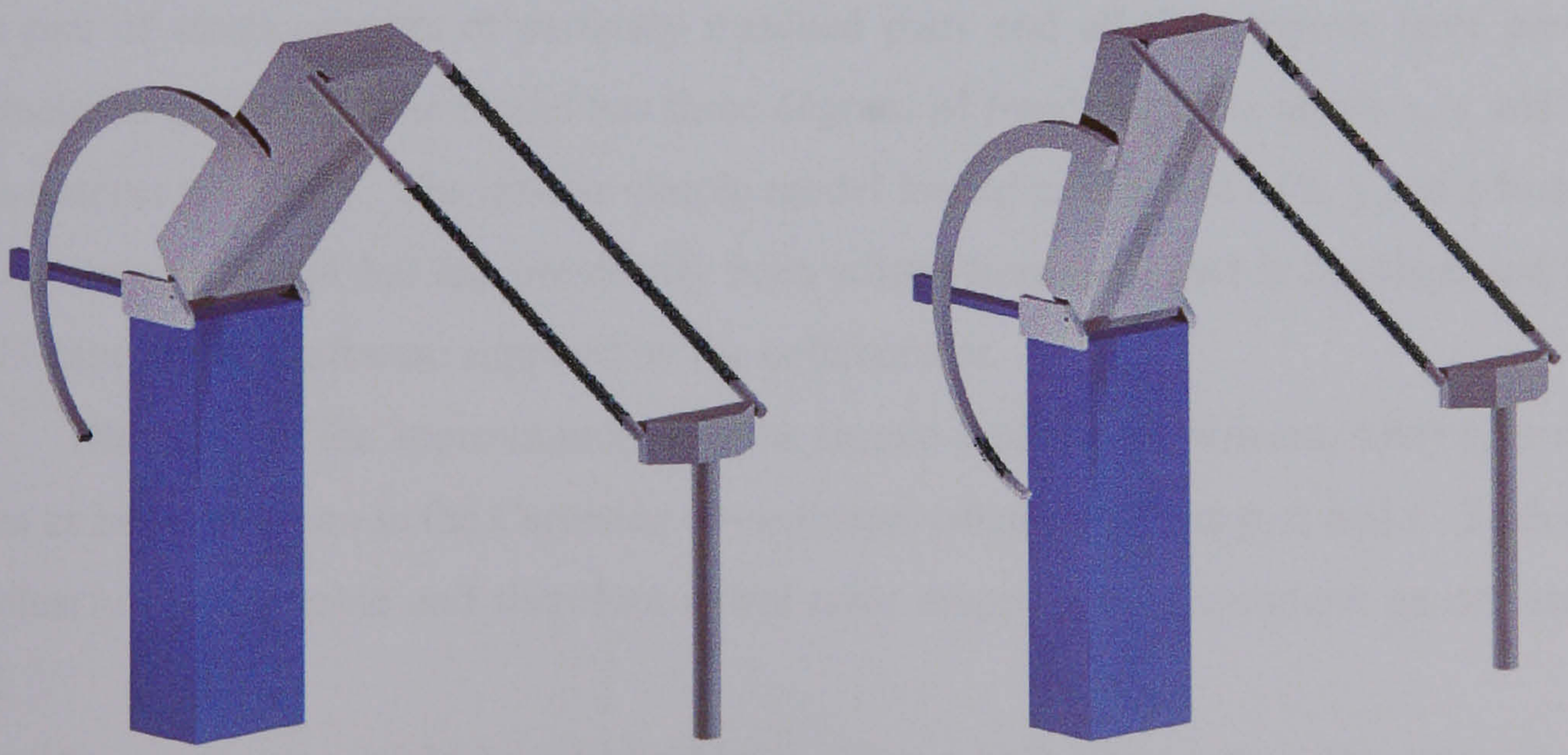

**Figure 10.3: Change in position of a single arm arrangement during motion of quill**

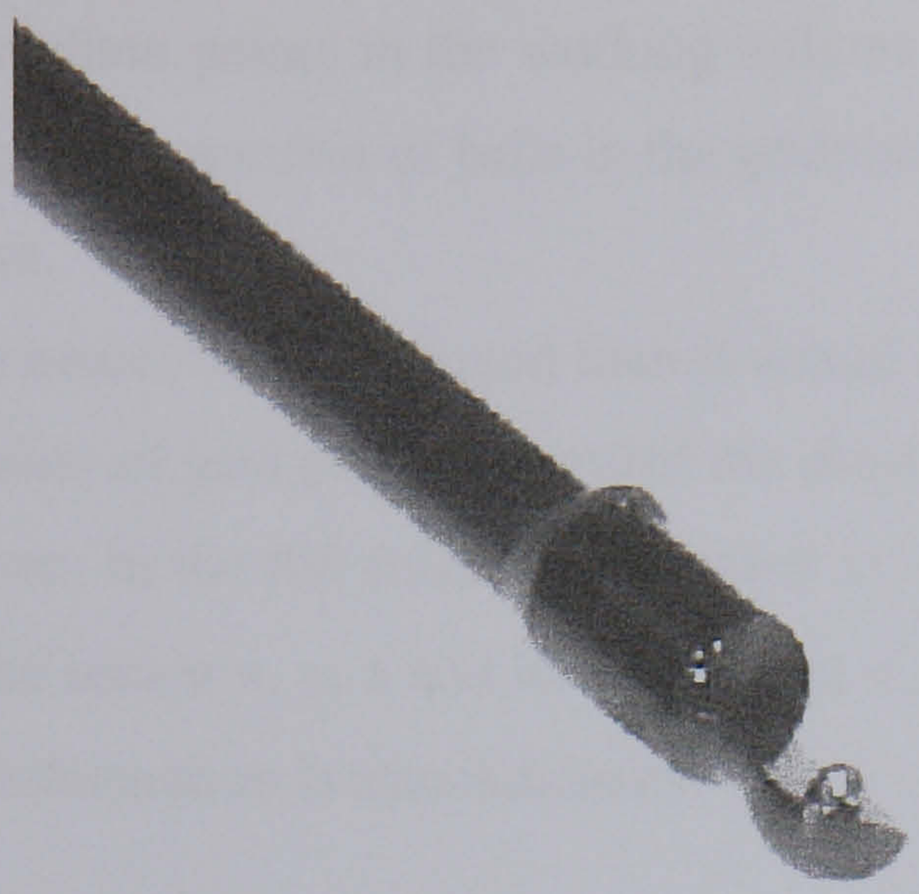

**Figure 10.4: UMD stay**

A repeatable datum for the angles is provided by a kinematic seating on the UMD column, into which a ball on the top of quill assembly can be rested. The seating is designed to have a repeatability of better than five microns.

## 10.03 UMD simple model

From a knowledge of the machine geometry it is possible to use a model of the UMD to convert the measured p, q and r into Cartesian coordinates. The collaborating company produced a 'simple' model of the UMD which made a number of assumptions. In this model each pair of struts consists of perfectly matched pairs and all the supports have perfectly symmetrical geometry. The model has three degrees of freedom, three inputs x, y and z and three outputs p, q and r. The inverse simple model for the calculation of x, y and z from p, q and r is more difficult but has previously been solved iteratively and is implemented in the UMD data capture software supplied by the collaborator.

The effect of the approximations in the simple model is significant. They give rise to errors as large as 8 mm in the Cartesian co-ordinates calculated from p, q and r. Such errors are clearly unacceptable and therefore either error mapping or a complete model must be used.

Error mapping could be achieved by probing a ballplate artefact. However, the time required to probe a sufficient number of balls is prohibitive. Furthermore, the error map will be sensitive to local distortion caused by any measurement error during the probing process.

The accuracy of the three dimensional interpolation routines required in the run time software to find intermediate points in the working volume between the grid points would be highly dependent upon the number of balls in the gridplate. Additionally, the cost of such an artefact is prohibitive.

If the complete model could be found then it would be possible to calculate an error map based on any number of grid points, provided the dimensions of all the components of the machine were known. In the full model it is desired to take the p, q and r and calculate the exact position of the sensor x, y, z and its orientation $\alpha_x$, $\alpha_y$ and $\alpha_z$ about the x, y and z axes. The opposite transformation is also necessary.

## 10.04 UMD full model

To develop the full model, the UMD was considered to be a hexapod in which the six strut lengths are related to x, y, z, $\alpha_x$, $\alpha_y$ and $\alpha_z$. With this description the full model has six degrees of freedom, the six outputs being the six strut lengths. The six inputs consist of the x, y and z coordinates of the sensor, the rotational tilts $\alpha x$, $\alpha y$ of the sensor about the x- and y- axes and its rotation $\alpha z$ about the z-axis. The position of the points of interaction on the barn doors and the sensor assembly must be known to find the strut lengths by performing simple calculations based on Pythagoras. The accuracy of the calculated strut lengths will depend on the accuracy of the assumed positions of the barn doors. These in turn depend on the assumed values of p, q and r. An iterative scheme is therefore required to find a consistent result.

Once a full model is available it is then possible to build an inverse model tc calculate x, y, z, $\alpha_x$, $\alpha_y$ and $\alpha_z$ from p, q and r. Using matrix notation, small changes in the non-Cartesian co-ordinates p, q and r are related to small changes in the Cartesian coordinates x, y and z by the approximate linearised relationships:

$$\begin{bmatrix} \delta p \\ \delta q \\ \delta r \end{bmatrix} = \begin{bmatrix} \frac{\partial p}{\partial x} & \frac{\partial p}{\partial y} & \frac{\partial p}{\partial z} \\ \frac{\partial q}{\partial x} & \frac{\partial q}{\partial y} & \frac{\partial q}{\partial z} \\ \frac{\partial r}{\partial x} & \frac{\partial r}{\partial y} & \frac{\partial r}{\partial z} \end{bmatrix} \begin{bmatrix} \delta x \\ \delta y \\ \delta z \end{bmatrix}$$

Equation 10.1

Which can be written

$$\Delta P = J\Delta X \qquad \text{Equation 10.2}$$

where the matrix $J$ is the Jacobian

$\Delta P$ is the vector of changes in p, q and r

$\Delta X$ is the vector of changes along the Cartesian axes.

It is possible to evaluate the Jacobian at the current location of the head using numerical differentiation and then to find the desired $\Delta X$ from the known $\Delta P$ by matrix manipulation.

Assuming J to be non-singular we have

$$\Delta X = J^{-1}\Delta P \qquad \text{Equation 10.3}$$

Thus an improved X is given by

$$X_i = X_{i+1} + \Delta X \qquad \text{Equation 10.4}$$

This value is then used iteratively to home in on X to the desired accuracy. The technique requires an initial guess of X that is sufficiently close to make the linearised equations valid.

### 10.04.1 The model building technique

A systematic approach was used to construct the model and software to ensure accuracy and ease of extension of the method to other similar problems. [94] The complex geometrical structure was broken down into subassemblies which were analysed separately before the inter-relation between the assemblies were considered. This approach lends itself to storing the data for each subassembly in a separate structure and the development of functions to operate on the subassemblies in a general way.

The stages in developing an analysis of a new machine design are:

1. Define one or more substructures of the machine.
2. Define three reference points in each substructure in local coordinates for the substructure.
3. Devise a method to calculate all other points in local co-ordinates in each substructure. This involves using either geometry or triangulation to find each successive point in

turn. The point found at each step can be used in later steps as one of the three reference points.

The UMD consists of several rigid subassemblies: the supports for the hinges, the barn doors and the sensor head assembly. Each can be assumed to be of fixed geometry provided thermal effects are ignored. The model build is implemented as follows:

1. Define the support structure for the barn doors as a solid three dimensional object in local Cartesian co-ordinates.
2. Define the sensor unit as a solid three-dimensional object in it own local Cartesian co-ordinates.
3. Define each of the barn doors as solid three-dimensional objects in their local Cartesian coordinates.
4. Begin loop
   - Each of the objects are rotated and translated in three dimensional space so that they are in their correct positions based on the simple model of the CMM.
   - The distances between the ends of the stays are then calculated by Pythagoras.
   - These six distances are then compared with the known stay lengths and the errors in length found.
   - Numerical differentiation is then used to find the 6*6 Jacobean relating small changes in the stay lengths to small changes in p, q, r and the three rotations of the sensor unit $\alpha_x$, $\alpha_y$ and $\alpha_z$.
   - The Jacobean is inverted and used to calculate the changes in p, q, r and the rotations of the sensor $\alpha_x$, $\alpha_y$ and $\alpha_z$ to reduce the errors in the stay lengths.
5. The loop is then repeated iteratively until the parameters are within tolerance.

A brief pseudo-code of the model is presented as Appendix F.

## 10.05 UMD calibration philosophy

For the full model to provide correct answers it is essential to have knowledge of the exact dimensions of each structural element. The ideal method of ensuring positioning accuracy in the UMD is to manufacture all components of the machine with known dimensions and assemble with zero tolerance. This solution is inappropriate, since the higher manufacturing cost does not meet with the company's need for an inexpensive system..

If the machine cannot be manufactured to explicit dimensions the errors must be assessed after assembly. This can be achieved by calibration against a known standard, such as a CMM. This method has two major drawbacks. The first is that the machine is designed to be built on the user's site and be inexpensive to calibrate. The need for a large CMM to calibrate the structure would invalidate this. The second problem derives from the configuration. Because of the highly non-linear nature of the machine the necessary error map would have to be of a very fine resolution. This would typically require a grid of up to $50 \times 50 \times 50$ points on a machine of 500mm cube working volume. This requirement for such a large number of measured points is extremely prohibitive, requiring automatic techniques such as tracking interferometers (section 2.02.8), automatic theodolites (section 2.02.4) or RoboTrak (section 2.02.6). This is again contrary to the philosophy of the company whereby standard metrology equipment could be used to calibrate the UMD so that the calibration cost to the customer could be as low as possible.

For these reasons, the MCG method of calibration is ideally suited. In order to validate the technique a ballplate artefact was manufactured at the collaborating company and measured on a high accuracy CMM. This allowed comparative data between the MCG calibration and the known values of the ballplate.

## 10.06 Three-dimensional ballplate artefact

The ballplate is a nominally square carbon-fibre plate. On it are mounted forty-nine ruby balls, of the type used on large probe tips. The plate can be repeatably raised to different heights using separators with kinematic locators to provide a 3-D grid of 7×7×6 data points. Because of problems with manoeuvring the UMD to extremities of the working volume, the grid was restricted to 5×5×5 for calibration during this testing phase. Figure 10.5 represents the ballplate used for this purpose, the terminology is given in table 10.1.

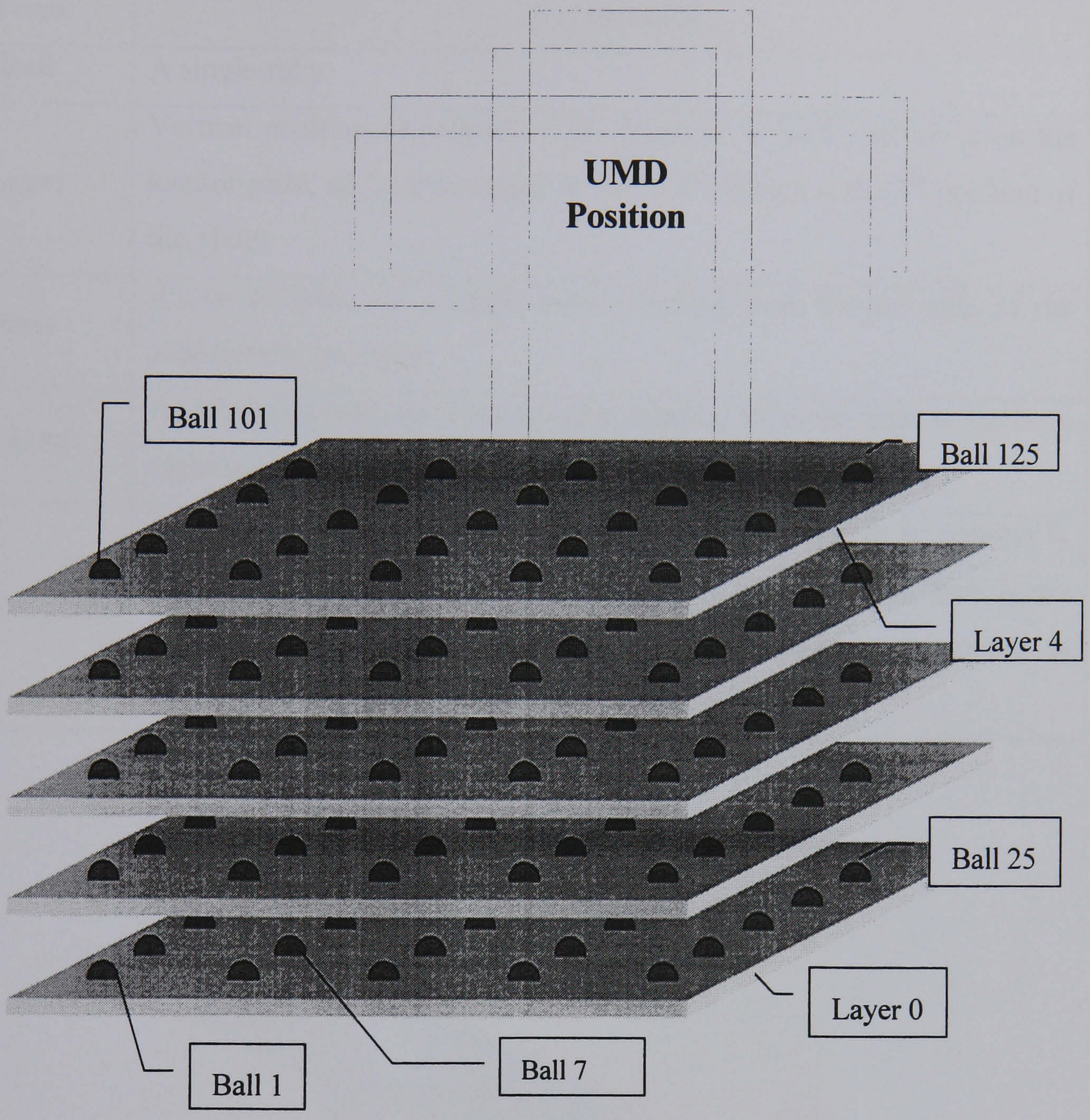


**Figure 10.5: Ballplate artefact numbered for calibration**

On the base of the plate are three locating feet that each consists of a ball bearing. Each ball then sits on a locator on the base, the locator being made from three cylinders, which would typically be found in a roller-bearing. Figure 10.6 shows the two parts of the locator, attached to different separator triangles. A reference position for the artefact is provided by an aluminium plate bolted to the granite bed. This plate provides three-point location using the same roller-locators as on the artefact.

**Table 10.1: Terminology for 3-D ballplate artefact**

| Term | Explanation |
|---|---|
| **Ball** | A single ruby |
| **Layer** | Vertical position of ballplate. This starts at 'layer 0', which is on the locator plate, and can be raised to 'layer 4' (Which is the 5$^{th}$ position of the plate) |
| **Row** | A row of balls, on a single layer, running from the left side of the calibrator to the right. |
| **Column** | A column of balls, on a single layer, running from the front to the back of the calibrator. |
| **Ball Number** | This references each ball. Ball 1 is that located at row 0, column 0, layer 0.The balls are then counted in rows, then columns, then layers up to the maximum grid point. For the full plate this corresponds to ball 294, for the restricted grid this is ball 125. |

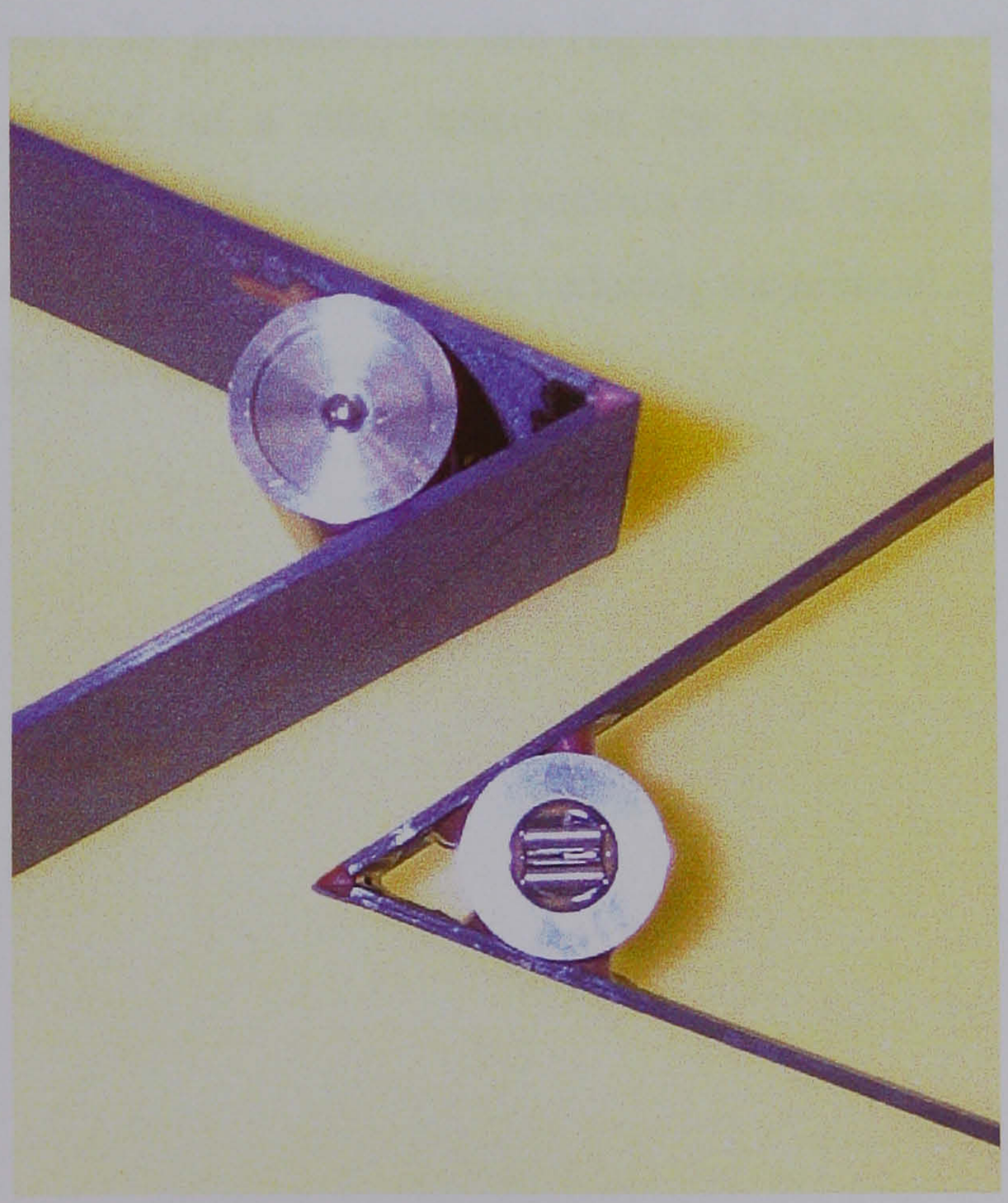

**Figure 10.6: Locator on ballplate artefact**

In order to allow three-dimensional data to be acquired, a number of triangles utilising the same locator techniques were also manufactured (figure 10.7). This allowed data to be taken

at six discrete vertical levels, which gave a total of 294 target positions through the working volume. Again, this was restricted to five layers during testing because of the construction of the UMD.

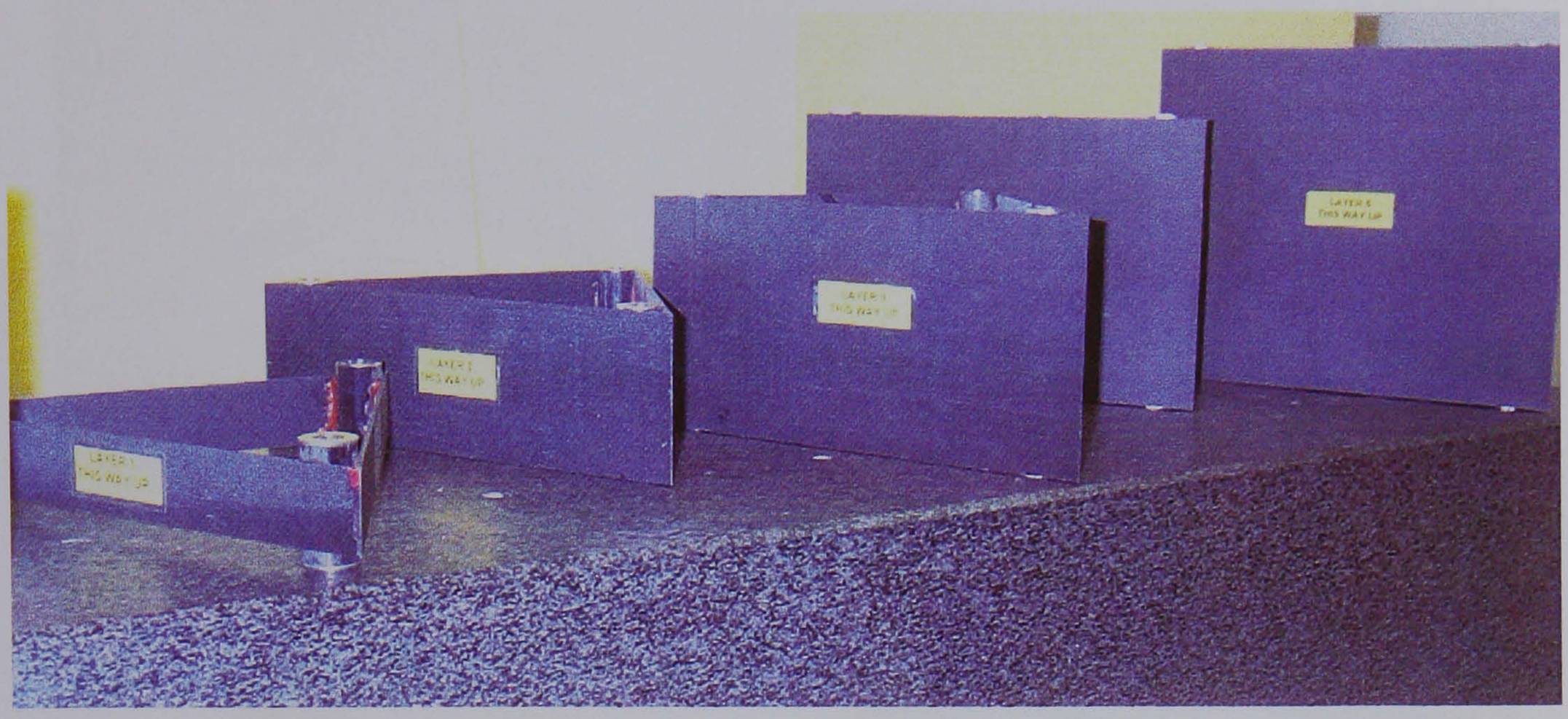

**Figure 10.7: Ballplate separators**

A minimum of four measurements is required to describe a sphere using a standard touch-trigger probe. To improve the efficiency of probing the ballplate, a special cup (3bcup) was manufactured to acquire the measurement data (figure 10.8). This cup consisted of three balls which, when seated on a ruby sphere on the ballplate, provided a repeatable measurement position. Using this device, the position of the centre of each ruby could be found with a single measurement, considerably reducing the amount of time required to find the position of each ball on the artefact.

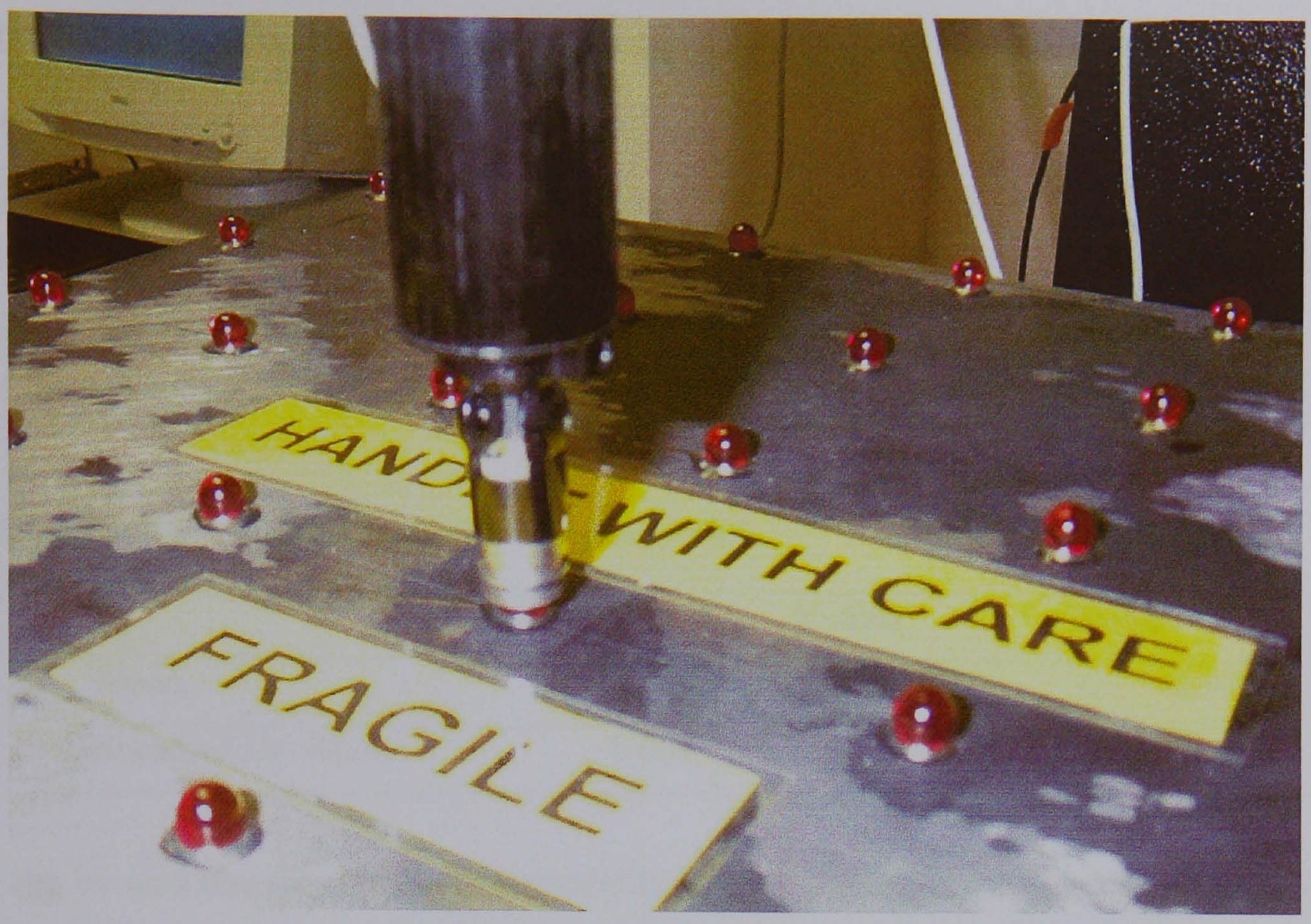


**Figure 10.8: Three ball cup (3bcup) seated on ballplate**

### 10.06.1 UMD vibration test

A simple test was performed to determine the influence of vibration on positional measurement. The UMD was positioned on a single ball using the 3bcup and a continuous log of position was then recorded. This data was then post-processed, using Excel, to determine the variation in measurement brought about by vibration. It was discovered (table 10.2) that any change is of the order of 1μm, and so can be ignored.

**Table 10.2: Short-term positional change**

| | X-Axis | Y-Axis | Z-Axis |
|---|---|---|---|
| Mean | 266.972 | 254.381 | 227.8343 |
| Standard Deviation | 0.000 | 0.000 | 0.000 |
| Range | 0.000 | 0.001 | 0.001 |
| Count | 14546 | 14546 | 14546 |

### 10.06.2 Repeatability of three-ball cup

The company specified a repeatability of better than five microns for the locators. Tests were performed on the UMD to validate this claim. The ballplate was located on the kinematic location base plate. The 3bcup was used to probe ball 1, moved away and probe again. This was repeated to obtain 25 data points. The following statistical data (table 10.3) describes the repeatability at this point.

**Table 10.3: Repeatability of seating using ball 1**

| | X-Axis | Y-Axis | Z-Axis |
|---|---|---|---|
| Mean | 84.166 | 41.476 | -8.976 |
| Standard Deviation | 0.002 | 0.002 | 0.003 |

It can be seen that the statistical repeatability was better than five microns for this test. Since this value constitutes the combined repeatability of the UMD and 3bcup it can be inferred that the repeatability of the 3bcup is within this value.

### 10.06.3 Repeatability of layers

To determine the repeatability of the ballplate location the ballplate was positioned on the three kinematic locators on layer 0. Ball 13 was probed 6 times, the plate removed, relocated and ball 13 probed a further 6 times. This was repeated until 25 data points had been taken. Table 10.4 presents the statistical repeatability of the process. Again, the statistical repeatability, which combines that of the UMD, 3bcup and layer locators was better than five microns.

**Table 10.4: Repeatability of layers using ball 13**

| | X-Axis | Y-axis | Z-Axis |
|---|---|---|---|
| Mean | 206.545 | 165.158 | -6.445 |
| Standard Deviation | 0.001 | 0.002 | 0.001 |

The test was then repeated by using layer 2 to introduce an additional uncertainty, with probing carried out on ball 88. Each time both the separator and the ballplate were removed

after six measurements had been taken. The results (table 10.5) again show repeatability of better than five microns.

**Table 10.5: Repeatability of layers using ball 88**

| | X-Axis | Y-Axis | Z-Axis |
|---|---|---|---|
| Mean | 206.299 | 160.138 | 164.259 |
| Standard Deviation | 0.001 | 0.001 | 0.001 |

The same test was repeated on ball 125, which required the use of the tallest separator. It was found that the repeatability was very poor (table 10.6).

**Table 10.6: Repeatability of probing ball 125**

| | X-Axis | Y-Axis | Z-Axis |
|---|---|---|---|
| Mean | 332.483 | 284.677 | 227.152 |
| Standard Deviation | 0.011 | 0.049 | 0.009 |
| Range | 0.040 | 0.175 | 0.032 |

Because the repeatability was poor it was decided to perform a repeated measurement on the same ball, but without relocation of the ballplate or separators. This would isolate the repeatability of the UMD and 3bcup for this grid position. Great care was taken to attempt to achieve the best possible results from the system. The results (table 10.7) show that the poor repeatability from the previous test is present and so can be attributed to the UMD, rather than the repeatability of the locators.

**Table 10.7: Repeatability of seating on ball 125**

| | X-Axis | Y-Axis | Z-Axis |
|---|---|---|---|
| Mean | 332.477 | 284.641 | 227.150 |
| Standard Deviation | 0.006 | 0.034 | 0.009 |
| Range | 0.018 | 0.099 | 0.026 |

It was noted during the test that the 3bcup seemed to rise out of its seating on the ruby ball. The reason for this position-dependent repeatability highlights the existence of singularities.

At a singularity, the UMD can no longer be relied upon to perform repeatably since the system theoretically requires no force for it to move. This flaw in the design of the UMD can be overcome by ensuring that the working volume of the machine is defined such that the UMD does not meet, or come close to one of these singularities during normal operation.

Since the singularities have most effect on the upper level near the UMD, the ballplate position was relocated further from the column, effectively moving the simple model position of ball 1 from $(84.171 \quad 41.487 \quad -8.976)$ to $(77.595 \quad 11.362 \quad -6.505)$.

Further tests were then undertaken to evaluate the repeatability of the UMD throughout the machine. The repeatability is taken from the standard deviation of twenty samples (table 10.8). The points mainly consisted of the balls in the top row for the top two layers, which are closest to a singularity and previous tests had shown to be the least repeatable. Where the repeatability was particularly poor, the test on the ball was repeated.

**Table 10.8: Repeatability of seating on selected balls**

| Ball | X (μm) | Y (μm) | Z (μm) |
|---|---|---|---|
| 50 | 2 | 1 | 1 |
| 80 | 4 | 1 | 0 |
| 85 | 4 | 5 | 2 |
| 90 | 30 | 103 | 19 |
| 95 | 8 | 15 | 1 |
| 95 | 7 | 17 | 1 |
| 100 | 7 | 23 | 1 |
| 100 | 6 | 19 | 1 |
| 105 | 6 | 4 | 1 |
| 110 | 4 | 4 | 2 |
| 115 | 17 | 25 | 6 |
| 120 | 26 | 88 | 19 |
| 120 | 13 | 36 | 7 |
| 125 | 7 | 33 | 5 |

Although moving the ballplate produced better repeatability at several points, the performance remained unacceptable at others. This problem could only be overcome by redesign of the machine, or by further restriction of the working volume. This was not practical since the grid had already been reduced and it was physically impossible to mount the plate further from the column.

## 10.07 Ballplate calibration of UMD

### 10.07.1 Test procedure

The calibration routine built into the UMD software was used to collect observed data from all 125 balls. This was immediately followed by two further calibrations. All data was saved into separate files for comparison.

Figure 10.9 shows the temperature during testing, with a marker indicating the start of each test. Even with the reduced number of probing positions and using the 3bc, the device is relatively time-consuming to use for gaining calibration data, taking of the order of twenty minutes for measurement of all one hundred and twenty five spheres. The duration of this measurement is high because the UMD is quite delicate to operate, especially when on the higher levels of the artefact. Although the shape of the graph shows changing temperature the overall temperature range is 0.2°C throughout the testing phase.

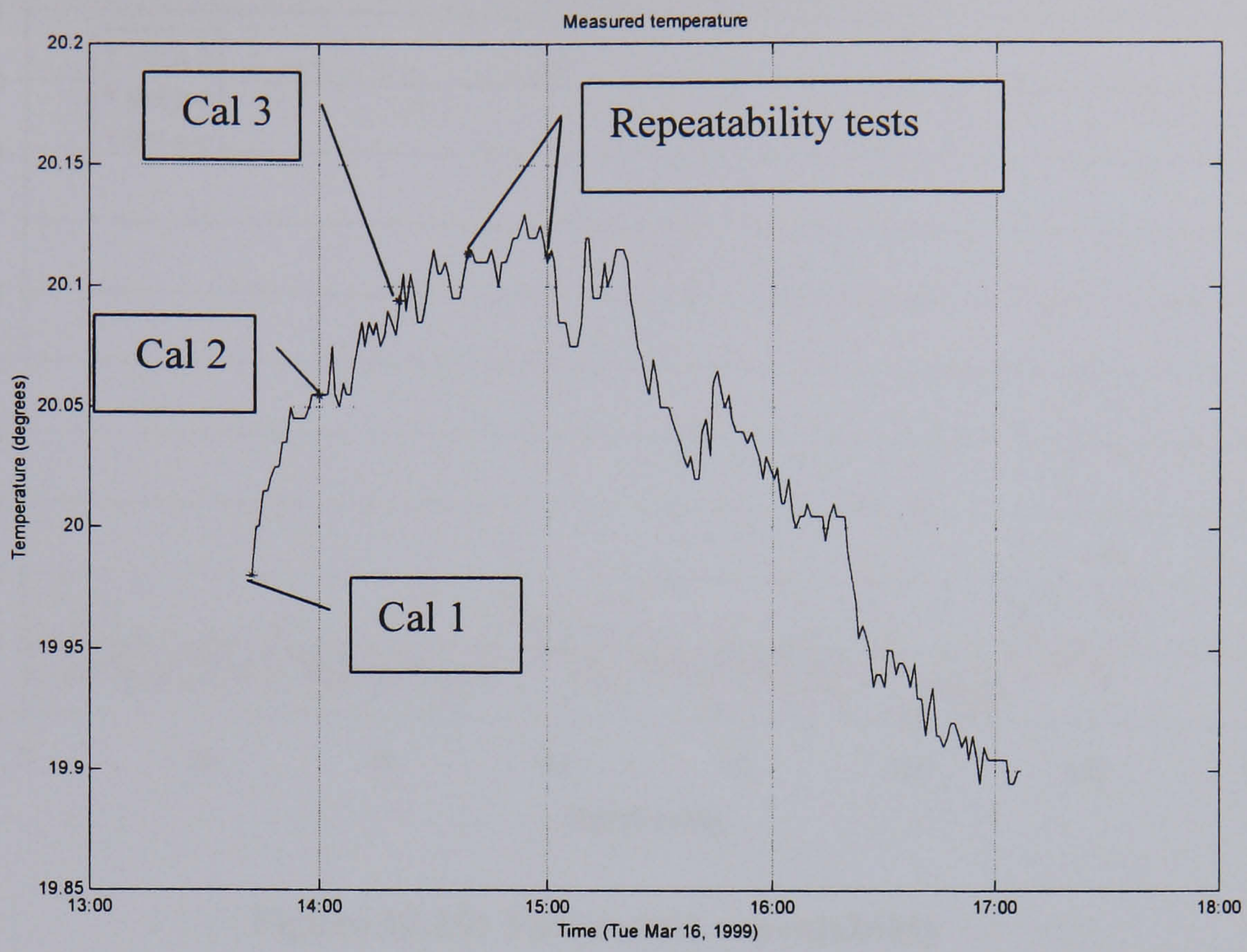


**Figure 10.9: Temperature changes during calibration time**

## 10.08 Results of calibration

The observed data from the three calibrations was put into Excel. This was then used to compare the values of the Cartesian coordinates for each ball (figure 10.10). It was found that the repeatability was within ±20μm for most points, with the greatest difference being on row five in the top two layers. This is consistent with the repeatability tests of the previous section.

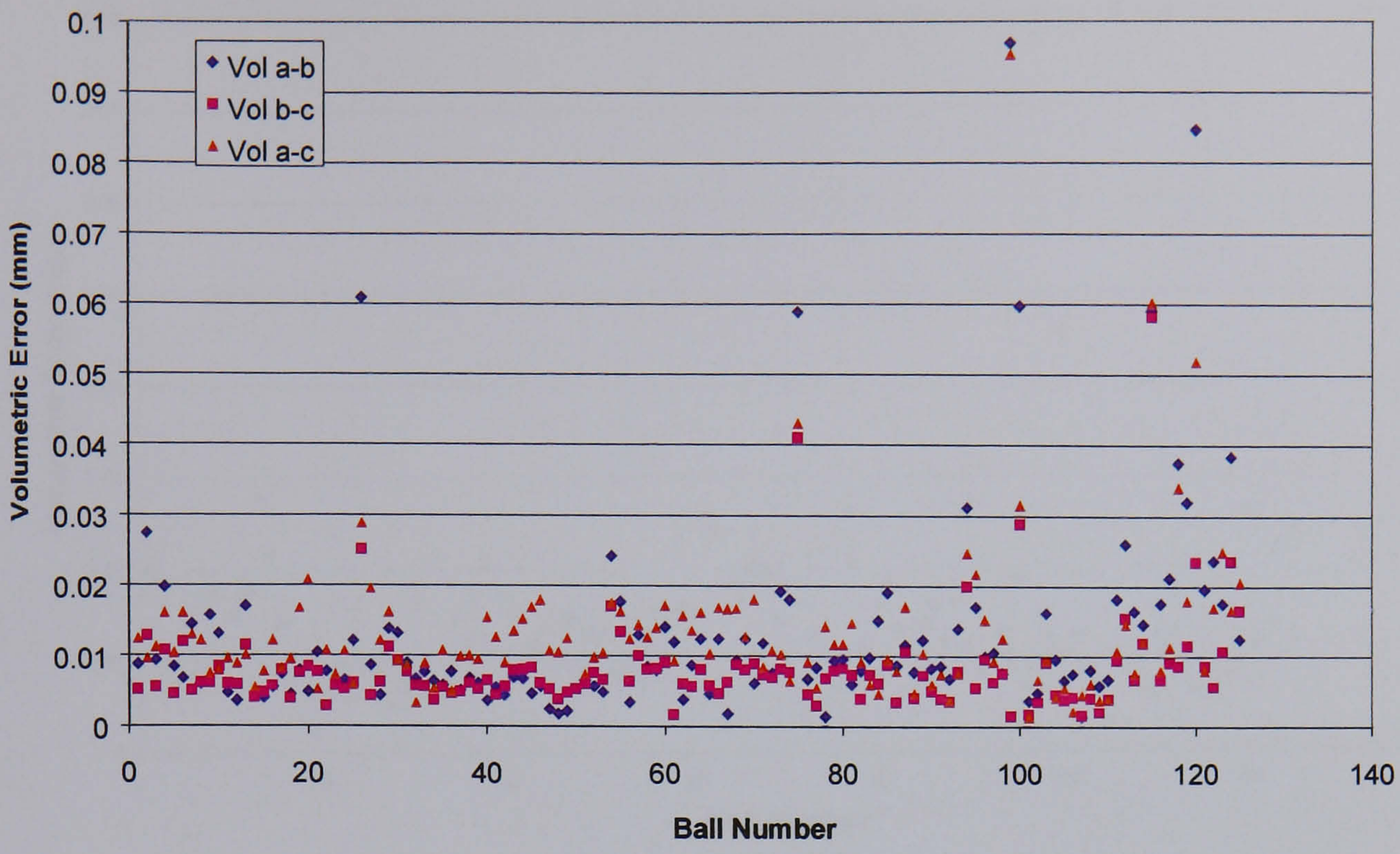


**Figure 10.10: Volumetric repeatability**

### 10.08.1 Calibration validation

A set of observed data was constructed from the three sets of data, and some further data that was taken to obtain a statistical measurement of the worst points. This data was then transformed into error maps using software written in PASCAL. Because the ballplate did not provide a regular grid, due to manufacturing errors, the grid had to be regularised within the software.

The 125 balls were probed, with the Cartesian positions being calculated from the new error map and recorded for evaluation. These values were then compared to the adjusted grid values. It can be seen from figure 10.11 that the volumetric accuracy was within 30μm for most points on the grid. The three balls whose accuracy is much worse than this correspond to points where the repeatability during the calibration is relatively poor.

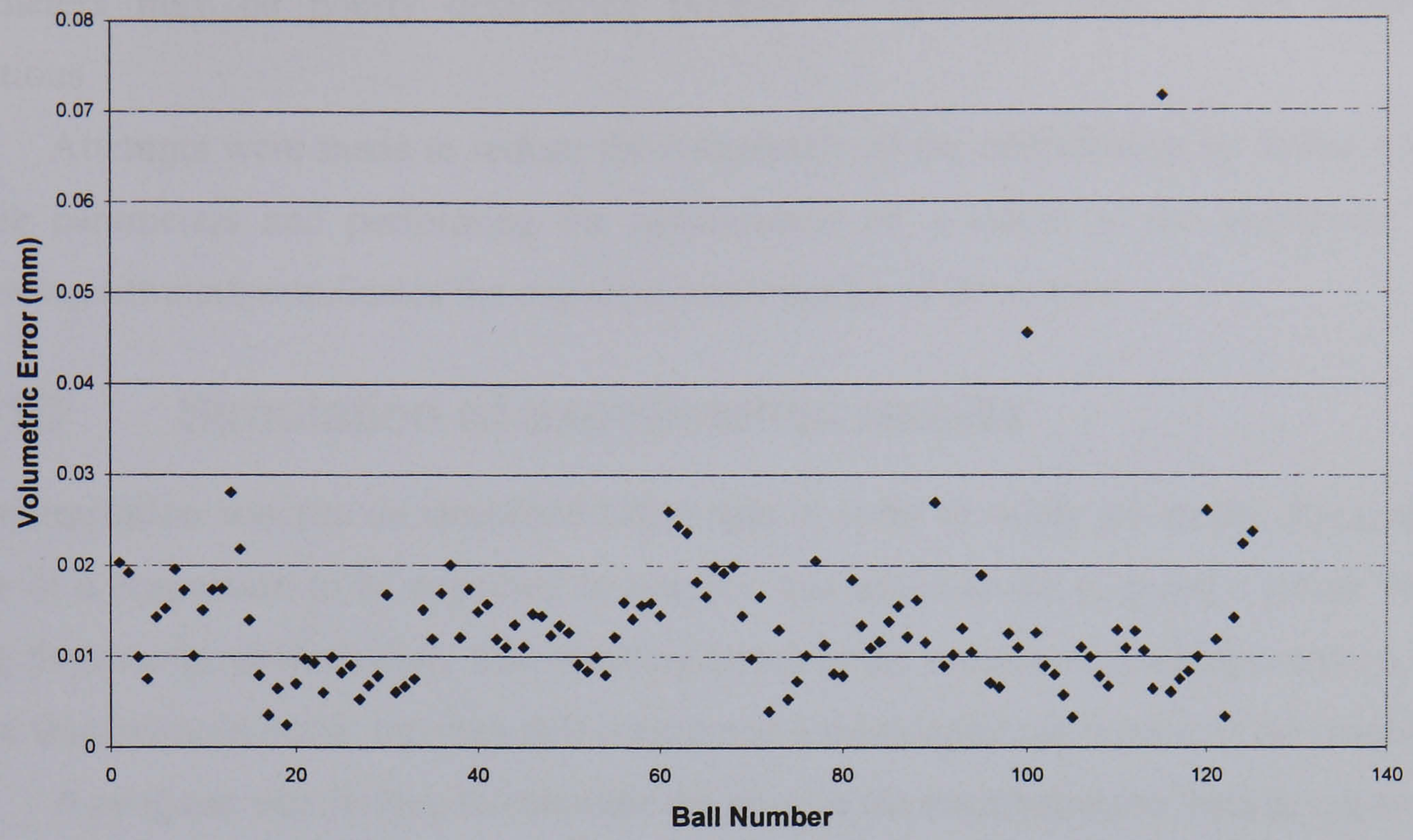


**Figure 10.11: Volumetric accuracy using ballplate test**

## 10.09 MCG on UMD

The results of the ballplate measurement indicate the likely accuracy achievable from the UMD. This data can be used for validation of the MCG method of calibration.

Measurement data from an MCG calibration was acquired. Again, this was not simple due to the delicacy of the prototype UMD. Initially, the force required to record a reading using the touch-trigger probe was so great that it produced deflection of the structure. Furthermore, the device took false measurements due to triggering on the fork of the MCG, rather than the measurement anvil. This problem was reduced by using a probe of a longer length, which requires less lateral force to trigger the mechanism.

Having collected the data it was necessary to use the reverse model of the UMD to calibrate the elements of the device using the technique described in section 8.05. Software written in Borland Pascal was used to achieve this. However, the model is extremely complex and required optimisation on 32 parameters. It was found that the length of time required to perform the optimisation was of the order of several weeks.

Determining the unknown parameters is problematic when attempting to resolve such a large number of parameters using optimisation from a single data source, such as the machine checking gauge. The problem is compounded by the likelihood that some of the

parameters may be poorly determined because of ill-conditioning of the modelling equations.

Attempts were made to reduce the complexity of the optimisation by fixing several of the parameters and performing the optimisation on a subset of the unknowns. The following simulation indicates the expected performance of the system.

## 10.10 Simulation of experimental results

An optimisation was run on simulated MCG data in order to verify the model. Rectangular noise of a magnitude to be expected in practice was added to the p, q and r values before using them in the optimisation. The resulting errors in the estimated parameters were a little larger than without noise, but they still constituted a meaningful calibration of the machine.

A program was written to calculate the error in the transformation from p, r, q to x, y, z for the whole working volume. Ideally, the errors at each point of the volume should be extremely small, but it is expected that larger errors will be present in regions of the volume not adequately covered by the spheres.

As with the optimisation method for the LaserTrace system, it was found that incorrect values of the parameters can give a low objective functions and the correct transformation between p, q, r and x, y, z. This implies that it is possible to include more parameters in the optimisation than are well determined, yet arrive at an optimisation to an incorrect model (in a physical sense) that correctly calibrates the machine in terms of the transformations. Such an optimised solution should be valid at least for the purpose of calibration. Some parameters may be well determined whilst others are related to each other by unknown equations. It is the robustness of the Simplex method that makes this possible.

Figure 10.12 and figure 10.13 give graphically the progress of optimisation in tests using three gauges with 30 points on each designed to cover the extremities of the volume. Table 10.9 summarises the results with and without simulated noise being added to p, q and r. It can be seen that many thousands of iterations are required for the objective function to minimise, requiring many hours of computation time on a Pentium 100.

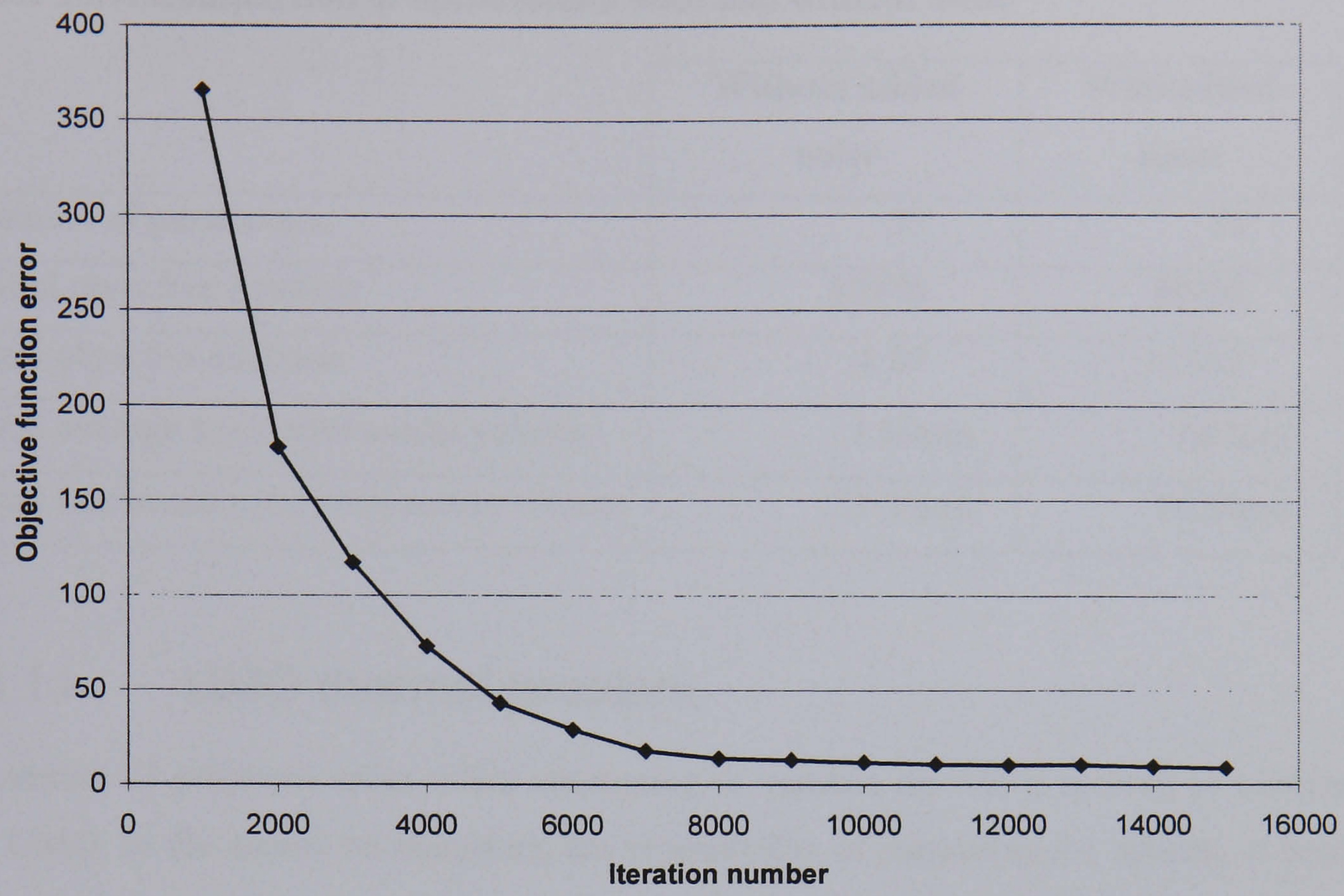


**Figure 10.12: The progress of the objective function during optimisation**

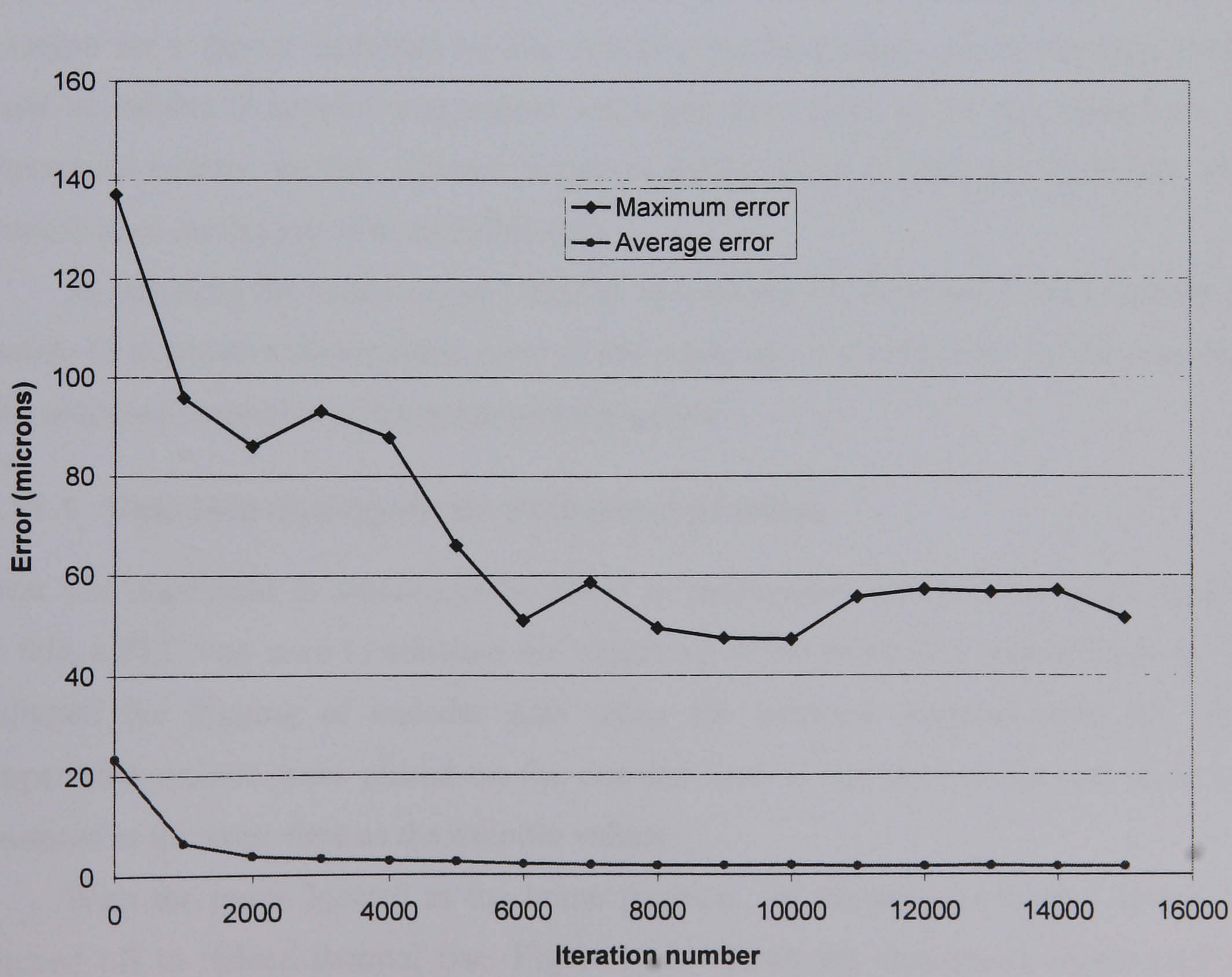


**Figure 10.13: Progress of the errors in X,Y,Z during optimisation**

**Table 10.9: Comparison of optimisation with and without noise**

| | Without added noise | With added noise |
|---|---|---|
| Number of parameters | 33 | 33 |
| Initial objective function | 87370 | 88798 |
| Final objective function | 8.69 | 113.42 |
| Final average x,y,z error across volume | 1.60μm | 1.67μm |
| Final maximum x,y,z error across volume | 51.50μm | 18.30μm |

## 10.11 UMD thermal problem

A number of problems arose while attempting to validate the MCG method of calibrating the UMD. In the course of examining the repeatability of measuring the spheres, it became clear that the earlier tests had only validated the short-term repeatability of probing the artefact. It became clear that the device is extremely sensitive to temperature variation, even within the temperature-controlled room in which the tests were performed. The UMD is a prototype for a device intended for use within a machine shop and so the final product would be subject to greater temperature variations than those of the test conditions. The temperature control facility allowed experimentation from a relatively thermally stable datum to give correlation with modelled data.

By adapting the model of the UMD to incorporate the thermally induced errors, it is possible to determine the resultant error at the probe tip. It would therefore be possible to make software correction of the measurement values.

### 10.11.1 Estimate of magnitude of thermal problem

A test was performed to determine the effect of temperature change on encoder readings. For this, a PLC was used to simulate the triggering of the probe at a regular interval. This facilitated the logging of encoder data using the software supplied with the UMD. Temperature sensors were placed on the encoder arcs of the three doors and these were monitored at the same time as the encoder values.

With the probe located at the home position, the temperature control system was switched off to induce thermal rise. Figure 10.14 shows the changes in temperature and

angles for the duration of the test. The change in temperature appears to correlate with the change in encoder values on all axes.

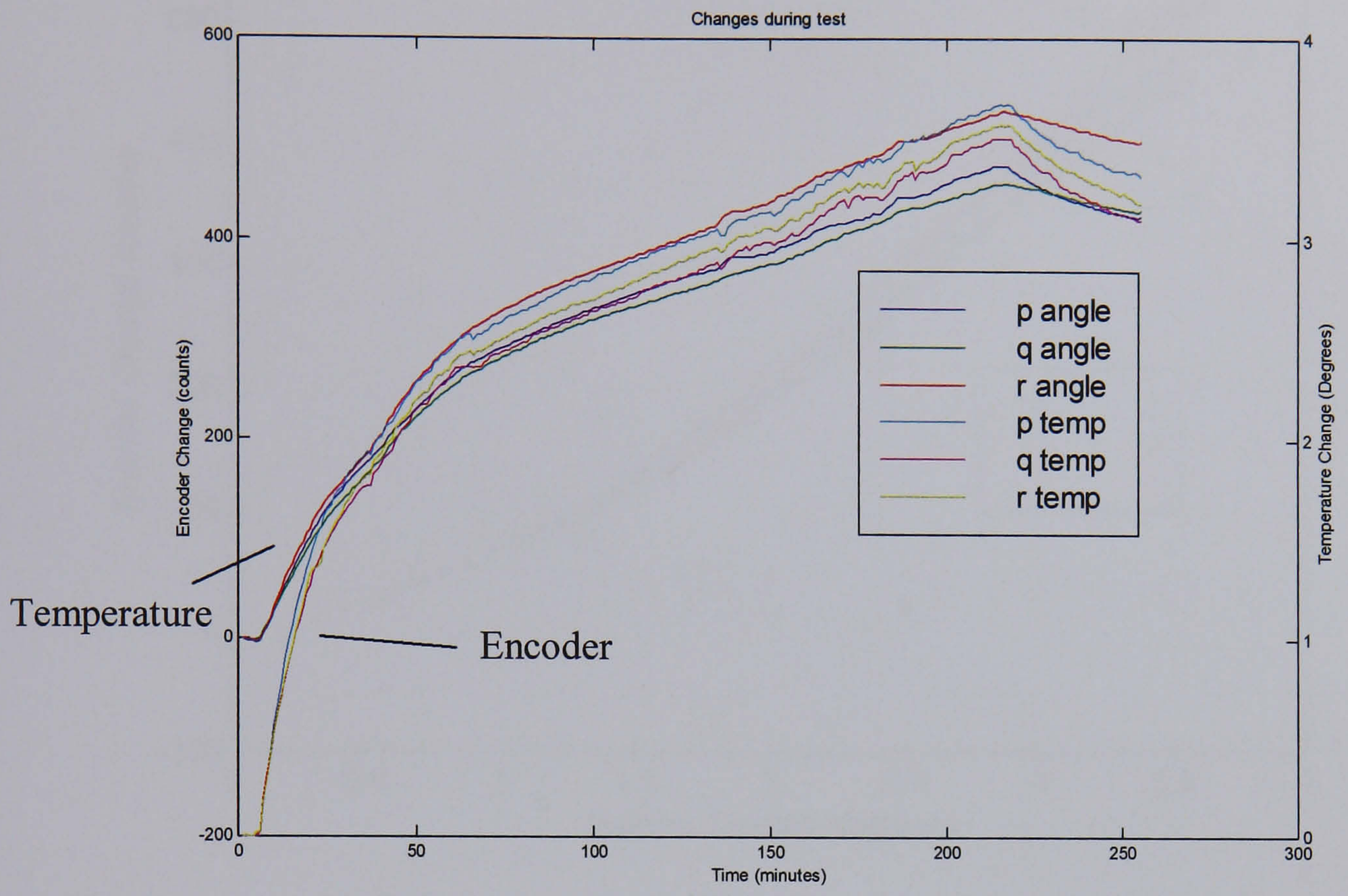


**Figure 10.14: Effect of thermal drift**

This relationship between temperature and change in encoder readings was further investigated by plotting angular change against thermal change (figure 10.15). There appears to be a curvilinear relationship between the encoder change and the rise in temperature. This form of graph seems reasonable when considering the non-linear nature of the UMD.

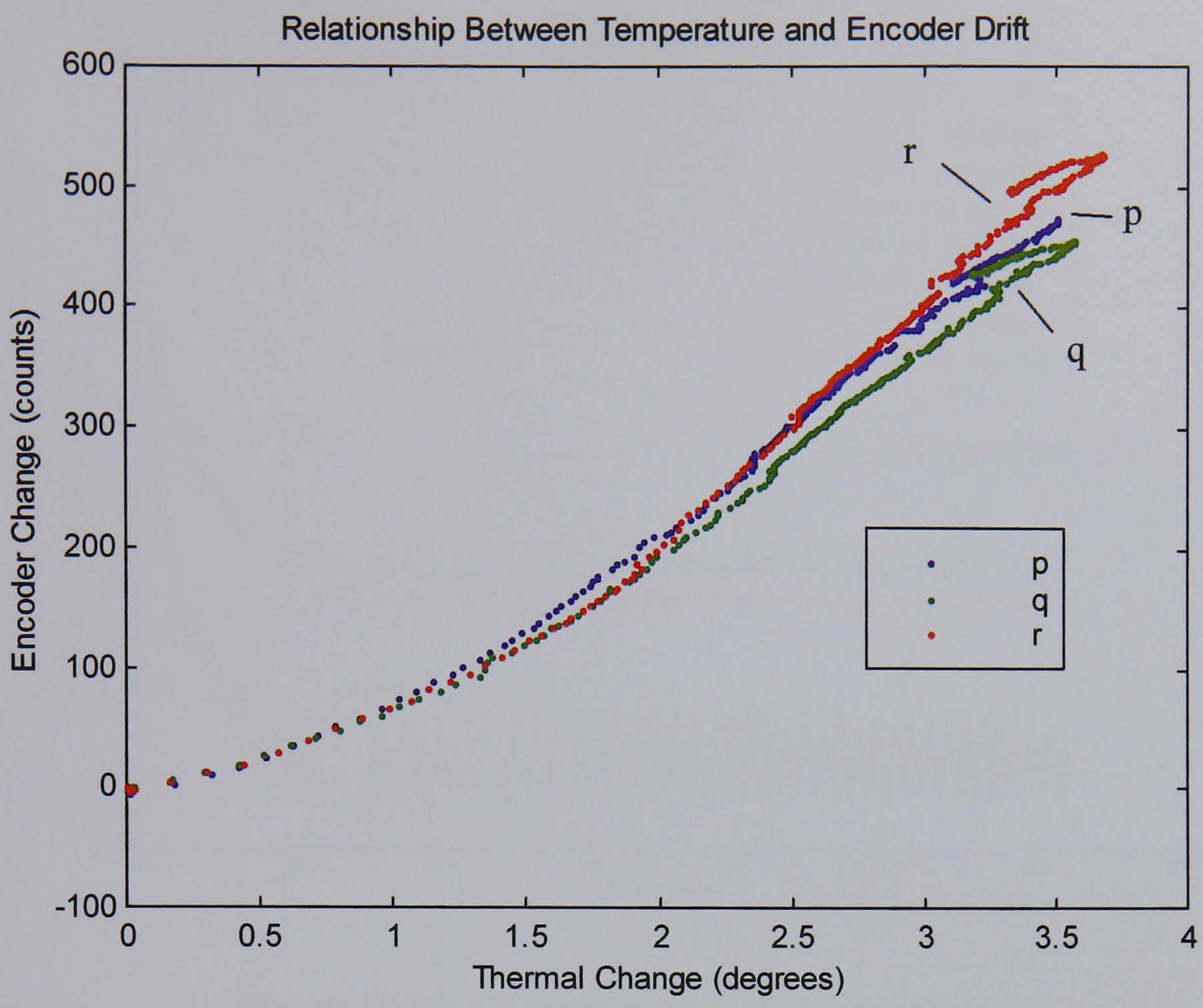


**Figure 10.15: Correlation between temperature and encoder drift**

The thermal behaviour was then monitored while the room returned to a stable temperature. Logging of temperature and encoder values was started immediately after the warming test ended. In effect, this means that the temperature control unit had been off for several hours. After five minutes of the test the air handling was switched on, and demanded to reduce the air temperature to a constant 20°C. The measurement was allowed to run overnight. The results are given in figure 10.16.

Again, the trends of encoder drift closely matched that of thermal change. The cycling effect in all the results derives from the level of control available from the air handling system in which the tests were carried out. The temperature achieves a mean value, but the air condition cycles on and off over a range of about one degree Celsius.

The values obtained from the cycling part of this test indicate the tightest level of control available when testing in the room whose temperature stability can only be guaranteed to ±1°C.

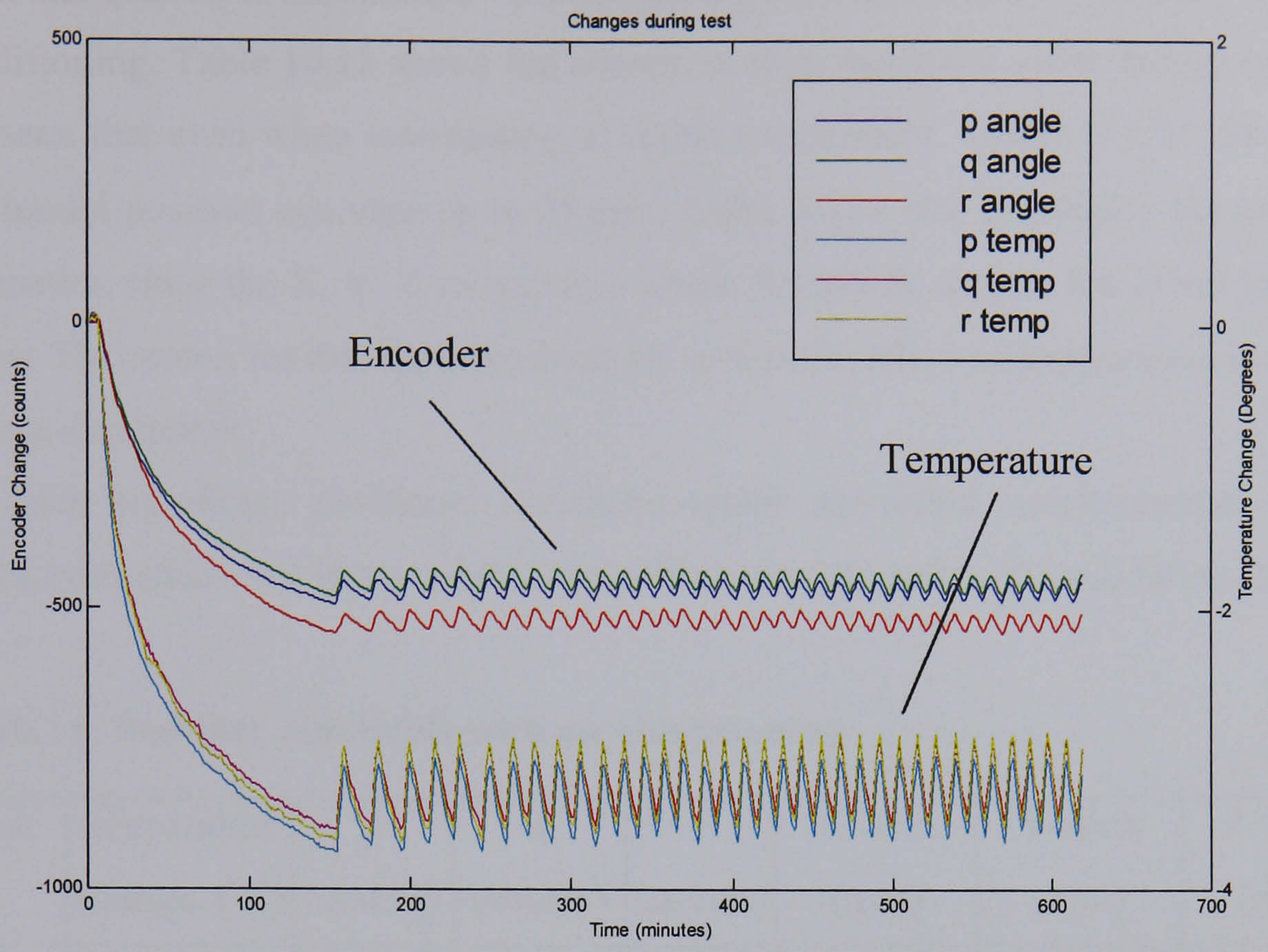


**Figure 10.16: Changes with falling temperature**

The above tests were performed with the UMD held at the home position. Further testing was performed with the 3-ball cup (3bcup) resting on specified balls on the calibration ballplate.

The first three tests were performed during normal workday conditions. Test IV experienced forced temperature changes to allow closer inspection of results. The following results (table 10.10) summarise the range of measurement values from the statistical analyses of the temperature and position data. The position drift is derived from the simple model calculation of x, y, z position.

**Table 10.10: Effect of temperature change on UMD**

| Test | temperature change ($^{o}$C) | position drift ($\mu$m) |
|---|---|---|
| I | 0.37 | 30 |
| II | 1.25 | 52 |
| III | 0.65 | 40 |
| IV | 1.37 | 88 |

Of particular interest is the encoder variation during the temperature cycling due to the room air conditioning. Table 10.11 shows the change in each measured value during two tests. It can be seen that even when maintaining a 'stable temperature' within ±½ °C, the measured simple model position can vary up to 25 μm. Table 10.11 also highlights the problems of compensation since the X, Y, Z errors were worse for test B, despite the lower temperature variation. The reason for this apparent anomaly is that the effect of temperature on the UMD is position-dependent.

Such significant positional variations under controlled environmental conditions introduce both additional input noise to the calibration data and to the validation data.

**Table 10.11: Stability attainable with air conditioning**

| Test | temperature change (°C) | p (counts) | q (counts) | r (counts) | X-Axis (mm) | Y-Axis (mm) | Z-Axis (mm) |
|---|---|---|---|---|---|---|---|
| A | 0.40 | 77 | 34 | 18 | 0.008 | 0.016 | 0.023 |
| B | 0.25 | 66 | 34 | 13 | 0.006 | 0.018 | 0.025 |

## 10.12 Temperature model of UMD

Because the use of the UMD is restricted by the sensitivity to temperature variations it was not possible to validate the MCG method of calibration. It was decided to attempt to model the thermal behaviour of the device in order that these limitations be overcome. An attempt was made to simulate the experiments similar to those above by calculating the change in encoder readings for a given change in temperature.

The UMD is a complex structure made of several elements of different materials and material thickness. The mathematical model of the UMD has been built up from the various subassemblies, which can be analysed individually. Three reference points define the local coordinates for each substructure.

For the thermal model, the subassemblies of the UMD are the base, column with the supports for the hinges, the barn doors, aluminium scales and the sensor head. The effect of thermal change on the subassemblies is modelled by expanding each element from its local origin.

A computer program was written in Borland Pascal in order to perform the necessary calculations. A brief pseudo-code of the model is given in Appendix G. Figure 10.17

provides a flow-diagram representation of the steps within the model and the calculation method by which the model was validated.

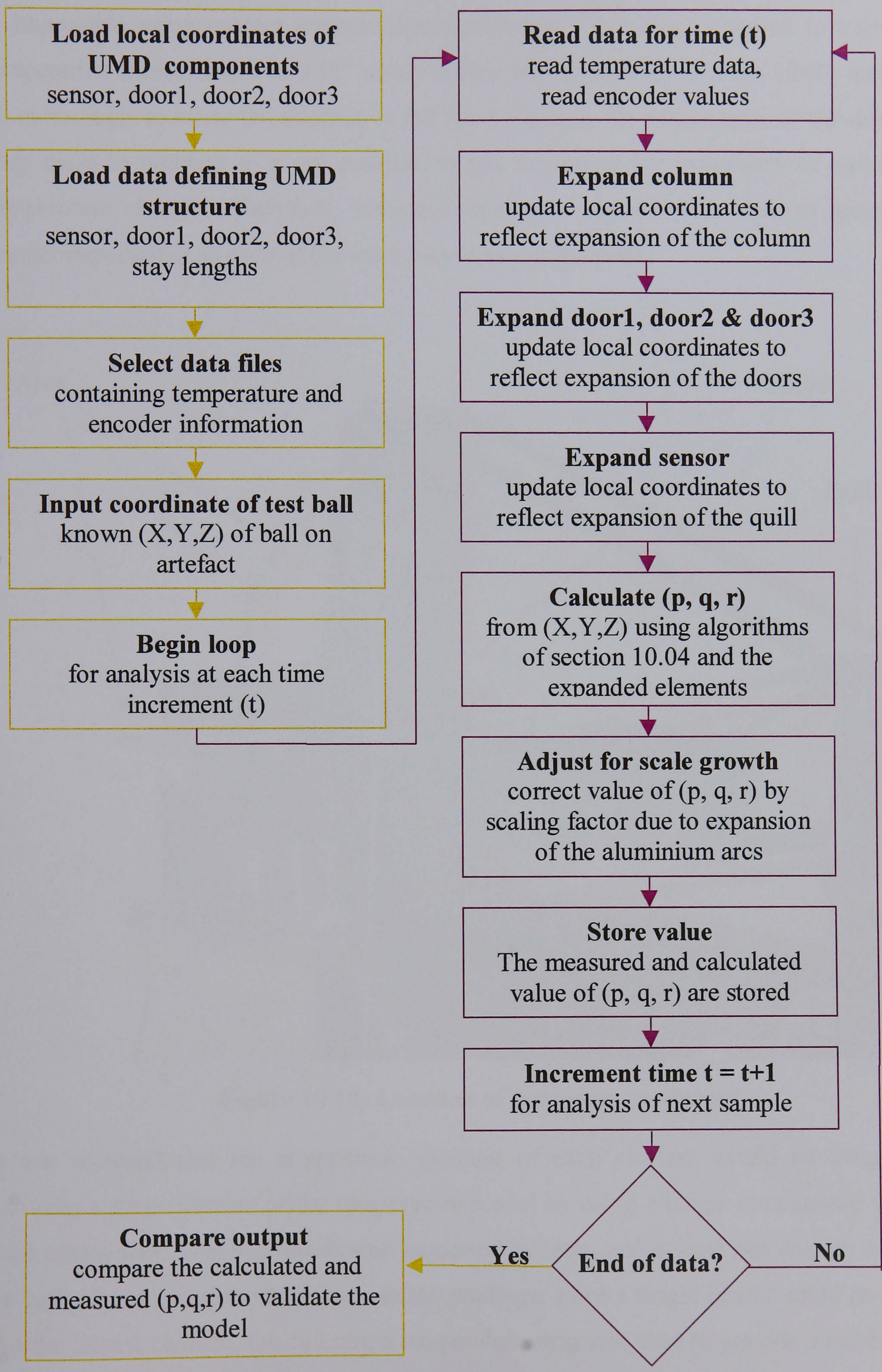


**Figure 10.17: Flow diagram of UMD thermal model**

### 10.12.1 Positioning of sensors

Since the system is so delicate, the measurement of temperature on all parts of the structure is impossible using contact measurement techniques. The wiring required to transfer the temperature measurement to a PC would inhibit normal operation of the UMD, and would be more likely to cause the machine to fall apart. Because the temperature of the structure is very close to ambient it is not possible to use thermography techniques to measure the temperature changes. Therefore, discrete temperature sensors were used to measure the temperature change in each of the most important components.

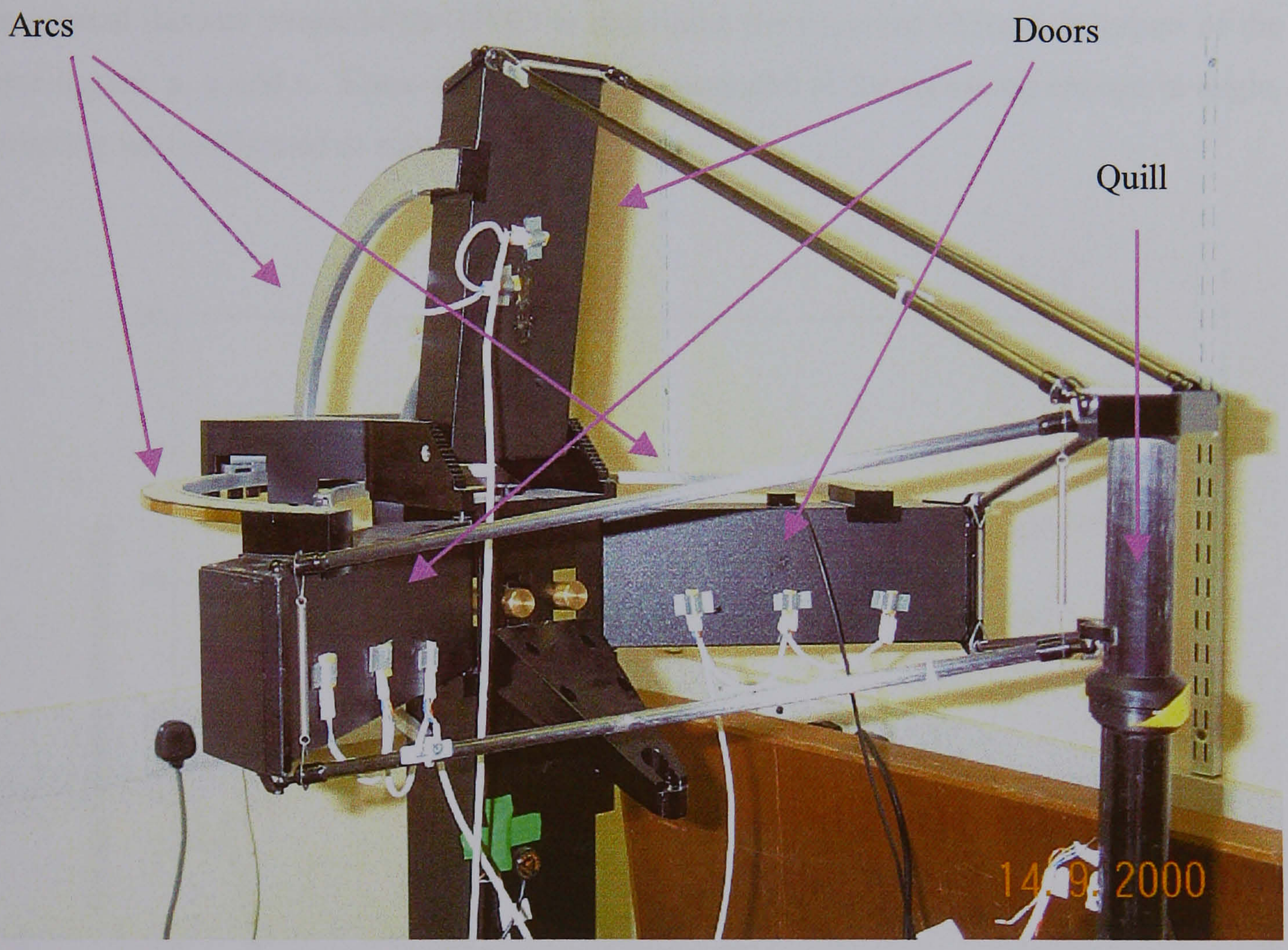


**Figure 10.18: Location of temperature sensors**

It was assumed that the temperature gradient of each element would be insignificant, allowing a simplification of the temperature model by using a single temperature value for each component. This hypothesis was supported by tests, and at least two sensors were used on each element to give confidence in the readings, since a single sensor could be in error. For the largest element, the column, a temperature strip was used to provide a more detailed

value for temperature. Analysis of test results show that no gradient is present for this element so it too was defined by a common temperature value in the model.

## 10.13 Validation of thermal model

In order to validate the thermal model of the UMD the temperatures of each of the important elements were sampled. Simultaneously, the values of the UMD angles were recorded using the PLC-based automatic triggering mechanism and data capture software.

During each test the three-ball cup was positioned on a specific sphere on the ball plate. Each ball has known Cartesian coordinates, which are given by the calibration of the ball plate on a CMM. From these coordinates and the temperature data it is possible to use the general thermal model of the UMD to determine the expected changes in values of the three angles, p, q and r. These values are then compared to the measured change in angle. Sampling was performed at sixty-second intervals.

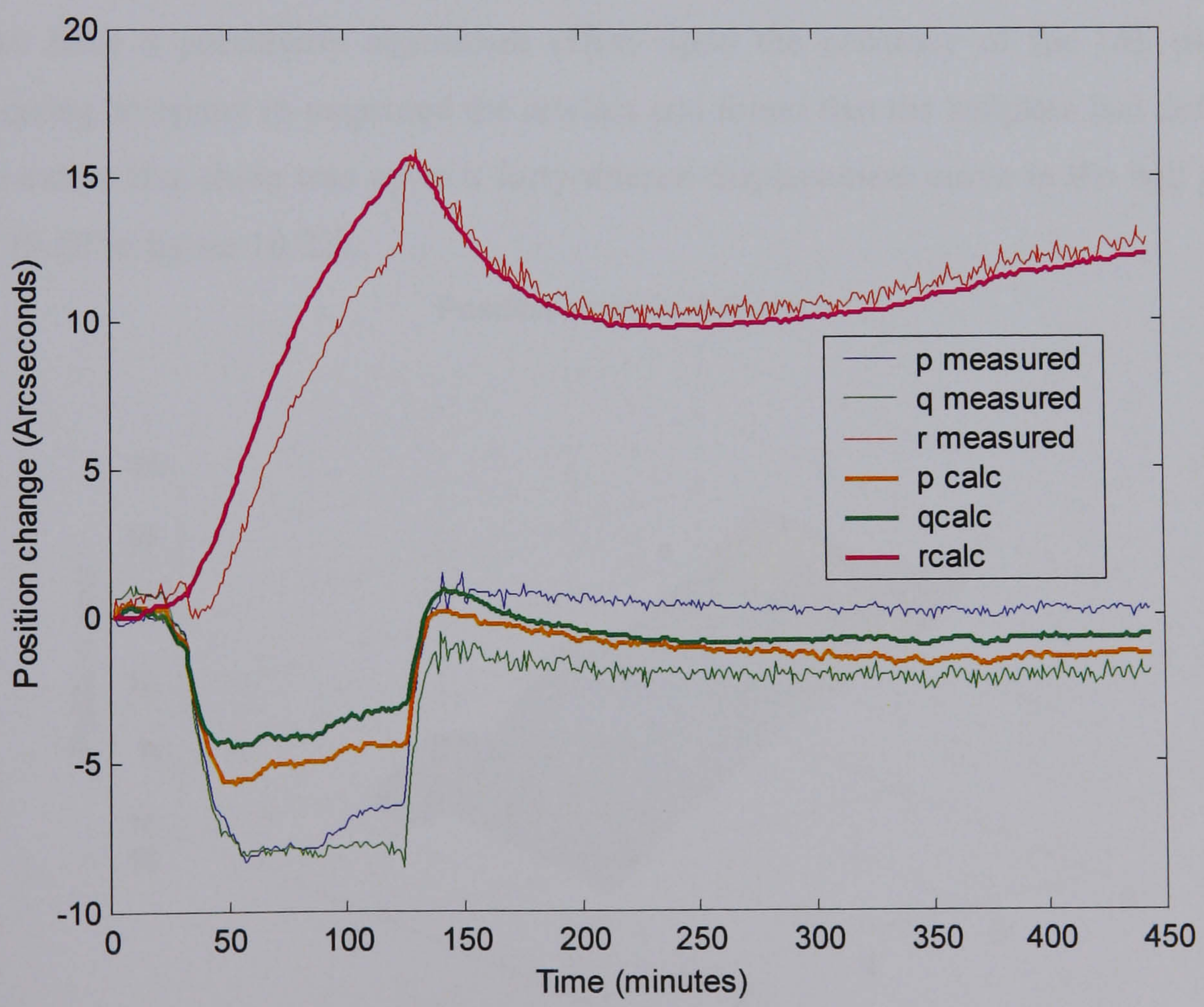


**Figure 10.19: Validation of model at ball 11**

Figure 10.19 shows the fit of the measured values of the angles against the values calculated for the probe at that position for the measured thermal drift. The artefact position chosen for

this test is ball 11, which is at the front, on the bottom layer of the gridplate. It can be seen that there is good correspondence between the model and measured angle changes, when considering the complexity of the model.

## 10.14 Hygroscopic problem

A further consideration has been the problem of the hygroscopic behaviour of carbon fibre. This is a concern raised by the collaborating company and is outside the scope of this project. It is known that carbon fibre will lengthen when in the presence of moisture, but it has further been suggested that the change in length may be permanent. Carbon fibre has the capability to absorb a 'significant' amount of moisture.

The company presents the following relationship:

$$\frac{change\_in\_length}{original\_length} = 0.00061 * \frac{change\_in\_mass}{original\_mass} \qquad \text{Equation 10.5}$$

The effect of the change in moisture will affect the carbon fibre elements of the UMD, but will also have a potentially significant effect upon the accuracy of the ball plate. The collaborating company re-measured the artefact and found that the ballplate had deflected to such an extent that there was up to a forty-micron displacement curve in the ball positions (figure 10.20 to figure 10.22).

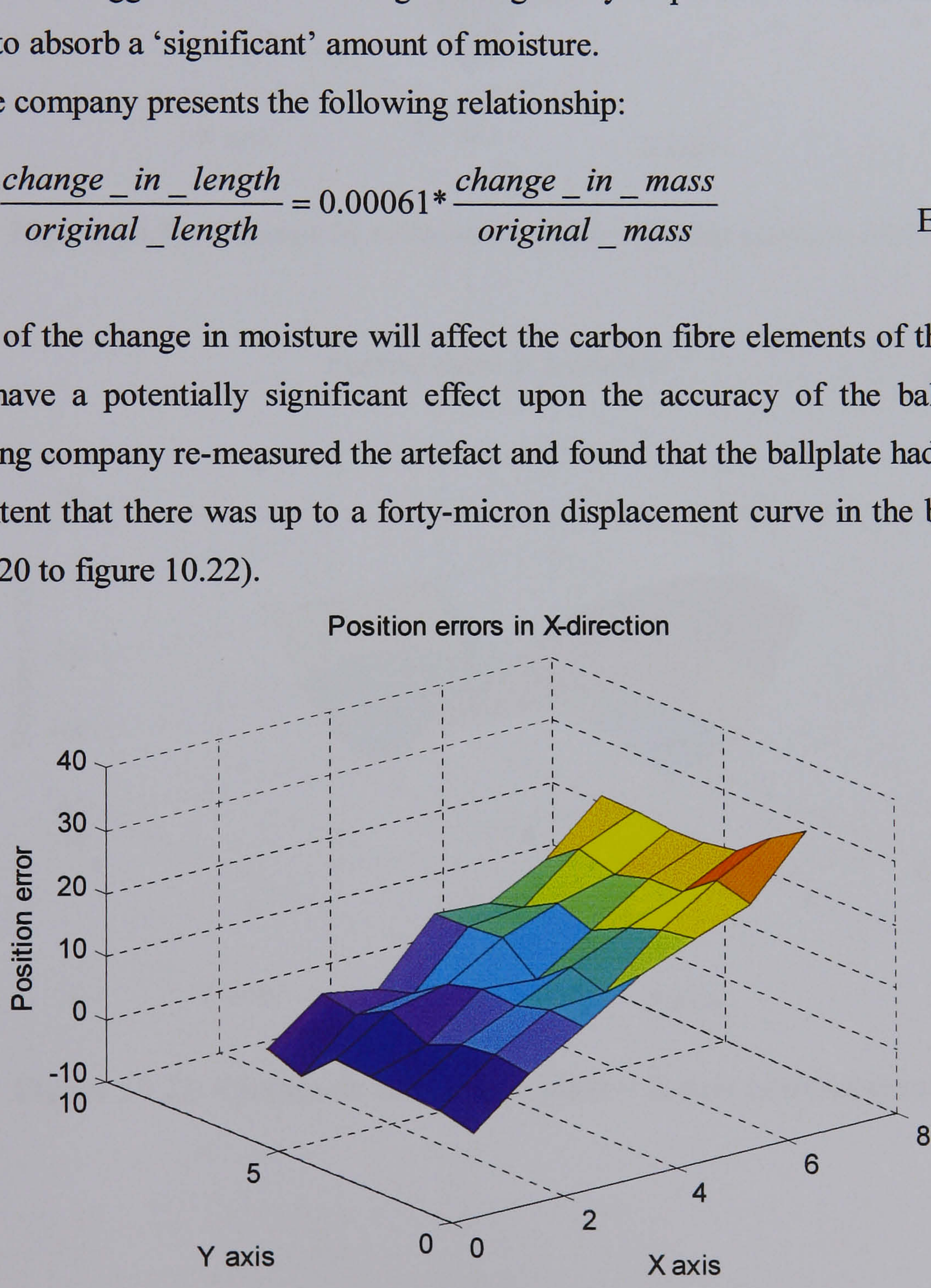


**Figure 10.20: Change in calibration plate – X-axis position errors**

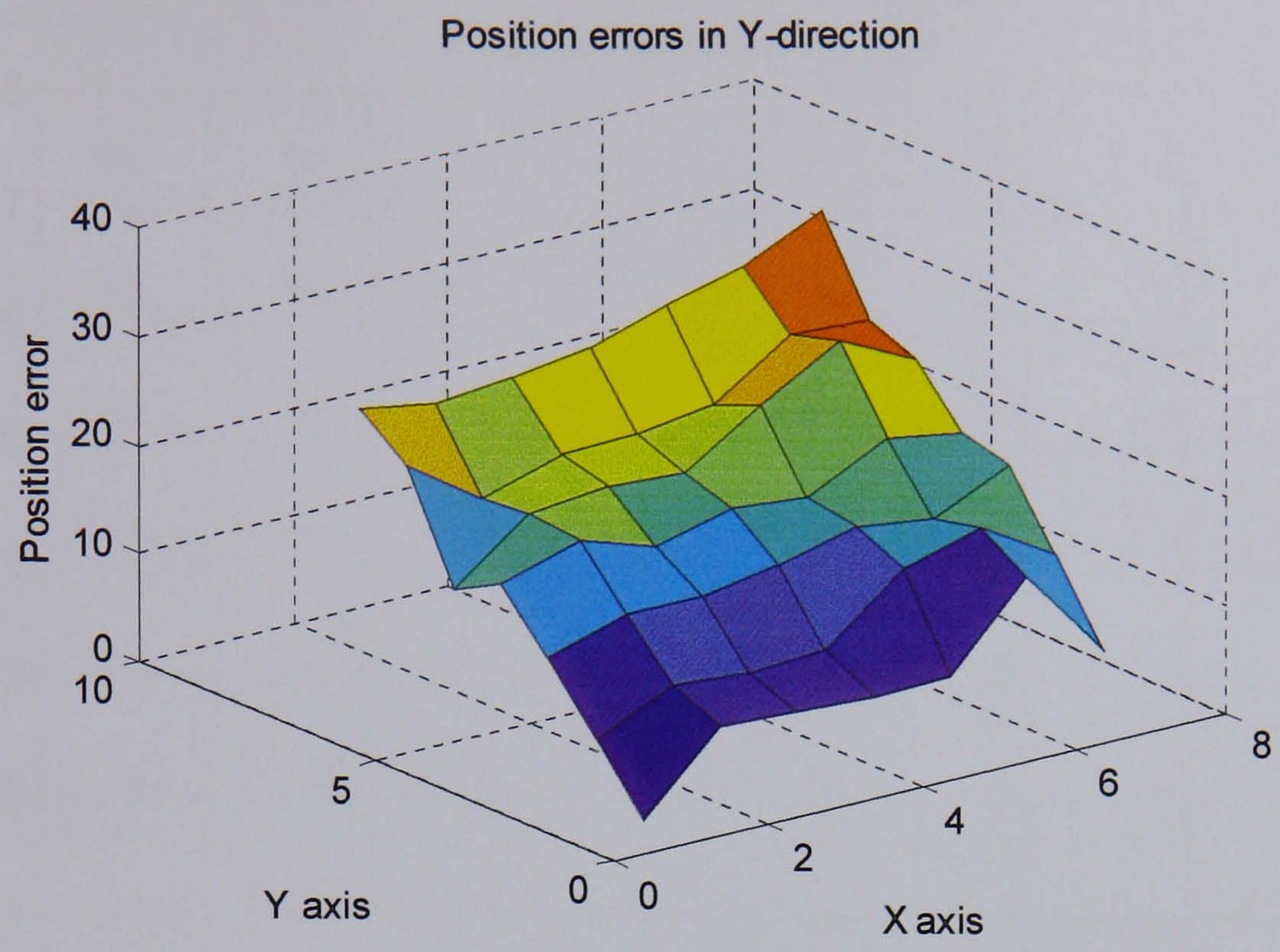


**Figure 10.21: Change in calibration plate – Y-axis position errors**

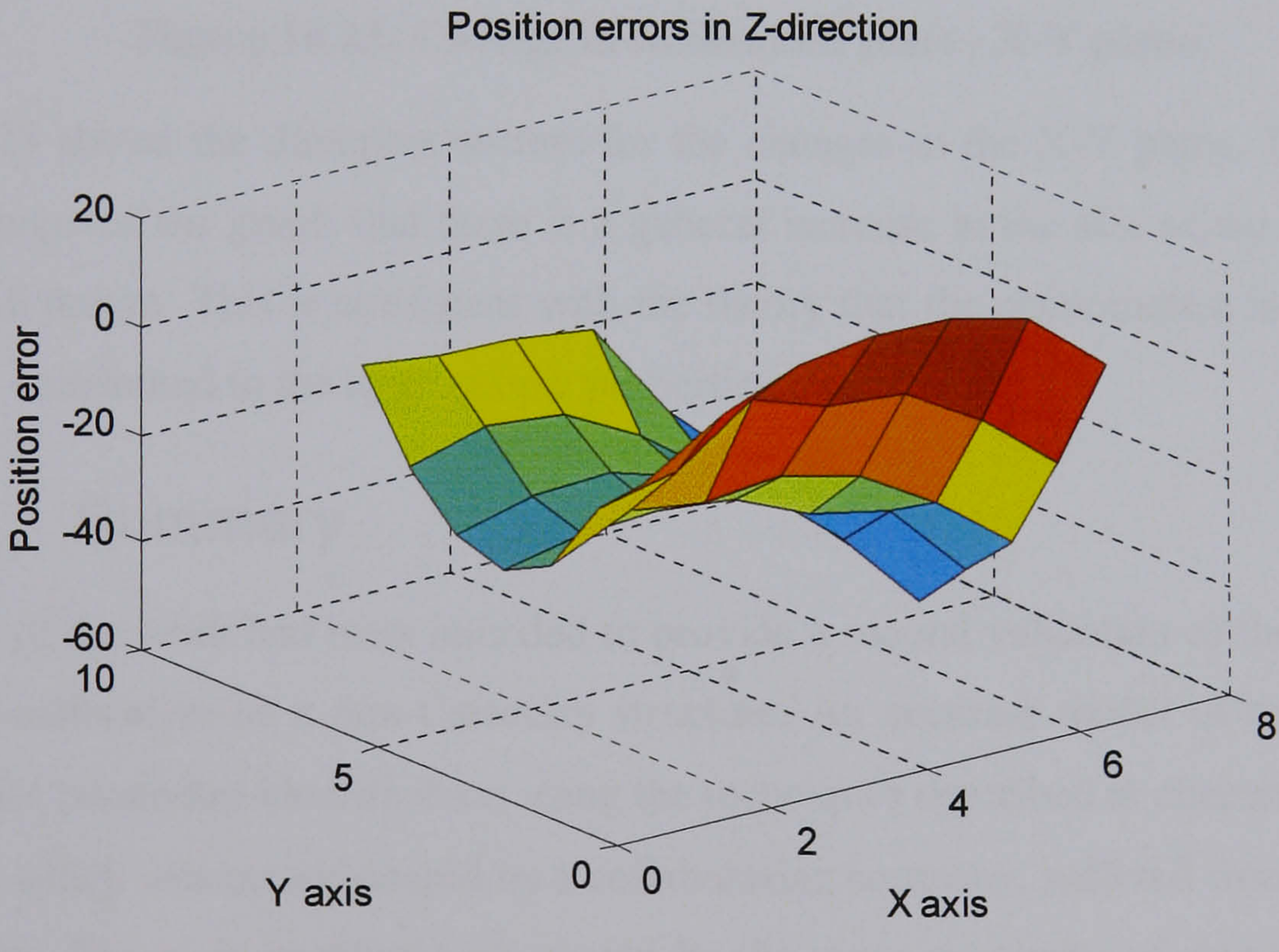


**Figure 10.22: Change in calibration plate – Z-axis position errors**

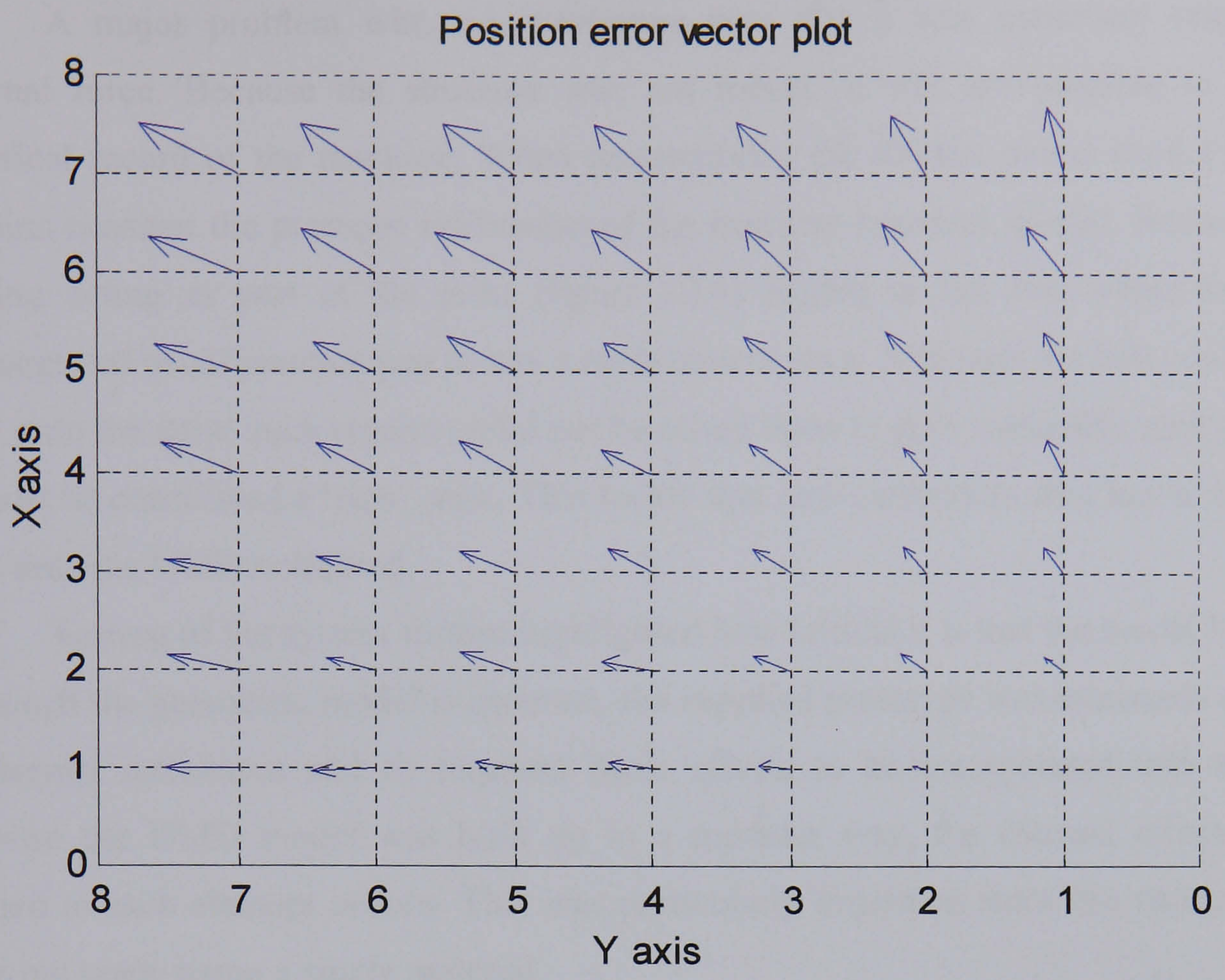


**Figure 10.23: Change in calibration plate - X-Y plane**

Figure 10.23 shows the direction vectors for the changes in the X-Y plane. It can be seen from the shape of the graph that there is a general increase in the size of the artefact from the first-ball datum. This is consistent with the theory that the phenomenon is related to an expansion – attributed to the hygroscopic properties.

## 10.15 Summary

This phase of the work had been intended to provide a second validation of the MCG-based method of calibration of a non-Cartesian structure. An accurate model of the device was generated for parameter identification using the techniques described in chapter 8. However, the device, which was manufactured by a collaborating company, suffered from a number of design flaws. The main problem was caused by the close proximity of singularities to the working volume. Theoretically, no force is required to move the device when it is at a singularity. This meant that the device became unstable when it approached such a point – at the rear of the working volume. If the machine had been built such that the working volume were further forward the singularities would not have had such a significant effect, rendering the system more stable and more repeatable throughout the volume.

A major problem with this prototype was that it was extremely responsive to external force. Because the structure was not robust, it was not possible to produce a historical record of the machine. When reassembling the device, unless each of the struts remains constant the previous calibration of the machine becomes invalid. Because the ball bearing acting as part of the joint (figure 10.4) tended to fall free when the machine disintegrated usual practice was to use a replacement strut. Although the ball could be glued back onto the strut, such repairs could not be relied upon to give repeatable strut length, and so must be considered a 'new' strut. This meant that new calibration data had to be acquired each time the UMD collapsed.

Testing of the system further highlighted how critical it is that the model be accurate. Although the geometric model is accurate, the supplied prototype was extremely susceptible to thermal influences and so required these effects to be incorporated into any model. Because the UMD model was built up in a modular way, the thermal effects could be applied to each element in turn. This was particularly important since the various elements were not made using a single material.

By modelling the complex nature of the response of the UMD to thermal changes it was hoped that corrections could be made by adjustments to the model of the UMD. The model has been shown to give good correspondence with measured data. This indicates that the thermal effect could be compensated in the UMD model for both the calibration data and, subsequently, any work the UMD would be required to perform.

The phase of work on thermal correction was not originally programmed as part of the research, since the effect of thermal influences had been expected to be relatively small. Nevertheless, the work fits neatly under objective 1.14 (e), since it has led to the production of a control algorithm for compensation of errors in the non-Cartesian system.

The information gathered from this investigation into the UMD prototype will be invaluable for revision of design for the final device. It has further shown, by simulation, that the MCG method of calibrating a non-Cartesian machine can be applied to complex structures, although the time required to solve the problem can be prohibitive.

Because of the design problems and the problem of deformation of the ballplate, the company decided not to implement thermal correction in the software for the UMD. This means that although the model has been proven by testing, it has yet to be applied within on-line software.

# Chapter 11 Conclusions and Suggestions for Further Work

## 11.01 Conclusions

Improved component accuracy and rate of production throughput are essential in many production environments. To achieve this, the ability of a machine to perform the task designated to it is of critical importance. To have a knowledge of machine capabilities, it is essential to be able to determine the capability of a machine designed for production to accurately produce a part; a measuring machine to reliably dimension a part or a handling machine to place a part in the appropriate position. By doing this, it is possible to determine the overall manufacturing capability of the workshop. In order to achieve this it is necessary to determine the geometric errors throughout the working volume of the machine.

A technique for solving the error measurement problem in Cartesian machines is to measure each of the contributory geometric error components directly using standard metrological equipment. These errors can then be combined using machine configuration-specific algorithms.

Having assessed the performance of manufacturing equipment there is often a desire to improve accuracy by applying correction for the measured errors. This can be achieved by adjusting the encoder feedback by an amount equal and opposite to the calculated error.

Such correction is usually applied to the axes to correct for errors at the end of the ram of the machine, denoted MCP.

A need has arisen for assessment of machines with tooling such that the cutting or probing occurs at a tool centre point (TCP) offset from the MCP. New terms have been added to standard geometric models to allow evaluation of the operational accuracy of a Cartesian machine with a probe or tool offset.

The models have then been further enhanced to allow calculation of the volumetric error at the TCP for a machine with geometric compensation at the MCP. A novel strategy for measuring angular error for evaluation of a compensated machine has been devised so the model can be correctly applied.

Any measurement system must conform to a traceable standard in order for the user to have confidence in their results. This is possible in Cartesian machines because the position-dependent geometric errors can be measured using standard metrological equipment and techniques. It has been found that the figure for volumetric accuracy also needs to be qualified by a value of its uncertainty, based upon that of each of the individual measurements. Methods for evaluating the uncertainty of each measurement have been devised, based upon axis stroke, measurement range, employed equipment and a set of assumptions. Furthermore, a method for incorporating a statistical propagation of the uncertainties in the measurement algorithm has been proposed. Simulation of this method produced a worst-case uncertainty of twenty-six microns for a one-metre cubed working volume. Results from a number of tests on similar turning machines has shown that the volumetric accuracy figure can, in practice, be significantly more repeatable.

A specification for volumetric assessment software incorporating these new features (ESP) has been devised and an alpha version produced for evaluation. This work is being performed in support of two European CRAFT projects [2, 3] and a version of the software is currently being used by an industry-based member of one project for calibration of CMMs.

An alternative method of evaluating the positional errors in a machine is by direct measurement. A system of lasers (LaserTrace) using the principles of triangulation has been investigated. A novel application of photogrammetry techniques was applied to the system in an attempt to produce an efficient calibration system requiring little additional hardware. This method was found to give poor results, probably because of necessary oversimplification of the model and the susceptibility to the significant amount of measurement noise.

Comparisons were then drawn between the LaserTrace and non-Cartesian machines. By accurate modelling of such systems the calibration problem can be expressed as a parameter identification task. A novel use of the principles of the machine checking gauge (MCG) was employed to acquire data for parameter identification on a model of the LaserTrace system that was generated from first principles. This method was successful, limited only by the resolution and repeatability of the LaserTrace control system. Because a large data set can be captured without a significant increase in measurement time, this principle was found to be less susceptible to noisy data.

At least three positions of the MCG are required to define the coordinate system. This means that a large area of the working volume is covered during the calibration. This provides more representative data than other single-point calibration techniques. Furthermore, additional positions for the MCG can be used to cover more of the volume.

Attempts were then made to transfer the MCG method to a second non-Cartesian device – the UMD. This required a more complex model, which was successfully calibrated by simulation. In practice, it was found that this method is limited as a commercial approach because of the length of time required for computation of the solution for a system with a high number of unknown parameters. This constraint is not applicable to the LaserTrace system since optimisation takes only a few minutes. Similarly, simple joint-and-link robots would have a lesser number of unknown parameters in their model.

The attempt to validate the method on the UMD was precluded by the sensitivity of the device to thermal changes and the lack of robustness of the prototype.

A thermal model of a non-Cartesian machine has been devised to allow correction for temperature changes. Comparative testing between the change in machine pose predicted by the model for a given temperature change and the actual change in the angles of the device have given satisfactory results. This model could be used to compensate for the thermally induced errors in the measuring device.

The findings from the work on the UMD will contribute to the redesign of the device by the collaborating company.

## 11.02 Suggested further work

### 11.02.1 Cartesian machines

- The system for evaluating errors on a three-axis Cartesian machine with a tool or probe extension has been shown to work successfully. An alpha version of the enhanced ESP

simulation software has been produced and is undergoing testing. A proposal for European funding is being drawn up to facilitate the development of the software into a commercially available package in the near future.

- This system can be further developed to incorporate the variety of machining heads that are becoming better established in the machining workplace. For example, the geometric effects of the fork head and angle head can be incorporated into the model, in addition to the effects of the three-axis geometric errors when using a machining head. This will require additional methods of measuring the errors inherent in the head.
- The techniques could also be applied within a compensation system. The compensation method currently used on machines does not provide sufficient communication with the machine controller to be able to detect which tool is being used at any given time, or at what angles a probe may be. By applying compensation within a controller, or by using a fieldbus to provide additional inputs to the compensation system it will be possible to supply this information, and so correct the errors. This work is being pursued in collaboration with an industrial partner.
- The consideration of machine repeatability and measurement uncertainty are critical to the acceptance of the suggested technique for machine evaluation. For the purposes of this project the values of uncertainty proposed by Knapp (table 4.2) have been assumed for all analysis work. Further work should be undertaken to determine whether these values are truly representative. Obviously, if values of uncertainty of measurement for the relevant geometric components are agreed upon at international standards level these will be used in the software package to provide a standard methodology.

### 11.02.2 MCG calibration method

- A more efficient optimisation technique is required for this method to become commercially practical for complex machines. For a commercial approach the calibration data must be taken, processed and validated within a working day. Currently the optimisation can take several weeks for a complex system. If methods could be devised to fix more of the parameters this would greatly reduce the time required for optimisation.

### 11.02.3 LaserTrace system

- Produce a jig with three pivot points for the MCG calibration arm. This will allow the parameters for the LaserTrace model to be specified on any machine. The centre of the

three spheres fixes the reference frame for the coordinate system. If the sphere centres are probed using the machine this can be directly related to the coordinate frame of the working volume of the machine. This will allow a portable calibration system.

- Refine software to perform all functions on-line. This will allow a single package which obtains calibration data, performs the necessary optimisation to determine the unknown parameters of the system model and uses the model to convert subsequent data to position measurements. Use of such a system will simplify the process of using the LaserTrace system as a calibration device.
- Hardwire the two controller units together so they maintain a common clock. Currently the system triggers each pod for each reading in order to remove the problem of timing between the two pods. This method reduces the rate at which data can be collected and so reduces the speed at which the machine under calibration can be moved in order to fully map the errors. For the system to be used to calibrate the dynamic errors introduced by fast movement of the tool a more rapid data acquisition technique is required.

### 11.02.3.1 Thermal

- The position of the sphere centres must be accurately known. Subsequent testing has shown that the CMM room temperature tolerance can be suspect during daily operation, due to other users of the facility. This leads to reduced confidence in the measurements. For example, the posts defining the sphere centre positions could have been expanding during the experiment, also the CMM values are suspect if temperature is not maintained. The calibration procedure should be adapted to measure the sphere centres before and after calibration in order to note any changes.
- It can also be noted that constant handling of the MCG artefact will cause expansion, and a change in the radius of the described sphere. In order to keep the optic stationary at each point on the sphere the device is counterbalanced. Initially this was achieved by using a counterbalance weight, whose distance from the fulcrum could be adjusted by a screwing action. This was found too cumbersome and was replaced by a large magnet that could be moved along the arm to set the balance. This method was more efficient but the large amount of human interaction with the arm of the artefact still results in heating during operation. A better method of artefact operation is required, either by

manufacturing the arm from a more thermally stable material or by using a more sophisticated counterbalance system to reduce the amount of handling required.

#### 11.02.3.2 Data requirements

- For the conducted experiments four 'spheres' of data were taken at 21 points per sphere. Obviously the greater the number of spheres or points, the more time-consuming is the calibration process in both physical measurements and computer processing time. Some analysis is required to determine a satisfactory compromise between accuracy and calibration time. Empirical testing is then required to validate this choice. By increasing the 'coverage' of the calibration points over the working volume it may be possible to improve the overall accuracy of this method.

#### 11.02.3.3 Dynamic

- Although the accuracy of the results of the dynamic testing of the LaserTrace is much worse than for the static testing, the reasons for this are understood. Since there is no common timing between the individual pods it is very difficult to ensure that a single sample from both pods represents a unique position in space. If hardwiring the two pods were not possible, further work could be performed to reduce the error by compensation. If the feedrate were known to be constant and the time delay between the two pods was also a known value it would be possible to build a correction factor into the model of the LaserTrace. However, since the correction of the encoder values is non-linear, this is not a trivial problem.

### 11.02.4 UMD

- Re-design and re-manufacture the UMD so that it is stable throughout testing, and reliably retains mechanical integrity.
- Produce a thermally stable version of the UMD, or a version where thermal expansion is uniform throughout the structure. This could be achieved by using a single material throughout.
- Further work is being undertaken by the collaborating company to produce a machine tool using a non-Cartesian configuration. The lessons learned from this investigation will be used to improve the design of the device.

# Chapter 12 References


1. Ford D.G., Postlethwaite S.R., Allen J.P. & Blake M.D., "Compensation algorithms for the real-time correction of time and spatial errors in a vertical machining centre", Proceedings of the Institution of Mechanical Engineers Vol. 214, Part B, 2000
2. European CRAFT project: SMS2-7839 (SMT4-CT98-5517) "Accuracy Verification of Co-ordinate Measuring Machines of all sizes, types and configurations using lasers and a universal artefact".
3. European CRAFT project: SMS2-7854 " An Investigation into New Machine Tool Performance Standards for the Dynamic, Thermal and Volumetric Calibration of Machine Tools". Millwood S, Postlethwaite S.R, Ford D.G (Co-ordinator)
4. Lee J., "Overview and perspectives on Japanese manufacturing strategies and production practices in machinery industry", International Journal of Machine Tools and Manufacture, Vol.37 No.10, 1997, pp1449-1463
5. Wang, C., "Improve your on-machine inspection accuracy", Quality Online (URL: http://www.qualitymag.com/articles/2001/feb01/0201f1.asp) , February 2001
6. Quinlan, J.C., "On-machine probing key to parts quality", Quality in Manufacturing, October 1998
7. Lorincz, J.A., "Are CMMs merging with machine tools?", Tooling and Production, April 1999

8. Ford D.G, "Machine tool structures – static, dynamic and thermal errors". Keynote speaker for "Sharing Tomorrow's Technology Today" May 1997.
9. Hewlett Packard Labs, 1501 Page Mill Road, Palo Alto, Canada, CA 94304-1126
10. Renishaw plc, New Mills, Wotton-under-Edge, Gloucestershire, GL12 8JR, United Kingdom
11. Automated Precision Inc., 7901-C Cessna Avenue, Gaithersburg, USA, MD 20879
12. Kakino, Y., Ihara, Y. & Shinohara, A., "Accuracy Inspection of NC-Machine Tools : Double Ball Bar Method", Edited by Dr Johannes Heidenhain, SBN: 1569901600, Hanser-Gardner Publications, 1993.
13. International Standard ISO 230-1, 'Geometric accuracy of machines operating under no-load or finishing conditions'.
14. International Standard ISO 230-2, 'Determination of accuracy of positioning of numerically controlled machine tool axes'.
15. Pettigrew, W., "CMMs are Machine Tools, Too", Modern Machine Shop Online, Gardner ublications, Inc., http://www.mmsonline.com/srticles/099405.html, Last accessed, October 2001
16. International Standard ISO 10360-2, "Coordinate metrology -- Part 2: Performance assessment of coordinate measuring machines", 1994
17. AMTRI report, "Basic structures for machine tools", DTI sponsored 1992
18. Ford D.G., "Machining to microns – error avoidance or compensation?" Proceedings for LAMDAMAP 95, Laser Metrology and Machine Performance II, Computational Mechanics, pp277-286, 1995.
19. Hollingum, J., "Hexapods to take over ?", Industrial Robot, vol. 24, no. 6, pp428-431, 1997
20. NEOS Robotics, Ritarslingan 22A 18766 Täby SWEDEN
21. Trevelyan, J. "Simplifying robotics - A challenge for research", Robotics and Autonomous Systems, v.21, no. 3, pp 207-220, 1997.
22. Rooks, B., "A record year for UK robot installations", Industrial Robot vol. 24, no. 5, pp 337-341, 1997
23. Wittenberg, G., "Developments in Off-line Programming: an Overview", Industrial Robot, vol. 22, no. 3, pp 21-23, 1995

24. Doiron, T.& Stoup, J., "Uncertainty and dimensional calibrations", Journal of Research of the National Institute of Standards and Technology, vol. 102, number 6, pp. 647-676, December 1997.
25. Taylor, B. N. & Kuyatt, C. E., "Guidelines for evaluating and expressing the uncertainty of NIST measurement results", NIST Technical Note 1297, Physical Laboratory, National Institute of Standards and Technology, Gaithersburg, MD 20899-0001, September 1994
26. BSI, "Accuracy of machine tools and methods of test – Specification for machining centres and computer numerically controlled milling machines, horizontal and vertical spindle types", BS 4656, Part 30, 1992
27. BS 7228: Section 4.1, British Standards Institute, 1996
28. Roth, Z. S., Mooring, B. W. & Ravani, B., "An Overview of Robot Calibration", IEEE Journal of Robotics and Automation, vol. RA-3, no. 5, October 1987.
29. Hidalgo, F., and Brunn, P., "Robot metrology and calibration systems – a market review", Industrial Robot, vol. 25, no. 1, pp 42-47, 1998.
30. SMX Corporation, 222 Gale Lane, Kennett Square, PA 19348 USA
31. Ferreira, P.M. (University of Illinois, Urbana), Liu, C.R. (Perdue University, W. Lafayette), "A method for estimating and compensating quasistatic errors of machine tools". Journal of Engineering for Industry, V115, P149-159, 1993.
32. Kiridena, V.S., Ferreira, P.M. (University of Illinois, Urbana), "Parameter estimation and model verification of first order quasistatic error model for three axis machining centres". International Journal of Machine Tools & Manufacturing, V34, N1, P101-125, 1994.
33. Kiridena, V.S., Ferreira, P.M. (University of Illinois, Urbana), "Kinematic modelling of quasistatic errors of three axis machining centres". International Journal of Machine Tools & Manufacturing, V34, N1, P85-100, 1994.
34. Postlethwaite, S.R. Ford, D.G., "Geometric analysis software for CNC machine tools", LAMDAMAP 97, University of Huddersfield, pp305-316, 1997.
35. Pathre, U., 'Simulation and calibration for off-line programming of industrial robots', Society of Manufacturing Engineers Technical Paper MS94-210, 1994
36. Zhuang, H., "Self-Calibration of Parallel Mechanisms with a Case Study on Stewart Platforms", IEEE Transactions on Robotics and Automation, vol. 13, no. 3, June 1997

37. Li, Y. F. "Characteristics and Signal Processing of a Proximity Sensor", Robotica, vol. 12, no. 4, pp 335-341, July 1994
38. Zhuang, H. & Liu, L., "Self-calibration of a class of parallel manipulators", Proceedings of the IEEE conference on Robot Automation, Minneapolis, pp 994-999, April 1996.
39. Robot Simulations Limited, Lynnwood Business Centre, Lynwood Terrace, Newcastle Upon Tyne, NE4 6UL.
40. Tetra Precision Inc., P.O. Box 20967 St. Petersburg, FL 33742, USA
41. Leica Geosystems AG, Mönchmattweg 5, CH-5035 Unterentfelden, Switzerland
42. Kyle, S. A. "Optical Methods for Calibrating and Inspecting Robots", Computing and Control Engineering Journal, pp 166-173, August 1995.
43. Sartori, S. (Institute of Metrology, Torino), Zhang, G.X. (University of Tianjin, China), "Geometric error measurement and compensation of machines". Annals of the CIRP, V44, N2, 1995.
44. Postlethwaite, S.R. "Electronic based accuracy enhancement of CNC machine tools". PhD thesis, 1992.
45. Blake, M.D., "Investigation into load effects on machine tool accuracy", MPhil thesis, University of Huddersfield, 1995.
46. Chen, J.S., Kou, T.W. & Chiou, S.H, "Geometric error calibration of multi-axis machines using an auto-alignment laser interferometer", Precision Engineering, V23, pp243-252, 1999
47. Lau, K., Ma, Q., Chu, X., Liu, Y. & Olson, S., "An advanced 6-degree-of-freedom laser system for quick CNC machine and CMM error mapping and compensation", Laser Metrology and Machine Performance IV (LAMDAMAP 99), Computational Mechanics Publications, pp421-434, 1999
48. Optodyne Inc. 1180 Mahalo Place, Compton, CA 90220, USA
49. Dr. Johannes Heidenhain, Str. 5, D-83301 Traunreut, Germany
50. ASME B5.54 - 1992 Standard, "Methods for Performance Evaluation of Computer Numerically Controlled Machining Centres," (reaffirmed in 1998)
51. Blackshaw, D.M.S., Chiles, V. & Jenkinson, D., "Development of CNC machine performance standards" Proceedings for LAMDAMAP 99, Laser Metrology and Machine Performance IV, Computational Mechanics, pp.89-98, July 1999
52. Morris, T.J., "A new slant on diagonal laser testing", Laser Metrology and Machine Performance V (LAMDAMAP 01), Wit Press, pp29-40, 2001.

53. Cincinnati Machine U.K. Ltd., Birmingham, England
54. Fowler, D., "Drilled for accuracy", *The Engineer*, 24 July 1998.
55. EN ISO 10360-2:1995 "Coordinate metrology – Part 2: Performance assessment of coordinate measuring machines"
56. "PH10 Motorised probe head series user's guide", H-1000-5070-09-A, Renishaw plc, New Mills, Wotton-under-Edge, Gloucestershire, GL12 8JR, United Kingdom
57. Caskey, G.W., Phillips, S.D. & Borchardt, B.R, "Results of the NIST National Ball Plate Round Robin", Journal of Research of the National Institute of Standards and Technology, V102, No.1, pp85-93, 1997
58. ISO, "International vocabulary of basic and general terms in metrology, second edition", (VIM), International Organisation for Standardisation, Geneva, Switzerland, 1993
59. Bell, S, "A beginner's guide to uncertainty of measurement", National Physical Laboratory, United Kingdom, August 1999.
60. Abernathy, R.B. & Benedict, R.P., "Measurement Uncertainty: A Standard Methodology", ISA Transactions V24, No.1, pp75-70, 1985
61. "Guide to the expression of uncertainty in measurement", ISO, 1995
62. Deutsch, C., *et al.* "Principles of Monte Carlo Simulation" a short-course given at the University of Alberta, USA, online at http://www.ualberta.ca/~cdeutsch/MCS-course.htm, February 2001
63. Knapp, W, "Measurement Uncertainty Examples (Swiss contribution)", ISO consultation document, 2000
64. Chen, J.S., Yuan, J.X., Ni, J., Wu, S.M. (University of Michigan), "Real-time compensation for time-variant volumetric errors on a machining centre". Journal of Engineering for Industry, Transactions of the ASME, V115, P473-479, 1993.
65. Chen, J.S., "Computer-aided accuracy enhancement for multi-axis CNC machine tool". International Journal of Machine Tools & Manufacturing, V35, N4, P593-605, 1995.
66. Chen, J.S., Ling, C.C., (National Chung Cheng University), "Improving the machine accuracy through machine tool metrology and error correction", International Journal of Advanced Manufacturing Technology, V11, P198-205, 1996.
67. Yang, S., Yuan, J., Ni, J. (University of Michigan), "Accuracy enhancement of a horizontal machining centre by real-time error compensation", Journal of Manufacturing Systems, V15, part 2, P113-124, 1996.

68. Lo, C., Yuan, J., Ni, J. (University of Michigan), "An application of real-time error compensation on a turning centre", 1995.
69. Ni, J., (University of Michigan), "CNC machine accuracy enhancement through real-time error compensation", Journal of Manufacturing Science and Engineering, V119, part 4B, P717-725, 1997.
70. Mou, J. (University of Illinois), Liu, C.R. (Purdue University, Indiana), "A robust error correction method for multi-axis machines". Dynamic Systems and Control, V2, P1011-1018, 1994.
71. Mou, J. (University of Illinois), Liu, C.R. (Purdue University, Indiana), "An adaptive methodology for machine tool error correction". Journal of Engineering for Industry, V117, P389-399, 1995.
72. Mou, J. (Arizona State University), "A systematic approach to enhance machine tool accuracy for precision manufacturing", International Journal of Machine tools & Manufacture, V37, part 5, P669-685, 1998.
73. Allen JP, Postlethwaite SR, Ford DG, "Practical Thermal Error Compensation for CNC Machine Tools", Proceedings of the eleventh annual meeting of the American Society for Precision Engineering, Monterey, California, pp 648-653, Nov. 1996
74. Hardwick, B., "The heat is off – thermal compensation for a machine tool", Manufacturing Engineer, June 22-25, 1989
75. Chen, J.S., Yuan, J.X., Ni, J., Wu, S.M, "Compensation of non-rigid body kinematic effect on a machining centre", NAMRC, 1992.
76. DG Ford, S. Postlethwaite, D. Morton, 'Error compensation applied to high precision machinery', Proceedings of 1st International Conference on Laser Metrology and Machine Performance - LAMDAMAP 1993, Southampton Institute, pp 105–112, July 1993
77. Postlethwaite, S.R., Ford, D.G., "A practical system for 5-axis volumetric compensation", LAMDAMAP 99, P379-388, 1997.
78. Fletcher, S., Postlethwaite, S.R. & Ford, D.G., "Volumetric compensation through the machine controller". Laser Metrology and Machine Performance V (LAMDAMAP 01), Computational Mechanics Publications, 2001.
79. Knapp, W., "Revision of ISO 230-2", ISO/TC 39 /SC 2 N 1308, June 2001.

80. Phillips, S.D., Estler, W.T., Levenson, M.S. & Eberhardt, K.R., "Calculation of measurement uncertainty using prior information", Journal of Research of the National Institute of Standards and Technology, V103, pp625-632, 1998
81. Blake, M.D., Ford, D.G., Postlethwaite, S.R., Morton, D., "Analysis of Machine Tool Non-Rigid Error Components", LAMDAMAP 95, P297-308, 1995.
82. Ford D.G., Postlethwaite S.R., & Blake M.D., "The identification of non-rigid errors in a vertical machining centre", Proceedings of the Institution of Mechanical Engineers Vol. 213, Part B, 1999
83. Caskey GW, Fronczek CJ, Phillips CD, "Laser Trackers: Traceability, Uncertainty and Standardization. A Report to the CMSC," *(U.S.) National Institute of Standards and Technology (MEL) Gaithersburg, MD*, September 1997
84. B89.4.19 working group: "Performance Evaluation of Laser Based Spherical Coordinate Measuring Systems", draft standard of the American Society of Mechanical Engineers,
85. Simon, G, "Optotrac – Cat's Eyes and Lasers", Industrial Robot, Vol. 21, No. 6, pp 18-21, 1994
86. Lansing Linde Ltd., Materials Handling Equipment, Kingsclere Road, Basingstoke, RG21 6XJ
87. Universidad Politecnica De Valencia, Camino de Vera, 46071 VALENCIA, Spain.
88. Mayer, J.R.R. & Parker, G.A., 'A Portable Instrument for 3-D Dynamic Robot Measurements Using Triangulation and Laser Tracking', *IEEE Transactions on Robotics and Automation*, Vol. 10, No. 4, August 1994.
89. Mayer, R & Parker, GA, "Optical considerations in a 3D laser tracking instrument", Proceedings of the 6th international conference on robot vision and sensory controls, pp217-228, 1986
90. Mayer, RR, Parker, GA, "Calibration and assessment of a laser based instrument for robot dynamic measurement" 11th Triennial world congress international world measurement confederation", October 1988
91. Abdel-Aziz, Y. I., Karara, H. M., "Direct Linear Transformation From Comparator Co-ordinates Into Object-space Co-ordinates", Close-range Photogrammetry. American Society Of Photogrammetry. pp1-18, 1971

92. Freeman, J., "The calibration of Co-ordinate Measuring Machines using Machine Checking Gauges (A Feasibility Study)", Internal Report, Precision Engineering Centre, University of Huddersfield, 1998
93. Press, W.H., "Numerical Recipes in C", 2nd Edition, Cambridge University Press, 1992
94. Freeman, J., "Derivation of Mathematical Routines For Non-Cartesian Machines", Internal Report, Precision Engineering Centre, University of Huddersfield, 1997

## 12.01 Published papers

95. Longstaff A.P., Mavromihales M. and Ford D.G. "Calibration and correction methods of spatial errors found in Cartesian manipulators." Laser Metrology and Machine Performance III (LAMDAMAP 97), Computational Mechanics Publications, pp 431-441, 1997
96. Longstaff A.P., Freeman J.M., Postlethwaite S.R. and Ford D.G. "Practical calibration of tracking laser systems." Laser Metrology and Machine Performance IV (LAMDAMAP 99), Computational Mechanics Publications, pp39-50, 1999
97. Freeman J.M., Longstaff A.P. and Ford D.G. "A novel use of artefacts in non-Cartesian machine calibration." Laser Metrology and Machine Performance IV (LAMDAMAP 99), Computational Mechanics Publications, pp403-412, 1999
98. Longstaff AP, Postlethwaite SR and Ford DG "Assessment of the Volumetric Accuracy of a Machine with Geometric Compensation" Laser Metrology and Machine Performance V (LAMDAMAP 01), Wit Press, pp41-50, 2001.

# Appendix A Results of Measurement Uncertainty Simulation

## A.1 Volumetric simulation (summation) - summary of results

### A.1.01 Measured at origin – 1m$^3$ volume.

Volumetric Accuracy is **60.0µm** at X 0, Y 1000, Z 1000 (mm)

X axis algebraic minimum error = 16.0µm at X 0, Y 0, Z 0(mm)

X axis algebraic maximum error = 48.0µm at X 0, Y 1000, Z 1000(mm)

X axis error range = 32.0µm

Y axis algebraic minimum error = 16.0µm at X 0, Y 0, Z 0(mm)

Y axis algebraic maximum error = 34.0µm at X 0, Y 0, Z 1000(mm)

Y axis error range = 18.0µm

Z axis algebraic minimum error = 12.0µm at X 0, Y 1000, Z 0(mm)

Z axis algebraic maximum error = 16.0µm at X 0, Y 0, Z 0(mm)

Z axis error range = 4.0µm

### A.1.02 Measured at origin – 0.3m$^3$ volume

Volumetric Accuracy is **11.1µm** at X 0, Y 300, Z 300 (mm)

X axis algebraic minimum error = 0.0µm at X 0, Y 0, Z 0(mm)

X axis algebraic maximum error = 9.6µm at X 0, Y 300, Z 300(mm)

X axis error range = 9.6µm

Y axis algebraic minimum error = 0.0µm at X 0, Y 0, Z 0(mm)

Y axis algebraic maximum error = 5.4µm at X 0, Y 0, Z 300(mm)

Y axis error range = 5.4µm

Z axis algebraic minimum error = -1.2µm at X 0, Y 300, Z 0(mm)

Z axis algebraic maximum error = 0.0µm at X 0, Y 0, Z 0(mm)

Z axis error range = 1.2µm

## A.1.03 Measured centrally – 1m$^3$ volume

Volumetric Accuracy is **43.0µm** at X 0, Y 1000, Z 1000 (mm)

X axis algebraic minimum error = 0.0µm at X 0, Y 0, Z 0(mm)

X axis algebraic maximum error = 32.0µm at X 0, Y 1000, Z 1000(mm)

X axis error range = 32.0µm

Y axis algebraic minimum error = 7.0µm at X 0, Y 0, Z 0(mm)

Y axis algebraic maximum error = 25.0µm at X 0, Y 0, Z 1000(mm)

Y axis error range = 18.0µm

Z axis algebraic minimum error = 14.0µm at X 0, Y 1000, Z 0(mm)

Z axis algebraic maximum error = 18.0µm at X 0, Y 0, Z 0(mm)

Z axis error range = 4.0µm

## A.1.04 Measured centrally – 0.3m$^3$ volume

Volumetric Accuracy is **11.1µm** at X 0, Y 300, Z 300 (mm)

X axis algebraic minimum error = 0.0µm at X 0, Y 0, Z 0(mm)

X axis algebraic maximum error = 9.6µm at X 0, Y 300, Z 300(mm)

X axis error range = 9.6µm

Y axis algebraic minimum error = 0.0µm at X 0, Y 0, Z 0(mm)

Y axis algebraic maximum error = 5.4µm at X 0, Y 0, Z 300(mm)

Y axis error range = 5.4µm

Z axis algebraic minimum error = -1.2µm at X 0, Y 300, Z 0(mm)

Z axis algebraic maximum error = 0.0µm at X 0, Y 0, Z 0(mm)

Z axis error range = 1.2µm

## A.2 Volumetric simulation (RMS) - summary of results

## A.2.01 Measured at origin – 1m$^3$ volume.

Volumetric Accuracy is **26.2µm** at X 0, Y 1000, Z 1000 (mm)

X axis algebraic minimum error = 9.8μm at X 0, Y 0, Z 0(mm)
X axis algebraic maximum error = 18.5μm at X 0, Y 1000, Z 1000(mm)
X axis error range = 8.7μm

Y axis algebraic minimum error = 9.8μm at X 0, Y 0, Z 0(mm)
Y axis algebraic maximum error = 15.1μm at X 0, Y 0, Z 1000(mm)
Y axis error range = 5.3μm

Z axis algebraic minimum error = 9.8μm at X 0, Y 0, Z 0(mm)
Z axis algebraic maximum error = 10.6μm at X 0, Y 1000, Z 0(mm)
Z axis error range = 0.8μm

## A.2.02 Measured at origin – 0.3m$^3$ volume.

Volumetric Accuracy is **18.0μm** at X 0, Y 300, Z 300 (mm)
X axis algebraic minimum error = 9.8μm at X 0, Y 0, Z 0(mm)
X axis algebraic maximum error = 10.9μm at X 0, Y 300, Z 300(mm)
X axis error range = 1.1μm

Y axis algebraic minimum error = 9.8μm at X 0, Y 0, Z 0(mm)
Y axis algebraic maximum error = 10.4μm at X 0, Y 0, Z 300(mm)
Y axis error range = 0.6μm

Z axis algebraic minimum error = 9.8μm at X 0, Y 0, Z 0(mm)
Z axis algebraic maximum error = 9.9μm at X 0, Y 300, Z 0(mm)
Z axis error range = 0.1μm

## A.2.03 Measured centrally – 1m$^3$ volume.

Volumetric Accuracy is **19.7μm** at X 0, Y 0, Z 0 (mm)
X axis algebraic minimum error = 9.8μm at X 0, Y 500, Z 500(mm)
X axis algebraic maximum error = 12.6μm at X 0, Y 0, Z 0(mm)
X axis error range = 2.8μm

Y axis algebraic minimum error = 9.8μm at X 0, Y 0, Z 500(mm)

Y axis algebraic maximum error = 11.4µm at X 0, Y 0, Z 0(mm)

Y axis error range = 1.6µm

Z axis algebraic minimum error = 9.8µm at X 0, Y 500, Z 0(mm)

Z axis algebraic maximum error = 10.0µm at X 0, Y 0, Z 0(mm)

Z axis error range = 0.2µm

## A.2.04 Measured centrally – 0.3m$^3$ volume.

Volumetric Accuracy is **19.7µm** at X 0, Y 0, Z 0 (mm)

X axis algebraic minimum error = 10.3µm at X 0, Y 300, Z 300(mm)

X axis algebraic maximum error = 12.6µm at X 0, Y 0, Z 0(mm)

X axis error range = 2.3µm

Y axis algebraic minimum error = 10.1µm at X 0, Y 0, Z 300(mm)

Y axis algebraic maximum error = 11.4µm at X 0, Y 0, Z 0(mm)

Y axis error range = 1.3µm

Z axis algebraic minimum error = 9.8µm at X 0, Y 300, Z 0(mm)

Z axis algebraic maximum error = 10.0µm at X 0, Y 0, Z 0(mm)

Z axis error range = 0.2µm

## A.3 Detailed results of 1m$^3$ simulation measured at origin

Volumetric Simulation - Detailed Results

X axis algebraic minimum error = 16.0µm at X 0, Y 0, Z 0(mm)

| | |
|---|---|
| X axis linear positioning error | 8µm ( 50%) |
| Y axis straightness error in the X axis direction | 4µm ( 25%) |
| Z axis straightness error in the X axis direction | 4µm ( 25%) |
| X axis angular error about the Y axis | 0µm |
| Y axis angular error about the Y axis | 0µm |
| X axis angular error about the Z axis | 0µm |
| Squareness error in the XZ plane | 0µm |
| Squareness error in the XY plane | 0µm |

X axis algebraic maximum error = 48.0µm at X 0, Y 1000, Z 1000(mm)

X axis linear positioning error 8μm ( 17%)
Y axis straightness error in the X axis direction 4μm ( 8%)
Z axis straightness error in the X axis direction 4μm ( 8%)
X axis angular error about the Y axis 4μm ( 8%)
Y axis angular error about the Y axis 4μm ( 8%)
X axis angular error about the Z axis 4μm ( 8%)
Squareness error in the XZ plane 10μm ( 21%)
Squareness error in the XY plane 10μm ( 21%)

Y axis algebraic minimum error = 16.0μm at X 0, Y 0, Z 0(mm)
Y axis linear positioning error 8μm ( 50%)
X axis straightness error in the Y axis direction 4μm ( 25%)
Z axis straightness error in the Y axis direction 4μm ( 25%)
X axis angular error about the X axis 0μm
Y axis angular error about the X axis 0μm
Squareness error in the YZ plane 0μm

Y axis algebraic maximum error = 34.0μm at X 0, Y 0, Z 1000(mm)
Y axis linear positioning error 8μm ( 24%)
X axis straightness error in the Y axis direction 4μm ( 12%)
Z axis straightness error in the Y axis direction 4μm ( 12%)
X axis angular error about the X axis 4μm ( 12%)
Y axis angular error about the X axis 4μm ( 12%)
Squareness error in the YZ plane 10μm ( 29%)

Z axis algebraic minimum error = 12.0μm at X 0, Y 1000, Z 0(mm)
Z axis linear positioning error 8μm ( 67%)
X axis straightness error in the Z axis direction 4μm ( 33%)
Y axis straightness error in the Z axis direction 4μm ( 33%)
X axis angular error about the X axis -4μm ( -33%)

Z axis algebraic maximum error = 16.0μm at X 0, Y 0, Z 0(mm)
Z axis linear positioning error 8μm ( 50%)

| | |
|---|---|
| X axis straightness error in the Z axis direction | 4μm ( 25%) |
| Y axis straightness error in the Z axis direction | 4μm ( 25%) |
| X axis angular error about the X axis | 0μm |

# Appendix B Volumetric Simulation Results for CMM1

Machine Details

Name: CMM1 Serial No: Location: Company A

By: AL Date: PhD

Configuration: All axes associated with movement of the tool

Directory: C:\esp\DATA\CMM1

Active Error Components

Linear [Y]:Y axis linear positioning error:Yposa.rtl

Straightness [X]:Y axis straightness error in the X axis direction:Yinx.sty

Straightness [Z]:Y axis straightness error in the Z axis direction:Yinz.sty

Angular [Y]:Y axis angular error about the Y axis:Yaby.rta

Angular [X]:Y axis angular error about the X axis:Yabx.rta

Angular [Z]:Y axis angular error about the Z axis:Yabz.rta

Linear [X]:X axis linear positioning error:Xpos.rtl

Straightness [Y]:X axis straightness error in the Y axis direction:Xiny.stx

Straightness [Z]:X axis straightness error in the Z axis direction:Xinz.stx

Angular [X]:X axis angular error about the X axis:Xabx.rta

Angular [Y]:X axis angular error about the Y axis:Xaby.rta

Angular [Z]:Not active

Linear [Z]:Z axis linear positioning error:Zpos.rtl

Straightness [Y]:Z axis straightness error in the Y axis direction:Ziny.stz

Straightness [X]:Z axis straightness error in the X axis direction:Zinx.stz

Squareness Components

Squareness [YX] = -2500.0µm/m

Squareness [YZ] = -650.0µm/m

Squareness [XZ] = 700.0µm/m

Axes Offsets

Offset [Y] = -2170.000mm

Offset [X] = -1400.000mm

Offset [Z] = -783.000mm

Simulation Setup Details

Y axis Travel Limits -4400 to 0mm

Y axis Sim. Limits -4400 to 0mm

Y axis Step 220mm and Direction Forward

X axis Travel Limits -2800 to 0mm

X axis Sim. Limits -2800 to 0mm

X axis Step 140mm and Direction Forward

Z axis Travel Limits -800 to 0mm

Z axis Sim. Limits -800 to 0mm

Z axis Step 40mm and Direction Forward

## B.1 Volumetric simulation - summary of results

Y axis algebraic minimum error = -4260µm at Y -220, X 0, Z 0 (mm)

Y axis algebraic maximum error = 3724µm at Y -1540, X -2800, Z -800 (mm)

Y axis error range = 7984µm

X axis algebraic minimum error = -381µm at Y -3080, X -2800, Z -800 (mm)

X axis algebraic maximum error = 860µm at Y 0, X -700, Z 0 (mm)

X axis error range = 1241µm

Z axis algebraic minimum error = -212µm at Y -2200, X -1960, Z -720 (mm)

Z axis algebraic maximum error = 86µm at Y -4180, X 0, Z -480 (mm)

Z axis error range = 298µm

Volumetric Accuracy 4293µm at Y -220, X 0, Z 0 (mm)

## B.2 Volumetric simulation - detailed results

Y axis algebraic minimum error = -4260µm at Y -220, X 0, Z 0 (mm)

| | |
|---|---|
| Y axis linear positioning error | -11µm ( 0%) |
| X axis straightness error in the Y axis direction | -14µm ( 0%) |
| Z axis straightness error in the Y axis direction | 0µm |
| Y axis angular error about the X axis | -36µm ( 1%) |
| X axis angular error about the X axis | -10µm ( 0%) |
| Y axis angular error about the Z axis | -179µm ( 4%) |
| Squareness error in the YZ plane | -509µm ( 12%) |
| Squareness error in the YX plane | -3500µm ( 82%) |

Y axis algebraic maximum error = 3724µm at Y -1540, X -2800, Z -800 (mm)

| | |
|---|---|
| Y axis linear positioning error | 121µm ( 3%) |
| X axis straightness error in the Y axis direction | 3µm ( 0%) |
| Z axis straightness error in the Y axis direction | 0µm |
| Y axis angular error about the X axis | 2µm ( 0%) |
| X axis angular error about the X axis | -1µm |
| Y axis angular error about the Z axis | 88µm ( 2%) |
| Squareness error in the YZ plane | 11µm ( 0%) |
| Squareness error in the YX plane | 3500µm ( 94%) |

X axis algebraic minimum error = -381µm at Y -3080, X -2800, Z -800 (mm)

| | |
|---|---|
| X axis linear positioning error | -138µm ( 36%) |
| Y axis straightness error in the X axis direction | -227µm ( 60%) |
| Z axis straightness error in the X axis direction | 0µm |
| Y axis angular error about the Y axis | 1µm |
| X axis angular error about the Y axis | -5µm ( 1%) |
| Squareness error in the XZ plane | -12µm ( 3%) |

X axis algebraic maximum error = 860µm at Y 0, X -700, Z 0 (mm)

| | |
|---|---|
| X axis linear positioning error | 285µm ( 33%) |
| Y axis straightness error in the X axis direction | -19µm ( -2%) |
| Z axis straightness error in the X axis direction | 0µm |

| | |
|---|---|
| Y axis angular error about the Y axis | 23µm ( 3%) |
| X axis angular error about the Y axis | 23µm ( 3%) |
| Squareness error in the XZ plane | 548µm ( 64%) |

Z axis algebraic minimum error = -212µm at Y -2200, X -1960, Z -720 (mm)

| | |
|---|---|
| Z axis linear positioning error | 10µm ( -5%) |
| Y axis straightness error in the Z axis direction | -82µm ( 39%) |
| X axis straightness error in the Z axis direction | -121µm ( 57%) |
| Y axis angular error about the Y axis | -19µm ( 9%) |

Z axis algebraic maximum error = 86µm at Y -4180, X 0, Z -480 (mm)

| | |
|---|---|
| Z axis linear positioning error | 22µm ( 26%) |
| Y axis straightness error in the Z axis direction | -9µm ( -10%) |
| X axis straightness error in the Z axis direction | 12µm ( 14%) |
| Y axis angular error about the Y axis | 61µm ( 71%) |

# Appendix C Volumetric Simulation Results for CMM2

Machine Details

Name: CMM2 Serial No: Location: University

By: AL Date: PhD

Configuration: All axes associated with movement of the tool

Directory: C:\esp\DATA\Cmm2

Active Error Components

Linear [X]:X axis linear positioning error:Xpos.rtl

Straightness [Y]:X axis straightness error in the Y axis direction:Xhoriz.stx

Straightness [Z]:X axis straightness error in the Z axis direction:Xvert.stx

Angular [X]:X axis angular error about the X axis:Xroll.rta

Angular [Y]:X axis angular error about the Y axis:Xpitch.rta

Angular [Z]:X axis angular error about the Z axis:Xyaw.rta

Linear [Y]:Y axis linear positioning error:Ypos.rtl

Straightness [X]:Y axis straightness error in the X axis direction:Yinx.sty

Straightness [Z]:Y axis straightness error in the Z axis direction:Yinz.sty

Angular [Y]:Y axis angular error about the Y axis:Yroll.rta

Angular [X]:Y axis angular error about the X axis:Ypitch.rta

Angular [Z]:Not active

Linear [Z]:Z axis linear positioning error:Zpos.rtl

Straightness [X]:Z axis straightness error in the X axis direction:Zinx.stz

Straightness [Y]:Z axis straightness error in the Y axis direction:Ziny.stz

Squareness Components

Squareness [XY] = -2.0µm/m

Squareness [XZ] = 1.0µm/m

Squareness [YZ] = -3.0µm/m

Axes Offsets

Offset [X] = 674.000mm

Offset [Y] = 258.000mm

Offset [Z] = -200.000mm

Simulation Setup Details

X axis Travel Limits 0 to 995mm

X axis Sim. Limits 0 to 995mm

X axis Step 45mm and Direction Forward

Y axis Travel Limits 0 to 965mm

Y axis Sim. Limits 0 to 965mm

Y axis Step 45mm and Direction Forward

Z axis Travel Limits -295 to 0mm

Z axis Sim. Limits -295 to 0mm

Z axis Step 10mm and Direction Forward

## C.1 Volumetric simulation - summary of results

X axis algebraic minimum error = -18µm at X 990, Y 360, Z -5 (mm)

X axis algebraic maximum error = 7µm at X 90, Y 945, Z -5 (mm)

X axis error range = 25µm

Y axis algebraic minimum error = -5µm at X 45, Y 765, Z -295 (mm)

Y axis algebraic maximum error = 0µm at X 270, Y 135, Z -295 (mm)

Y axis error range = 5µm

Z axis algebraic minimum error = -9µm at X 495, Y 450, Z -35 (mm)

Z axis algebraic maximum error = 4µm at X 990, Y 45, Z -295 (mm)

Z axis error range = 13µm

Volumetric Accuracy 18µm at X 990, Y 360, Z -5 (mm)

## C.2 Volumetric simulation - detailed results

X axis algebraic minimum error = -18µm at X 990, Y 360, Z -5 (mm)

| | |
|---|---|
| X axis linear positioning error | -4µm ( 24%) |
| Y axis straightness error in the X axis direction | -6µm ( 33%) |
| Z axis straightness error in the X axis direction | -1µm |
| X axis angular error about the Y axis | -9µm ( 53%) |
| Y axis angular error about the Y axis | 3µm ( -16%) |
| X axis angular error about the Z axis | 0µm |
| Squareness error in the XZ plane | 0µm |
| Squareness error in the XY plane | 0µm |

X axis algebraic maximum error = 7µm at X 90, Y 945, Z -5 (mm)

| | |
|---|---|
| X axis linear positioning error | 6µm ( 80%) |
| Y axis straightness error in the X axis direction | 0µm |
| Z axis straightness error in the X axis direction | -1µm |
| X axis angular error about the Y axis | -1µm |
| Y axis angular error about the Y axis | 4µm ( 48%) |
| X axis angular error about the Z axis | 0µm |
| Squareness error in the XZ plane | 0µm |
| Squareness error in the XY plane | -1µm ( -18%) |

Y axis algebraic minimum error = -5µm at X 45, Y 765, Z -295 (mm)

| | |
|---|---|
| Y axis linear positioning error | -4µm ( 81%) |
| X axis straightness error in the Y axis direction | 0µm |
| Z axis straightness error in the Y axis direction | 0µm |
| X axis angular error about the X axis | 0µm |
| Y axis angular error about the X axis | -1µm |
| Squareness error in the YZ plane | 0µm |

Y axis algebraic maximum error = 0µm at X 270, Y 135, Z -295 (mm)

| | |
|---|---|
| Y axis linear positioning error | -2µm ( 412%) |
| X axis straightness error in the Y axis direction | 1µm (-254%) |
| Z axis straightness error in the Y axis direction | 0µm |

X axis angular error about the X axis 0µm

Y axis angular error about the X axis 0µm

Squareness error in the YZ plane 0µm

Z axis algebraic minimum error = -9µm at X 495, Y 450, Z -35 (mm)

Z axis linear positioning error 0µm

X axis straightness error in the Z axis direction -7µm ( 83%)

Y axis straightness error in the Z axis direction -2µm ( 22%)

X axis angular error about the X axis 0µm

Z axis algebraic maximum error = 4µm at X 990, Y 45, Z -295 (mm)

Z axis linear positioning error 3µm ( 73%)

X axis straightness error in the Z axis direction 0µm

Y axis straightness error in the Z axis direction 1µm

X axis angular error about the X axis 0µm

# Appendix D LaserTrace Commands

## D.1 Controller local controls

1. PHOTOCELL connector. Must be connected to the cable assembly supplied. Horizontal axis Control also provides PSU connections for photocell preamp contained in Pod.
2. C.A.T. connector. Must be connected to cable assembly supplied.
3. PHOTOCELL O/P lamp- Illuminated when laser is positioned on target sufficiently accurately to maintain or achieve TRACK mode.
4. PHOTOCELL LATCH lamp. Indicates that PHOTOCELL O/P lamp HAS BEEN illuminated since last POSITION command was issued. Used when searching for target.
5. POSITION lamp. Illuminated in POSITION mode, and extinguished in TRACK mode. Note that when TRACK/POSITION control is LOCAL, it is possible (though unusual) to operate with one axis TRACKing , and the other axis POSITIONing.
6. POSITION displays. 4-digit Hex display of current C.A.T. position. Range of display is 0000 to FFFF, which corresponds to the angular range marked on the inside of the hinged front cover. 0000 corresponds to the bottom/right of the target plane, as viewed from the Pod. (Note that it is Possible to force incorrect data onto this display by operating the LOCAL DATA LOAD switch whilst in TRACK mode.)
7. LOCAL DATA LOAD switch. Enters local POSITION and/or RANGE data when LOCAL is selected for either of these functions.
8. POSITION/TFRACK REMOTE/LOCAL switch. Selects computer (REMOTE) or front-panel (LOCAL) control of POSITION/TRACK modes.
9. TRACK/POSITION switch. Active only when LOCAL selected.
10. LOCAL POSITION SET switches. Hex data entry for use in LOCAL POSITION mode. 8000 corresponds to the nominal mid-point of the axis. This data is entered by operating the LOCAL DATA LOAD switch.
11. RANGE CONTROL REMOTE/LOCAL switch. Selects computer (REMOTE) or front panel (LOCAL) control of range data. When REMOTE is selected, range is entered in multiples of 0.1m. (e.g. for a range of 3m, enter 30).

    Note that loop instability can result if this data is set for a range shorter than the actual operating range. Optimum tracking performance will be realised only if the correct data is used.

12. LOCAL RANGE switches. This sets the gain for the control loop.

## D.2 Command list

**Notation**

'n' is a single decimal digit (O to 9).

'h' is a single hexadecimal character (O to 9, A to F).

'D' after a number shows that it is decimal.

'H' after a number shows that it is hexadecimal.

The character set used throughout is ASCII.

Commands sent to the Interface are executed only after receiving a carriage return, <cr> or line feed, <lf> terminator. Both may be sent, in either order, if desired. A number of commands may be sent as a single string, provided that the string length does not exceed 254 characters.

Some commands take two, or more parameters. These parameters may be separated from each other by any non-numeric character (commas are used in this text).

All output data is terminated with a <cr><lf> sequence.

All command characters may be sent as upper or lower case letters.

### D.2.01 Status

COMMAND - A :

SYNTAX - A

USE - Reads the current status of LaserTrace, including the mode (Track or Position), the Photocell and Latch outputs, and the two auxiliary input ports.

RETURNS - Two characters. The first is either 'T' or 'P', indicating TRACK or POSITION mode. The second is a 7 hexadecimal character, made up as follows:

BIT 0 - Photocell Output (I=beam on target)

BIT I - Photocell Latch Output (I=latch set)

BIT 2 - Signalling Input f1 (I=contacts closed) :BIT 3 - Signalling Input r2 (I=contacts closed)

### D.2.02 Centre

COMMAND - C :

SYNTAX - C

USE - Positions the beam to the nominal centre of the operating window (i.e. 32768D,3276E3D or E300OH'SOOOH).

10 0.1

## D.2.03 Datalog

COMMAND - D

SYNTAX - Dr,n

PARAMETERS r : Rate of data acquisition

The Datalog command is only actioned if LaserTrace is on target, in TRACK mode.

Readings are logged to the Interface card's internal memory until the log has finished, when the recorded data may be read.

1+ the log was terminated by an Abort command then the first string returned is the number of data pairs that have been logged - otherwise the first string returned is the Status as at the end of the log (in the same format as +or the 'A' command).--The data 11-ogged is returned next, in pairs, formatted as for the 'HV?' command (i.e. 'x,y' where 'x' and Iy' are in the selected number base).

## D.2.04 Find track

COMMAND - F

SYNTAX Fx,y

PARAMETERS x,y : Permitted values are valid numbers in the selected number base.

USE - Positions beam to horizontal angle 'x' and vertical angle I y', then enters TRACK mode as soon as possible (i.e. assuming a target is present, after transition time and overshoot time).

## D.2.05 Set horizontal

COMMAND – H

SYNTAX - Hx

PARAMETERS x : Permitted values are valid number in the selected number base.

USE - Sets beam horizontal position to 'x'.

DEFAULT - The beam is centred at power-on (i.e. x=32768D,BOOOH).

NOTE - If this command is followed by a Set Vert. command, then only one data strobe is issued (if enabled).

## D.2.06 Read horizontal

COMMAND - H?

SYNTAX - H?

USE - Reads beam horizontal position.

RETURNS - A number in the selected format.

## D.2.07 Read both axes

COMMAND – HV?

SYNTAX HV? USE - Reads beam horizontal and vertical positions. Only one data strobe is issued, (if enabled), thus axes are read simultaneously.

RETURNS - Two numbers, separated by a comma (,), in the selected format (i.e. 'x,y').

## D.2.08 Laser control

COMMAND - L

SYNTAX Ln

PARAMETERS - Permitted values are n=0 : Laser off n=l : Laser on

USE - Controls laser power. DEFAULT - LI

## D.2.09 Strobe mode

COMMAND – M

SYNTAX - Mn

PARAMETERS - Permitted values are :

n=0 Issue data strobe with all read/write commands.

n=l No strobe except with 'C' command.

USE - Permits synchronisation of multi-pod LaserTrace systems.

DEFAULT – M0

## D.2.10 Number format

COMMAND – N

SYNTAX - Nn

PARAMETERS - Permitted values are :

n=0 1. Selects decimal number format. This defines all written/read numbers to be integers in the range 0 to 65535. Numbers received from LaserTrace are always six digits long, with leading zeros as required.

n=l Selects hexadecimal number format. This defines all numbers to be in the form hhhh.

DEFAULT – N0

## D.2.11 Position

COMMAND – P

SYNTAX - P

USE - Sets LaserTrace in Position mode - Default.

COMMAND - q : Data Strobe SYNTAX - 0

USE - The Im' and 10. commands are provided so that the acquisition of data from moving targets can be synchronised.

## D.2.12 Set range

COMMAND – R

SYNTAX - Rx

PARAMETERS x : Permitted values are : valid numbers in the selected format, equal to distance from Pod to target, expressed in multiples of 0.1m. Maximum value is 99D or 0099H.

USE - Sets gain of Axis Controllers for optimum performance. DEFAULT - 0099H.

## D.2.13 Search about a point

COMMAND – S

SYNTAX Sh,v,width,height,d

PARAMETERS –

h : Horizontal position of centre of search

v : Vertical position of centre of search width horizontal size of search area height vertical size of search area

d : horizontal increment of vertical sweeps All parameters are valid---numbers in the selected format.

USE - To search for, and lock onto, a target believed to be at or near a point.

This command first checks the Status to see if the beam is already on-target - if so, Track mode is entered. Otherwise, the search proceeds by making a vertical sweep from the start position, incrementing horizontally by d then repeating. When the target is crossed, the last vertical swept line is searched until the target is found, when Track mode is entered.
The value of 'd' used should be such as to produce horizontal increments of about 2mm.

## D.2.14 Track

COMMAND – T

SYNTAX - T

USE Sets LASERTRACE in Track mode.

NOTE This command is ignored if beam is not on target. As a safeguard, LASERTRACE reverts to Position mode if Track is

lost for any reason.

## D.2.15 Set vertical

COMMAND – V

SYNTAX - V

PARAMETERS x : Permitted values are valid number in the selected number base.

USE - Sets beam vertical position to 'x'.

DEFAULT - The beam is centred at power-on (i.e. x=32768D,BOOOH).

## D.2.16 Read vertical

COMMAND - V?

SYNTAX - V? USE - Reads beam vertical position.

RETURNS - A number in the selected format.

## D.2.17 Search window

COMMAND – W

SYNTAX - Whl,vl,h2,v2,d

PARAMETERS

h1 : Horizontal position of start of search

v1 : Vertical position of start of search

h2 : Horizontal position of end of search

v2 : Vertical position of end of search

d horizontal increment of vertical sweeps All parameters are valid numbers in the selected format.

USE - To search for, and lock onto, a target believed to be in the specified area.

This command first checks the Status to see if the beam is already on-target - if so, Track mode is entered. Otherwise the search proceeds by making a vertical sweep from the start position, incrementing horizontally by d and repeating. When the target is crossed, the last vertical swept line is searched until the target is found, when Track mode is entered.

The value of 'd' used should be such as to produce horizontal increments of about 2mm.

## D.2.18 Read all data

COMMAND ?

SYNTAX - ?

USE - To read LASERTRACE Status and beam coordinates.

RETURNS - A string consisting of the Status and horizontal and vertical positions, all separated by commas (i.e. Ia,hhhh,vvvv').

## D.2.19 Abort

COMMAND - <Esc>

SYNTAX - <Esc>, (ASCII 27)

USE - To abort a datalog.

NOTE - This command is recognised without any termination

# Appendix E Selected LaserTrace control program code

## E.1 poderror.c

```
// This file contains the error handling for communication with LaserTrace
// and laser status interpretation

#include "podfunc.h"
#include "headers.h"
#include "chpib.h"
short error;            /*Error function return value*/
//*****************************************************************
//***                  ERROR HANDLER              ***
//*****************************************************************

void error_handler (int error, char *routine)
{
char      well;
if (error != NOERR)
    {
        printf ("Error in call to %s \n", routine);
        printf ("     Error = %d : %s \n", error, errstr(error));
        printf ("Press <Q> to exit, any other key to continue: ");
        well=toupper(getch());
        printf("Continue:\n");
        if(well=='Q') abort();
    }
}

char *errstr (int errval)
{
 switch (errval) {
    case NOERR:     return (" No error ");
```

```
case EUNKNOWN:  return (" Unknown error ");
case ESEL:      return (" Invalid select code or device address ");
case HERANGE:   return (" Value out of range ");
case ETIME:     return (" Timeout ");
case ECTRL:     return (" HP-IB must be controller ");
case EPASS:     return (" Pass control not permitted ");
case ENUMB:     return (" Invalid Number ");
    case EADDR:     return (" Improper addressing ");
    case EFILE:     return (" File I/O Error ");
    }  /* end switch */
return (" Unexpected error!!! ");
}

//*************************************************************************
//***                    STATUS COMMAND ERROR HANDLER                   ***
//*************************************************************************
int analyse_status(char *status,int disperr)
// Disperr is used for displaying messages
//  1 - all explanatory, 2 message code and explanatory, 0 - nothing
{
    int available;
    int READY=0,NOT_ON=1,CORRUPTION=2,ILLEGAL=3;

    if (disperr= =2){
    printf("Track message is: %s\t",status);
     disperr=1;
  }
if (status= ="ILL"){
    if (disperr= =1)printf("ILLEGAL CALL TO LASERS.\n");
    available=ILLEGAL;
}
switch(status[0]){
     case 'T':if (disperr==1)printf("Laser in track mode\t");
```

```
                available=READY;
                break;
case 'P': if (disperr==1)printf("Laser in position mode\t");
                available=NOT_ON;
                break;
case 'I':  available=ILLEGAL;
                break;
     default: if (disperr==1)printf("First bit contains unknown character.\n");
                available=CORRUPTION;
                break;
 }
if (disperr==1){
 switch(status[1]){
     case '0':  printf("Beam off target\t Latch not set.\n");
                break;
     case '1':  printf("Beam on target\t Latch not set.\n");
                break;
case '2':  printf("Beam off target\t Latch set.\n");
                break;
case '3':  printf("Beam on target\t Latch set.\n");
                break;
case '4':  printf("Beam off target\t Latch not set.\n");
                printf("Input 1 closed\t Input 2 open\n");
                break;
case '5':  printf("Beam on target\t Latch not set.\n");
                printf("Input 1 closed\t Input 2 open\n");
                break;
case '6':  printf("Beam off target\t Latch set.\n");
                printf("Input 1 closed\t Input 2 open\n");
                break;
case '7':  printf("Beam on target\t Latch set.\n");
                printf("Input 1 closed\t Input 2 open\n");
                break;
```

```
case '8':  printf("Beam off target\t Latch not set.\n");
                printf("Input 1 open\t Input 2 closed\n");
                break;
case '9':  printf("Beam on target\t Latch not set.\n");
                printf("Input 1 open\t Input 2 closed\n");
                break;
case 'A': printf("Beam off target\t Latch set.\n");
                printf("Input 1 open\t Input 2 closed\n");
                break;
case 'B': printf("Beam on target\t Latch set.\n");
                printf("Input 1 open\t Input 2 closed\n");
                break;
case 'C': printf("Beam off target\t Latch not set.\n");
                printf("Input 1 closed\t Input 2 closed\n");
                break;
case 'D': printf("Beam on target\t Latch not set.\n");
                printf("Input 1 closed\t Input 2 closed\n");
                break;
case 'E': printf("Beam on target\t Latch set.\n");
                printf("Input 1 closed\t Input 2 closed\n");
                break;
case 'L':   if(available!=ILLEGAL) available=CORRUPTION;
                break;        // ILL message handler
default:      printf("Second bit contains unknown character.\n");
                available=CORRUPTION;
                break;
}
}
else if((available!=ILLEGAL)&&status[1]=='L') available=CORRUPTION;
     // ILL Message handler for non-display case
 return(available);
}
```

# Appendix F Brief pseudo-code of the UMD model

## F.1 Initialisation of the UMD data

Load the 14 simple model parameters

Load the full model data:

Input_Sensor(sensor,'sensor.sen'); {Read in local coordinates for the sensor head from file 'sensor.sen' into data structure sensor}

Input_Sensor(door1,'door1.sen'); {Read in local coordinates for door1.....}

Input_Sensor(door2,'door2.sen'); {Read in local coordinates for door2.....}

Input_Sensor(door3,'door3.sen'); {Read in local coordinates for door3.....}

set_values(tri_geom); {Read in the data defining the structure of the UMD. The numerical values and the definitions are required in the full model. The file is chosen at run time by menu from all the available *.geo files and also contains details enabling a wire-frame model that can be drawn on screen.

Input_Stay_Lengths(Obs_Stay_Len,'Stays.sen'); {Read in the lengths of the 6 stays}

## F.2 Model algorithms

## F.2.01 The general model

Procedure General_Model (var Paras:Vector_Type;

No_Para:integer;

Obs_Stay_Len:Vector_Type;

x,y,z:extended;

Tol:real);

{ This routine takes as input x, y, z and calculates p, q, r, and the three tilts of the sensor all stored in the array Paras. Paras must initially have a starting guess of the p, q and r values but the tilts can be set initially to zero. It is best to use the simple model to find the initial p,q,r}

{'Alph' is a structure set up locally to contain the x,y,z rotations of the sensor}

count:=0; s:=1;

```
REPEAT

 Set all delta[i] for all parameters =0.1;
 p=paras[1]; q=paras[2];  r=paras[3];
 alph.xrot = paras[4];  alph.yrot = paras[5];  alph.zrot = paras[6];
 Calc_Stays(tri_geom,alph,p, q, r,x,y,z,Calc_Stay_Len);
{Find stay lengths by Pythagoras}

  For all parameters error[i] =calc_Stay_Len[i]-Obs_Stay_Len[i];
{Find errors in stay lengths}
{Perform 0.1 mm perturbations to find derivatives dp/dx  etc that make up J.  Uses first
order differences only }
 for each parameter     paras[i] = paras[i] + delta[i];  {Add perturbations}
                        p:=paras[1];          q:=paras[2];          r:=paras[3];
                        alph.xrot:=paras[4];  alph.yrot:=paras[5];  alph.zrot:=paras[6];
                        Calc_Stays(tri_geom,alph,p, q, r,x,y,z,pert);
                                                          {Find new stay lengths}
                        for each parameter  J[k,i]:=(pert[k]-Calc_Stay_Len[k])/delta[i];
                                                          {Find partial derivative}
                        paras[i]:=paras[i]-delta[i]; { Subtract perturbations }

Invert_Todd_Mat(J,INVJ,No_Para);   {Invert the J matrix}

for each parameter      delta[i]:=0;
                        for each parameter k, delta[i]=delta[i]+INVJ[i,k]*error[k];
                                                          {Calculate corrections}
for each parameter  paras[i]:=paras[i]-s*delta[i];        {Apply corrections }
count:=count+1;
until within_tolerance (delta,6,tol);  { Repeats until magnitude of all delta < tol}
```

## F.2.02 The general inverse model

```
Procedure General_Inverse_Model(var Paras:Vector_Type;
                                No_Para:integer;
```

```
                    Obs_Stay_Len:Vector_Type;
                    p,q,r:extended;
                    Tol:real);
{ This routine takes as input p,q,r and calculates x,y,z,
  and the three tilts of the sensor all stored in the array Paras
  Paras must initially have a starting guess of the x, y and z values but
  the tilts can be set initially to zero. It is best to use the simple inverse
   model to find the initial x,y,z}

count:=0;  s:=1;
REPEAT
 For all parameters   delta[i]=0.1;
 x:=paras[1];   y:=paras[2];   z:=paras[3];
 alpha.xrot:=paras[4];   alpha.yrot:=paras[5];   alpha.zrot:=paras[6];

 Calc_Stays(tri_geom,alpha,p, q, r,x,y,z,Calc_Stay_Len);
 for i:=1 to No_Para do error[i]:=calc_Stay_Len[i]-Obs_Stay_Len[i];
{Calculate stay errors}
                {0.1 mm perterbations to find derivatives dp/dx etc that make up J. Uses first
order differences only }
 For all parameters
    paras[i]:=paras[i]+delta[i];
    x:=paras[1];
    y:=paras[2];
    z:=paras[3];
    alpha.xrot:=paras[4];
    alpha.yrot:=paras[5];
    alpha.zrot:=paras[6];
    Calc_Stays(tri_geom,alpha,p, q, r,x,y,z,pert);

    for k:=1 to No_Para do    J[k,i]:=(pert[k]-Calc_Stay_Len[k])/delta[i];
                                        {Calcualte the Jacobean}
    paras[i]:=paras[i]-delta[i];
```

```
Invert_Todd_Mat(J,INVJ,No_Para);

For all parameters delta[i]:=0;
For all parameters  delta[i]:=delta[i]+INVJ[i,k]*error[k];
 For all parameters  paras[i]:=paras[i]-s*delta[i];
 count:=count+1;
until within_tolerance(delta,6,tol); {Until absolute value of all delta < tol}
```

## F.2.03 Calculation of all stay lengths by Pythagoras

```
Procedure Calc_Stays(var Tri_Geom:Triangulation_Array_Type;
                     alp:angle_Type;
                     pp, qp, rp:extended;
                     xp,yp,zp:extended;
                     var Calc_Stay_Len:Vector_Type);
with tri_geom do
{Rotate sensor by best guess of tilt of sensor}
    rotate_z(sensor,rotated_sensor,alp.zrot);
                          {Rotates sensor about z by alp.zrot to give rotated_sensor}
rotate_x(rotated_sensor,rotated_sensortemp,alp.xrot);
rotate_y(rotated_sensortemp,rotated_sensor,alp.yrot);
{Now move sensor to correct x,y,z position}
Translate_Sensor(rotated_sensor,translated_sensor,xp-rotated_sensor[7].x
                 ,yp-rotated_sensor[7].y,zp-rotated_sensor[7].z);
{Now combine sensor with tri_geom}
Add_Sensor_To_Record(Translated_Sensor,tri_geom,7,14);

{Now rotate door1 by rp and slight errors in orientation}
Rotate_x(door1,rotated_sensor,rp);
{Now translate door1}
Rotate_y(rotated_sensor,rotated_sensortemp,
          (trian[6].zz-trian[5].zz)/(trian[6].xx-trian[5].xx));
Rotate_z(rotated_sensortemp,rotated_sensor,
          (trian[6].yy-trian[5].yy)/(trian[6].xx-trian[5].xx));
```

```
Translate_Sensor(rotated_sensor,translated_sensor,trian[5].xx,
        trian[5].yy,trian[5].zz);
  {Now add door 1 to tri_geom}
Add_Sensor_To_Record(Translated_Sensor,tri_geom,15,16);
{Now rotate door2 by pp and slight errors in orientation}
Rotate_z(door2,rotated_sensor,pp);
{Now translate door2}
Rotate_x(rotated_sensor,rotated_sensortemp,
            (trian[3].yy-trian[1].yy)/(trian[1].zz-trian[3].zz));
Rotate_y(rotated_sensortemp,rotated_sensor,
            (trian[3].xx-trian[1].xx)/(trian[1].zz-trian[3].zz));

Translate_Sensor(rotated_sensor,translated_sensor,trian[3].xx,
        trian[3].yy,trian[3].zz);
{Now add door 2 to tri_geom}
Add_Sensor_To_Record(Translated_Sensor,tri_geom,17,18);

{Now rotate door3 by qp and slight errors in orientation}
Rotate_z(door3,rotated_sensor,-qp);
{Now translate door 3}
Rotate_x(rotated_sensor,rotated_sensortemp,
            (trian[4].yy-trian[2].yy)/(trian[2].zz-trian[4].zz));
Rotate_y(rotated_sensortemp,rotated_sensor,
            (trian[4].xx-trian[2].xx)/(trian[2].zz-trian[4].zz));

Translate_Sensor(rotated_sensor,translated_sensor,trian[4].xx,
        trian[4].yy,trian[4].zz);
{Now add door 3 to tri_geom}
Add_Sensor_To_Record(Translated_Sensor,tri_geom,19,20);


{ Now calculate six strut lengths as distance between points 11,15 ; 12,16 etc}
```

```
Calc_Stay_Len[1]:=Distance_Between(tri_geom,11,15);{Uses Pythagoras on known
x,y,z's}
Calc_Stay_Len[2]:=Distance_Between(tri_geom,12,16);
Calc_Stay_Len[3]:=Distance_Between(tri_geom,7,18);
Calc_Stay_Len[4]:=Distance_Between(tri_geom,10,17);
Calc_Stay_Len[5]:=Distance_Between(tri_geom,8,20);
Calc_Stay_Len[6]:=Distance_Between(tri_geom,9,19);
```

## F.2.04 Calculation of distance between two points by Pythagoras

```
Function Distance_Between(var tri_geo:triangulation_array_type;
                          Point1,Point2:integer):extended;
{Finds the distance between point Point1 and Point2 in record tri_geo}
using record  tri_geo
    if point1>=0 then

        if point2>=0 then
          distance_Between = sqrt( sqr(trian[point1].xx-trian[point2].xx)
                  +sqr(trian[point1].yy-trian[point2].yy)
                  +sqr(trian[point1].zz-trian[point2].zz))
        else
          distance_Between = sqrt( sqr(trian[point1].xx-trian[abs(point2)].xxalt)
                  +sqr(trian[point1].yy-trian[abs(point2)].yyalt)
                  +sqr(trian[point1].zz-trian[abs(point2)].zzalt))
    else

        if point2>=0 then
          distance_Between:= sqrt( sqr(trian[abs(point1)].xxalt-trian[point2].xx)
                  +sqr(trian[abs(point1)].yyalt-trian[point2].yy)
                  +sqr(trian[abs(point1)].zzalt-trian[point2].zz))
        else
          distance_Between:= sqrt( sqr(trian[abs(point1)].xx-trian[abs(point2)].xxalt)
                  +sqr(trian[abs(point1)].yy-trian[abs(point2)].yyalt)
```

```
+sqr(trian[abs(point1)].zz-trian[abs(point2)].zzalt))
```

## F.2.05 Pack sensor or door into record

```
Procedure Add_Sensor_To_Record(sensor:points_type;
                    var tri_geo:triangulation_array_type;
                    Start_point,End_point:integer);

using record  tri_geo
   for  all points I from Start_point to End_point
          tri_geo.trian[i].xx:=sensor[i-Start_point+1].x;
          tri_geo.trian[i].yy:=sensor[i-Start_point+1].y;
          tri_geo.trian[i].zz:=sensor[i-Start_point+1].z;
```

## F.2.06 Rotate  sensor or door about x axis

```
Procedure Rotate_X(var sensor,rotated_sensor:points_type;angle:extended);


 for i=1 to sensor[1].N    { ie. for all points}
    rotated_Sensor[i].N =sensor[i].N;
    rotated_sensor[i].x = sensor[i].x;
    rotated_sensor[i].y = sensor[i].y*cos(angle) - sensor[i].z*sin(angle);
    rotated_sensor[i].z = sensor[i].y*sin(angle) + sensor[i].z*cos(angle);
```

## F.2.07 Rotate  sensor or door about y axis

```
Procedure Rotate_Y(var sensor,rotated_sensor:points_type;angle:extended);


  for i=1 to sensor[1].N do   { ie. for all points}
    rotated_Sensor[i].N =sensor[i].N;
    rotated_sensor[i].x =+sensor[i].x*cos(angle) + sensor[i].z*sin(angle);
    rotated_sensor[i].y =sensor[i].y;
    rotated_sensor[i].z =-sensor[i].x*sin(angle) + sensor[i].z*cos(Angle);
```

## F.2.08 Rotate  sensor or door about z axis

```
Procedure Rotate_Z(var sensor,rotated_sensor:points_type;angle:extended);
```

```
for I=1 to sensor[1].N do   { ie. for all points}
    rotated_Sensor[i].N =sensor[i].N;
    rotated_sensor[i].x =+sensor[i].x*cos(angle) - sensor[i].y*sin(angle);
    rotated_sensor[i].y =+sensor[i].x*sin(angle) + sensor[i].y*cos(angle);
    rotated_sensor[i].z =sensor[i].z;
end;
end;
```

## F.2.09 Translate sensor or door

```
Procedure Translate_Sensor(var sensor,Translated_sensor:points_type;x,y,z:extended);
 for i=1 to sensor[1].N  { ie. for all points}
  begin
  Translated_Sensor[i].N:=sensor[i].N;
  Translated_sensor[i].x:=sensor[i].x+x;
  Translated_sensor[i].y:=sensor[i].y+y;
  Translated_sensor[i].z:=sensor[i].z+z;
   end;
end;
```

# Appendix G Brief pseudo-code of the UMD thermal model

## G.1 Initialisation of UMD data

```
expcoal:=0.000022; {expansion coefficient of aluminium per DegC}
expcocf:=0.000001; {expansion coefficient of carbon fibre per DegC}

{Read in local sensor coordintes}
Input_Sensor(sensor,'acsensor.sen');        {Reads in local coordintes for sensor}
Input_Sensor(door1,'acdoor1.sen');          {Reads in local coordintes for door 1}
Input_Sensor(door2,'acdoor2.sen');          {Reads in local coordintes for door 2}
Input_Sensor(door3,'acdoor3.sen');          {Reads in local coordintes for door 3}
set_values(tri_geom);                       {Read in data defining the structure of the UMD}
Input_Stay_Lengths(Obs_Stay_Len,'Stays.sen'); {Read in the lengths of the 6 stays}
set_arc_datum(pdatum,qdatum,rdatum)         {Set the thermal datum for the scale arcs}
Load_L_Values(L0,'nom.dat')                 {Load nominal values for simple model
                                             parameters}
Load_L_Values(L,'full_par.dat')             {Load nominal values for full model
                                             parameters}
Get_test_data(temps_file, pgr_file, xx, yy, zz)
                                            {Select thermal and encoder data files for
the test and specify the x, y and z position of the ruby that was used}
```

## G.2 Model algorithms

### G.2.01 Main procedure

```
odoor1:=door1; odoor2:=door2; odoor3:=door3;   {saves copy of unexpanded doors}
otri_geom:=tri_geom;                           {saves copy of unexpanded UMD}
oObs_Stay_Len:=Obs_Stay_Len;                   {saves copy of unexpanded stays}
osensor:=sensor;                               {saves copy of unexpanded stays}
```

```
        {Load first value of encoders – the datum for the test}
        for ai:=1 to 3 do begin
    read(pqrfile,pqrorig[ai]);
        end;
reset(pqrfile);
pqrinconv:=3600*180/PI;              {conversion factor from radians to arcseconds}
ai:=0;{set ai as the loop counter}
while not(eof(pqrfile))do begin      {This is the main loop}
 ai:=ai+1;
 if not (eof(pqrfile)) then begin
   {Now read p,q,r values}
   read(pqrfile,ttempval);                          {read p into temporary double}
   ttempval:=(ttempval-pqrorig[1])*pqrinconv;       {remove datum and convert to radians}
   sety(graphpms,ai,ttempval);                      {put p value into storage vector)
   read(pqrfile,ttempval);                          {read q into temporary double}
   ttempval:=(ttempval-pqrorig[2])*pqrinconv;       {remove datum and convert to radians}
   sety(graphqms,ai,ttempval);                      {put q value into storage vector)
   read(pqrfile,ttempval);                          {read r into temporary double}
   ttempval:=(ttempval-pqrorig[3])*pqrinconv;       {remove datum and convert to radians}
   sety(graphrms,ai,ttempval);                      {put r value into storage vector)

        {Now read temperature values for each component}
for aj:=1  to no_temps do
    begin                                           {loop for each component}
     read(temps_file,therm[aj]);
    if ai=1 then
       origtherm[aj]:=therm[aj];                    {store datum temperatures}
    end;                          {Finished reading in temperatures for this time increment}

Find_Angles(xx,yy,zz,L0,p0,q0,r0);       {provides p,q,r estimates from simple model}

{Simulate heating of column}
 heat_col(otri_geom,tri_geom,therm[5]-origtherm[5],expcoal);
```

```
{Calculate thermal expansion in each of the three doors}
 Heat_door(odoor1,door1,therm[6]-origtherm[6],expcoal);
 Heat_door(odoor2,door2,therm[7]-origtherm[7],expcoal);
 Heat_door(odoor3,door3,therm[8]-origtherm[8],expcoal);

{Calculate thermal expansion in the quill}
 Heat_sensor(osensor,sensor,therm[10]-origtherm[10],expcocf);

{Now obtain p, q, r and quill tilts from the general model
 General_Model(Paras,6,Obs_Stay_Len,xx,yy,zz,0.0000001);

 pp:=paras[1];  {p,q,r from full model}
 qp:=paras[2];
 rp:=paras[3];
 alpha.xrot:=paras[4]; {quill tilts from full model}
 alpha.yrot:=paras[5];
 alpha.zrot:=paras[6];

{Calculate thermal expansion in the scales}
 pp:=(pp+pdatum)*(1+expcoal*(therm[2]-20))-pdatum;
qp:=(qp+qdatum)*(1+expcoal*(therm[2]-20))-qdatum;
rp:=(rp+rdatum)*(1+expcoal*(therm[2]-20))-rdatum;
 if ai=1 then begin        {store datum value for calculated p, q, r}
    por:=pp;     qor:=qp;     ror:=rp;
 end;

          {Convert to arcseconds and remove datum}
     sety(graphp,ai,3600*180/PI*(pp-por));
     sety(graphq,ai,3600*180/PI*(qp-qor));
     sety(graphr,ai,3600*180/PI*(rp-ror));
end                                                    {complete loop}
```

## G.2.02 Heat door

```
Procedure Heat_door(origdoor:points_type;
                    var newdoor:points_type;
                    deltatemp:real;
                    expco:real);
Begin
    for i:=1 to 4 do begin
    newdoor[i].x:=origdoor[i].x+origdoor[i].x*deltatemp*expco;
    newdoor[i].y:=origdoor[i].y+origdoor[i].y*deltatemp*expco;
    newdoor[i].z:=origdoor[i].z+origdoor[i].z*deltatemp*expco;
    end
End;
```

## G.2.03 Heat sensor

```
Procedure Heat_sensor(origsensor:points_type;
                      var newsensor:points_type;
                      deltatemp:real;
                      expco:real);
Begin
    for i:=1 to 8 do
    begin
    newsensor[i].x:=origsensor[i].x+origsensor[i].x*deltatemp*expco;
    newsensor[i].y:=origsensor[i].y+origsensor[i].y*deltatemp*expco;
    newsensor[i].z:=origsensor[i].z+origsensor[i].z*deltatemp*expco;
    end
End;
```

## G.2.04 Heat column

```
Procedure Heat_col(tri_geom:triangulation_array_type;
                   var expanded_tri_geom:triangulation_array_type;
                   deltatemp:real;
                   expco:real);
Begin
```

```
xmid:=(tri_geom.trian[1].xx+tri_geom.trian[2].xx)/2;
ymid:=(tri_geom.trian[1].yy+tri_geom.trian[5].yy)/2;

for i:=1 to 6 do
begin
   expanded_tri_geom.trian[i].xx:=(1+deltatemp*expco)*
                                  (tri_geom.trian[i].xx-xmid)+xmid;
   expanded_tri_geom.trian[i].yy:=(1+deltatemp*expco)*
                                  (tri_geom.trian[i].yy-ymid)+ymid;
   expanded_tri_geom.trian[i].zz:=(1+deltatemp*expco)*
                                  tri_geom.trian[i].zz;
end
End;
```